

INFORMATION TO USERS

This manuscript has been reproduced from the microfilm master. UMI films the text directly from the original or copy submitted. Thus, some thesis and dissertation copies are in typewriter face, while others may be from any type of computer printer.

The quality of this reproduction is dependent upon the quality of the copy submitted. Broken or indistinct print, colored or poor quality illustrations and photographs, print bleedthrough, substandard margins, and improper alignment can adversely affect reproduction.

In the unlikely event that the author did not send UMI a complete manuscript and there are missing pages, these will be noted. Also, if unauthorized copyright material had to be removed, a note will indicate the deletion.

Oversize materials (e.g., maps, drawings, charts) are reproduced by sectioning the original, beginning at the upper left-hand corner and continuing from left to right in equal sections with small overlaps.

**ProQuest Information and Learning
300 North Zeeb Road, Ann Arbor, MI 48106-1346 USA
800-521-0600**

UMI[®]

A Study of Bubble Dynamics and Some Metals Processing

Applications

Ali Reza Naji Meidani

Department of Mining, Metals and Materials Engineering
McGill University
Montreal, Canada.

A thesis submitted to the Faculty of Graduate Studies and Research
in partial fulfillment of the requirement for the degree of
Doctor of Philosophy.

© Ali Reza Naji Meidani

July, 2001



**National Library
of Canada**

**Acquisitions and
Bibliographic Services**

**395 Wellington Street
Ottawa ON K1A 0N4
Canada**

**Bibliothèque nationale
du Canada**

**Acquisitions et
services bibliographiques**

**395, rue Wellington
Ottawa ON K1A 0N4
Canada**

Your file Votre référence

Our file Notre référence

The author has granted a non-exclusive licence allowing the National Library of Canada to reproduce, loan, distribute or sell copies of this thesis in microform, paper or electronic formats.

The author retains ownership of the copyright in this thesis. Neither the thesis nor substantial extracts from it may be printed or otherwise reproduced without the author's permission.

L'auteur a accordé une licence non exclusive permettant à la Bibliothèque nationale du Canada de reproduire, prêter, distribuer ou vendre des copies de cette thèse sous la forme de microfiche/film, de reproduction sur papier ou sur format électronique.

L'auteur conserve la propriété du droit d'auteur qui protège cette thèse. Ni la thèse ni des extraits substantiels de celle-ci ne doivent être imprimés ou autrement reproduits sans son autorisation.

0-612-75666-1

Canada

ABSTRACT

In this research the dynamics of a non-reactive and a reactive gas bubble under various pressure fields are studied. Comprehensive mathematical models have been developed to simulate the dynamic behavior of different gas bubbles. On the basis of these models several features of thermo-fluid mechanical behavior of gas bubbles are then discussed and their applications for the metals processing operations are described. The mathematical models form a set of coupled, highly nonlinear and stiff differential equations, which have been solved numerically by a modified Gear method.

The first part of this study is concerned with the transient dynamic behavior of a hydrogen gas bubble in a solidifying aluminium-3.4 wt pct copper alloy melt under various ultrasonic pressure fields. During the process of bubble collapse, the melt pressure surrounding the bubble is seen to increase very rapidly. The variations of pressure and supercooling in the melt surrounding the bubble can cause bulk crystallization. If the pressure in the vicinity of the dendrites exceeds a threshold value, dendrite fracturing takes place. Dendrite fragments become nuclei during metal crystallization in an ultrasonic field, which lead to the refined crystalline structure of the metal. The results show that adjacent to the bubble surface, the peak pressure generated in the melt is in the order of several hundreds to thousands atmospheres depending on the initial bubble size, pressure of undisturbed melt and the ultrasonic's specifications. Moreover, the results, which are obtained for pre-resonant, resonant and post-resonant frequencies, show that the ultrasonic frequencies, beyond the resonance frequency of the bubble, do not have any useful effect on the melt.

The second part of this study is related to the dynamics of a stable bubble under various ultrasonic pressure fields. When the imposed pressure field is beyond a threshold value, dissolved gas in the liquid flows into the gas bubbles by rectified diffusion. In this case, the bubbles grow sufficiently to float to the surface due to the hydrodynamic buoyancy force. The threshold pressure and the effects of bubble size and ultrasonic specifications on rectified diffusion of the dissolved air in water with different initial

concentrations are studied. The results show that the air bubble grows and the time-averaged bubble volume reaches several times of its initial value when the ultrasonic pressure amplitude is more than the threshold pressure. Also, the numerical results show that, above the threshold pressure a hydrogen bubble grows and the bubble volume increases several times its initial value by rectified diffusion of dissolved hydrogen present in a molten aluminium alloy.

In order to validate the mathematical model of bubble growth by rectified diffusion, an aqueous physical modelling has been developed. The experimental-setup was designed to carry out a physical study concerning the bubble growth under an ultrasonic pressure field. The results of aqueous physical modelling for bubble growth are compared with the results of the mathematical model, which show a reasonable agreement between the experiments and the predictions.

The final part of this study consists of the complex dynamic behavior of a reactive gas bubble immersed in a nonreactive liquid under various liquid impulse pressures. Numerical investigations are conducted into the collapse and explosion of an isolated oxygen-hydrogen bubble immersed in water and in glycerin. The results show that, if the imposed pressure field is strong enough, the bubble is seen to explode. The maximum gas temperature and gas pressure that the bubble attains depends directly upon the initial oxygen-hydrogen content. Also, in the liquid with high viscosity, the amplitude of bubble radius oscillation clearly decreases due to high level of viscous damping. A comparison of the numerical results with the available experimental data shows a good agreement between the mathematical model and the experiment.

RÉSUMÉ

Dans ce projet de recherche, la dynamique de bulles de gaz réactif et non réactif sous des champs de pression variables a été étudiée. Des modèles mathématiques ont été développés pour simuler le comportement dynamique des différentes bulles de gaz. Sur la base de ces modèles, plusieurs caractéristiques du comportement thermo-fluide mécanique des bulles de gaz sont discutés et leurs applications durant les opérations de production sont décrites. Les modèles mathématiques forment une série couplée, hautement non-linéaire et inflexible d' équations différentielles, qui ont été résolus numériquement par une méthode modifiée de Gear.

La première partie de cette étude concerne le comportement dynamique en régime transitoire de bulles d'hydrogène lors de la solidification d'un alliage d'aluminium contenant 3.4% poids de cuivre sous différents champs de pression ultrasonique. Durant le processus d'effondrement, la pression dans la région liquide entourant la bulle augmente rapidement. Les variations de pressions ainsi que le refroidissement super rapide du liquide autour de la bulle peut causer une cristallisation de masse. Si la pression à l'interface des dendrites excède la valeur seuil, les dendrites fissurent. Les fragments de dendrites deviennent des sites de germination pour la cristallisation dans un champ ultrasonique, ce qui mène a un raffinement de la structure cristalline du métal. Les résultats montrent que la pression maximale générée dans le bain, adjacent à la surface de la bulle, est de l'ordre de centaines à milliers d'atmosphères, dépendant de la dimension initiale des bulles, pression du bain non troublé et des spécifications ultrasoniques. De plus, les résultats obtenus avant, après et à les fréquences des résonances montrent que les fréquences ultrasoniques au dessus de la fréquence de résonance des bulles n'ont aucuns effect utiles sur le bain.

La deuxième partie de cette étude ayant rapport à la dynamique d'une bulle stable sous différents champs de pression ultrasonique. Lorsque que le champ de pression imposé est en dessus du seuil, le gaz dissous dans le liquide s'écoule dans les bulles de gaz par diffusion rectifiée. Dans ce cas, les bulles grossissent et deviennent capables de flotter à la surface due aux forces hydrodynamiques de flottabilité. Le seuil de pression et

l'effet de la dimension des bulles et des spécifications ultrasoniques sur la diffusion rectifiée de l'air dissous dans l'eau sous différentes concentrations initiales été étudié. Les résultats montrent que les bulles d'air grossissent et que le volume moyen de celle-ci en fonction du temps des bulles atteint plusieurs fois sa valeur initiale lorsque l'amplitude de la pression ultrasonique est supérieure à la pression seuil. De plus, les résultats numériques montrent qu'en dessus de la pression seuil, une bulle d'hydrogène grossit et que le volume de la bulle augmente plusieurs fois sa valeur initiale par diffusion rectifiée d'hydrogène dissout présent dans un alliage d'aluminium fondu.

Dans le but de valider le modèle mathématique du grossissement de bulles par diffusion rectifiée, une modélisation physique en milieu aqueuse a été développée. L'appareillage expérimental a été conçu pour pouvoir produire une étude physique concernant le grossissement des bulles sous des champs de pression ultrasonique. Le résultat de la modélisation physique en milieu aqueuse pour le grossissement des bulles est comparable avec les résultats des modèles mathématiques, ce qui démontre une similarité raisonnable entre les expériences et les prédictions.

La dernière partie de cette étude consistait à l'analyse du comportement dynamique complexe d'une bulle de gaz réactive immergée dans un liquide non-réactif sous différentes impulsions de pression de liquide. Des investigations numériques ont été conduites lors de l'effondrement et l'explosion de bulles isolées d'un mélange d'oxygène et d'hydrogène immergées dans l'eau et la glycérine. Les résultats démontrent que si la pression imposée est assez puissante, la bulle explose. La température du gaz maximale ainsi que la pression atteinte dans la bulle dépendent directement de la quantité initiale d'oxygène et d'hydrogène. De plus, dans le liquide à viscosité plus élevée, l'amplitude de l'atténuation de l'oscillation du rayon des bulles diminue clairement dû au haut niveau de viscosité. La comparaison des résultats numériques avec les données expérimentales disponibles démontre un bon accord entre le modèle mathématique et les expériences.

ACKNOWLEDGMENTS

I would like to express my sincere gratitude and appreciation to my supervisor, Professor M. Hasan for his guidance, helpful advice, continuous support and encouragement during the course of this work. His invaluable suggestions which arose from many discussions throughout the research work and the time spent in reviewing the manuscript are all well acknowledged.

I would like to thank my seminar committee, especially Professor R. I. L. Guthrie, for their encouragement, helpful suggestions and great discussions that they have provided to me.

Thanks are due to Dr. Alan C Hindmarsh for making available LSODE subroutine.

I am also grateful to Mr. Mathieu Brochu who provided me with the French translation of the abstract.

I am indebted to my wife, Maryam, for her sacrifices, continuous encouragement and patience and to my children for their never-ending love. I would also like to express my appreciation to my parents for their kindness and endless patience. They were great moral supporters for me during these busy years.

TABLE OF CONTENTS

ABSTRACT.....	i
RÉSUMÉ.....	iii
ACKNOWLEDGMENTS.....	v
TABLE OF CONTENTS.....	vi
LIST OF FIGURES.....	xii
LIST OF TABLES.....	xx

CHAPTER 1

INTRODUCTION

1.1 Bubble Dynamics.....	1-1
1.1.1 Non-reactive Bubble Dynamics.....	1-1
1.1.2 Reactive Bubble Dynamics.....	1-3
1.2 Practical Motivations.....	1-3
1.3 Objectives.....	1-4
1.4 Thesis Outline.....	1-4

CHAPTER 2

A REVIEW OF SOME IMPORTANT ASPECTS OF BUBBLE-DYNAMICS

2.1 General Equations of Bubble Dynamics.....	2-1
2.2 Rayleigh-Plesset Equation.....	2-2
2.3 Apfel's Derivation for a Gas Bubble.....	2-5
2.4 Nucleation and Cavitation Inception.....	2-6
2.5 Acoustic Cavitation.....	2-7
2.6 Stable Cavitation.....	2-7
2.6.1 Damping of Stable Bubbles.....	2-8

2.7 Nonlinear Effects.....	2-9
2.8 Bjerknes Forces.....	2-10
2.9 Rectified Mass Diffusion.....	2-12
2.9.1 Degassing Process.....	2-16
2.10 Transient Cavitation.....	2-16
2.10.1 Transient Cavitation Thresholds.....	2-17
2.11 Liquid Compressibility Effects.....	2-18
Nomenclature.....	2-23
References.....	2-25

CHAPTER 3

MODELS DEVELOPMENT AND NUMERICAL SOLUTION METHODS

3.1 Introduction.....	3-1
3.2 Models Development.....	3-2
3.3 Numerical Solution Methods.....	3-3
3.3.1 Initial Value Problem.....	3-3
3.3.2 Stiff Problems.....	3-4
3.3.3 Accuracy of the Method.....	3-5
3.3.4 Linear Multistep Method (BDF).....	3-6
3.3.5 Corrector Iteration Method.....	3-8
3.3.6 Newton-Raphson Iteration.....	3-10
3.4 LSODE Subroutine.....	3-11
3.4.1 Program Structure.....	3-13
References.....	3-14

CHAPTER 4

EFFECT OF A HYDROGEN BUBBLE IN A SOLIDIFYING AL-CU ALLOY MELT UNDER VARIOUS ULTRASONIC PRESSURE FIELDS

4.1 Introduction.....	4-1
4.1.1 Hydrogen Bubble Formation.....	4-1
4.1.2 Ultrasonic Treatment.....	4-3
4.2 Literature Review.....	4-4
4.3 Mathematical Modelling.....	4-6
4.3.1 Transformed and Non-dimensional Equations.....	4-9
4.3.2 Initial Conditions.....	4-10
4.3.3 Boundary Conditions.....	4-11
4.4 Numerical Solution Methods.....	4-12
4.5 Results and Discussion.....	4-13
4.6 Concluding Remarks.....	4-16
Nomenclature.....	4-18
References.....	4-20

CHAPTER 5

MATHEMATICAL MODELLING OF BUBBLE GROWTH BY RECTIFIED DIFFUSION IN GASSY LIQUIDS UNDER VARIOUS ULTRASONIC PRESSURE FIELDS

5.1 Introduction.....	5-1
5.2 Literature Review.....	5-2
5.3 Mathematical Modelling.....	5-5
5.3.1 Transformed and Non-dimensional Equations.....	5-7
5.3.2 Initial Conditions.....	5-8

5.3.3 Boundary Conditions.....	5-9
5.4 Numerical Solution Methods.....	5-12
5.5 Results and Discussion.....	5-13
5.5.1 Results and Discussion for Water Modelling.....	5-13
5.5.2 Results and Discussion for Liquid Metal.....	5-15
5.6 Concluding Remarks.....	5-17
Nomenclature.....	5-19
References.....	5-21

CHAPTER 6

AN AQUEOUS EXPERIMENTAL INVESTIGATION OF BUBBLE GROWTH BY RECTIFIED DIFFUSION UNDER AN ULTRASONIC PRESSURE FIELD

6.1 Basic Theory of Ultrasound.....	6-1
6.1.1 Historical Prospective.....	6-1
6.1.2 Ultrasonic Waves.....	6-2
6.1.2.1 Specific Acoustic Impedance.....	6-3
6.1.2.2 Acoustic Intensity.....	6-4
6.1.2.3 Wave Reflection and Transmission.....	6-6
6.1.2.4 Attenuation of Plane Waves.....	6-6
6.1.3 Standing Acoustic Waves.....	6-7
6.1.4 Bubble Entrapped in Standing Waves.....	6-7
6.2 Ultrasonic Technology.....	6-9
6.2.1 Ultrasonic Transducers.....	6-9
6.2.1.1 Magnetostrictive Transducers.....	6-10
6.2.1.2 Piezoelectric Transducers.....	6-11
6.2.2 Piezoelectric Probe Receivers (Hydrophones).....	6-12
6.2.3 Types of Sonicator System.....	6-13
6.2.3.1 Ultrasonic Probe.....	6-13

6.2.3.2 Ultrasonic Cleaning Bath.....	6-14
6.3 Experimental Investigation.....	6-14
6.3.1 Experimental Apparatus and Procedure.....	6-15
6.3.1.1 Preparation of Water (in the column).....	6-16
6.3.2 Measuring System.....	6-17
6.3.2.1 Bubble Diameter Measurement.....	6-17
6.3.2.2 Ultrasonic Pressure Amp. and Freq. Measurement.....	6-17
6.3.2.3 Measurement of Dissolved Oxygen in Water.....	6-18
6.3.3 Experimental Results and Comparison with Math. Model.....	6-18
6.3.4 Experimental Error Analysis.....	6-19
6.3.4.1 General Uncertainty in the Experimental Results.....	6-20
References.....	6-22

CHAPTER 7

A NUMERICAL STUDY OF THE COMPLEX DYNAMICS BEHAVIOR OF A REACTIVE GAS BUBBLE IN NON- REACTIVE LIQUIDS

7.1 Introduction.....	7-1
7.2 Literature Review.....	7-1
7.3 Mathematical Modelling.....	7-3
7.3.1 Transformed and Non-dimensional Equations.....	7-6
7.3.2 Initial Conditions.....	7-8
7.3.3 Boundary Conditions.....	7-8
7.4 Numerical Solution Methods.....	7-10
7.5 Results and Discussion.....	7-11
7.5.1 Sustained Liquid Impulse Pressure.....	7-13
7.5.2 Gaussian Liquid Impulse Pressure.....	7-17
7.5.3 History of Gas Pressure	7-20

7.6 Comparison with Experimental Data.....	7-21
7.7 Concluding Remarks.....	7-22
Nomenclature.....	7-24
References.....	7-26

CHAPTER 8

SUMMARY AND CONCLUDING REMARKS

8.1 Overall Conclusions	8-1
8.2 Contribution to Knowledge	8-4
8.3 Recommendations for Future Work	8-4
APPENDIX A.....	A-1
APPENDIX B.....	B-1

LIST OF FIGURES

Figure

- 2.1 Schematic of a spherical bubble in an infinite liquid.
- 2.2 Portion of the spherical bubble surface.
- 2.3 Typical history of bubble radius for a stable bubble.
- 2.4 Bubble damping components and the total damping as a function of the equilibrium bubble radius, R_0 , for water.
- 2.5 Numerically computed amplitudes of radial oscillation of a bubble of radius $1 \mu\text{m}$ in water at a mean ambient pressure of 1 bar plotted as a function of ω / ω_r for various amplitudes of oscillation. The numbers above the peaks indicate the order of the resonance.
- 2.6 Typical history of bubble radius for a transient bubble.

- 3.1 Structure of the computational solver.
- 3.2 General flowchart of the computational solver.

- 4.1 Schematic of high pressure waves generated in a solidifying melt due to violent collapse of an entrapped bubble.
- 4.2 Schematic diagram of the fragmentation of the dendrite arms.
- 4.3 History of bubble radius in an aluminium-3.4 pct copper alloy melt under an ultrasonic pressure field $P_{ap} = 1.1-5.0 \sin(2\pi ft)$, $f = 0.8 \text{ MHz}$ and $d_0 = 10 \mu\text{m}$.
- 4.4 High pressure waves generated in the melt near the bubble surface. The conditions correspond to those of Fig. 4.3.
- 4.5 Temperature history in the melt adjacent to the bubble surface. The conditions correspond to those of Fig. 4.3.
- 4.6 Temperature history of hydrogen gas at the bubble center.
- 4.7 High pressure waves generated in the melt adjacent to the bubble surface under the ultrasonic frequency of 100 kHz.

- 4.8 High pressure waves generated in the melt adjacent to the bubble surface under the ultrasonic frequency of 2 MHz.
 - 4.9 History of bubble radius under the ultrasonic frequency of 100 kHz as well as the curve of the ultrasonic pressure field.
 - 4.10 History of bubble radius under the ultrasonic frequency of 2 MHz as well as the curve of the ultrasonic pressure cycles.
 - 4.11 Variations of high pressure with distance from the bubble surface for different instants in time during the collapse of the bubble. The conditions correspond to those of Figure 4.4.
 - 4.12 History of bubble radius with the initial diameter of 5 μm under an ultrasonic pressure field of $P_{\text{ap}} = 1.1-5.0 \text{ Sin}(2\pi f t)$, $f = 0.8 \text{ MHz}$.
 - 4.13 High pressure waves generated in the melt near the bubble surface. The conditions correspond to those of Figure 4.12.
 - 4.14 Variations of high pressure with distance from the bubble surface for different instants in time during the collapse of the bubble. The conditions correspond to those of Figure 4.12.
 - 4.15 History of bubble radius with the initial diameter of 20 μm under an ultrasonic pressure field of $P_{\text{ap}} = 1.1-5.0 \text{ Sin}(2\pi f t)$, $f = 0.8 \text{ MHz}$.
 - 4.16 High pressure waves generated in the melt near the bubble surface. The conditions correspond to those of Figure 4.15.
 - 4.17 High pressure waves generated in the melt adjacent to the bubble surface under the ultrasonic frequency of 100 kHz. The conditions correspond to those of Figure 4.15.
 - 4.18 Tensile strength of a typical aluminium-cooper alloy versus temperature.
-
- 5.1 Rectified diffusion.
 - 5.2 Formation of a large gas bubble from a tiny gas bubble by the process of rectified diffusion.
 - 5.3 Time variations of average bubble radius and average mass contained in the bubble

under an ultrasonic pressure field of $P_{ap} = 1.01-0.2 \sin(2\pi f t)$, $f = 35$ kHz, $C_0 = 100$ % Saturation, $R_0 = 0.07$ mm.

- 5.4 Time variations of average bubble radius for different ultrasonic pressure amplitudes, $P_{ap} = 1.01-P_m \sin(2\pi f t)$, $f = 35$ kHz, $C_0 = 100$ % Saturation, $R_0 = 0.07$ mm.
- 5.5 Time variations of average mass contained in the bubble for different ultrasonic pressure amplitudes, $P_{ap} = 1.01-P_m \sin(2\pi f t)$, $f = 35$ kHz, $C_0 = 100$ % Saturation, $R_0 = 0.07$ mm.
- 5.6 Time variations of average mass contained in the bubble for different liquid concentrations under an ultrasonic pressure field of $P_{ap} = 1.01-0.6 \sin(2\pi f t)$, $f = 25$ kHz, $R_0 = 0.10$ mm.
- 5.7 Time variations of average mass of gas contained in the bubble for different ultrasonic frequencies, $P_{ap}=1.01-0.3 \sin(2\pi f t)$, $C_0 = 100$ % Saturation, $R_0 = 0.07$ mm.
- 5.8 Time variations of average mass of gas contained in the bubble for different ultrasonic frequencies, $P_{ap} = 1.01-0.5 \sin(2\pi f t)$, $C_0 = 100$ % Saturation, $R_0 = 0.07$ mm.
- 5.9 Time variations of average bubble radius and average mass of gas contained in the bubble under an ultrasonic pressure field of $P_{ap} = 1.01-0.5 \sin(2\pi f t)$, $f = 25$ kHz, $C_0 = 100$ % Saturation, $R_0 = 0.10$ mm.
- 5.10 History of average mass of gas contained in the bubble for different bubble initial radii under an ultrasonic pressure field of $P_{ap}=1.01-0.5 \sin(2\pi f t)$, $C_0 = 100$ % Saturation and $f = 25$ kHz.
- 5.11 Time variations of average bubble radius and average mass of hydrogen gas contained in the bubble under an ultrasonic pressure field of $P_{ap} = 1.056-1.3 \sin(2\pi f t)$, $f = 25$ kHz, $R_0 = 0.015$ mm and $C_0 = 100$ % Saturation.
- 5.12 Time variations of average bubble radius and average mass of hydrogen gas contained in the bubble under an ultrasonic pressure field of $P_{ap}= 1.056-1.3 \sin(2\pi f t)$, $f = 25$ kHz, $R_0 = 0.020$ mm and $C_0 = 100$ % Saturation.

- 5.13 History of average mass of hydrogen gas contained in the bubble for different bubble initial radii under an ultrasonic pressure field of $P_{ap}=1.056-1.3 \sin (2\pi f t)$, $C_0 = 100 \% \text{ Saturation}$, $f = 25 \text{ kHz}$.
- 5.14 History of average mass of hydrogen gas contained in the bubble for different ultrasonic frequencies, $P_{ap}=1.056-1.3 \sin (2\pi f t)$, $C_0 = 100 \% \text{ Saturation}$ and $R_0 = 0.020 \text{ mm}$.
- 5.15 History of average mass of hydrogen gas contained in the bubble for different ultrasonic pressure amplitudes, $P_{ap}=1.056-P_m \sin (2\pi f t)$, $C_0 = 100 \% \text{ Sat.}$, $f = 35 \text{ kHz}$ and $R_0 = 0.015 \text{ mm}$.
- 5.16 History of average mass of hydrogen gas contained in the bubble for different initial concentrations of dissolved hydrogen, $P_{ap}=1.056-1.3 \sin (2\pi f t)$, $f = 25 \text{ kHz}$ and $R_0 = 0.020 \text{ mm}$.
- 5.17 History of average mass of hydrogen gas contained in the bubble for different hydrostatic pressures, $P_{ap}= P_b-1.3 \sin (2\pi f t)$, $P_b = 1.056 \text{ bar}$, 1.102 bar , 1.148 bar $R_0 = 0.015 \text{ mm}$, $C_0 = 100 \% \text{ Saturation}$ and $f = 25 \text{ kHz}$.
- 6.1 Sound motion in a liquid medium.
- 6.2 Reflection and transmission for normal incidence at a plane boundary.
- 6.3 Variation of amplitude A with distance X from the source of a stationary wave system.
- 6.4 Envelope of stationary wave pattern showing nodes N and antinodes A.
- 6.5 Magnetostrictive transducer used in an ultrasonic degasifier, 1) water-cooled cell; 2) magnetostrictive transducer; 3) aluminium-melt; 4) titanate bit; 5) degassing automation block; 6) telpher.
- 6.6 Sandwich transducer with ceramic piezoelectric elements.
- 6.7 Schematic construction of a hydrophone with a hollow piezoelectric cylinder transducer.
- 6.8 Schematic construction of a hydrophone with a piezoelectric disc transducer.
- 6.9 Schematic diagram of the experimental set up.
- 6.10 Bubble attached to the wire coated with paraffin wax.

- 6.11 Photograph of the experimental set up.
 - 6.12 Photograph of the needle type hydrophone.
 - 6.13 Typical print out of the oscilloscope screen.
 - 6.14 Comparison of the mathematical model's calculations with the experimental results for the bubble growth under an ultrasonic pressure field of $P_{ap} = 1.01 - 0.9 \sin(2\pi f t)$, $f = 38.5 \text{ kHz}$, $R_0 = 0.3 \text{ mm}$, $C_0 = 95 \%$ Saturation.
 - 6.15 Uncertainty in the experimental results.
-
- 7.1 Schematic of temperature profile at the phase boundary.
 - 7.2 History of bubble radius and gas temperature in water for a mixture of 90% Ar + 10 % (2H₂ + O₂) under a sustained liquid pressure of 8 bars ($d_0 = 5 \text{ mm}$).
 - 7.3 History of bubble radius and gas temperature in water for a mixture of 90% Ar + 10% (2H₂ + O₂) under a sustained liquid pressure of 4 bars ($d_0 = 5 \text{ mm}$).
 - 7.4 History of bubble radius and gas temperature in water for a mixture of 90% Ar + 10% (2H₂ + O₂) under a sustained liquid pressure of 2 bars ($d_0 = 5 \text{ mm}$).
 - 7.5 History of bubble radius and gas temperature in water for a mixture of 70% Ar + 30% (2H₂ + O₂) under a sustained liquid pressure of 8 bars ($d_0 = 5 \text{ mm}$).
 - 7.6 History of bubble radius and gas temperature in water for a mixture of 70% Ar + 30% (2H₂ + O₂) under a sustained liquid pressure of 4 bars ($d_0 = 5 \text{ mm}$).
 - 7.7 History of bubble radius and gas temperature in water for a mixture of 70% Ar + 30% (2H₂ + O₂) under a sustained liquid pressure of 2 bars ($d_0 = 5 \text{ mm}$).
 - 7.8 Temporal behavior of bubble radius and gas temperature in water for a mixture of 70% Ar + 30% (2H₂ + O₂) under a sustained liquid pressure of 8 bars ($d_0 = 2.5 \text{ mm}$).
 - 7.9 Temporal behavior of bubble radius and gas temperature in water for a mixture of 70% Ar + 30% (2H₂ + O₂) under a sustained liquid pressure of 4 bars ($d_0 = 2.5 \text{ mm}$).
 - 7.10 Temporal behavior of bubble radius and gas temperature for a mixture of 70% Ar + 30% (2H₂ + O₂) under a sustained liquid pressure of 2 bars in water ($d_0 = 2.5 \text{ mm}$).

- 7.11 Temporal behavior of bubble radius and gas temperature for a mixture of 70% Ar + 30% (2H₂ + O₂) under a sustained liquid pressure of 2 bars in glycerin (d₀ = 2.5 mm).
- 7.12 History of bubble radius in glycerin under different sustained liquid pressures of A = 8 bar, B = 4 bar and C = 2 bar for a mixture of 90% Ar+10%(2H₂ + O₂), d₀ = 5 mm.
- 7.13 History of bubble radius in glycerin under different sustained liquid pressures of A = 8 bar, B = 4 bar and C = 2 bar for a mixture of 90% Ar +10%(2H₂ + O₂), d₀ = 2.5 mm.
- 7.14 History of bubble radius and gas temperature for a mixture of 90% Ar + 10% (2H₂ + O₂) under a gaussian liquid pressure profile in glycerin, P_{max} = 5 bar, RT = 0.1 msec (d₀ = 5 mm).
- 7.15 History of bubble radius and gas temperature for a mixture of 90% Ar + 10% (2H₂ + O₂) under a gaussian liquid pressure profile in glycerin, P_{max} = 5 bar, RT = 0.2 msec (d₀ = 5 mm).
- 7.16 History of bubble radius and liquid pressure at the bubble surface for a mixture of 90% Ar + 10% (2H₂ + O₂) under a gaussian liquid pressure profile in glycerin, P_{max} =10 bar (d₀ = 5 mm).
- 7.17 History of bubble radius and liquid pressure at the bubble surface for a mixture of 90% Ar + 10% (2H₂ + O₂) under a gaussian liquid pressure profile in glycerin, P_{max} =10 bar (d₀ = 5 mm).
- 7.18 History of bubble radius and gas temperature for a mixture of 90% Ar + 10% (2H₂ + O₂) under a gaussian liquid pressure profile in water, P_{max} = 5 bar (d₀ = 2.5 mm).
- 7.19 History of bubble radius and gas temperature for a mixture of 90% Ar + 10% (2H₂ + O₂) under a gaussian liquid pressure profile in glycerin, P_{max} = 5 bar (d₀ = 2.5 mm).
- 7.20 History of bubble radius and liquid pressure at the bubble surface for a mixture of 90% Ar + 10% (2H₂ + O₂) under a gaussian liquid pressure profile in water, P_{max} = 5 bar (d₀ = 2.5 mm).

- 7.21 History of bubble radius and liquid pressure at the bubble surface for a mixture of 90% Ar + 10% (2H₂ + O₂) under a gaussian liquid pressure profile in glycerin, P_{max} = 5 bar (d₀ = 2.5 mm).
- 7.22 History of bubble radius and gas temperature in water for a mixture of 70% Ar + 30% (2H₂ + O₂) under a gaussian liquid pressure profile, P_{max} = 10 bar (d₀ = 5 mm).
- 7.23 History of bubble radius and gas temperature in glycerin for a mixture of 70% Ar + 30% (2H₂ + O₂) under a gaussian liquid pressure profile, P_{max} = 10 bar (d₀ = 5 mm).
- 7.24 History of bubble radius and gas temperature in water for a mixture of 70% Ar + 30% (2H₂ + O₂) under a gaussian liquid pressure profile, P_{max} = 5 bar (d₀ = 2.5 mm).
- 7.25 History of bubble radius and gas temperature in glycerin for a mixture of 70% Ar + 30% (2H₂ + O₂) under a gaussian liquid pressure profile, P_{max} = 5 bar (d₀ = 2.5 mm).
- 7.26 History of bubble radius and gas pressure in glycerin for a mixture of 70% Ar + 30% (2H₂ + O₂) under a gaussian liquid pressure profile, P_{max} = 10 bar (d₀ = 2.5 mm).
- 7.27 History of bubble radius and gas pressure in glycerin for a mixture of 70% Ar + 30% (2H₂ + O₂) under a gaussian liquid pressure profile, P_{max} = 5 bar (d₀ = 2.5 mm).
- 7.28 History of bubble radius and gas pressure in glycerin for a mixture of 70% Ar + 30% (2H₂ + O₂) under a sustained liquid pressure profile of 8 bars (d₀ = 2.5 mm).
- 7.29 History of bubble radius and gas pressure in glycerin for a mixture of 70% Ar + 30% (2H₂ + O₂) under a sustained liquid pressure profile of 4 bars (d₀ = 2.5 mm).
- 7.30 Comparison of the model's calculation with the Fujiwara experiment for a mixture of 70% Ar + 30% (2H₂ + O₂) and d₀ = 10 mm.

A.1 Elimination of columnar structure and formation of fine equiaxed grains in ultrasonically treated of a steel (H25T), (Abramov, 1987).

LIST OF TABLES

<u>Table</u>	Page
3.1 Method coefficients for backward differentiation formula given by Gear	3-7
3.2 Description of subprograms used in LSODE	3-16
4.1 Input parameters for the solidifying melt	4-11
5.1 Input Parameters for computations	5-11
6.1 Acoustic velocities and characteristic impedances for some commonly used materials at room temperature	6-5
7.1 Input Parameters for computations	7-12
A.1 The effect of ultrasound on mechanical properties of steels (Abramov, 1987)....	A-1

INTRODUCTION

1.1. Bubble Dynamics

1.1.1 Non-reactive Bubble Dynamics

A gas bubble in liquid, when subjected to a time varying (usually acoustic) pressure field, undergoes a radial motion of the interface of gas and liquid. The response of the bubble to the external pressure field has been called bubble dynamics. Generally, two distinct types of bubble interface motion are possible: in the first category are transient bubbles that exist for less than one, or at most a few, acoustic cycles, whereas in the second category are stable bubbles that oscillate for many periods of the applied sound field. The basic problem of bubble dynamics is to determine the pressure, temperature and velocity fields in the two-fluid medium, together with the motion of the bubble wall when subjected to an external time-dependent pressure field. The problem to be solved represents a complex nonlinear process in which two phases are coupled through a moving boundary while mass and heat transfer may take place across the interface of gas and liquid. If the bubble contains a reactive gas mixture, the heat generation by chemical reactions complicates the bubble dynamics. The latter is taken into consideration through an additional term in the gas energy balance equation. Bubble dynamics is a relatively very fast process and is governed by complex physico-chemical phenomena. Due to having significant different time and length scales in the bubble dynamics problem, it would be a difficult task indeed to solve the complete set of governing equations for the variables of interest within and surrounding the bubble.

The word 'Cavitation' refers to the formation and the subsequent dynamic life of bubbles in liquids. These bubbles can be either gas or vapor filled and form in a wide variety of liquids under a wide range of conditions. Cavitation occurs in water, organic solvents, biological fluids, liquid helium, and molten metals, as well as many other fluids. It may be hydrodynamic, thermal, or acoustic in origin. This study solely deals with the acoustic cavitation. Acoustic cavitation can affect a liquid through two possible avenues. The first is the bubble itself. The liquid is disrupted by the inhomogeneous presence of the bubble. The second avenue through which cavitation affects a fluid is bubble dynamics. The bubble's interior and the liquid immediately surrounding the bubble are regions that undergo continual change. The bubble's diameter continually changes; the gas pressure within the bubble and the liquid pressure surrounding the bubble fluctuate rapidly; concentration of dissolved gas in the liquid at the bubble interface varies and the dissolved gas in the liquid diffuses into and out of the bubble during each cycle. The bubble radiates acoustic energy as it oscillates; thermal and viscous damping hinder the bubble oscillations. Each of these processes manifests itself differently, but they all lead to changes in the properties of the liquid surrounding the bubble.

Two important characteristics of acoustic cavitation should be mentioned here. The first is that generally it is a nonlinear process in that the change in the radius of the bubble is not proportional to the sound pressure. The second is that the high compressibility of the gas bubbles means that potential energy is obtained from the sound waves when the bubbles expand and that kinetic energy is concentrated when the bubbles collapse. In transient cavitation, this transformation of a low energy density sound wave into a high energy density collapsing bubble occurs since the motion is nonlinear. Because it concentrates the energy into very small volumes it can produce very high pressures and temperatures, which can erode or break solids, initiate chemical reactions and produce luminescence.

When a gas bubble is caused to pulsate by an acoustic pressure field, gas will diffuse in and out of the bubble during each cycle. There exists a threshold for which more gas diffuses in than out over an acoustic cycle and the stable gas bubble is caused to grow as a result of the sound field. This concept is called 'rectified diffusion' and the

words are an adequate description of the phenomenon. It is a slow process, however, requiring thousands of cycles. In degassing, the process of rectified diffusion is continued for some 20,000 times per second or above, therefore large gas bubbles can be formed rapidly which can float to the surface due to the buoyancy force.

1.1.2 Reactive Bubble Dynamics

A bubble is called a reactive gas bubble when the bubble contains a reactive gas mixture. In addition to treating the common features of bubble dynamics, the chemical reaction of the gas mixture has to be taken into account in the mathematical formulation. A reactive gas bubble, when subjected to an impulse pressure of sufficient strength, will undergo compression. The temperature of the gas mixture in the bubble increases and can reach the ignition point of the reactant. When the ignition point is reached the bubble gas explodes. The pressure and the temperature of the gas within the bubble increase very rapidly.

1.2 Practical Motivations

Many phenomena can arise from bubble dynamics. It can be useful and it can also be a nuisance. Two of the useful applications of bubble dynamics are: their effects on a solidifying melt under an ultrasonic pressure field (grain refinement) and ultrasonic degassing. Both of these aspects of dynamics of transient and stable bubbles will be studied in detail in the present work. Bubble dynamics can also cause harmful and destructive effects, as in sonar propagation, in oil drilling and in erosion of ship propellers.

In the case of reactive bubbles, the shock waves generated by an explosion inside the water (underwater explosion) are used in various metal processing applications, such as forming, welding, consolidation and compaction of powders and punching holes in pipe walls. Usually, this phenomenon takes place in a suitable pressure vessel, which is designed to focus shock waves for practical metal processing usage. Another motivation

to study the reactive bubble phenomenon is the fact that in nuclear power plant accidents, oxygen-hydrogen bubbles, which may develop in abnormally high-temperature water, can constitute an explosion hazard.

1.3 Objectives

The main objective of the present study is to develop comprehensive mathematical models, which will enable us to predict qualitatively and quantitatively the behavior of a gas bubble and associated dynamics and transport processes in a solidifying melt and in a gassy liquid (melt) when they are subjected to an ultrasonic pressure field. Theoretical as well as aqueous experimental studies are carried out in order to elucidate the physical aspects of these complex physico-chemical phenomena. Specifically, the following objectives are followed:

- (1) To simulate numerically the effects of bubble dynamics on a solidifying melt under various ultrasonic pressure fields in order to achieve grain refinement.
- (2) To model ultrasonic degassing of a gassy liquid through the study of the dynamic behavior of a single gas bubble.
- (3) To validate the mathematical model of bubble growth by rectified diffusion through an aqueous physical modelling.
- (4) To develop a mathematical model for the complex dynamic behavior of a spherical reactive bubble in a nonreactive liquid and compare the theoretical results with the available experimental measurements.

1.4 Thesis Outline

This study is presented in the eight subsequent chapters. The second chapter involves a review of some important aspects of bubble dynamics related to this study. A brief literature review as well as explanations in terms of mathematical formulations and physical understanding of the phenomena are provided.

Chapter 3 is concerned with the models development and the numerical solution methods. A detailed description about the nonlinear and stiff specifications of the governing equations is presented and the numerical schemes employed to solve them are introduced.

In Chapter 4, the effect of a hydrogen bubble in a solidifying Al-Cu alloy melt under various ultrasonic pressure fields is studied. The work is carried out to demonstrate the possibility of the dynamic grain refinement of aluminium alloys by utilizing externally applied high-powered ultrasonic waves and the hydrogen bubbles present in the melt. In this regard, a mathematical model is developed to simulate the dynamic behavior of a hydrogen gas bubble present in the mushy region of a solidifying aluminium-3.4 wt pct copper alloy melt under various applied ultrasonic pressure fields.

Chapter 5 deals with the mathematical modelling of bubble growth by rectified diffusion in gassy liquids under various ultrasonic pressure fields. The threshold pressure and the effects of ultrasonic specifications on rectified diffusion of the dissolved air in water as well as dissolved hydrogen in a molten aluminium alloy with different initial concentrations are studied.

In chapter 6, a brief review of the basic theory of ultrasound, and ultrasonic technology is first provided. Then, an aqueous experimental investigation is carried out to study bubble growth by rectified diffusion under an ultrasonic pressure field. The experimental results of aqueous physical modelling for bubble growth are compared to the results of the mathematical model which is already presented in Chapter 5.

Chapter 7 presents a numerical study of the complex dynamic behavior of a reactive bubble in a non-reactive liquid. In this study, numerical investigations are conducted into the collapse and explosion of an isolated oxygen-hydrogen bubble immersed in water and in glycerin. The mathematical model of the bubble's radial motion is based on the modified Rayleigh-Plesset equation of the bubble dynamics. The exothermicity of the bubble's gas content is varied by changing the mole fraction of the mixture of stoichiometric oxygen-hydrogen with the inert gas, argon, as a diluent. The numerical results are compared with the experimental data.

Chapter 8 provides a summary of the important findings made, contributions to knowledge and some suggestions and recommendations for future work.

A REVIEW OF SOME IMPORTANT ASPECTS OF BUBBLE DYNAMICS

2.1 General Equations of Bubble Dynamics

Consider a spherical bubble in an infinite domain of liquid. Every parameter then depends on one space variable, r , the distance from the bubble center and, t , time. We now have a hydrodynamic problem of a moving spherical bubble wall separating gas and/or vapor from a liquid.

This can be solved to find the pressure, velocity and temperature at any point in the gas or liquid when the bubble is excited by a time-varying pressure field, by applying the laws of conservation of mass, momentum and energy for both gas and liquid. We also need a set of equations to express the physical laws like the equation of state for the gas and liquid, gas diffusion equation in liquid as well as time-dependent boundary conditions.

The equation of state for the gas is the perfect gas law and the equation of state for liquid is constant density while the liquid is assumed to be incompressible. If this assumption is not valid, a more complicated equation of state involving compressibility of the liquid has to be used.

The task of solving this set of nonlinear and coupled differential equations with a fast moving boundary is very complex. In its generality, the problem is only amenable to

numerical calculations. It can only be carried out analytically for small-amplitude motion in which the equations can be linearized.

2.2 Rayleigh-Plesset Equation

In modelling bubble dynamics problems, for the sake of generality, it is occasionally assumed that a gas bubble contains some small quantity of vapor. Although in most practical cases, the amount of vapor inside the gas bubble is negligible. At 20 °C the vapor pressure of water is about 0.02 bars, which is very small compared with the partial pressure of the gas.

We now consider a spherical gas bubble of radius, $R(t)$ (where t is time), in an infinite domain of liquid whose temperature and pressure far from the bubble are T_∞ and $P_\infty(t)$, respectively (Figure 2.1). The temperature, T_∞ , is assumed to be a simple constant. On the other hand, the pressure, $P_\infty(t)$, is assumed to be a known (and perhaps controlled) input which regulates the growth or collapse of the bubble. Though compressibility of the liquid can be important in the context of bubble collapse, in the present study it will be assumed that the liquid density, ρ_l , is a constant. Furthermore, the dynamic viscosity, μ_l , is assumed constant and uniform. It is also assumed that the gas temperature, $T_g(t)$, and the gas pressure, $P_g(t)$ within the bubble are uniform that is independent of the radial position. These assumptions may not be justified in all the circumstances studied here and will be identified and relaxed as the analysis proceeds.

Conservation of mass for the liquid requires that:

$$u(r, t) = \frac{F(t)}{r^2} \quad (2.1)$$

where $F(t)$ is related to $R(t)$ by a kinematic boundary condition at the bubble surface. In the idealized case of zero mass transport across this interface, it is clear that $u(R, t) = dR/dt$ and hence:

$$F(t) = R^2 \frac{dR}{dt} \quad (2.2)$$

But this is often a good approximation even when mass transport is occurring at the interface.

Assuming a Newtonian liquid, the Navier-Stokes equation for motion in spherical coordinate is:

$$-\frac{1}{\rho_l} \frac{\partial p}{\partial r} = \frac{\partial u}{\partial t} + u \frac{\partial u}{\partial r} - \nu_l \left[\frac{1}{r^2} \frac{\partial}{\partial r} \left(r^2 \frac{\partial u}{\partial r} \right) - \frac{2u}{r^2} \right] \quad (2.3)$$

After substituting for u from $u = F(t) / r^2$ in the above equation, one gets:

$$-\frac{1}{\rho_l} \frac{\partial p}{\partial r} = \frac{1}{r^2} \frac{dF}{dt} - \frac{2F^2}{r^5} \quad (2.4)$$

Note that the viscous terms vanish; indeed, the only viscous contribution to the Rayleigh-Plesset comes from the dynamic boundary condition at the bubble surface. Equation (2.4) can be integrated to give:

$$\frac{P - P_\infty}{\rho_l} = \frac{1}{r} \frac{dF}{dt} - \frac{1}{2} \frac{F^2}{r^4} \quad (2.5)$$

after application of the condition $P \rightarrow P_\infty$ as $r \rightarrow \infty$.

To complete this part of the analysis, a dynamic boundary condition on the bubble surface must be constructed. For this purpose consider a control volume consisting of a small, infinitely thin lamina containing a segment of interface (Figure 2.2). The net force on this lamina in the radially outward direction per unit area is:

$$\frac{\text{force}}{\text{area}} = (\tau_{rr})_{r=R} + P_g - \frac{2\sigma}{R} \quad (2.6)$$

where

$$(\tau_{rr})_{r=R} = -P_B(t) + 2\mu_l \left. \frac{\partial u}{\partial r} \right|_{r=R} \quad (2.7)$$

By using Equations (2.1), (2.2), (2.6) and (2.7), the force per unit area is:

$$\frac{\text{force}}{\text{area}} = P_g - P_B(t) - \frac{4\mu_l}{R} \frac{dR}{dt} - \frac{2\sigma}{R} \quad (2.8)$$

where $P_B(t) = P[r = R(t), t]$ is the pressure exerted by the liquid on the “wet” side of the bubble surface. In the absence of mass transport across the boundary this force must be zero. Therefore we have:

$$P_B(t) = P_g - \frac{4\mu_l}{R} \frac{dR}{dt} - \frac{2\sigma}{R} \quad (2.9)$$

Applying Equations (2.9) and (2.2) in Equation (2.5) yields the generalized Rayleigh-Plesset equation for the bubble dynamics:

$$\frac{P_g(t) - P_\infty(t)}{\rho_l} = R \frac{d^2R}{dt^2} + \frac{3}{2} \left(\frac{dR}{dt} \right)^2 + \frac{4\nu_l}{R} \frac{dR}{dt} + \frac{2\sigma}{\rho_l R} \quad (2.10)$$

Given $P_\infty(t)$ this represents an equation that can be solved to find $R(t)$ provided $P_g(t)$ is known. In the absence of the surface tension and viscous terms, it was first derived and used by Rayleigh (1917).

In order to obtain $P_g(t)$ values accurately, one is required to solve the coupled mass, momentum and energy equations for the gas combined with the appropriate boundary conditions which will include a thermal boundary layer at the bubble wall.

In the absence of any significant thermal effects, it might be assumed that the behavior of the gas in the bubble is polytropic so that:

$$P_g(t) = \left(P_0 + \frac{2\sigma}{R_0} \right) \left(\frac{R_0}{R(t)} \right)^{3\eta} \quad (2.11)$$

where η is approximately constant. Clearly $\eta = 1$ implies a constant bubble temperature (isothermal) and $\eta = \gamma$ would model adiabatic behavior where γ is ratio of specific heats.

With the above assumptions the Rayleigh-Plesset equation becomes:

$$\frac{1}{\rho_l} \left(P_0 + \frac{2\sigma}{R_0} \right) \left(\frac{R_0}{R} \right)^{3\eta} - \frac{P_\infty(t)}{\rho_l} = R \frac{d^2R}{dt^2} + \frac{3}{2} \left(\frac{dR}{dt} \right)^2 + \frac{4\nu_l}{R} \frac{dR}{dt} + \frac{2\sigma}{\rho_l R} \quad (2.12)$$

Equation (2.12) without the viscous term was first derived and used by Notingk and Neppiras (1950,1951); the viscous term was investigated first by Poritsky (1952). He integrated this equation by a combined graphical and numerical procedure for cases both with and without surface tension. He found the rate of growth and collapse to be strongly affected by both viscosity and surface tension. Viscosity tends to decrease both the growth rate and collapse rate, whereas surface tension tends to decrease the growth rate but increase the collapse rate. During the growth phase, surface tension decreases the expansion rate in the early stages but not in the later stages. Similarly, the later stages of collapse show the greatest effect of surface tension.

Equation (2.12) can be readily integrated numerically to find $R(t)$ given the input $P_{\infty}(t)$. Initial conditions are also required. Analytic solutions to Equation (2.12) are limited to the case of a sustained step function change in P_{∞} . With a constant value of P_{∞} , it is integrated by multiplying through out by $2R^2\dot{R}$ and forming time derivatives. Only the viscous term cannot be integrated in this way, and what follows is confined to the inviscid case.

When a sound field exists in the liquid, the bubble expands and contracts in response to the pressure sound field. For acoustic excitation, $P_{\infty}(t) = P_0 - P_A \sin 2\pi ft$ can be used in Equation (2-12) where P_0 , P_A and f are the pressure of undisturbed liquid, amplitude and frequency of the driving pressure, respectively.

A spherical bubble in a liquid can be viewed as a nonlinear oscillator that can be set into radial oscillations by the sound field. For very small pressure amplitudes the response is linear. At larger oscillation amplitudes this oscillation must become nonlinear because the bubble can be expanded from its equilibrium radius to arbitrary large radius values, and also can be compressed down to near zero radius. Bubbles of different radius at rest (R_0) respond differently to the same sound field.

2.3 Apfel's Derivation for a Gas Bubble

An interesting and simple derivation of Eq. (2.10), which is worth mentioning here, has been provided by Apfel (1981). The Kinetic energy of the mass of liquid surrounding a pulsating spherical bubble of radius R is given by $1/2M_{\text{eff}}\dot{R}^2$, where $\dot{R} = dR/dt$ and M_{eff} is the effective mass 'felt' by the bubble, given by three times the mass of liquid that would fill the bubble; that is $M_{\text{eff}} = 3\rho_l(4\pi/3)R^3$. This kinetic energy minus the energy dissipation at the bubble surface due to the viscous effects is equal to the work done by the surface tension σ , gas pressure P_g and the far field pressure in the liquid P_∞ .

$$\frac{1}{2}M_{\text{eff}}\dot{R}^2 - \int_{R_0}^R \left(-\frac{4\mu_l}{R} \frac{dR}{dt} \right) 4\pi R^2 dR = \int_{R_0}^R \left(P_g - P_\infty - \frac{2\sigma}{R} \right) 4\pi R^2 dR \quad (2.13)$$

By differentiating the above equation with respect to R and dividing by $4\pi R^2 \rho_l$ one gets:

$$\underbrace{R\ddot{R} + \frac{3}{2}\dot{R}^2}_{\text{inertial terms}} + \underbrace{\frac{4\mu_l}{\rho_l} \frac{\dot{R}}{R}}_{\text{effect of viscous stress at surface}} + \underbrace{\frac{2\sigma}{\rho_l R}}_{\text{surface tension effect}} + \underbrace{\frac{P_\infty - P_g}{\rho_l}}_{\text{pressure effect}} = 0 \quad (2.14)$$

where P_g is given by Eq. (2.11).

2.4 Nucleation and Cavitation Inception

The theoretical tensile strength of water at room temperature is about 1000 atm. This might suggest that acoustically induced cavitation would require a sound pressure amplitude of at least 1000 atm. However, cavitation is observed with pressure amplitude of the order of 1 atm, implying the presence of pre-existing nuclei within the liquid. The most obvious nucleus to consider is a small free spherical bubble in the liquid. Such a

free small bubble, however, will diffuse into the liquid. Epstein and Plesset (1950) estimate that a 10 μm radius air bubble in air-saturated water will take about 7s to dissolve.

The fact that a micro-bubble should dissolve within seconds leaves unresolved the question of why cavitation nuclei persist indefinitely. In the literature, various stabilization mechanisms have been proposed and still are the object of investigations. One possible explanation is that the interface of a gas bubble is immobilized by the effects of surface contamination. Another is an "organic skin" that gives the free surface of the bubble sufficient elasticity to withstand a high pressure. The most favored is that put forward by Harvey *et al.* (1944) which suppose that a pocket of gas is trapped in a small-angled crevice or crack in the container surface or in an imperfectly wetted particle. Ordinary tap water may contain thousands of solid particles per cubic centimeter of liquid. By careful filtration most of these can be removed, allowing the highly purified water to withstand negative pressures of about 200 atm as reported by Greensan and Tschiegg (1967).

2.5 Acoustic Cavitation

On this subject Neppiras (1980) provided a critical review with many references. Prosperetti (1984) has given an excellent account on this subject. In acoustic cavitation a sound wave imposes a sinusoidally varying pressure on the steady ambient pressure. The effect on the bubbles (cavities) may be rather gentle or quite violent. These two types of bubble behavior are called stable and transient cavitation. Although we imply that these two situations follow with increasing the acoustic pressure amplitude, it is important to note that other factors are important in determining the kind of response a bubble will deliver for a given oscillating pressure field. One of the factors in this regard is the relationship between the frequency, f , of the imposed oscillations and the resonance frequency, f_r , of the bubble. Another important factor in determining whether the response is stable or transient is the relationship between the pressure oscillation amplitude, P_A , and the pressure of undisturbed liquid, P_0 .

2.6 Stable Cavitation

Stable bubbles oscillate, often non-linearly, around some equilibrium size. They may continue oscillating for many cycles of the sound pressure (Figure 2.3). In a stable bubble, the time-scale is typically so long that mass-diffusion of gas as well as thermal diffusion, can occur, resulting in significant long-term effects. Stable bubbles may evolve into transients in the course of time. This is significant in gassy liquids like water where stable gas bubble can grow by a second-order effect called “ rectified diffusion”.

2.6.1 Damping of Stable Bubbles

There are three ways in which the bubble oscillations can be damped:

1. *Viscosity* acts at the bubble surface as a brake, whether the bubble is expanding or contracting. Consequently, more energy is required to compress the bubble than is regained in the subsequent expansion.
2. *Sound radiation damping* occurs because an oscillating bubble radiates spherical waves thereby expending some of its energy.
3. *Thermal damping*, thermal conduction from the gas within the bubble to the liquid will tend to lower any increase in the temperature and pressure in the bubble. Thermal damping is the most important source of damping in most cases. Theoretical discussions on thermal damping of stable bubbles can be found in Plesset and Hsieh (1960) and Hsieh (1965).

Chapman and Plesset (1971) have presented a useful summary of the three primary contributions to the damping of bubble oscillations, namely that due to liquid viscosity, that due to liquid compressibility through acoustic radiation, and that due to thermal conductivity. It is particularly convenient to represent the three components of

damping as three additive contributions to an effective liquid viscosity, μ_E , which can then be employed in the Rayleigh-Plesset equation in place of the actual liquid viscosity:

$$\mu_E = \mu_l + \mu_T + \mu_A \quad (2.15)$$

where the acoustic viscosity, μ_A , is given by:

$$\mu_A = \frac{\rho_l \omega^2 R_0^3}{4 C_l} \quad (2.16)$$

where C_l is the velocity of sound in the liquid. The thermal viscosity, μ_T , is given by:

$$\mu_T = \frac{(P_0 + 2\sigma / R_0)}{4\omega} \text{Im}\{\lambda\} \quad (2.17)$$

where λ is:

$$\lambda = \frac{3\gamma}{1 - 3(\gamma - 1)i\chi \left[\left(\frac{i}{\chi} \right)^{1/2} \coth \left(\frac{i}{\chi} \right)^{1/2} - 1 \right]} \quad (2.18)$$

and

$$\chi = \alpha_g / \omega R_0^2 \quad (2.19)$$

The relative magnitudes of the three components of damping (or effective viscosity) can be quite different for different bubble sizes. This is illustrated by the data for air bubbles in water at 20°C and atmospheric pressure, which is taken from Chapman and Plesset (1971) and is reproduced as Figure 2.4. Note that the viscous component dominates for very small bubbles, the thermal component is dominant for most bubbles of practical interest, and the acoustic component only dominates for large bubbles.

2.7 Nonlinear Effects

Plesset and Prosperetti (1977) in their study of the subject have shown that single bubbles exhibit a number of interesting and important nonlinear phenomena. When a liquid that will inevitably contain microbubbles is irradiated with a sound wave of a given

frequency, ω , the nonlinear response results in harmonic dispersion, which not only produces harmonics with frequencies that are integer multiples of ω (superharmonics) but, more unusually, subharmonics with frequencies less than ω of the form ' $m\omega/n$ ' where m and n are integers. Both the superharmonics and subharmonics become more prominent as the amplitude of excitation is increased. The production of subharmonics was first observed experimentally by Esche (1952), and possible origins of this nonlinear effect were explored in detail by Noltingk and Neppiras (1950,1951), Flynn (1964), Borotnikova and Soloukin (1964), and Neppiras (1969), among others. Neppiras (1969) also surmised that subharmonic resonance could evolve into transient cavitation. These analytical and numerical investigations use numerical solutions of the Rayleigh-Plesset equation to explore the nonlinear characteristics of a single bubble excited by an oscillating pressure with a single frequency, ω . As might be expected, different kinds of responses occur depending on whether ω is greater or less than the resonance frequency of the bubble, ω_r .

Lauterborn (1976) examined numerical solutions for a large number of different excitation frequencies and was able to construct frequency response curves of the kind shown in Figure 2.5. In this figure the numbers above the peaks indicate the order of the resonance, m/n , which means m cycles of the oscillations take place during n cycles of the driving pressure field. Notice the progressive development of the peak responses at subharmonic frequencies as the amplitude of the excitation is increased. Nonlinear effects not only create these subharmonic peaks but also cause the resonant peaks (both the main resonance near $\omega / \omega_r = 1$ and the subharmonic resonances) to be skewed to the left, creating the discontinuities indicated by the dashed vertical lines. These correspond to bifurcations or sudden transitions between two valid solutions, one with a much larger amplitude than the other. Prosperetti (1977) has provided a theoretical analysis of these transitions. More review of the subject can be found in Brennen (1995) and Feng and Leal (1997).

2.8 Bjerknes Forces

A different nonlinear effect is the force experienced by a bubble in an acoustic field due to the finite wavelength of the sound waves. In an acoustic field where a pressure gradient ∇P exists, a body of volume V is acted on by a force $-V(t)\nabla P(x,t)$. Since V and P vary with time, it is necessary to consider a time-averaged (vector) force:

$$\langle F \rangle = -\langle V(t)\nabla P(x,t) \rangle \quad (2.20)$$

where bracket $\langle \rangle$ indicates the average over a cycle. Consider now a bubble located at position x in a standing wave pressure field of the form:

$$P(x,t) = P_0 + 2P_A \sin kx \cos \omega t \quad (2.21)$$

where k is the wave number ($2\pi/\lambda$) of the sound field and P_A is the pressure amplitude of the incident wave. Gravity will be ignored, enabling us to treat P_0 as a constant. Further, it will be assumed that $2P_A \ll P_0$, so that a bubble of radius R (well removed from the resonant radius) will oscillate linearly with $R = R_0 + \zeta_0 \cos(\omega t + \alpha)$, where the phase angle α allows for the fact that the oscillation of the radius may not be in phase with the oscillation of the pressure, and where the amplitude of oscillation ζ_0 is much less than R_0 . The volume $V = 4/3\pi R^3$ of the bubble may now be written as:

$$V = V_0 \left[1 + \frac{3\zeta_0}{R_0} \cos(\omega t + \alpha) \right] \quad (2.22)$$

where $V_0 = 4/3\pi R_0^3$ is the initial volume of the bubble.

Now for the bubbles driven with $\omega < \omega_r$ (implying $R_0 > R_r$), the sound pressure and volume are out of phase (the volume is largest when the pressure is least) and so

$\alpha = \pi$ in Equation (2.22). For bubbles driven with $\omega > \omega_r$ (implying $R_0 < R_r$), the sound pressure and volume are in phase and $\alpha = 0$ in Eq. (2.22).

In this study, the bubble resonance size, R_r , is obtained by inserting the frequency of the applied sound field into the resonance frequency equation. The resonance frequency equation for small amplitude oscillations is given by:

$$\omega_r = \frac{1}{R_0 \rho_1^{1/2}} \left[3\gamma \left(P_0 + \frac{2\sigma}{R_0} \right) - \frac{2\sigma}{R_0} - \frac{4\mu_1^2}{\rho_1 R_0^2} \right]^{1/2} \quad (2.23)$$

Substituting Equations (2.21) and (2.22) into Equation (2.20) leads to:

$$F_x = -2 P_A k V_0 |\cos kx| \left(\left(1 - \frac{3\zeta_0}{R_0} \cos \omega t \right) (\cos \omega t) \right) \quad (2.24)$$

leading to

$$F_x = \frac{3P_A k \zeta_0 V_0 |\cos kx|}{R_0} \quad \text{for bubbles with } R_0 > R_r \quad (2.25)$$

and to

$$F_x = \frac{3P_A k \zeta_0 V_0 |\cos kx|}{R_0} \quad \text{for bubbles with } R_0 < R_r \quad (2.26)$$

Comparing Equations (2.25) and (2.26) with the $\sin kx$ variation of the amplitude of the pressure field [Eq. (2.21)] leads to the conclusion that large bubbles (compared to those of the resonant size) will experience a force directed from a pressure antinode towards a pressure node. Conversely, small bubbles will experience a force directed from a pressure node towards a pressure antinode. This also means that the direction of the radiation force depends on the relative frequency ω / ω_r . Thus, a relatively small bubble whose resonance frequency ω_r is greater than the driving frequency ω will be driven from a pressure node to a pressure antinode. Bubbles of subresonant sizes are important biologically. Since they move to maxima of P they are set into vibration of high amplitude, and cause alterations in cells and other structures in these regions. Blake

(1949a) was probably the first person to give a satisfactory account of the origin of this force. His explanation draws on principles first formulated by Bjerknes in 1906, and the force is often called the *primary Bjerknes force*.

2.9 Rectified Mass Diffusion

A different nonlinear effect arises under appropriate circumstances involving the mass transfer of dissolved gas between the liquid and the bubble. This important nonlinear diffusion effect occurs in the presence of an acoustic field and is known as "rectified mass diffusion" (Blake 1949b). The threshold pressure from which the tiny gas bubbles, oscillating around some equilibrium radius, start growing by rectified diffusion is appropriately called the threshold for rectified diffusion. Analytical models of this phenomenon were first put forward by Hsieh and Plesset (1961) and Eller and Flynn (1965), and reviews of the subject can be found in Crum (1980, 1984) and Young (1989).

A complete mathematical description of the general diffusion problem for a gas bubble in a liquid and in the presence of an acoustic field would require an equation of motion, diffusion equation, and heat-conduction equations, in both the liquid and the bubble, with appropriate boundary conditions at the bubble wall. The problem is further complicated by the fact that these equations are coupled and the boundary conditions at the bubble wall must be applied at the moving boundary. The equation of motion is nonlinear and is coupled with the diffusion equation in two ways. First, and most important, the diffusion equation depends on the equation of motion through the convective term $u \cdot \nabla C$. Second, the equation of motion depends on the diffusion through P_g , which is a function of n , the amount of gas in the bubble.

As has been customary, the problem is simplified in different ways. A relatively simple application of these equations is to solve the static diffusion problem for a bubble in the absence of an applied sound field. This problem was treated by Epstein and Plesset (1950) in the following manner. A gas bubble is initially at rest in an infinite solution.

As gas begins to diffuse either into or out of the bubble, the bubble wall and the surrounding liquid will move. However, this motion will be very slow and may be neglected by omitting the convective term in the diffusion equation, which is then written as $\partial C / \partial t = D \nabla^2 C$. The diffusion equation no longer depends on the equation of motion and may now be solved independently.

The first solution of the dynamic diffusion problem was obtained by Blake (1949b). He avoided the nonlinearities of the equation of motion by assuming very small sinusoidal oscillations of the bubble. To avoid the problem of the moving boundary in the diffusion equation, he assumed the bubble wall to be fixed in space, but allowed the concentration of gas at the bubble wall and the area of the wall to vary as they would if the bubble wall were moving.

Hsieh and Plesset (1961) obtained a solution that does include the shell effect. The problem of the moving boundary was solved by expanding the boundary condition in a Taylor series about the equilibrium position of the bubble wall. One of the limitations of their solution is that it is restricted to small sinusoidal oscillations.

Eller and Flynn (1965) divided the general problem into an equation for the motion of the bubble wall and a diffusion equation for the concentration of the gas dissolved in the liquid. They pointed out that the convective term in the diffusion equation should not be neglected. They assumed that the number of moles of gas in the bubble was approximately constant during a single oscillation as well as invoked isothermal or polytropic relation for the gas pressure within the bubble. The equation of motion for the gas bubble is given by:

$$R\ddot{R} + \frac{3}{2}\dot{R}^2 + \frac{1}{\rho_l} \left\{ \left(P_0 + \frac{2\sigma}{R_0} \right) \left[1 - \left(\frac{R_0}{R} \right)^{3\eta} \right] - P_A \cos \omega t + \rho_l R_0 \omega_r b \dot{R} \right\} = 0 \quad (2.27)$$

where R and R_0 are the instantaneous and initial values of the bubble radius. Also, η is the polytropic exponent of the gas contained within the bubble, ω_r the small amplitude resonance frequency and 'b' a damping term applied to the bubble pulsations. Notice that

the damping term in Eq. (2.27) will be accurate when the bubble is driven near the resonance frequency.

The diffusion equation for the gas in the liquid is governed by Fick's law of mass transfer and is given by:

$$\frac{\partial C}{\partial t} + u \cdot \nabla C = D \nabla^2 C \quad (2.28)$$

where C is the concentration of dissolved gas in the liquid, u is the velocity of the liquid at a point and D is the mass diffusion constant. They found an approximate solution of the diffusion equation which was solved by the method of successive approximations. The expression for the flux of gas at the bubble wall was obtained and integrated over the surface of the bubble to give the rate of change in the number of moles of gas in the bubble.

$$\frac{dn}{dt} = 4\pi D R_0 C_0 \left[\left\langle \frac{R}{R_0} \right\rangle + R_0 \left(\frac{\langle (R/R_0)^4 \rangle}{\pi D t} \right)^{1/2} \right] H \quad (2.29)$$

where C_0 is the saturation concentration of the gas in the liquid in moles per unit volume. The pointed brackets in equation (2.29) imply time average, t is the time and H is defined by:

$$H = \frac{C_i}{C_0} - \frac{\langle (R/R_0)^4 (P_g/P_0) \rangle}{\langle (R/R_0)^4 \rangle} \quad (2.30)$$

where C_i is the concentration of dissolved gas in the liquid far from the bubble.

The values of R/R_0 to be used in the above equations are obtained by assuming a series solution of Eq. (2.27) in the form:

$$\frac{R}{R_0} = 1 + \alpha \left(\frac{P_A}{P_0} \right) \cos(\omega t + \delta) + \alpha^2 K \left(\frac{P_A}{P_0} \right)^2 + \dots \quad (2.31)$$

where

$$\alpha^{-1} = \left(\frac{\rho_l R_0^2}{P_0} \right) \left[(\omega^2 - \omega_r^2)^2 + (\omega \omega_r b)^2 \right]^{1/2} \quad (2.32)$$

$$K = \frac{(3\eta + 1 - \beta^2) / 4 + (\sigma / 4R_0 P_0)(6\eta + 2 - 4 / 3\eta)}{1 + (2\sigma / R_0 P_0)(1 - 1 / 3\eta)} \quad (2.33)$$

$$\delta = \tan^{-1} \left(\frac{\omega \omega_r b}{\omega^2 - \omega_r^2} \right) \quad (2.34)$$

and

$$\beta^2 = \frac{\rho_l \omega^2 R_0^2}{3\eta P_0} \quad (2.35)$$

In order to use the above set of equations, one needs to know the damping of the bubble pulsations when the bubble is driven near resonance. The expression given below is due to Eller (1970) which expresses the total damping constant b in terms of the contributions due to thermal, viscous and radiation effects:

$$b = b_t + b_v + b_r \quad (2.36)$$

where b_t is given by:

$$b_t = 3(\gamma - 1) \left[\frac{\chi(\sinh \chi + \sin \chi) - 2(\cosh \chi - \cos \chi)}{\chi^2(\cosh \chi - \cos \chi) + 3(\gamma - 1)\chi(\sinh \chi - \sin \chi)} \right] \quad (2.37)$$

and

$$\chi = R_0 \left(\frac{2\omega}{\alpha_g} \right)^{1/2} \quad (2.38)$$

$$b_v = \frac{4\omega \mu_l}{3\eta P_0} \quad (2.38)$$

$$b_r = \frac{\rho_l R_0^2 \omega^3}{3\eta P_0 C_1} \quad (2.39)$$

2.9.1 Degassing Process

Consider a gas bubble in a gassy liquid. It will grow in the acoustic field by the process of rectified diffusion until it becomes large enough to separate out by the hydrodynamic buoyancy force. This illustrates the *degassing process*, a well-known effect of stable cavitation. It is used industrially in such applications as degassing metal melts,

optical glass, resins and photographic emulsions. It is clear that degassing occurs within a restricted range of R_0 and P_A and its rate can be maximized by choosing appropriate values of P_A and frequency for the expected bubble size distribution.

2.10 Transient Cavitation

The pioneer studies of Noltingk and Neppiras (1950, 1951) showed that a small change in either P_A , f or R_0 could sometimes have a dramatic effect on the character of the radius-time curve calculated from Eq. (2.12). For instance, it was found that for small bubbles $R_0 \ll R_r$, the change in radius occurred as P_A was increased above P_0 . This change is characterized by a growth of the bubble to at least double, and often many times its original size. In other words, the bubble expands to a radius much greater than the maximum radius reached during stable cavitation, followed by a rapid and violent collapse during which the speed of the bubble wall reaches at least the speed of sound in the liquid (Fig. 2.6). This is called a transient bubble. Transient bubbles generally exist for less than one, or at most a few, acoustic cycles. They often disintegrate into a mass of smaller bubbles. For a transient bubble, it is usual to assume that there is no time for any mass-flow by diffusion of gas into or out of the bubble. On collapse, transient bubbles produce very high pressures and temperatures, which cause such phenomena as erosion, sonoluminescence, sonochemical and biological effects. In the ultrasonic treatment of a solidifying melt, transient bubbles can cause breakdown of the dendrite arms.

2.10.1 Transient Cavitation Thresholds

The generation of transient bubbles for small increases in the acoustic pressure amplitude of a stable bubble is unexpected, but Flynn (1964,1975) explains how this transformation comes about by writing the acceleration of the bubble interface \ddot{R} in terms of two acceleration functions:

$$\ddot{R} = IF + PF \quad (2.40)$$

where

$$IF = -\frac{3 \dot{R}^2}{2 R} \quad (2.41)$$

and

$$PF = \frac{1}{\rho R} \left[\left(P_0 + \frac{2\sigma}{R_0} \right) \left(\frac{R_0}{R} \right)^{3\eta} - \frac{2\sigma}{R} - (P_0 + P(t)) \right] \quad (2.42)$$

We have ignored $P(t) = -P_A \sin \omega t$, which is small at the start of the collapse. Flynn calls IF the inertial function because it represents the part of the acceleration due to spherical contraction of the liquid. It is always an inward acceleration except at the maximum radius R_{\max} , when it vanishes. As R decreases in magnitude from R_{\max} , IF rapidly increases in magnitude and is, of course, negative. IF is a function of both R and \dot{R} and hence for each R - t curve there corresponds a different IF function as a function of R .

On the other hand, Flynn calls PF the pressure function because it is a function only of R and hence is the same for all R - t curves for a given bubble in a specific liquid. It is a net pressure at the interface divided by the radius. At the maximum radius R_{\max} , the function PF is a small inward acceleration but eventually becomes a large outward acceleration that ultimately arrests the inward motion of the bubble. At some radius R_k between R_{\max} and R_0 , the function PF will have a minimum. The essential characteristic of PF is that this function changes very little for all radii between the maximum radius R_{\max} and the position R_k of the minimum of PF. Over this range of R , the pressure at the interface is almost constant and the bubble behaves as a Rayleigh cavity (bubble) between R_{\max} and R .

Whether a bubble becomes a transient bubble on collapse depends on the competition between IF and PF. If R_{\max} is large enough, a bubble will accelerate to a high inward speed under the influence of IF before PF takes effect and decelerates it. Flynn (1964) states that it is possible to show if IF lies below PF at R_k , then the bubble will be transformed into a transient bubble. The condition for this transformation is that the

relative maximum radius R_{\max}/R_0 on expansion should be greater than a minimum value given by:

$$\left(\frac{R_{\max}}{R_0}\right) = \left(\frac{7.48 P_{g0}}{P_0}\right)^{1/3} \quad (2.43)$$

where P_{g0} is the initial pressure of the gas in the bubble and P_0 is the ambient pressure in the liquid.

2.11 Liquid Compressibility Effects

For rapid bubble collapse, the compressibility of the liquid must be taken into account and the simplest way to account for the compressibility effect is to consider a constant stiffness (i.e. constant sound velocity C_1). This is called “acoustic approximation” and can be used as the equation of state $\partial P / \partial \rho = C_1^2$. It limits the analysis to cases where the bubble wall velocity \dot{R} is always small compared to C and introduce a loss of energy by sound radiation. By using this approximation, Flynn (1964) showed that the compressible form of bubble dynamics equation is:

$$R\ddot{R} + \frac{3}{2}\dot{R}^2 = \frac{1}{\rho_l} \left[P_B(t) + \frac{R}{C_1} \left(1 - \frac{\dot{R}}{C_1} \right) \frac{dP_B(t)}{dt} - P_\infty \right] \quad (2.44)$$

where $P_B(t) = P[r = R(t), t]$.

Herring (1941) included a better description of the storage of energy through compression of the liquid as well as sound radiation, and obtained:

$$\left(1 - \frac{2\dot{R}}{C_1} \right) R\ddot{R} + \frac{3}{2} \left(1 - \frac{4\dot{R}}{3C_1} \right) \dot{R}^2 = \frac{1}{\rho_l} \left[P_B(t) + \frac{R}{C_1} \left(1 - \frac{\dot{R}}{C_1} \right) \frac{dP_B(t)}{dt} - P_\infty \right] \quad (2.45)$$

Gilmore(1952) was able to account for the formation of shock waves when the bubble wall velocity approaches the velocity of sound using Kirkwood-Bethe (1942) approximation, which states that the waves are propagated with a velocity equal to the sum of the sound velocity and the fluid velocity. This leads to:

$$\left(1 - \frac{\dot{R}}{C_1}\right)R\ddot{R} + \frac{3}{2}\left(1 - \frac{\dot{R}}{3C_1}\right)\dot{R}^2 = \left(1 + \frac{\dot{R}}{C_1}\right)H + \frac{R}{C}\left(1 - \frac{\dot{R}}{C_1}\right)\frac{dH}{dt} \quad (2.46)$$

where H is the difference in the liquid enthalpy between the bubble wall and infinity. Both H and C_1 are functions of the motion, thus giving a complex equation but a very accurate one. More details of the subject can be found in Knapp (1979).

Trilling (1952) presented another equation for the collapse and rebound of a gas bubble in a slightly compressible liquid based on the acoustic approximation. He assumed that the velocity potential ϕ would satisfy approximately the acoustic equation for diverging spherical waves:

$$\left(\frac{\partial}{\partial t} + C_1 \frac{\partial}{\partial r}\right)r\phi = 0 \quad (2.47)$$

This expresses the condition that the quantity $r\phi$ is propagated through the liquid with sonic velocity C_1 . If gravity and viscosity are neglected, the equation of motion for the radial liquid flow is:

$$\frac{\partial u}{\partial t} + u \frac{\partial u}{\partial r} + \frac{1}{\rho_1} \frac{\partial P}{\partial r} = 0 \quad (2.48)$$

which integrates to:

$$-\frac{\partial \phi}{\partial t} + \frac{u^2}{2} + \int_{P_\infty}^{P(r)} \frac{dP}{\rho} = 0 \quad (2.48a)$$

where $P(r)$ is the local pressure in the liquid, P_∞ is the pressure at infinity in the liquid, and ϕ and u equal zero at infinity.

Combining Eq. (2.47) with Eq. (2.48a) one gets:

$$ru \frac{\partial u}{\partial t} + \frac{r}{\rho_1} \frac{\partial P}{\partial t} + \frac{C_1 u^2}{2} + C_1 \int_{P_\infty}^{P(r)} \frac{dP}{\rho_1} + C_1 r u \frac{\partial u}{\partial r} + \frac{C_1 r}{\rho_1} \frac{\partial P}{\partial r} = 0 \quad (2.49)$$

The pressure and velocity at the bubble wall will satisfy the equations:

$$\begin{aligned} \frac{dP}{dt} &= \frac{\partial P}{\partial t} + U \frac{\partial P}{\partial r} \\ \frac{dU}{dt} &= \frac{\partial u}{\partial t} + U \frac{\partial u}{\partial r} \end{aligned} \quad (2.50)$$

where the capital letters refer to bubble wall values. The conservation of mass in radial flow can be written as:

$$\frac{1}{\rho_1 C_1^2} \frac{\partial P}{\partial t} + \frac{u}{\rho_1 C_1^2} \frac{\partial P}{\partial r} + \frac{\partial u}{\partial r} + \frac{2u}{r} = 0 \quad (2.51)$$

where $C_1^2 = dp/d\rho$. Solving the four simultaneous equations (2-48), (2.50) and (2.51) for four partial derivatives of P and u at the bubble wall and using them in Eq. (2.49) one gets the motion of the liquid at the bubble wall as:

$$R \frac{dU}{dt} \left(1 - \frac{2U}{C_1}\right) + \frac{3}{2} U^2 \left(1 - \frac{4U}{3C_1}\right) = \frac{R}{\rho_1 U} \frac{dP}{dt} \left(\frac{U}{C_1} - \frac{U^2}{C_1^2} + \frac{U^3}{C_1^3}\right) + \int_{P_\infty}^P \frac{dP}{\rho_1} \quad (2.52)$$

In the last term, variations in ρ from its mean value are proportional to $(U/C_1)^2$. If we neglect higher-order terms and use $dR = U dt$, the approximate result is:

$$RU \frac{dU}{dR} \left(1 - \frac{2U}{C_1}\right) + \frac{3}{2} U^2 \left(1 - \frac{4U}{3C_1}\right) = \frac{RU}{\rho_1 C_1} \frac{dP}{dR} + \frac{P_B - P_\infty}{\rho_1} \quad (2.53)$$

or

$$\left(1 - \frac{2\dot{R}}{C_1}\right) R\ddot{R} + \frac{3}{2} \left(1 - \frac{4\dot{R}}{3C_1}\right) \dot{R}^2 = \frac{1}{\rho_1} \left[P_B(t) - P_\infty + \frac{R}{C_1} \frac{dP_B(t)}{dt} \right] \quad (2.54)$$

Keller and Kolodner (1956) took into account the compressibility of water in the case of an underwater explosion when a bubble of gas is formed at high pressure. This bubble expands rapidly until its pressure falls to that of the surrounding water, but inertia causes it to overexpand. After it ceases to expand, the pressure of the surrounding water compresses it again to a high pressure. This cycle of expansion and contraction continues with oscillations of diminishing amplitude. If the water is treated as incompressible, theory yields undamped oscillations of constant period. However, by treating the water as slightly compressible, Keller and Koloner predicted damped oscillations with diminishing period. Comparison of predicted and observed radius-time curves showed good agreement.

Prosperetti (1993) introduced a general Keller-Herring equation as the equation of spherical bubble dynamics in a slightly compressible liquid:

$$\left[1 + (\lambda + 1) \frac{\dot{R}}{C_1}\right] R\ddot{R} + \frac{3}{2} \left[1 - \left(\lambda + \frac{1}{3}\right) \frac{\dot{R}}{C_1}\right] \dot{R}^2 = \left[1 + (\lambda - 1) \frac{\dot{R}}{C_1} + \frac{R}{C_1} \frac{d}{dt}\right] \frac{P_B - P}{\rho_1} \quad (2.55)$$

where P must be regarded as the pressure at the position occupied by the bubble center in the absence of the bubble. For $\lambda = 0$, this equation reduces to the form given by Keller in 1956, while with $\lambda = 1$, it becomes the equation suggested by Herring in 1941.

Nomenclature

b	damping constant	
C	concentration of dissolved gas in liquid	Kg/m^3
C_0	saturation concentration of dissolved gas in liquid	Kg/m^3
C_i	concentration of dissolved gas in liquid far from bubble	Kg/m^3
C_1	sound speed of liquid	m/s
D	mass diffusion constant	m^2/s
f	frequency	$1/\text{s}$
f_r	resonance frequency	$1/\text{s}$
k	wave number	
P	pressure	Pa
P_0	static pressure in liquid	Pa
P_∞	far field pressure in liquid	Pa
R, R_0	bubble radius and initial bubble radius	m
\dot{R}, \ddot{R}	bubble wall velocity and bubble wall acceleration	$\text{m/s}, \text{m/s}^2$
r	distance from bubble center	m
T	temperature	K
t	time	s
V	bubble volume	m^3
ρ	density of gas	kg/m^3
ρ_l	density of liquid	kg/m^3
α_g	thermal diffusion constant for the gas	m^2/s
α	phase angle	
λ	wave length	m
η	polytropic index of gas	
γ	ratio of specific heats of gas	
σ	surface tension of liquid	N/m
ν_1, μ_1	kinematic and dynamic viscosity of liquid	$\text{m}^2/\text{s}, (\text{N}\cdot\text{s})/\text{m}^2$

ω	angular velocity	1/s
ω_r	resonance angular velocity	1/s
τ_n	normal stress	Pa

Subscripts

g	gas
l	liquid
0	initial state

References

- Apfel, R. E., *Methods of Experimental Physics*, Vol. 19, *Ultrasonics*, Academic Press., p.373, 1981.
- Blake, F. G., Bjerknes Forces in Stationary Sound Fields, *J. Acoust. Soc. Am.*, Vol. 21, p. 551, 1949a.
- Blake, F. G., The Onset of Cavitation in Liquids, *Acoustics Res. Lab., Harvard Univ., Tech. Memo.*, No. 12, 1949b.
- Brennen, C. E., *Cavitation and Bubble Dynamics*, Oxford University Press, 1995.
- Chapman, R. B. and Plesset, M. S., Thermal Effects in the Free Oscillation of Gas Bubbles, *ASME J. Basic Eng.*, Vol. 93. pp. 373-376, 1971.
- Crum, L. A., Measurement of the Growth of Air Bubbles by Rectified Diffusion, *J. Acoust. Soc. Am.*, Vol. 68, pp. 203-211, 1980.
- Crum, L. A., Rectified Diffusion, *Ultrasonics*, Vol. 22, pp. 215-223, 1984.
- Eller, A. I. and Flynn, H. G., Rectified Diffusion During Nonlinear Pulsation of Cavitation Bubbles, *J. Acoust. Soc. Am.*, Vol. 37, pp. 493-503, 1965.
- Eller, A. I., Damping Constants of Pulsating Bubbles, *J. Acoust. Soc. Am.*, Vol. 47, pp. 1469-1470, 1970.
- Epstein, P. S. and Plesset, M. S., On the Stability of Gas Bubbles in Liquid-Gas Solutions, *J. Chem. Phys.*, Vol. 18, pp. 1505-1509, 1950.
- Esche, R., Untersuchung der Schwingungskavitation in Flüssigkeiten, *Acustica*, Vol. 2, pp. AB208-AB218, 1952.
- Feng, Z. C. and Leal, L. G., Nonlinear Bubble Dynamics, *Annu. Rev. Fluid Mech.*, Vol. 29, pp. 201-243, 1997.
- Flynn, H. G., Physics of Acoustic Cavitation in Liquids, *Physical Acoustics*, Vol. 1B, W. P. Mason (ed), Academic Press, Chap. 9, p.76, 1964.
- Flynn, H. G., Cavitation Dynamics. II. Free Pulsations and Methods for Cavitation Bubbles, *J. Acoust. Soc. Am.*, Vol. 58, p. 1160, 1975.
- Gilmore, F R., The Growth or Collapse of a Spherical Bubble in a Viscous Compressible Liquid, California Institute of Tech., Hydrodynamics Lab. Report No. 26-4, 1952.

- Greenspan, M. and Tschiegg, C. E., Radiation-Induced Acoustic Cavitation; Apparatus and Some Results, *J. Res. Natn. Bur. Stands, Sec. C*, Vol. 71, p. 229, 1967.
- Harvey, E. N., Barnes, D. K., McElroy, W. D., Whiteley, A. H., Pease, D. C., and Cooper, K. W., Bubble Formation in Animals, *J. Cell. Comp. Physiol*, Vol. 24, No. 1, pp. 1-22, 1944.
- Herring, C., Theory of the Pulsations of the Gas Bubble Produced by an Underwater Explosion, Office of Science Research and Development, Report No. 236, (NDRC Report C-4-sr 10-010, Columbia University), 1941.
- Hsieh, D. Y. and Plesset, M. S., Theory of Rectified Diffusion of Mass into Gas Bubbles, *J. Acoust. Soc. Am.*, Vol. 33, pp. 206-215, 1961.
- Hsieh, D. Y., Some Analytical Aspects of Bubble Dynamics, *J. Basic Engng*, Vol. 87D, p. 991, 1965.
- Keller, J. B. and Kolodner, I. I., Damping of Underwater Explosion Bubble Oscillations, *J. Appl. Phys.*, Vol. 27, p. 1152, 1956.
- Kirkwood, J. G. and Bethe, H. A., The Pressure Wave Produced by an Underwater Explosion, Office of Science Research and Development Report, p. 588, 1942.
- Knapp, R., T., James, W., D. and Hammitt, F., G., *Cavitation*, Institute of Hydraulic Research, University of IOWA, 1979.
- Lauterborn, W., Numerical Investigation of Nonlinear Oscillations of Gas Bubbles in Liquid, *J. Acoust. Soc. Am.*, Vol. 59, pp. 283-293, 1976.
- Neppiras, E., A. and Noltingk, B. E., Cavitation Produced by Ultrasonics: Theoretical Conditions for the Onset of Cavitation, *Proc. Phys. Soc.*, London, Vol. 64B, pp. 1032-1038, 1951.
- Neppiras, E. A., Subharmonic and Other Low-Frequency Emission from Bubbles in Sound-Irradiated Liquids, *J. Acoust. Soc. Am.*, Vol. 46, pp. 587-601, 1969.
- Neppiras, E. A., Acoustic Cavitation, *Phys. Rep.*, Vol. 61, pp. 160-251, 1980.
- Noltingk, B. E. and Neppiras, E. A., Cavitation Produced by Ultrasonics, *Proc. Phys. Soc.*, London, Vol. 63B, pp. 674-685, 1950.
- Plesset, M. S., and Hsieh, D. Y., Theory of Gas Bubble Dynamics in Oscillating Pressure Fields, *Physics of Fluids*, Vol. 3, pp. 882-892, 1960.

- Plesset, M. S. and Prosperetti, A., Bubble Dynamics and Cavitation, *Ann. Rev. Fluid Mech.*, Vol. 9, pp. 145-185, 1977.
- Poritsky, H., The Collapse or Growth of a Spherical Bubble or Cavity in a Viscous Fluid, *Proc. First Nat. Cong. in Appl. Math.*, pp. 813-82, 1952.
- Prosperetti, A., Bubble Phenomena in Sound Fields: part one and part two, *Ultrasonics*, Vol. 22, pp. 69-77, 1984.
- Prosperetti, A., Application of the Subharmonic Threshold to the Measurement of the Damping of Oscillating Gas Bubbles, *J. Acoust. Soc. Am.*, Vol. 61, pp. 11-16, 1977.
- Prosperetti, A., Bubble Dynamics: Some Things We Did Not Know 10 Years Ago, *Proc. IUTM Sym.*, Birmingham, pp. 3-16, 1993.
- Rayleigh, L., On the Pressure Developed in a Liquid During the Collapse of a Spherical Cavity, *Phil. Mag.*, Vol. 34, pp. 94-99, 1917.
- Trilling, L., The Collapse and Rebound of a Gas Bubble, *J. Appl. Phys.*, Vol. 23, No. 14, pp. 14-17, 1952.
- Young, F. R., *Cavitation*, McGraw-Hill Company, 1989.

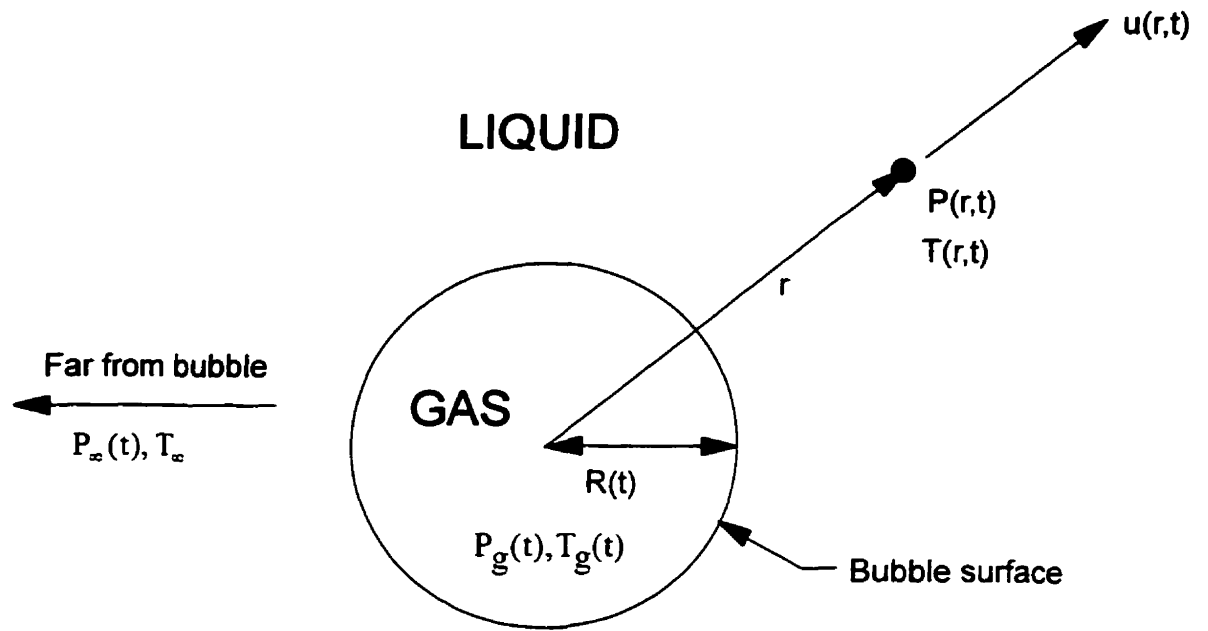


Fig. 2.1. Schematic of a spherical bubble in an infinite liquid

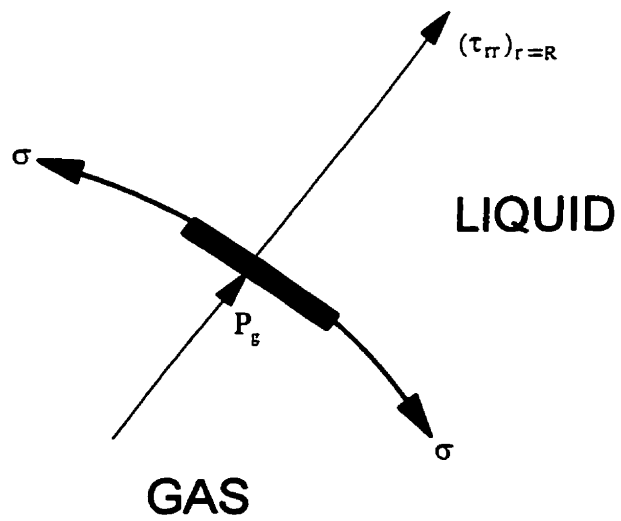


Fig. 2.2. Portion of the spherical bubble surface

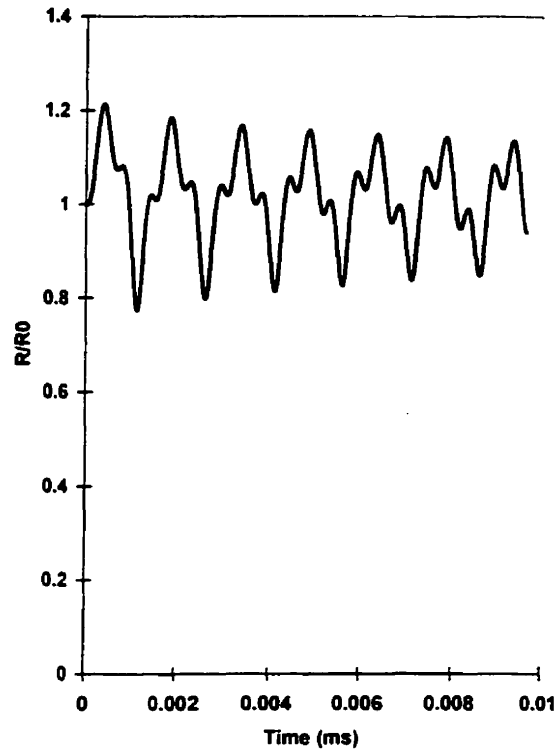


Fig. 2.3. Typical history of bubble radius for a stable bubble.

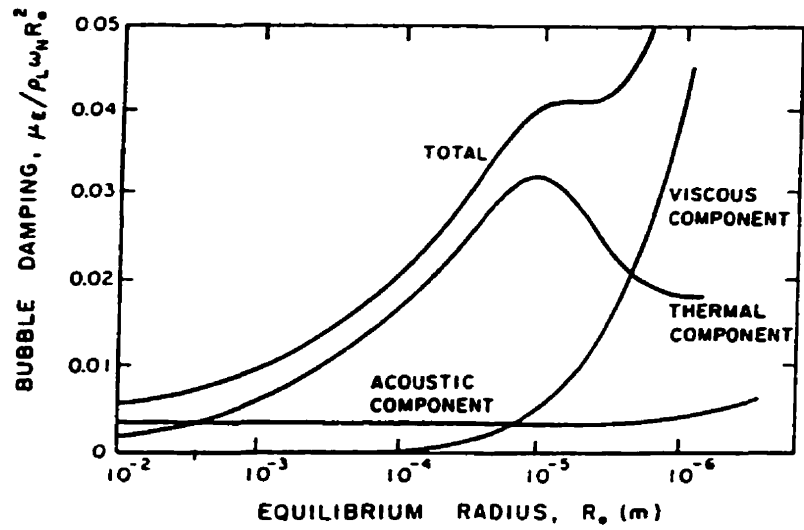


Fig. 2.4. Bubble damping components and the total damping as a function of the equilibrium bubble radius, R_0 , for water.

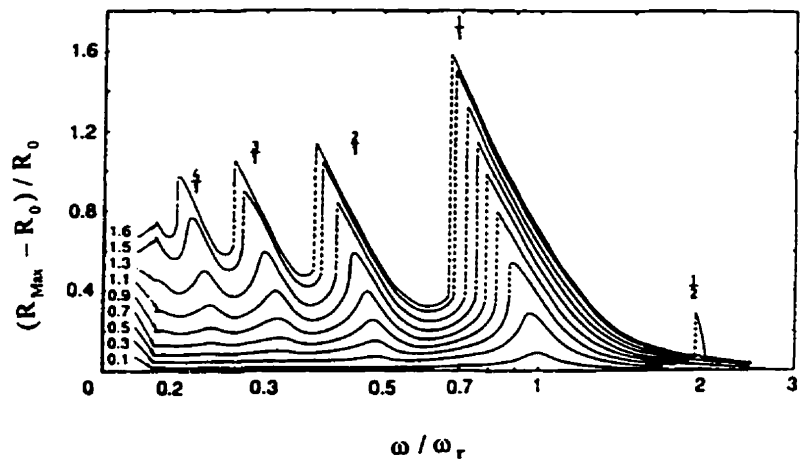


Fig. 2.5. Numerically computed amplitudes of radial oscillation of a bubble of radius $1\ \mu\text{m}$ in water at a mean ambient pressure of 1 bar plotted as a function of ω / ω_r for various amplitudes of oscillation. The numbers above the peaks indicate the order of the resonance.

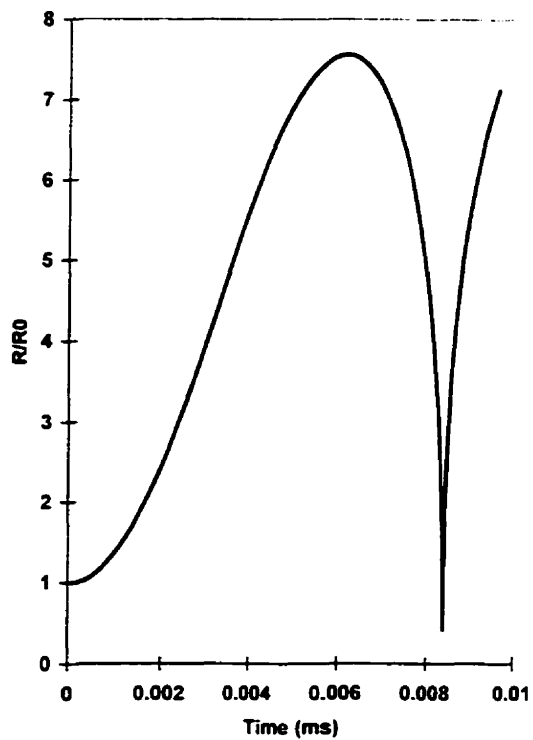


Fig. 2.6. Typical history of bubble radius for a transient bubble.

MODEL DEVELOPMENT AND NUMERICAL SOLUTION METHODS

3.1 Introduction

Bubble dynamics is a very fast moving boundary phenomenon and variables change rapidly with time. In transient bubble dynamics, the pressure waves generated in the liquid adjacent to the bubble surface can be in the order of several hundreds to thousands atmospheres. For accurate computations of the high pressure waves generated due to violent collapse of the bubble, a special numerical procedure is required to capture the high pressure waves. On the other hand, in reactive bubble dynamics, the reactive gas mixture explodes when it reaches the ignition point of the gas mixture. The chemical reactions that occur in this case are very fast and the time scale for exothermic reactions are very small. Therefore, due to having significantly different time and length scales in the mathematical models, the problems are stiff. Stiffness is one of the most difficult aspects of these types of problems and often controls the method of solution of the modeled differential equations.

The task of solving comprehensive mathematical models in bubble dynamics is very complex. A comprehensive mathematical model, which is free of any unrealistic assumptions and restrictions, is only amenable to the specific numerical methods. Almost invariably a numerical solution method is required for this class of problems and solutions can only be carried out analytically for small-amplitude motions in which the equations can be linearized.

This chapter first gives an overview of the models development and then describes the numerical methods used for solving the comprehensive mathematical models which are presented in the following chapters. The solution method is based on using a FORTRAN subroutine, LSODE, the Livermore Solver for Ordinary Differential Equations (Hindmarch, 1980 and 1981). In the computational solution, the main program and the associated subroutines that define the ODE system, the analytical Jacobian matrix and other necessary subprograms required by the main program have been written.

3.2 Models Development

Comprehensive mathematical models have been developed to simulate the dynamic behavior of different gas bubbles. The mass, momentum and energy equations have been taken into account for both gas and liquid regions. In the case of reactive gas, the chemical reaction has been modeled by using a two-step Arrhenius-type reaction model. The physical phenomena occurring at the interface have been considered including heat and mass transfer. The mathematical models include the constitutive equations of state for the gas and the medium surrounding the bubble. The equation of state for the gas is perfect gas law. The liquid surrounding the bubble is assumed to be slightly compressible with constant sound speed. The mathematical models form a set of coupled, highly nonlinear and stiff differential equations. The equation for bubble dynamics is an ordinary differential equation while the other equations concerning heat and mass transfer are partial differential equations. In order to convert the PDEs into a system of stiff ODEs, the partial differential equations are discretized only in space direction using a *semi-discrete* method. Generally, this technique is based on the Lagrangian solution method.

For the ease of numerical work, it is convenient to have a fixed rather than a moving boundary of the bubble. Therefore, the model equations are transformed using an appropriate variable [$\zeta = r / R(t)$] to freeze the moving boundary of the bubble. Also, in order to decrease the number of parameters and minimize computational errors, the governing equations are non-dimensionalized. The transformed and non-dimensional

form of the mathematical model equations, which constitute an initial value problem, have been solved numerically.

3.3 Numerical Solution Methods

3.3.1 Initial Value Problem

An initial value problem in the form of a system of first-order ordinary differential equation is shown in Equation (3.1). Second or higher order equations can almost always be reduced to systems of first order equations.

$$\left. \begin{aligned} \underline{\dot{y}} &\equiv \frac{d\underline{y}}{d\xi} = \underline{f}(\underline{y}(\xi), \xi) \\ \underline{y}(\xi_0) &= \underline{y}_0 = \text{Given} \end{aligned} \right\} \quad (3.1)$$

where \underline{y} , \underline{y}_0 , $\underline{\dot{y}}$, and \underline{f} are column vectors with $N(\geq 1)$ components and ξ is the independent variable, time. In component form, equation (3.1) may be written as:

$$\left. \begin{aligned} \frac{dy_i(\xi)}{d\xi} &= f_i(y_1(\xi), \dots, y_N(\xi), \xi) \\ y_i(\xi_0) &= y_{i,0} = \text{Given} \end{aligned} \right\} \quad i = 1, \dots, N \quad (3.2)$$

The above set of equations form what is called the initial value problem. In this problem, it is required to find the solution function \underline{y} at one or more values of ξ in a prescribed integration interval $[\xi_0, \xi_{\text{end}}]$, when the initial value of \underline{y} , \underline{y}_0 , at $\xi = \xi_0$ is given. The endpoint, ξ_{end} , may not be known in advance as, for example, when asymptotic values of \underline{y} are required as $\xi \rightarrow \infty$.

In order to solve this class of problems, it is normally assumed that the problem is well posed and possesses a solution that is unique in the interval of interest. Solution existence and uniqueness are guaranteed if, in the region of interest, \underline{f} is defined and continuous and for any two vectors \underline{y} and \underline{y}^* in that region there exists a positive constant L such that (Shampine, 1975 and Lambert, 1973):

$$\| \underline{f}(\underline{y}, \xi) - \underline{f}(\underline{y}^*, \xi) \| \leq L \| \underline{y} - \underline{y}^* \| \quad (3.3)$$

which is known as a Lipschitz condition. Here $\| \cdot \|$ denotes a vector norm, and the constant L is known as a Lipschitz constant of \underline{f} with respect to \underline{y} .

3.3.2 Stiff Problems

Initial value, stiff ODE's arise in many fields, such as chemical kinetics, electric network analysis and any system that displays boundary layer-type behavior. A system will have boundary layer behavior when there is a small length scale that is important in a small region and a longer scale that is important in the remainder of the system. Many problems arising from parabolic differential equations. When finite differenced, these turn out to be equivalent to solving a stiff system of ordinary differential equations (Ferziger, 1981). Physically, stiffness occurs when the problem contains widely disparate time or length scales. Shampine and Gear (1979) discuss some fundamental issues related to stiffness and how it arises. An approximate description of a stiff ODE system is that it contains both very rapidly and very slowly decaying terms. Also, a characteristic of such a system is that the $N \times N$ Jacobian matrix \mathbf{J} ($= \partial \underline{f} / \partial \underline{y}$), with element J_{ij} defined as:

$$J_{ij} = \partial f_i / \partial y_j, \quad i, j = 1, \dots, N \quad (3.4)$$

has eigenvalues $\{\lambda_i\}$ with real parts that are predominantly negative and also vary widely in magnitude. A quantitative measure of stiffness is usually given by the stiffness ratio

$\max[-\operatorname{Re}(\lambda_i)] / \min[-\operatorname{Re}(\lambda_i)]$. A problem with stiffness ratio of order 1000 would be considered stiff.

The difficulty with stiff problems is the prohibitive amounts of computer time required for their solution by classical ODE solution methods, such as the popular explicit Runge-Kutta and Adams methods. The reason for prohibitive computer time requirements is the excessively small step sizes that these methods must use to satisfy stability requirements. Because of the approximate nature of the solutions generated by numerical integration methods, errors are inevitably introduced at every step. For a numerical method to be stable, errors introduced at any one step should not grow unbounded as the calculation proceeds. To maintain numerical stability, classical ODE solution methods must use small step sizes of order $1 / \max[-\operatorname{Re}(\lambda_i)]$ even after the rapidly decaying components have decreased to negligible levels. Examples of the step size pattern used by an explicit Runge-Kutta method in solving stiff ODE problems arising in combustion chemistry are given by Radhakrishnan (1986). The size of the integration interval for the evolution of the slowly varying components is of the order $1 / \min[-\operatorname{Re}(\lambda_i)]$. Consequently, the number of steps required by classical methods to solve the problem is of the order $\max[-\operatorname{Re}(\lambda_i)] / \min[-\operatorname{Re}(\lambda_i)]$, which is very large for stiff ODE's and imply a lot of roundoff (computer related) errors.

3.3.3 Accuracy of the Method

Accuracy of a numerical method refers to the magnitude of the error introduced in a single step or, more precisely, the local truncation or discretization error. The local truncation error \underline{d}_n at ξ_n is the difference between the computed approximation and the exact solution, with both starting the integration at the previous mesh point ξ_{n-1} and using the exact solution $\underline{y}(\xi_{n-1})$ as the initial value. The local truncation error on any step is therefore the error incurred on that step under the assumption of no past errors.

The accuracy of a numerical method is usually measured by its order. A method is said to be of order q if the local truncation error varies as h_n^{q+1} . More precisely, a

numerical method is of order q if there are quantities \underline{C} and $h_0 (> 0)$ such that (Shampine, 1975 and Dahlquist, 1974):

$$|\underline{d}_n| \leq \underline{C} h_n^{q+1} \quad \text{for all} \quad 0 < h_n \leq h_0 \quad (3.5)$$

$$h_n = \xi_n - \xi_{n-1} \quad (3.6)$$

where h_n is the spacing between any two mesh points and $|\underline{d}_n|$ is an N -dimensional column vector containing the absolute values of the $d_{i,n}$ ($i = 1, \dots, N$). The coefficient vector \underline{C} may depend on the function defining the ODE and the total integration interval, but it should be independent of the step size h_n . Accuracy of a numerical method refers to the smallness of the error introduced in a single step; stability refers to whether or not this error grows in subsequent steps.

3.3.4 Linear Multistep Method (BDF)

The numerical method generates approximate solutions \underline{Y}_n to the stiff ordinary differential equation at discrete points ξ_n ($n = 1, 2, \dots$). Assuming that the approximate solutions \underline{Y}_{n-j} have been computed at the mesh points ξ_{n-j} ($j = 1, 2, \dots$), this method advances the solution to the current value ξ_n of the independent variable by using linear multistep formula of the type:

$$\underline{Y}_n = \underline{\psi}_n + h_n \beta_0 \underline{f}_n = \underline{\psi}_n + h_n \beta_0 \underline{f}(\underline{Y}_n) \quad (3.7)$$

where $\underline{\psi}_n$ contains previously computed information and is given by:

$$\underline{\psi}_n = \sum_{j=1}^q \alpha_j \underline{Y}_{n-j} \quad (3.8)$$

The term BDF “backward differentiation formula” is used to describe the method because equation (3.7), upon division by $h_n \beta_0$ and rearrangement of terms, can be

regarded as an approximation for $\dot{y}(\xi_n)$ in terms of $Y_n, Y_{n-1}, \dots, Y_{n-q}$ (Byrne et al., 1987).

The coefficients $\{\alpha_j\}$ and $\{\beta_j\}$ are determined such that equations (3.7) will be exact if the solution to equation (3.1) is a polynomial of degree q or less. Stability characteristics limit q in equation (3.6) to 6. The coefficients $\{\alpha_j\}$ and $\{\beta_j\}$ are given by Gear (1971a) for $q \leq 6$ and reproduced in Table 3.1.

Table 3.1. Method Coefficients for Backward Differentiation Formula given by Gear

q	2	3	4	5	6
β_0	$\frac{2}{3}$	$\frac{6}{11}$	$\frac{12}{25}$	$\frac{60}{137}$	$\frac{60}{147}$
α_1	$\frac{4}{3}$	$\frac{18}{11}$	$\frac{48}{25}$	$\frac{300}{137}$	$\frac{360}{147}$
α_2	$-\frac{1}{3}$	$-\frac{9}{11}$	$-\frac{36}{25}$	$-\frac{300}{137}$	$-\frac{450}{147}$
α_3		$\frac{2}{11}$	$\frac{16}{25}$	$\frac{200}{137}$	$\frac{400}{147}$
α_4			$-\frac{3}{25}$	$-\frac{75}{137}$	$-\frac{225}{147}$
α_5				$\frac{12}{137}$	$\frac{72}{147}$
α_6					$-\frac{10}{147}$

In equation (3.7) the subscript n has been attached to the step size h , indicating that h_n is the step size to be attempted on the current step. When the step size is changed, the data at the new spacing required to continue the integration are obtained by interpolating from the data at the original spacing.

To satisfy accuracy requirements, the BDF method may have to use small step sizes of the order $1 / \max[-\text{Re}(\lambda_i)]$ in regions where the most rapid exponentials are active. However, outside these regions, which are usually small relative to the total integration interval, larger step sizes may be used.

3.3.5 Corrector Iteration Method

If $\beta_0 = 0$ in equation (3.7), the method is called explicit because it involves only the known values $\{\underline{Y}_{n-j}\}$ and $\{\underline{f}_{n-j}\}$, and equation (3.7) is easy to solve. If, however, $\beta_0 \neq 0$, the method is called implicit and, in general, solution of equation (3.7) is expensive. In equation (3.7), β_0 is positive for each q and because \underline{f} is, in general, nonlinear, some type of iterative procedure is needed to solve equation (3.7). Nevertheless, implicit method is preferred because it is more stable, and hence can use much larger step sizes, than explicit method and is also more accurate for the same order and step size (Lambert, 1973 and Gear, 1971a). Explicit method is used as predictor, which generates an initial guess for \underline{Y}_n . The implicit method corrects the initial guess iteratively and provides a reasonable approximation to the solution of equation (3.7).

The predictor-corrector process for advancing the numerical solution to ξ_n therefore consists of first generating a predicted value, denoted by $\underline{Y}_n^{[0]}$, and then correcting this initial estimate by iterating equation (3.7) to convergence. That is, starting with the initial guess $\underline{Y}_n^{[0]}$, approximations $\underline{Y}_n^{[m]}$ ($m = 1, 2, \dots, M$) are generated by Newton-Raphson iterations until the magnitude of the difference in two successive approximations approaches zero within a specified accuracy. The quantity $\underline{Y}_n^{[m]}$ is the approximation obtained on the m th iteration, the integer M is the number of iterations required for convergence, and we accept $\underline{Y}_n^{[M]}$ as an approximation to the exact solution \underline{y} at ξ_n and therefore denote it by \underline{Y}_n although, in general, it does not satisfy equation (3.7) exactly.

At each iteration m the quantity $h_n \dot{Y}_n^{[m]}$, which is defined here, is computed from $Y_n^{[m]}$ by the relation:

$$Y_n^{[m]} = \psi_n + h_n \beta_0 \dot{Y}_n^{[m]} \quad (3.9)$$

Now, if $Y_n^{[m]}$ converges as $m \rightarrow \infty$, the limit, that is, $\lim_{m \rightarrow \infty} Y_n^{[m]}$, must be a solution of equation (3.7) and $\dot{Y}_n^{[m]}$ converges to $\underline{f}_n [= f(Y_n)]$, the approximation to $\dot{y}(\xi_n)$. Hence $h_n \dot{Y}_n^{[m]}$ is the m th estimate for $h_n \underline{f}_n$ and $\lim_{m \rightarrow \infty} h_n \dot{Y}_n^{[m]} = h_n \underline{f}_n$. The predicted value of $h_n \underline{f}_n$, denoted by $h_n \dot{Y}_n^{[0]}$, is also obtained from equation (3.9) (by setting $m = 0$). In practice, we terminate the calculation sequence at a finite number M of iterations and accept as an approximation to $h_n \underline{f}_n$ the quantity $h_n \dot{Y}_n \equiv h_n \dot{Y}_n^{[M]}$, which is obtained from $Y_n^{[M]}$ by using equation (3.9). Note that \dot{Y}_n is only an approximation to \underline{f}_n because $Y_n^{[M]}$ does not, in general, satisfy equation (3.7) exactly. Moreover, because $\dot{Y}_n^{[M]}$ is defined to satisfy the solution method, in the sense of equation (3.9), it is not necessarily equal to $\underline{f}(Y_n^{[M]})$. Therefore $Y_n^{[M]}$ and $\dot{Y}_n^{[M]}$ do not necessarily satisfy the ODE, equation (3.1). Thus, in practice, to advance the solution, the method uses the $\{\dot{Y}_j\}$ rather than the $\{\underline{f}_j\}$ as written in equation (3.7).

After convergence of the estimates $Y_n^{[m]}$, we could define $\dot{Y}_n^{[M]}$ to be equal to $\underline{f}(Y_n^{[M]})$, so that $Y_n^{[M]}$ and $\dot{Y}_n^{[M]}$ satisfy the ODE exactly.

The predicted values at ξ_n , $Y_n^{[0]}$, is generated by a q th-order explicit formula similar to equation (3.7) (Gear, 1967 and 1969):

$$Y_n^{[0]} = \sum_{j=1}^q \alpha_j \cdot Y_{n-j} + h_n \beta_1 \cdot \dot{Y}_{n-1} \quad (3.10)$$

In the equation (3.10) \underline{Y}_{n-j} is the approximation to \underline{f}_{n-j} computed on the step $[\xi_{n-j-1}, \xi_{n-j}]$. The coefficients $\{\alpha_j^*\}$ and $\{\beta_j^*\}$ are selected such that equation (3.10) will be exact if the solution to equation (3.1) is a polynomial of degree q or less.

The predictor step can be generalized as:

$$\underline{Y}_n^{[0]} = \underline{\psi}_n^* \quad (3.11)$$

where $\underline{\psi}_n^*$ is given by the right-hand sides of equations (3.10).

To correct the initial estimate given by equation (3.11), that is, to solve equation (3.7), Newton-Raphson iteration method is used.

3.3.6 Newton-Raphson Iteration

Newton-Raphson (NR) iteration converges quadratically and can use much larger step sizes than other iteration techniques (Lapidus et al., 1971). Rapid improvement in the accuracy of the estimates is especially important because the corrector is iterated to convergence. The reason for iterating to convergence is to preserve the stability characteristics of the corrector. If the correction process is terminated after a fixed number of iterations, the stability characteristics of the corrector are lost, with disastrous consequences for stiff problems.

To drive the NR iteration procedure, we rewrite equation (3.7) as:

$$\underline{R}(\underline{Y}_n) = \underline{Y}_n - \underline{\psi}_n - h_n \beta_0 \underline{f}(\underline{Y}_n) = 0 \quad (3.12)$$

so that solving equation (3.7) is equivalent to finding the zero of \underline{R} . The quantity $\underline{R}(\underline{Y}_n^{[m]})$ is the residual vector on the m th iteration; that is, it is the amount by which $\underline{Y}_n^{[m]}$ fails to satisfy equation (3.7). To obtain the $(m+1)$ th estimate, we expand equation (3.12) in a Taylor series about the m th estimate, neglect the second and higher derivatives, and set $\underline{R}(\underline{Y}_n^{[m+1]}) = 0$ because we seek a $\underline{Y}_n^{[m+1]}$ that produces this result.

Performing these operations and then rearranging terms give the following relation for the NR iteration technique:

$$\mathbf{P}(\underline{Y}_n^{[m+1]} - \underline{Y}_n^{[m]}) = -\underline{R}(\underline{Y}_n^{[m]}) = \underline{\psi}_n + h_n \beta_0 f(\underline{Y}_n^{[m]}) - \underline{Y}_n^{[m]} \quad (3.13)$$

where the $N \times N$ matrix \mathbf{P} is given by:

$$\mathbf{P} = \frac{\partial \underline{R}}{\partial \underline{Y}} = \mathbf{I} - h_n \beta_0 \mathbf{J} \quad (3.14)$$

In equation (3.14), \mathbf{I} is the $N \times N$ identity matrix and \mathbf{J} is the Jacobian matrix.

We now define the vector function $\underline{g}(\underline{y})$ by:

$$\underline{g}(\underline{y}) = h_n f(\underline{y}) + \frac{\underline{\psi}_n - \underline{y}}{\beta_0} \quad (3.15)$$

Comparing equation (3.15) and (3.12) shows that:

$$\underline{R}(\underline{Y}) = -\beta_0 \underline{g}(\underline{Y}) \quad (3.16)$$

so the equation (3.13) can be rewritten as follows:

$$\underline{Y}_n^{[m+1]} = \underline{Y}_n^{[m]} + \beta_0 \mathbf{P}^{-1} \underline{g}(\underline{Y}_n^{[m]}) \quad (3.17)$$

The NR iteration procedure for $h_n \dot{\underline{Y}}_n$ is derived by subtracting equation (3.9) from the $(m+1)$ th estimate equation and then using equation (3.17). The result is:

$$h_n \dot{\underline{Y}}_n^{[m+1]} = h_n \dot{\underline{Y}}_n^{[m]} + \mathbf{P}^{-1} \underline{g}(\underline{Y}_n^{[m]}) \quad (3.18)$$

This iteration will converge provided that the predicted value is sufficiently accurate. The prediction method, equation (3.11), provides a sufficiently accurate initial estimate that the corrector will converge after a few steps (typically three) (Lambert, 1973).

3.4 LSODE Subroutine

The LSODE has been designed for the numerical solution of a system of first-order stiff ordinary differential equations (ODE's) given the initial values. Second or higher order equations can be reduced to systems of first order equations. It is based on, and in many ways resembles, the subroutine Gear, which, in turn, is based on the code DIFSUB, written by Gear (1971b). All three codes use integration methods that are based on a constant step size but are implemented in a manner that allows for the step size to be dynamically varied throughout the problem. When the step size is changed, the data at the new spacing required to continue the integration are obtained by interpolating from the data at the original spacing (Byrne et al., 1987).

The solution method replaces the ODE's with difference equations and then solves them step by step. Starting with the initial conditions at ξ_0 , approximations $\underline{Y}_n (= Y_{i,n}, i = 1, \dots, N)$ to the exact solution $\underline{y}(\xi_n) [= y_i(\xi_n), i = 1, \dots, N]$ of the ODE's are generated at the discrete mesh points $\xi_n (n = 1, 2, \dots)$, which are themselves determined by the subroutine.

For stiff problems, LSODE uses the backward differentiation formula (BDF) method (Gear, 1971a), which is among the most popular currently used methods for such problems. The BDF method possesses the property of stiff stability and therefore does not suffer from the stability step size constraint once the rapid components have decayed to negligible levels. In this subroutine, BDF's of order up to only 5 are used because of additional stability considerations (Shampine et al., 1979). Throughout the integration the step size is limited only by accuracy requirements imposed on the numerical solution.

The code starts the integration with a first-order method and, as the integration proceeds, automatically adjusts the method order and the step size for optimal efficiency while satisfying prescribed accuracy requirements. At each step the method employs a predictor-corrector scheme, wherein an initial guess for the solution is first obtained and then the guess is improved upon by iteration. That is, starting with an initial guess,

denoted by $\underline{Y}_n^{[0]}$, successively improved estimates $\underline{Y}_n^{[m]}$ ($m = 1, \dots, M$) are generated until the iteration converges, that is, further iteration produces little or no change in the solution. Here $\underline{Y}_n^{[m]}$ is the approximation computed on the m th iteration, and M is the number of iterations required for convergence.

A standard explicit predictor formula, a Tylor series expansion method devised by Nordsieck (1962), is used to generate the initial estimate for the solution. A modified Newton-Raphson iteration technique is used for correcting this estimate.

3.4.1 Program Structure

The double-precision version of the code consists of the main core integration subroutine, LSODE along with the 20 other subprograms and a block data module for loading some variables. Table 3.2 lists the subprograms in the order they appear in the code and briefly describes each subprogram. The structure of the computational solver is illustrated in Figure 3.1, wherein a line connecting two subroutines indicates that the lower subroutine is called by the upper one. LSODE has been designed to be used as a single unit, and in normal circumstances the user needs to communicate with only a single subroutine. In addition to input parameters whose values are required by the code, the user can set values for several other parameters to control the solution methods and the output from the code.

In Figure 3.1, F is a subroutine that computes the derivatives $dy_i / d\xi$ ($i = 1, \dots, N$), where y_i is the i th component of \underline{y} and N is the number of ODE's. The subroutine JAC is also a subroutine that computes the analytical Jacobian matrix $J (= \partial \underline{f} / \partial \underline{y})$, where $\underline{f} = d\underline{y} / d\xi$. Both subroutines have been written and created in this study. All input parameters and other necessary subprograms (like time-averaged calculations in Chapter 5 and calculations of temperature-dependent thermodynamic parameters in Chapter 7) required by the main program have been written.

References

- Byrne, G. D. and Hindmarsh, A. C., Stiff ODE Solvers: A Review of Current and Coming Attractions, *J. Comput. Phys.*, Vol. 70, No. 1, pp. 1-62, 1987.
- Dahlquist, G., *Numerical Methods*, Translated by: Ned Anderson, Prentice-Hall, Englewood Cliffs, NJ, 1974.
- Ferziger, J. H., *Numerical Methods for Engineering Application*, John Wiley & Sons, 1981.
- Gear, C. W., *Numerical Initial Value Problems in Ordinary Differential Equations*, Prentice-Hall, Englewood Cliffs, NJ, 1971a.
- Gear, C. W., Algorithm 407, DIFSUB for Solution of Ordinary Differential Equations, *Comm. ACM*, Vol. 14, No. 3, pp. 185-190, 1971b.
- Gear, C. W., The Automatic Integration of Stiff Ordinary Differential Equations, *Information Processing*, A. J. H. Morrel, ed., North-Holland Pub. N.Y., pp. 187-193, 1969.
- Gear, C. W., The Numerical Integration of Ordinary Differential Equations, *Math. Comput.*, Vol. 21, pp. 146-156, 1967.
- Henrici, P., *Discrete Variable Methods in Ordinary Differential Equations*, Willey, New York, 1962.
- Hindmarch, A. C., LSODE and LSODI, Two New Initial Value Ordinary Differential Equation Solvers, *ACM SIGNUM Newsletter*, Vol. 15, No. 4, pp. 10-11, 1980.
- Hindmarch, A. C., ODE Solver for Use with the Method of Lines, *Advances in Computer Methods for Partial Differential Equations*, IMACS publishing Co., pp. 312-316, 1981.
- Lambert, J. D., *Computational Methods in Ordinary Differential Equations*, Willey & Sons, New York, 1973.
- Lapidus, L. and Seinfeld, J. H., *Numerical Solution of Ordinary Differential Equations*, Academic Press, New York, 1971.
- Nordsieck, A., On Numerical Integration of Ordinary Differential Equations, *Math. Comput.*, Vol. 16, pp. 22-49, 1962.

Shampine, L. F. and Gordon, M. K., *Computer Solution of Ordinary Differential Equations: The Initial Value Problem*, W. H. Freeman and Co., San Francisco, CA, 1975.

Shampine, L. F. and Gear, C. W., A User's View of Solving Stiff Ordinary Differential Equations, *SIAM Rev.*, Vol. 21. pp. 1-17, 1979.

Radhakrishnan, K., New Integration Technique for Chemical Kinetic Rate Equations, I. Efficiency Comparison, *Combust. Sci. Technol.*, Vol. 46, pp. 59-81, 1986.

Table 3.2. Description of Subprograms used in LSODE

Subprogram	Description
LSODE	Main core integration subroutine. Checks legality of input, sets work array pointers, initializes work arrays, computes initial integration step size, manages solutions of ODE's, and return to calling subroutine with solution and errors.
INTDY	Computes interpolated values of the specified derivative of the dependent variables.
STODE	Advances the solution of the ODE's by one integration step. Also, computes step size and method order to be attempted on the next step.
CFODE	Sets method coefficients for the solution and test constants for local error test and step size and method order selection.
PREPJ	Computes the iteration matrix and either manages the subprogram call for its LU-decomposition or computes its inverse.
SOLSY	Manages solution of linear system arising from chord iteration.
EWSET	Sets the error weight vector.
VNORM	Computes weighted root-mean-square norm of a vector.
SRCOM	Saves and restores contents of common blocks LS0001 and EH0001.
DIMACH	Computes unit roundoff of the computer.
XERRWV	Handles error messages.
XSETF	Resets print control flag.
XSETUN	Resets logical unit number for error messages.
DGEFA	Performs LU-decomposition of a full matrix by Gaussian elimination.
DGESL	Solves a linear system of equations using a previously LU-decomposed full matrix.
DGBFA	Performs LU-decomposition of a banded matrix by Gaussian elimination.
DGBSL	Solves a linear system of equations using a previously LU-decomposed banded matrix.
DAXPY	Forms the sum of one vector and another times a constant.
DSCAL	Scales a vector by a constant.
DDOT	Computes dot product of two vectors.
IDAMAX	Identifies vector component of maximum absolute value.

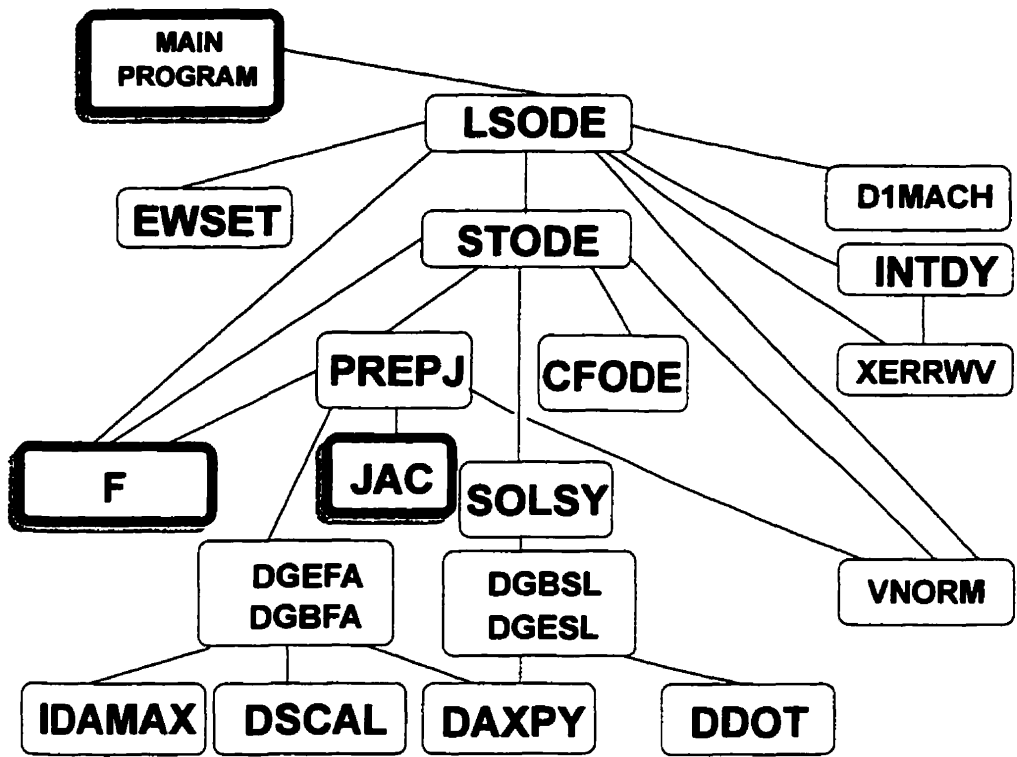


Fig. 3.1. Structure of the computational solver

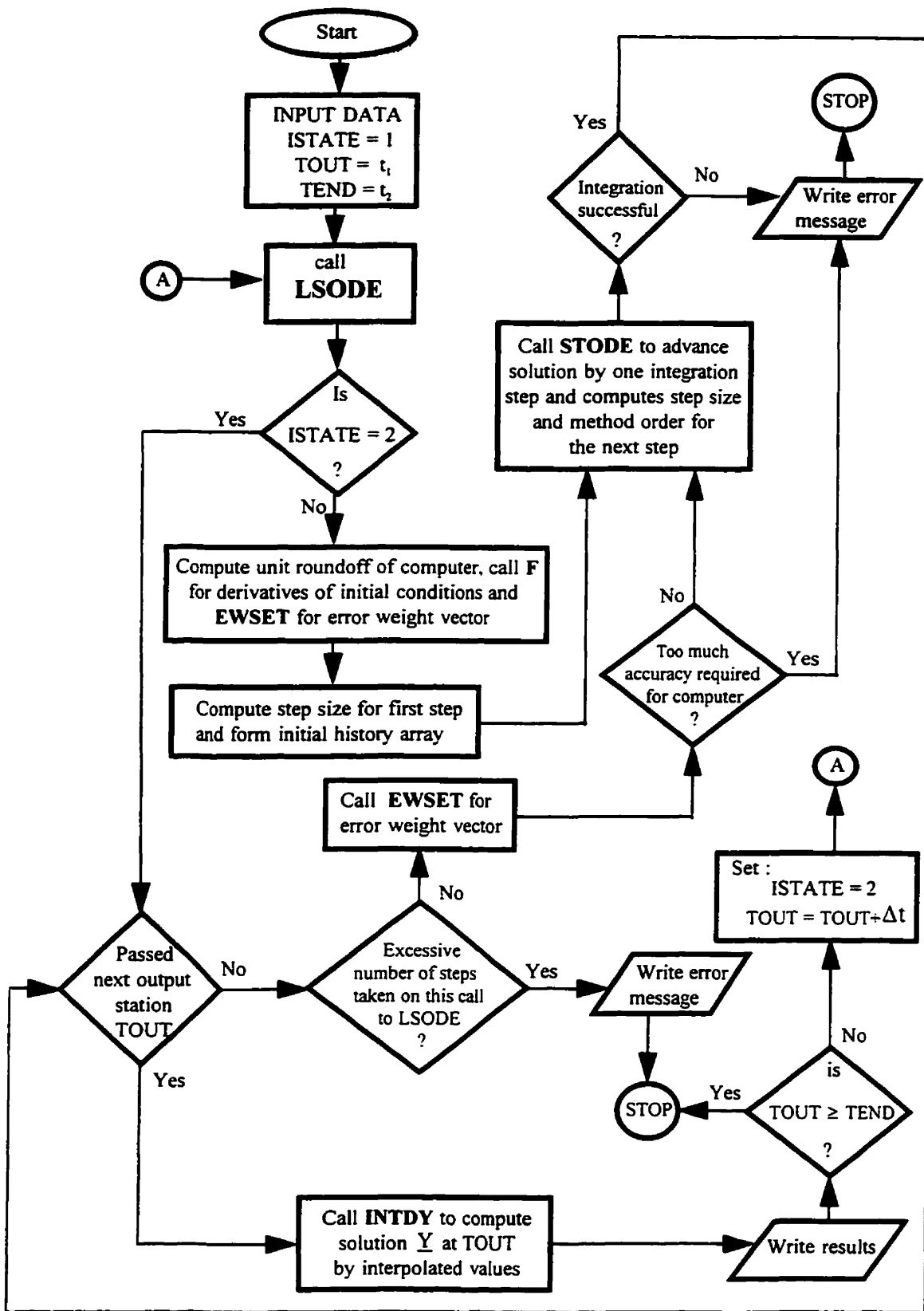


Fig. 3.2. General flowchart of the computational solver

EFFECT OF A HYDROGEN BUBBLE IN A SOLIDIFYING AL-CU ALLOY MELT UNDER VARIOUS ULTRASONIC PRESSURE FIELDS

4.1. Introduction

4.1.1 Hydrogen Bubble Formation

The soundness of any metal is largely determined by the behavior of gases entrapped in the solidifying melt. A gas, which dissolves freely in the molten metal, is much less soluble in the solidified state of the metal. Therefore, as the metal solidifies, gas is usually forced out of solution. Once the dendrites have already formed during solidification, the bubbles of expelled gas become trapped by the dendrite arms and are prevented from rising to the surface. Most of the aluminium alloys and some of the copper alloys are susceptible to *in situ* 'gassing' of this type, caused mainly by hydrogen dissolved from the furnace atmosphere. At the surface of the liquid aluminum there is a lot of water vapor and new crucibles always contain some moisture in their pores. The products of combustion of most fuels contain 10% to 20% water vapor. Natural gas will produce up to 2m³ of water vapor for each cubic meter of gas burned. Most hydrogen

,which finds its way into molten aluminium, comes from the dissociation of moisture (water vapor).

In order for a spherical gas bubble to exist in a melt, its internal pressure, P_i , must be sufficient to overcome all of the external forces which can act to make it collapse.

These are:

- the atmospheric pressure acting on the melt surface P_{atm} ;
- the metallostatic head pressure P_H ;
- the forces due to the surface tension of the melt $2\sigma / R$;

While P_{atm} and P_H are not excessively large in most casting operations, the surface tensions of metals are very high, and of course when a gas bubble begins to form, the bubble radius is extremely small. Thus, the term $2\sigma / R$ is very large, and high values of the internal pressure are necessary to form a bubble. This internal pressure is made up of two components:

- 1) P_G , the internal gas (hydrogen) pressure. This is significant only in the very last stages of freezing when large amounts of hydrogen have accumulated in the pockets of interdendritic liquid due to the decrease in solubility in the solid.
- 2) P_S , the shrinkage pressure, best viewed as a tensile stress in the pockets of interdendritic liquid due to the solidification shrinkage of this liquid, and the inability of this shrinkage to be fed through the almost completely frozen dendrite mesh.

In order for a gas bubble to be stable and to grow, the following condition must prevail:

$$P_g + P_s \geq P_{atm} + P_H + 2\sigma / R$$

The above condition can prevail only in the final stages of the freezing process. Since usually the combined sum of the gas pressure P_G and the shrinkage pressure P_S is insufficient to cause bubble nucleation, some *foreign particles* (nonwetable by the melt) are necessary to assist in heterogeneous nucleation of the gas bubbles [see Gruzeleski (1990)].

4.1.2 Ultrasonic Treatment

Conventional methods of casting cannot provide the quality of metal needed for some modern requirements to the properties of alloy products. Among the newer physical methods for treating solidifying metals, one of the most promising is ultrasonic treatment (UST) at high intensity [Eskin (1996)].

The high-powered ultrasonic treatment of a crystallizing aluminium alloy melt can play an important role in obtaining fine crystals and a greater number of nuclei. The grain refinement can be achieved by the effect of bubble dynamics when the solidifying melt is subjected to an imposed sinusoidal pressure field of a particular frequency and amplitude. In ultrasonic treatment of a solidifying melt, the high pressure waves generated due to violent collapse of the entrapped bubbles create special conditions abetting the crystallization process. The high pressure waves must be taken into account as one of the factors responsible for breakdown of the dendrites. Dendrite fragments become nuclei during metal crystallization process in an ultrasonic field, which lead to the refined crystalline structure of the metal. Figures 4.1 and 4.2 show schematically how the fracture of dendrite arms during ultrasonic treatment of a solidifying melt might take place.

The high pressure waves are also a source of local disruption of thermodynamic equilibrium in the melt. The pressures generated in the melt can effect an upward shift of the melting point. An increase in the pressure in the melt is analogous to an increase in the supercooling and can give rise to an increase in the nucleation rate of the crystallization centers. Grain multiplication mechanisms, such as the effect of ultrasonic treatment of the melt, result in more equiaxed structures that are more isotropic and compositionally homogeneous. Grain refinement is best when the melt is cooled slowly with the ultrasonic irradiation continuing until solidification is nearly complete.

4.2. Literature Review

Metallurgical effects of ultrasonic waves were reviewed extensively by Hiedmann (1954). Although, he explicitly pointed out the significant reduction in grain size as the consequence of the ultrasonic treatment of a melt but he could not explain the real mechanisms behind the observed effects. Nikolaichik (1958) introduced ultrasonic irradiation to melts of both gray and white cast iron. Modifications were noted to both structure and mechanical properties. Graphite formations were refined as well as the uniformity in their distribution in the ultrasonically cast product was increased by up to 10 times. Mechanical properties reported included increase in U.T.S. from 150 MPa to 500 MPa, increase in ductility from 0% to 4% and increase in hardness from 1600 HB to 1800 HB. Hunt and Jackson (1966) demonstrated experimentally that nucleation of solid occurs when a cavity collapses. They found extremely large pressure in the melt due to the collapse of a cavity. The change of melting temperature with pressure was described by the Clapeyron equation (1968) which provided the undercooling required for the nucleation. Campbell (1981) published a review of the available knowledge in this field, including various experimental results concerning the effects of vibration frequencies and amplitudes of the imposed ultrasonic field.

The mechanism of metal solidification in an ultrasonic field and associated structural changes in ingots was described qualitatively by Abramov (1987). He showed that when a solidifying melt is treated by ultrasound, fine equiaxed grains are formed and columnar structure are eliminated (Figure A.1). He reported that, in the case of ultrasonic treatment of carbon steels, the grain size reduces from 200 microns to 25 microns. The columnar structure is eliminated and fine equiaxed grains are formed with corresponding increases (40%) in ductility and (30%) in mechanical strength of the metals (Table A.1).

Cherepanov and Popov (1986) studied numerically the influence of an alternating external pressure on the evolution of a gas bubble in a melt. They pointed out that, if the field amplitude and frequency are sufficiently high, equal (or close) to the bubble's natural frequency, sealing of the bubble might be possible, followed by emission of high pressure waves near the bubble. Numerical analysis of the dynamics of variation of a

bubble's radius and the pressure in the melt near the bubble's surface was carried out by Sobolev (1985), (1989). He studied the behavior of a gas bubble under an applied sinusoidal pressure for the resonant, pre-resonant, and post-resonant frequencies.

All of the above investigators, for the sake of simplification, have assumed that the gas pressure inside the bubble changes adiabatically during the collapse and rebound cycles. They altogether have neglected the energy equation for the gas inside the bubble as well as the energy equation for the melt surrounding the bubble. By ignoring and neglecting the energy equations in their assumptions these authors have made remarkable errors in their numerical results. In order to predict the temperature field in the melt surrounding the bubble it is necessary to incorporate the energy equation in the modeling of bubble dynamics under the present situation. Also, the numerical methods used by these authors (i.e., Runge-Kutta) were not appropriate schemes for solving their stiff set of modeled equations. For the calculations of the temporal variations of the bubble radius and the pressure in the melt during the rapid collapse and rebound of the gas bubble more accurate and sensitive numerical schemes are necessary due to the fast motion of the bubble surface.

Eskin (1994) carried out an investigation of solidification of light alloys in an ultrasonic field. He observed that cavitation, especially when it is well developed in a solidifying melt, has a considerable grain refining effect. He studied the influence of cavitation treatment on the impurities, mainly oxide particles, in the aluminium alloy melts. He pointed out that these particles, less than equivalent to $1.0 \mu\text{m}$ in size, being non-wettable by the melt and do not take part in the solidification process. The cavitation treatment of the melt generates high pressure pulses in the melt which effect physical changes on these particles. The defects on oxide particle surfaces filled with the matrix melt ensure the transformation of these non-controlled impurities to active solidification nuclei. Guyon and Yavari (1994) performed experiments on the microstructural effects of ultrasonic vibrations applied during planar flow casting of steels. They used sound waves in the frequency range of tens of kilohertz to the melt crucible during the planar flow casting of Fe-Cr steels. The 10 mm wide strips were obtained with and without the application of the ultrasound. The strips obtained from the ultrasonic treatment of the

melt showed some modifications of texture and microstructure as well as destruction of directional solidification pattern.

4.3. Mathematical Modelling

In order to mathematically tackle the effect of the ultrasonic pressure field on bubble dynamics and the resulting affect on the crystallization of a solidifying Al-Cu melt, a number of reasonable assumptions about the physical characteristics of the phenomenon are made:

- i) The bubble remains spherical and the bubble center is motionless.
- ii) The melt surrounding the bubble is quasi-homogenous.
- iii) The gas pressure within the bubble is uniform while the gas temperature and gas density are non-uniform (the characteristic time of temperature equalization in the bubble exceeds the time of pressure equalization).
- iv) The bubble gas is thermally perfect but calorically imperfect.

The mathematical model, to be developed in the following section, is based on the differential form of the following conservation equations:

- 1- Mass conservation equations for the gas and the melt surrounding the bubble.
- 2- Conservation of the momentum of the gas within the bubble and the melt.
- 3- Conservation of energy for the gas and the melt.

The differential form of the above equations in the spherical coordinates can be written as follows:

Mass conservation equation for the gas:

$$\frac{\partial \rho}{\partial t} + \nabla \cdot (\rho \mathbf{u}) = 0 \quad (4.1)$$

Mass conservation equation for the melt:

$$\frac{1}{r^2} \frac{\partial}{\partial r} (r^2 v) = 0 \quad (4.2)$$

The mushy zone of the solidifying melt surrounding the bubble was modeled based on the concept of porous media formulation.

The momentum equation for the melt, in the spherical coordinates, can be written in the following form [Sobolev (1985)]:

$$\frac{\partial v}{\partial t} + v \frac{\partial v}{\partial r} = - \frac{1}{\rho_l} \frac{\partial p}{\partial r} - \frac{\mu}{\rho_l m} v + \frac{\mu}{\rho_l r^2} \left[\frac{\partial}{\partial r} \left(r^2 \frac{\partial v}{\partial r} \right) - 2v \right] \quad (4.3)$$

In this study, the momentum equation for the melt flow inside the mushy region formed by the growing dendrites of the solidifying melt is based on the Brinkman-Darcy equation for a flow in a porous media. The permeability of the porous media, as a function of porosity (liquid fraction), was calculated using the well-known Carman-Kozney equation:

$$m = \frac{\varepsilon^3}{D_0 (1 - \varepsilon)^2} \quad (4.4)$$

where D_0 depends on the morphology of the porous media. Here it has been estimated from the expression given by the experimental results of Diao et al. (1994):

$$D_0 = \frac{180}{d^2} \quad (4.5)$$

where 'd' is assumed to be a constant and is in order of the secondary dendrite arm spacing (SDAS).

From the continuity equation of the melt one can easily show that:

$$v = \frac{R^2}{r^2} \frac{dR}{dt} \quad (4.6)$$

The equation for the bubble radius is based on the modified Rayleigh-Plesset equation of bubble dynamics:

$$\frac{3}{2}\rho_l \dot{R}^2 + \rho_l R \ddot{R} = P - P_{ap} - \frac{2\sigma}{R} - \frac{4\mu\dot{R}}{R} - \frac{\nu}{m}\rho_l R \dot{R} \quad (4.7)$$

The energy equation for the gas within the bubble is given by:

$$\rho \frac{Dh}{Dt} - \frac{Dp}{Dt} = \nabla \cdot (K_g \nabla T_g) \quad (4.8)$$

The ideal gas equation of state is:

$$P = \frac{\rho \bar{R} T_g}{M_w} \quad (4.9)$$

From equations (4.1), (4.8) and (4.9) one can obtain the following expressions for the velocity field and gas pressure rate within the bubble.

$$u = \frac{1}{\gamma P} \left((\gamma - 1) K \frac{\partial T_g}{\partial r} - \frac{r \dot{P}}{3} \right) \quad (4.10)$$

$$\dot{P} = \frac{3}{R} \left[(\gamma - 1) K \frac{\partial T_g}{\partial r} \Big|_R - \gamma P \dot{R} \right] \quad (4.11)$$

By using the above equations, the energy equation for the gas (4.8) can be written in the following form:

$$\frac{\partial T_g}{\partial t} + \left(\frac{(\gamma - 1) K_g}{\gamma P} \frac{\partial T_g}{\partial r} - \frac{r \dot{P}}{3\gamma P} \right) \frac{\partial T_g}{\partial r} - \frac{(\gamma - 1) T_g}{\gamma P} \dot{P} = \frac{(\gamma - 1) T_g K_g}{\gamma P} \nabla^2 T_g \quad (4.12)$$

The energy equation for the solidifying melt can be written in the following form [Epstein (1994)]:

$$C_m \frac{\partial T_l}{\partial t} + \frac{\varepsilon \rho_l C_l R^2}{r^2} \frac{dR}{dt} \frac{\partial T_l}{\partial r} = K_m \left(\frac{\partial^2 T_l}{\partial r^2} + \frac{2}{r} \frac{\partial T_l}{\partial r} \right) + \mu \phi \quad r \geq R \quad (4.13)$$

where ε is the liquid fraction (porosity) in the dendritic mushy region, C_m is weighted average specific heat and K_m is weighted average thermal conductivity.

$$C_m = \varepsilon \rho_l C_l + (1-\varepsilon) \rho_s C_s \quad (4.14)$$

$$K_m = \varepsilon K_l + (1-\varepsilon) K_s \quad (4.15)$$

$$\phi = 12 \frac{V_r^2}{r^2} \quad (4.16)$$

4.3.1. Transformed and Non-dimensional Equations

For the numerical work, it is convenient to have a fixed rather than a moving boundary of the bubble. Therefore, the governing equations are transformed using a suitable variable (ζ) that “freezes” the moving boundary of the bubble. Also, in order to decrease the number of parameters and minimize computational errors, the governing equations are non-dimensionalized. The transformed and non-dimensional forms of the mathematical model equations are:

$$\bar{R} = -\frac{3 \bar{R}^2}{2 \bar{R}} - \frac{1 \bar{R}}{\text{Re} \bar{R}^2} - \frac{1}{\text{We}} \frac{1}{\bar{R}^2} + \frac{1}{M^2} \frac{\bar{P} - \bar{P}_{ap}}{\bar{R}} - \frac{\mu t_0}{m \rho_m} \bar{R} \quad (4.17)$$

$$\bar{P} = \frac{3}{\bar{R}} \left[(\gamma - 1) \frac{\theta_g}{\bar{R}} \frac{\partial \bar{T}_g}{\partial \zeta} \Big|_{\zeta=1} - \gamma \bar{P} \bar{R} \right] \quad (4.18)$$

$$\dot{\bar{T}}_g = -\frac{\theta_g (\gamma - 1)}{\gamma \bar{P} \bar{R}^2} \left(\frac{\partial \bar{T}_g}{\partial \zeta} - \frac{\partial \bar{T}_g}{\partial \zeta} \Big|_{\zeta=1} \right) \frac{\partial \bar{T}}{\partial \zeta} + \frac{(\gamma - 1) \bar{T}_g \bar{P}}{\gamma \bar{P}} + \frac{\theta_g (\gamma - 1) \bar{T}_g}{\gamma \bar{P} \bar{R}^2} \nabla^2 \bar{T}_g \quad (4.19)$$

$$\dot{\bar{T}}_1 = \frac{1}{\bar{R}^2} \left[K_m \cdot \frac{\partial^2 \bar{T}_1}{\partial \zeta^2} + \left(-C_1 \cdot \frac{\bar{R}\dot{\bar{R}}}{\zeta^2} + \bar{R}\dot{\bar{R}}\zeta + \frac{2K_m}{\zeta} \right) \frac{\partial \bar{T}_1}{\partial \zeta} + 12\mu \cdot \frac{\bar{R}^2}{\zeta^6} \right] \quad (4.20)$$

where

$$\frac{1}{Re} = \frac{4\mu t_0}{\rho_1 R_0^2} \quad \frac{1}{We} = \frac{2\sigma t_0^2}{\rho_1 R_0^3} \quad \frac{1}{M^2} = \frac{t_0^2 P_0}{\rho_0 R_0^2} \quad \zeta = \frac{r}{R(t)}$$

$$\theta_s = \frac{K_g T_0 t_0}{R_0^2 P_0} \quad C_1 = \frac{\varepsilon \rho_1 C_1}{C_m} \quad K_m = \frac{K_m t_0}{C_m R_0^2} \quad \mu = \frac{\mu}{C_m T_0 t_0}$$

$$\bar{R} = \frac{R}{R_0} \quad \dot{\bar{R}} = \frac{\dot{R} t_0}{R_0} \quad \bar{T}_g = \frac{T_g}{T_0} \quad \bar{T}_1 = \frac{T_1}{T_0}$$

$$\bar{t} = \frac{t}{t_0} \quad \bar{P} = \frac{P}{P_0} \quad \bar{\rho} = \frac{\rho}{\rho_0} \quad \gamma = \frac{C_p}{C_v} \quad (4.21)$$

4.3.2. Initial Conditions

The initial conditions for the set of equations are:

at

$$\bar{t} = 0$$

$$\bar{R} = 1, \quad \dot{\bar{R}} = 0, \quad \bar{P} = 1, \quad (\bar{T}_g)_j = 1, \quad j = 1 \text{ to } 150$$

$$(\bar{T}_1)_j = 1, \quad j = 1 \text{ to } 50 \quad (4.22)$$

Initially, the bubble is at rest and is in equilibrium with the surrounding melt. In Table 4.1, input parameters for this study are shown. The following equations are used for the equilibrium condition:

$$\rho_0 = \frac{P_0 M_w}{\mathcal{R} T_0}, \quad P_0 = P_u + \frac{2\sigma}{R_0}, \quad T_0 = 915.0 \text{ K} \quad (4.23)$$

Table 4.1. Input Parameters for the Solidifying Melt

Parameter [unit]	Al - 3.4 Pct Cu
K_s [W/ (m-K)]	158.0
K_l [W/ (m-K)]	100.0
C_s [J/(kg-K)]	1150.0
C_l [J/(kg-K)]	1250.0
ρ_s [kg/m ³]	2590.0
ρ_l [kg/m ³]	2410.0
μ [(N-s)/m ²]	1.5×10^{-3}
σ [N/m]	0.914
SDAS [m]	90.0×10^{-6}
ε	0.5

In this study, the pressure of the undisturbed melt, P_u is taken as 1.1×10^5 Pa. For the calculation of the characteristic bubble collapse time t_0 , the period of linearized oscillation due to a small perturbation around P_u with damping decrement δ is used [Sobolev (1989)].

$$t_0 = \frac{2\pi}{\omega_0}, \quad \omega_0 = \left(\frac{a_1}{\rho_l R_0^2} - \delta^2 \right)^{0.5}$$

$$a_1 = 3\gamma P_0 - \frac{2\sigma(1-3\gamma)}{R_0}$$

where

$$\delta = \frac{2\mu}{\rho_l R_0^2} \left(1 + \frac{R_0^2}{4m} \right)$$

(4.24)

4.3.3. Boundary Conditions

The boundary conditions for equation (4.19) are:

$$0 \leq \zeta \leq 1$$

$$\frac{\partial \bar{T}_g}{\partial \zeta} = 0 \quad \text{for } \zeta = 0 \quad (4.25)$$

$$\bar{q}_g|_{\zeta=1} = \bar{q}_l|_{\zeta=1} \quad \text{and} \quad \bar{T}_g = \bar{T}_{int} \quad \text{for } \zeta = 1$$

The boundary conditions for the equation (4.20) are:

$$1 \leq \zeta \leq 1.34$$

$$\bar{q}_l|_{\zeta=1} = \bar{q}_g|_{\zeta=1} \quad \text{and} \quad \bar{T}_l = \bar{T}_{int} \quad \text{for } \zeta = 1 \quad (4.26)$$

$$\bar{T}_l = 1 \quad \text{for } \zeta \geq 1.34$$

In the calculations all physical properties were considered to be temperature dependent.

The dynamic pressure field in the melt surrounding the bubble can be obtained by integrating the momentum equation for the melt [Eq. (4.3)] with respect to r and combining it with the equation of continuity [Eq. (4.2)].

$$P(r, t) = P_{ap} + \frac{2\rho_l R \dot{R}^2}{r} + \frac{\rho_l R^2 \ddot{R}}{r} - \frac{\rho_l R^4 \dot{R}^2}{2r^3} + \frac{\mu R^2 \dot{R}}{mr} \quad (4.27)$$

4.4. Numerical Solution Methods

The mathematical model forms a set of coupled, highly nonlinear and stiff differential equations. In order to convert the PDEs into a system of ODEs, the partial differential equations were discretized only in space direction using the second order central difference scheme.

The number of grid points within the bubble and surrounding the bubble (inside the liquid) were taken to be 150 and 50, respectively. Therefore, the non-dimensional

inter-grid distance is $1/(M-1)$, where M is the number of equi-spaced grid points within the bubble. In this case the number of non-linear, coupled ordinary differential equations, which have been solved in each iteration, was 203. These equations are; equation for the bubble radius, equation for the bubble wall velocity and equation for the gas pressure. The gas pressure was considered uniform within the bubble. The gas temperature field inside the bubble and the liquid temperature field surrounding the bubble constitute 150 and 50 equations, respectively. As described previously, due to having significantly different time and length scales in the mathematical model, the problem is stiff. Therefore, the modified Gear method, which is good for solving a set of nonlinear stiff ordinary differential equations, was applied.

To verify the algorithm, numerical tests were performed to ensure that the solutions were “grid independent”. Four different grid point numbers have been used and are designated as case A, case B, case C and case D. In case A the number of grids within the bubble and surrounding the bubble (inside the liquid) were taken to be 150 and 50, respectively. While in case B the number of grids within the bubble and inside the liquid were considered to be 200 and 100, respectively. In case C the number of grids within the bubble and inside the liquid were assumed to be 450 and 150, respectively. In the latter case the number of ordinary differential equations, which have been solved in each iteration, was 603. In case D the number of grids within the bubble and inside the liquid were assumed to be 20 and 10, respectively. Figures 4.3 to 4.6 show that the results from the grid distribution for the case A are almost identical to those from cases B and C. Therefore, for the sake of computational costs, the case A grid distribution is used for all computations reported here.

4.5. Results and Discussion

During the ultrasonic treatment of the aluminium-3.4 wt pct copper alloy melt, the pressure experienced by the gas bubble is $P_{ap} = P_u - P_m \sin(2\pi f t)$, where P_u is the pressure of undisturbed melt and P_m and f are the ultrasonic pressure field’s amplitude and frequency, respectively. In order to obtain the most effective use of the bubble

dynamics under the ultrasonic pressure field one needs to know how it is affected by the key process variables namely, R_0 , ω , P_u and P_m . In conformity with the bubble sizes in a typical Al-Cu alloy melt, the initial diameter of hydrogen bubbles are assumed to be 5, 10 and 20 μm and the pressure of the undisturbed melt and the ultrasonic pressure amplitude are considered to be 0.11 and 0.5 MPa, respectively. In Figures 4.3-4.11, the initial diameter of bubble is assumed to be 10 μm . For Figures 4.3-4.6, the ultrasonic frequency is chosen near the bubble's resonant frequency (0.8 MHz) which was calculated from Eqs. 4.23. Figure 4.3 shows the history of bubble radius. The action of bubble dynamics is based on the generation of a pressure wave due to the violent collapse of the gas bubble. As shown in Figure 4.4, the peak pressure near the bubble surface is in the order of several hundreds to thousands atmospheres. The high pressure pulse must be taken into account, first, as one of the factors responsible for the breakdown of the dendrites and, second, as a source of local disruption of thermodynamic equilibrium in the melt. Dendrite fragments become nuclei during metal crystallization in an ultrasonic field, which lead to the refined crystalline structure of the metal. The high pressure generated in the melt can effect an upward shift of the melting point. An increase in pressure in the melt is analogous to an increase in the supercooling and can give rise to an increase in the nucleation rate of the crystallization centers. It is to be noted that under an alternative pressure field, the temperature within the bubble rises (Figure 4.6) due to compression work on the bubble and the assumption of ideal gas. The heat energy from the gas inside the bubble is transformed into the melt, which tends to heat up the zone immediately adjacent to the collapsing bubble. But as shown in Figure 4.5 due to thermal boundary layer in the melt side of the bubble the amount of temperature increase is not remarkable, compared to the increase of supercooling, to inhibit the nucleation of new crystallization centers. Figure 4.6 shows that due to violent collapse of hydrogen bubble the gas temperature at the bubble center reaches a maximum value of about 3050 K.

Figures 4.7 and 4.8 show the history of the melt pressure adjacent to the bubble surface for ultrasonic frequencies of 100 kHz and 2 MHz, respectively. In the case of ultrasonic frequency of 2 MHz the peak pressure reaches about 0.5 MPa, which is not an effective value for the microstructural refinement. In fact, the gas bubble can not collapse

deeply if the frequency of the ultrasonic wave is more than its resonant frequency. In Figures 4.9 and 4.10 the history of bubble radius as well as the ultrasonic pressure cycles of 100 kHz and 2 MHz are shown. Figure 4.10 shows that the gas bubble does not collapse deeply but the bubble radius oscillates around its initial radius in a complex manner. In other words, the bubble does not reach its minimum radius before the ultrasonic pressure field has changed sufficiently to cause it to expand. This statement is also true for the expansion cycles of the gas bubble.

In Figure 4.11 variations of the melt pressure with distance from the bubble surface for different instants in time during the violent collapse of the bubble is shown. In this figure the conditions correspond to those of Figure 4.4. It is to be noted that the vertical axis is in a logarithmic scale and the distance from the bubble is non-dimensionalized with the initial bubble radius. As shown, the high pressure generated in the melt is in the range of 235 MPa at very close to the bubble surface and reduces rapidly to 2.5 MPa at the non-dimensional distance of 20 at the time instant of 0.0036 msec.

Figures 4.12-4.17 are plotted to portray the effects of the initial bubble diameter on bubble dynamics and the high pressure generated in the melt surrounding the bubble. In Figures 4.12-4.14 the initial bubble diameter is chosen to be 5 μm which is half of the previous cases. Also, the ultrasonic frequency is assumed to be 800 kHz while the resonant frequency of the bubble is 2170 kHz (pre-resonant case). The pressure of the undisturbed melt and the ultrasonic pressure amplitude are considered to be 0.11 and 0.5 MPa, respectively. As shown in Figures 4.13 and 4.14, the pressure generated in the melt is in the range of 340 MPa at very near the bubble surface and drops down to 3.5 MPa at the non-dimensional distance of 20 at the time instant of 0.001 ms.

In Figures 4.15-4.17, the initial bubble diameter is chosen to be 20 μm . In Figures 4.15 and 4.16, the ultrasonic frequency is assumed to be 800 kHz while the resonant frequency of the bubble is 332 kHz (post-resonant case). Figure 4.15 shows that the gas bubble does not collapse deeply and in this case the peak pressure reaches only about 0.8 MPa (see Figure 4.16). As shown in Figure 4.17, when the ultrasonic frequency is chosen to be 100 kHz (pre-resonant case), the peak pressure in the melt surrounding the bubble reaches 18 MPa.

In order to obtain the tensile strength of dendrite arms, a regression analysis was used to establish the relationship between the tensile strength of the aluminium copper alloy and temperature (see Figure 4.18). The data used in plotting the graph were obtained from the Metals Handbook (1990). By using the equation shown in Figure 4.18, the calculated tensile strength of dendrite arms is found to be around 1.027 MPa. The dendrite arms are subjected to the impulsive pressure produced during the violent collapse of the bubbles. Figures 4.11 and 4.14 demonstrate that even far from the bubble, the impulsive pressure is sufficiently high to fracture the dendrite arms.

4.6. Concluding Remarks

In this study, a mathematical model, along with a numerical scheme, has been developed to predict the dynamic behavior of a spherical hydrogen bubble in an aluminium-3.4 wt pct copper alloy melt under an ultrasonic pressure field. The radial motion of the bubble is considered to be governed by the modified Rayleigh-Plesset bubble dynamics equation. The mushy zone surrounding the bubble was modeled based on the transport equations for a porous medium. The thermal energy exchange between the bubble and the surrounding melt is taken into account by solving both energy balance equations for the gas within the bubble as well as the melt surrounding the bubble. In order to demonstrate the concept of the model, the ultrasonic treatment of the aluminium-3.4 pct copper alloy melt with hydrogen bubbles is studied for pre-resonant, resonant and post-resonant frequencies. It is found that the ultrasonic frequencies beyond the resonance frequency of bubbles do not have any useful effect on the melt. Also, the computed dynamic pressure in the melt surrounding the hydrogen bubble demonstrates that even far from the bubble surface, the melt pressure is sufficiently high and can cause the dendrite arms to fracture. The action of bubble dynamics on the solidifying melt is based on the generation of high pressure waves due to the violent collapse of the gas bubble. The high pressure waves must be taken into account, first, as one of the factors responsible for breakdown of the dendrites. Dendrite fragments become nuclei during metal crystallization in an ultrasonic field, which can lead to the refined structure of the cast.

The high pressure waves are also a source of local disruption of thermodynamic equilibrium in the melt. The high pressure generated in the melt can effect an upward shift of the melting point.

The history of bubble radius and pressure and temperature history of the melt adjacent to the bubble surface have been obtained for different frequencies of the ultrasonic pressure field. The results show that the peak pressure generated in the melt may reach several hundreds to thousands atmospheres depending on the initial bubble size and the characteristics of the imposed ultrasound field.

Nomenclature

C_v, C_p	specific heat at constant volume and constant pressure	J/(kg-K)
K	thermal conductivity	W/(m-K)
M_w	molecular weight of gas	g/mole
m	permeability of melt in the mushy zone	m^2
P	pressure of gas inside the bubble	Pa
P_0	initial pressure of gas inside the bubble	Pa
P_{ap}	applied pressure in melt	Pa
P_u	pressure of undisturbed melt	Pa
P_b	melt pressure adjacent to the bubble surface	Pa
R, R_0	bubble radius at any time and initial bubble radius	m
\dot{R}, \ddot{R}	bubble wall velocity and bubble wall acceleration	m/s, m/s^2
r	distance from bubble center	m
SDAS	secondary dendrite arm spacing	m
T	temperature	K
T_0	initial temperature	K
t	time	s
ϵ	porosity of melt in the mushy zone	
ρ_s	solidus density	kg/m^3
ρ_l	liquidus density	kg/m^3
σ	surface tension of melt	N/m
μ	dynamic viscosity of melt	(N-s)/ m^2
\bar{R}	universal gas constant	J/(kg-mole-K)

Superscripts

– variable non-dimensionalized by reference parameter

Subscripts

g	gas-mixture
int	interface
0	initial-state
l	liquid
s	solid

References

- Abramov, O. V., Action of High Intensity Ultrasound on Solidifying Metal, *Journal of Ultrasound*, Vol. 25, pp. 73-82, 1987.
- ASM International Handbook Committee, *Metals Handbook*, Vol. 2, 10th ed., Properties and Selection of Nonferrous Alloys and Special-Purpose Materials, Aluminium and Aluminium Alloys Sections, 1990.
- Campbell, J., Effect of Vibration During Solidification, *Int. Metals Reviews*, Vol. 2, pp. 71-108, 1981.
- Cherepanov, A. N. and Popov, V. N., The Effect of an Alternating Pressure Field on the Behavior of a Gas Bubble in the Two-Phase Zone, *Izvestiya Akademii, Metall, Nauk SSSR*, Vol. 6, pp. 73-82, 1986.
- Diao, Q. Z. and Tasi, H. L., Modelling of the Formation of Under-Riser Macroseggregation During Solidification of Binary Alloys, *Metall. and Mats. Trans. A*, Vol. 25A, pp. 1051-1062, 1994.
- Frawley, J. J. and Childs, W. J., Dynamic Nucleation of Supercooled Metals, *Transaction of the Metallurgical Society of AIME*, Vol. 242, pp. 256-263, 1968.
- Epstein, M., A Similarity Solution for Combined Hydrodynamic and Heat Transfer Controlled Bubble Growth in a Porous Medium, *Journal of Heat Transfer*, Vol. 116, pp. 516-518, 1994.
- Eskin, G. I., Influence of Cavitation Treatment of Melts on the Processes of Nucleation and Growth of Crystals During Solidification of Ingots and Casting from Light Alloys, *Ultrasonic Sonochemistry*, Vol. 1, pp. 59-63, 1994.
- Eskin, G. I., Degassing, Filtration, and Grain Refinement Process of Light Alloys in a Field of Acoustic Cavitation, *Advanced in Sonochemistry*, Vol. 4, pp. 101-159, 1996.
- Gruzleski, J. E., and Bernard, M. C., *The Treatment of Liquid Aluminium-Silicon Alloys*, Des Plaines, Ill, American Foundrymen's Society, pp. 143-152, 1990.
- Guyon, F. and Yavari, A. R., Microstructural Effects of Ultrasonic Vibrations Applied During Planar Flow Casting of Steels, *Materials Science & Engineering A*:

Structural Materials: Properties, Microstructure & Processing, Vol. 181-182, pp. 1305-1309, 1994.

Hiedeman, E. A., Metallurgical Effects of Ultrasonic Waves, *Journal of the Acoustical Society of America*, Vol. 26. No. 6, pp. 831-842, 1954.

Hunt, J. D., and Jackson, K. A., Nucleation of Solid in an Undercooled Liquid by Cavitation, *Journal of Applied Physics*, Vol. 37, pp. 256-263, 1966.

Nikolaichik, N., Lit. Proizvodstvo (in Russian), Vol. 2, p. 123, 1958.

Popov, V. N. and Cherepanov, A. N., Dynamics of the Behavior of a Gas Bubble Nucleous in a Heterophase Medium, *Zhurnal Prikladnoi Mekhanikii Tekhnicheskoi Fiziki*, Vol. 5, pp. 68-76, 1986.

Sobolev, V. N., The Effect of Cavitation on Crystallization of Metal in the Process of Ultrasonic Treatment of a Melt, *Izvestiya Akademii, Metally*, Vol. 5, pp. 52-59, 1989.

Sobolev, V. N., Dynamic Behavior of Gas Bubbles in a Solidifying Melt, *Izvestiya Akademii, Metally*, Vol. 5, pp. 56-63, 1985.

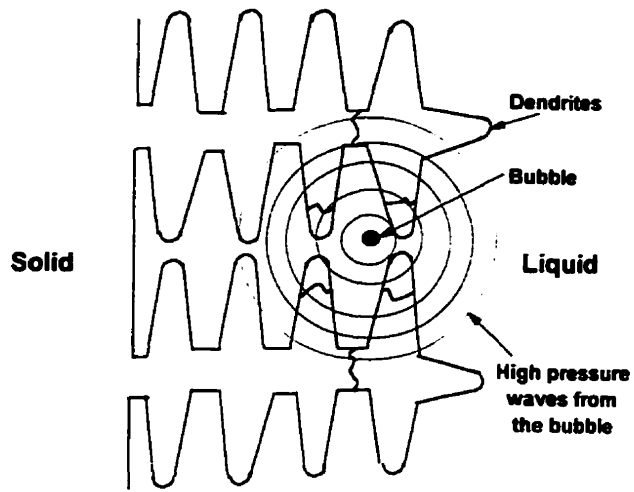


Fig. 4.1. Schematic of high pressure waves generated in a solidifying melt due to violent collapse of an entrapped bubble.

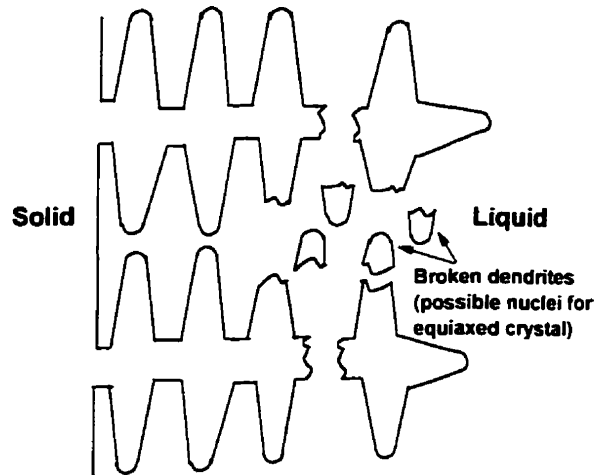


Fig. 4.2. Schematic diagram of the fragmentation of the dendrite arms.

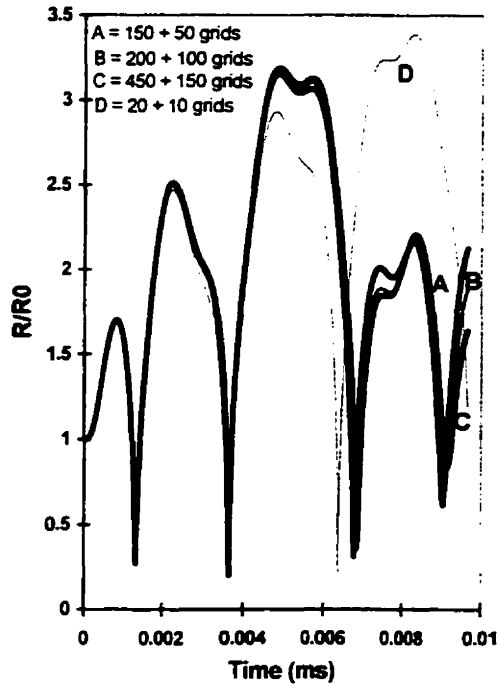


Fig. 4.3. History of bubble radius in an aluminium-3.4 pct copper alloy melt under an ultrasonic pressure field $P_{ap} = 1.1-5.0 \sin(2\pi ft)$, $f = 0.8$ MHz and $d_0 = 10 \mu\text{m}$.

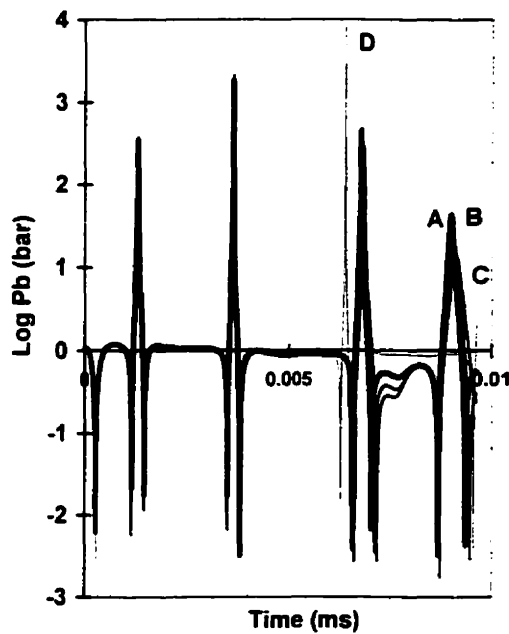


Fig. 4.4. High pressure waves generated in the melt near the bubble surface. The conditions correspond to those of Fig. 4.3

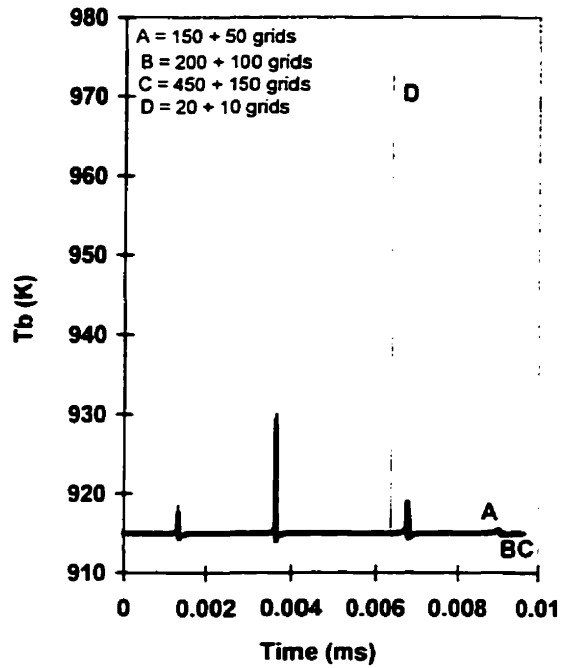


Fig. 4.5. Temperature history in the melt adjacent to the bubble surface. Conditions correspond to those of Fig. 4.3

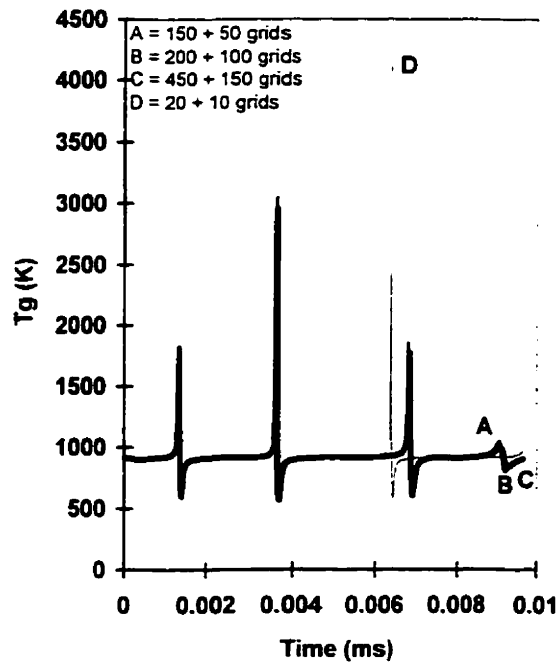


Fig. 4.6. Temperature history of hydrogen gas at the bubble center.

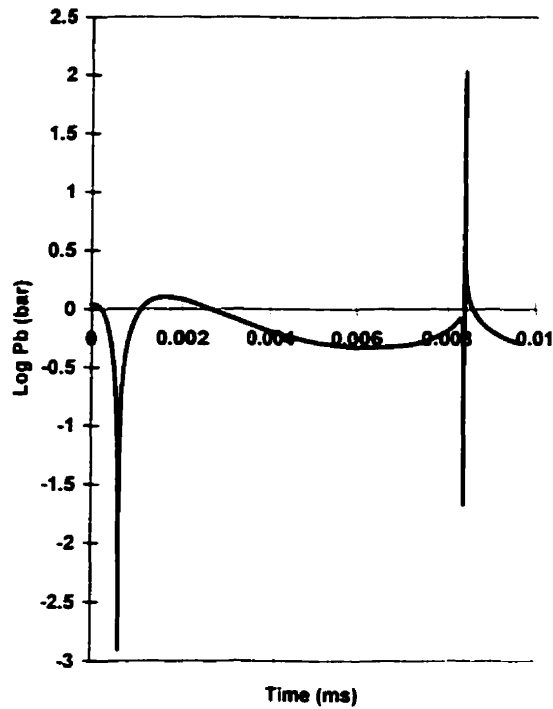


Fig. 4.7. High pressure waves generated in the melt adjacent to the bubble surface under the ultrasonic frequency of 100 kHz.

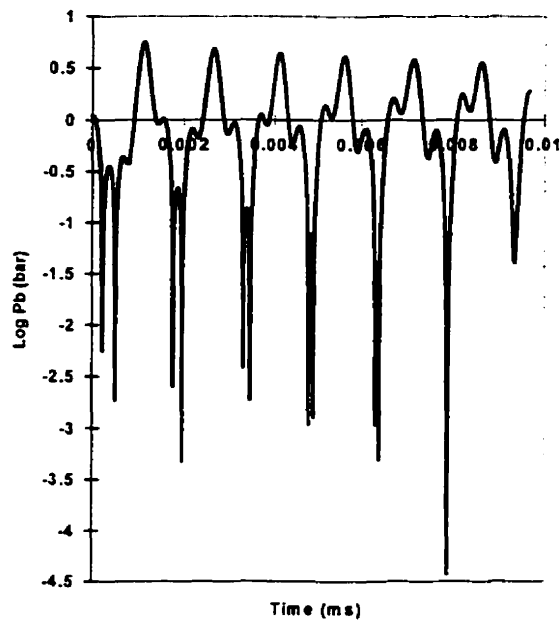


Fig. 4.8. High pressure waves generated in the melt adjacent to the bubble surface under the ultrasonic frequency of 2 MHz.

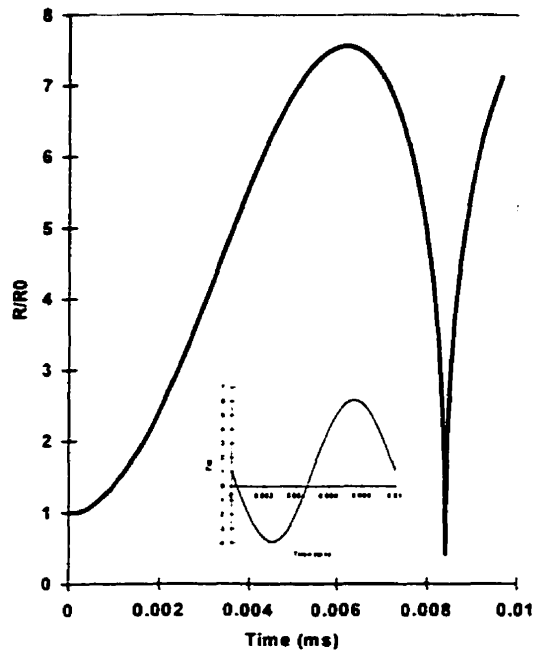


Fig. 4.9. History of bubble radius under the ultrasonic frequency of 100 kHz as well as the curve of the ultrasonic pressure field.

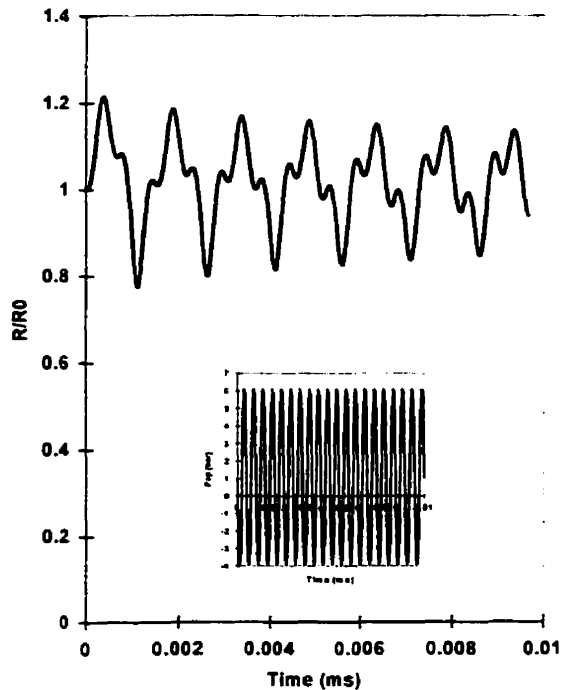


Fig. 4.10. History of bubble radius under the ultrasonic frequency of 2 MHz as well as the curve of the ultrasonic pressure cycles.

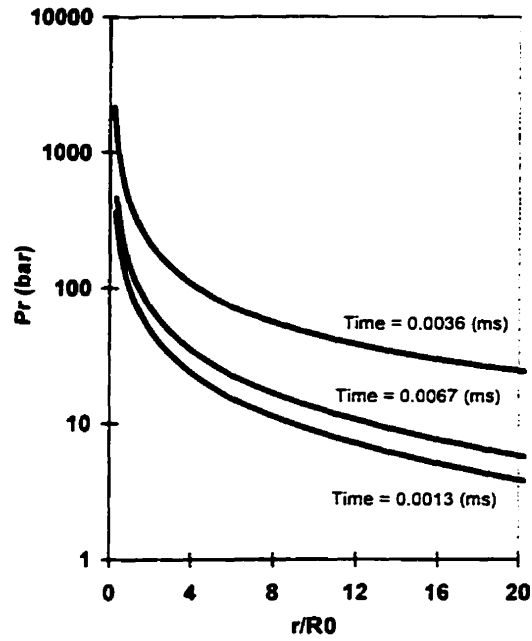


Fig. 4.11. Variations of high pressure with distance from the bubble surface for different instants in time during the collapse of the bubble. The conditions correspond to those of Fig. 4.4.

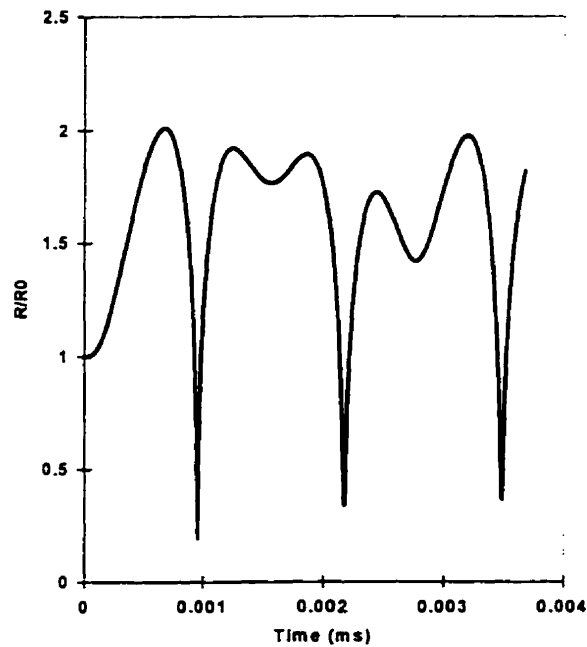


Fig. 4.12. History of bubble radius with the initial diameter of $5 \mu\text{m}$ under an ultrasonic pressure field of $P_{ap} = 1.1-5.0 \sin(2\pi f t)$, $f = 0.8 \text{ MHz}$.

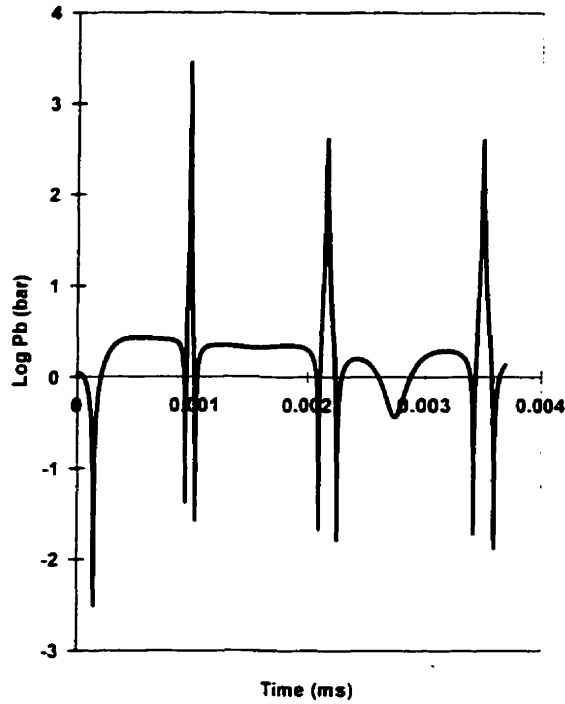


Fig. 4.13. High pressure waves generated in the melt near the bubble surface. The conditions correspond to those of Fig. 4.12.

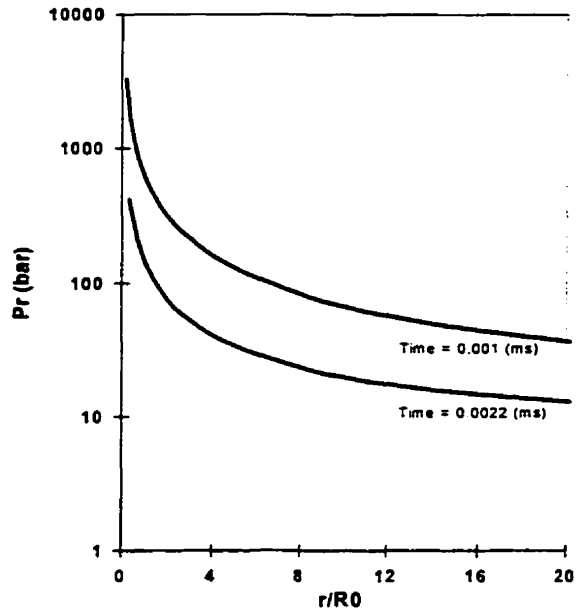


Fig. 4.14. Variations of high pressure with distance from the bubble surface for different instants in time during the collapse of the bubble. The conditions correspond to those of Fig. 4.12.

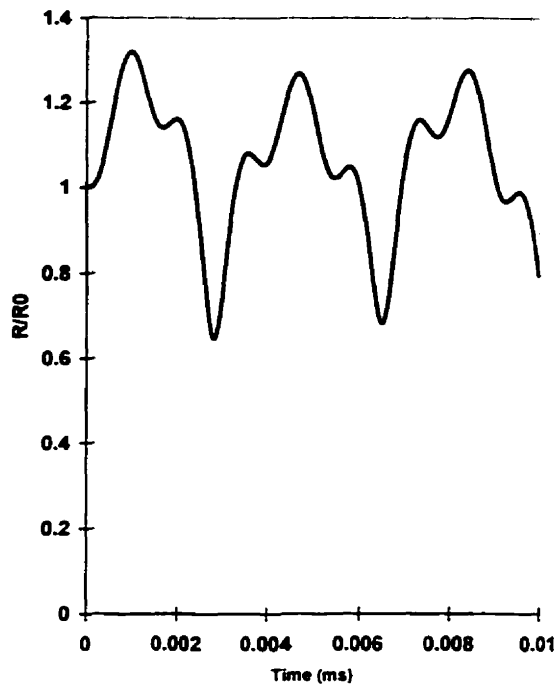


Fig. 4.15. History of bubble radius with the initial diameter of $20 \mu\text{m}$ under an ultrasonic pressure field of $P_{ap} = 1.1-5.0 \sin(2\pi f t)$, $f = 0.8 \text{ MHz}$.

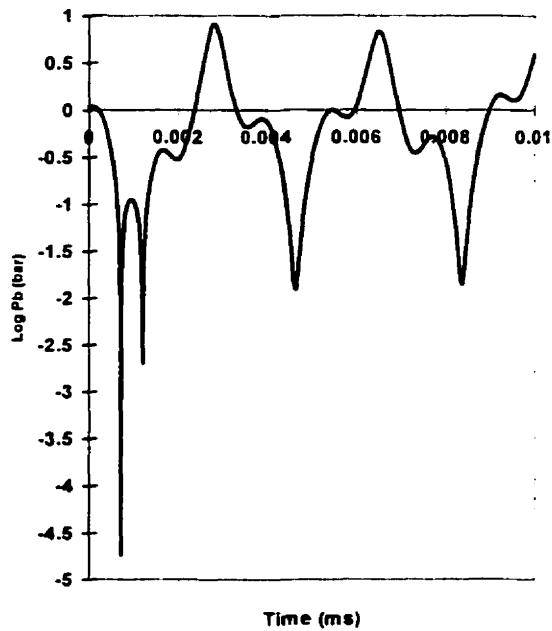


Fig. 4.16. High pressure waves generated in the melt near the bubble surface. The conditions correspond to those of Fig. 4.15.

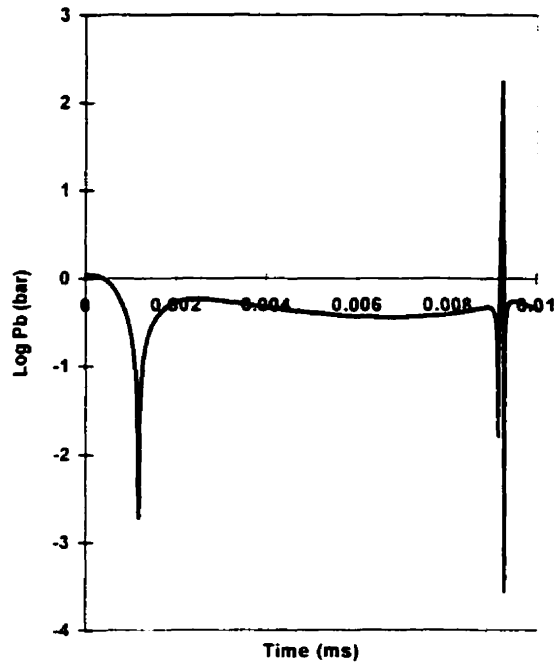


Fig. 4.17. High pressure waves generated in the melt adjacent to the bubble surface under the ultrasonic frequency of 100 kHz. The conditions correspond to those of Fig. 4.15.

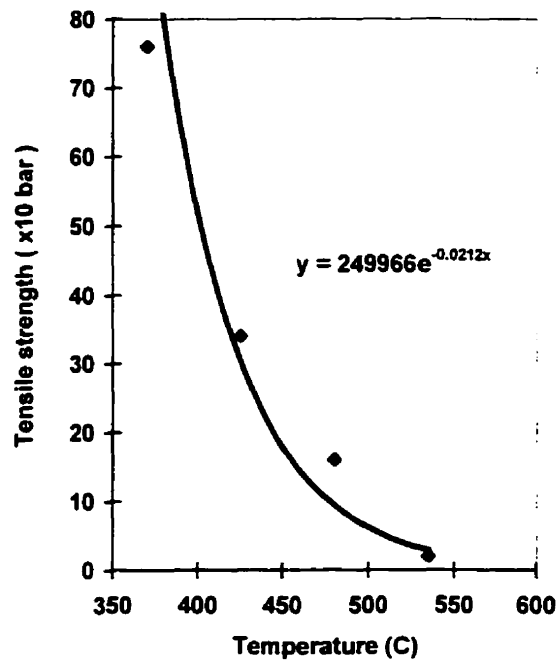


Fig. 4.18. Tensile strength of a typical aluminium-cooper alloy versus temperature.

MATHEMATICAL MODELLING OF BUBBLE GROWTH BY RECTIFIED DIFFUSION IN GASSY LIQUIDS UNDER VARIOUS ULTRASONIC PRESSURE FIELDS

5.1. Introduction

By subjecting a gassy liquid to an imposed sinusoidal pressure field of a particular frequency and amplitude, cavitation bubbles can be formed in the presence of nucleation sites. An inhomogeneity in the liquid in the form of microscopic gas bubbles is thought to be the most likely candidate for nucleation sites. If the imposed pressure field is beyond a threshold value, the tiny gas bubbles repeatedly expand and compress and dissolved gas in the liquid flows into the gas bubbles by rectified diffusion. Figure 5.1 shows schematically how the process of rectified diffusion takes place. Rectified diffusion consists of two effects. The first effect is an “area” effect. During bubble pulsation, the surface area of the expanded bubble is much higher than that of the compressed bubble. Therefore, the amount of gas that enters the bubble during its expansion is higher than the amount of gas leaving the bubble during its compression and so the bubble will gain considerable amount of gas over many cycles. The second effect is the “shell” effect. The gas diffusion is controlled by the thickness of a diffusion layer or a shell that is formed in the liquid surrounding the bubble (take a constant mass of liquid surrounding the bubble). When the bubble is expanded, the shell becomes thinner and the

concentration gradient increases. In this case, the flow rate of gas to the bubble also increases. When the bubble is compressed, the shell is thicker and, as a result the concentration gradient decreases. The combination of the “area effect” and the “shell effect” is that under certain conditions, a small quantity of gas is pumped into the bubble in each acoustic cycle. These effects are opposed by the normal tendency of a bubble existing in a gassy liquid to dissolve. Because of surface tension, the pressure inside the bubble (P_g) is higher than that in the liquid immediately adjacent to the bubble (P_l). This so-called Laplace pressure, given by the expression, $P_g - P_l = 2\sigma / R$, where σ is the surface tension and R is the radius of the bubble, can be quite large for very small bubbles. The end result of the above competing diffusion effects is that for a particular frequency of the sound field there is a threshold acoustic pressure amplitude, above which a bubble of a given size will grow, and below which it will tend to dissolve. The threshold pressure is quite sensitive to the dissolved gas concentration in the liquid and the ultrasonic frequency. In degassing, the process of rectified diffusion can be continued for some 20,000 times per second or above, and large gas bubbles can be formed quite rapidly, which can then easily float to the surface due to the hydrodynamic buoyancy force (Figure 5.2).

5.2. Literature Review

In the mathematical modelling, the convective-diffusion equation for the dissolved gas concentration in the liquid depends strongly on the equation of bubble radius. The equation of bubble radius is nonlinear and to solve the convective-diffusion equation, the boundary condition at the bubble wall must be applied which is a moving boundary. Both the above equations are couple through the convective term in the diffusion equation and the gas pressure term in the equation of bubble radius. The first solution of these problems was obtained by Blake (1949). He avoided the nonlinearities of the equation of bubble radius by assuming very small sinusoidal oscillations of the bubble. To avoid the problem of moving boundary in the convective-diffusion equation,

he assumed the bubble wall to be fixed in the place, but allowed for the variations of concentration of gas at the bubble wall and also allowed the area of the wall to vary as they would if the bubble wall were moving.

Hsieh and Plesset (1961) obtained a solution that does include the shell effect. The problem of the moving boundary was solved by expanding the boundary condition in terms of a Taylor series about the equilibrium position of the bubble wall. One of the limitations of their solution is that it is restricted to small sinusoidal oscillations. Eller and Flynn (1965) divided the general problem into an equation for the motion of the bubble wall and a diffusion equation for the concentration of gas dissolved in the liquid. They obtained a numerical solution of the nonlinear equation of bubble radius after simplifying the governing equation and invoking some drastic assumptions. They assumed that the number of moles of gas in the bubble was approximately constant during a single oscillation as well as invoked an isothermal or a polytropic relation for the gas pressure within the bubble. They also found an approximate solution of the convective-diffusion equation, which was solved by the method of successive approximations. The expression for the flux of gas at the bubble wall was obtained and integrated over the surface area of the bubble to account for the rate of change in the number of moles of gas in the bubble. The theory of Eller and Flynn has been widely used in the literature for rectified diffusion of large amplitude bubble oscillations (see section 2.9). Later, in the study of bubble growth under an 11 kHz sound field, Eller (1972) pointed out that the calculated threshold for growth is consistent with their experimental observation, but the calculated times of growth exceeded the observed times by factors of about 10-100.

A history of the gradual development of the theories of rectified diffusion was given by Crum (1984). His modeling approach is similar to that of Eller and Flynn. Experiments carried out by Crum (1980) have shown that threshold values of the pressure amplitude for bubble growth match those given by the Eller-Flynn theory for saturated conditions. However, away from saturation, some differences were found. Furthermore, the growth rate seemed to be underpredicted by the theory. It is to be noted that in the limited number of experiments so far appeared in the literature, the bubble radius was obtained by allowing the bubble to rise through a known distance. Actually, for obtaining

the bubble radius, measuring the time required to transverse a known distance and using an approximate drag law inherently imply lots of errors.

Crum and Prosperetti (1983) demonstrated that gas bubbles that were caused to pulsate in a liquid under the action of an acoustic pressure field could display nonlinear properties such as the presence of harmonic resonances in their oscillations. They studied the pulsation amplitude of an individual air bubble that was levitated in a glycerin-water mixture by a stationary acoustic wave operating at a frequency of 22.2 kHz. Fyrrillas and Szeri (1994) performed a theoretical study of rectified diffusion without invoking the limiting assumptions inherent in the Eller and Crum formulations. They split the convection-diffusion problem into two parts: the oscillatory and the smooth problems. Both problems were treated by singular perturbation methods: the oscillatory problem was solved through the boundary-layer analysis, and the smooth problem was solved by the method of multiple scales in time. Recently, Roberts and Wu (1998) made a theoretical attempt to refine Eller-Flynn's solution scheme. They evaluated an additional term over that of Eller & Flynn's model and used an asymptotic method for solving the radius vs. time of an oscillating bubble. They pointed out that the extra term they introduced is significant if the radius of the bubble is small or if the amplitude of its oscillations is large.

In liquid metals power ultrasound can be used for the rapid degassing of molten metal prior to solidification. The degassing of liquid metals under the action of ultrasound was first revealed in the 1930's. Hiedmann (1954) studied the metallurgical effects of ultrasonic waves, including the degassing. Investigations on the mechanism and the industrial applications of ultrasonic degassing of light alloy melts began in the 1960s. Cavitation mechanism of ultrasonic degassing of light alloy melts has been studied by Eskin (1995). He found that under certain conditions, the ultrasonic degassing reduced the hydrogen content in ingots and casts by about fifty percent. He also found that degassing of the melt resulted in improvements in the density and plasticity of as-cast metal, which retained higher strengths and increased the service reliability of deformed semifinished products.

In this chapter, a comprehensive mathematical model has been presented for rectified diffusion of dissolved gas in the liquid. The mass conservation equation for the gas, the energy conservation equations for the gas and the liquid along with the equation of state for the gas have been solved simultaneously. The bubble radius has been calculated from the Trilling (1952) equation and the mass transfer of dissolved gas into the bubble has been computed from the general convective-diffusion equation. It is to be noted that these equations are coupled and boundary conditions must be applied at a fast moving boundary of the bubble. By using appropriate variables, the model equations have been transformed into the new coordinates system. In this way the moving boundary of the bubble has been immobilized with respect to the time variable. In order to validate the mathematical model, a set of experiments have been carried out and the theoretical results for the bubble growth have been compared with the experiments. The experimental set up as well as the experimental results obtained will be presented in the next chapter.

5.3. Mathematical Modelling

In order to mathematically tackle the bubble growth in a gassy liquid under the ultrasonic pressure fields a number of reasonable assumptions about the physical characteristics of the phenomenon are made:

- i) The bubble remains spherical and the bubble center is motionless.
- ii) The gas in the bubble is thermodynamically uniform except in a thin layer near the interface.
- iii) The bubble gas is thermally perfect (ideal gas) but calorically imperfect (heat capacities are temperature-dependent)

The mathematical model is based on the following equations:

- i) Mass conservation equation for the gas
- ii) Equation for the bubble radius
- iii) Equation of state for the gas
- iv) Conservation of energy for the gas and the liquid
- v) Convective-mass diffusion equation for the dissolved gas in the liquid

The differential form of these equations in the spherical coordinates can be written as follows:

Mass conservation equation for the gas within the bubble:

$$\frac{d}{dt}(\rho \frac{4}{3} \pi R^3) = \dot{m}_t \quad (5.1)$$

where
$$\dot{m}_t = 4 \pi R^2 D \left. \frac{\partial C}{\partial r} \right|_{r=R} \quad (5.2)$$

The equation for bubble radius is based on the Trilling equation:

$$\left(1 - 2 \frac{\dot{R}}{C_0}\right) R \ddot{R} + \frac{3}{2} \left(1 - \frac{4}{3} \frac{\dot{R}}{C_0}\right) \dot{R}^2 = \frac{1}{\rho_\infty} \left[P_B(t) - P_{ap} + \frac{R}{C_0} \frac{dP_B(t)}{dt} \right] \quad (5.3)$$

where
$$P_B(t) = P_g - \frac{2\sigma}{R} - \frac{4\mu\dot{R}}{R} \quad (5.4)$$

and
$$P_{ap} = P_b - P_m \sin(2\pi f t) \quad (5.5)$$

The Trilling equation has been chosen because it accounts for the bubble acoustic damping. In order to obtain Eq. (5.3), Trilling assumed that the liquid surrounding the bubble is slightly compressible and the sound speed is constant. The derivatives of the density have been replaced by corresponding derivatives of the pressure with the help of the sound-speed relationship, $C_0^2 = dP / d\rho$.

The ideal gas equation of state is:

$$P_g = \frac{\rho \bar{R} T_g}{M_w} \quad (5.6)$$

The overall energy balance for the bubble gas is given by:

$$\frac{dE}{dt} = -\dot{W} + \dot{Q}_l + \dot{m}_t C_p T_{int} \quad (5.7)$$

where
$$E = \rho \forall C_v T_g \quad (5.8)$$

$$\dot{W} = P_B \frac{d\forall}{dt} \quad (5.9)$$

$$\dot{Q}_1 = 4\pi R^2 K_1 \left. \frac{\partial T_1}{\partial r} \right|_{r=R} \quad (5.10)$$

Here, \dot{W} is the rate of work done on the gas bubble during the collapse of the bubble or the rate of work against the pressure in the liquid during the bubble growth. Also in the above equation, P_B is the liquid pressure at the bubble boundary, \dot{Q}_1 is the rate of heat loss between the gas bubble and the surrounding liquid and \dot{m}_1 is the rate of mass transfer across the bubble interface. The differential energy balance equation for the liquid is:

$$\frac{\partial T_1}{\partial t} + \frac{R^2 \dot{R}}{r^2} \nabla T_1 = \alpha \nabla^2 T_1 + \frac{\mu}{\rho_1 C_{p1}} \phi_\gamma \quad r > R \quad (5.11)$$

where the viscous dissipation function is:

$$\phi_\gamma = 12 \frac{V_r^2}{r^2} \quad (5.12)$$

The velocity of liquid V_r can be found from the continuity equation in spherical coordinates to be:

$$V_r = \frac{R^2}{r^2} \dot{R} \quad (5.13)$$

The differential equation governing the convection and diffusion of the dissolved gas in the liquid outside the spherically symmetric bubble is:

$$\frac{\partial C}{\partial t} + \frac{R^2 \dot{R}}{r^2} \nabla C = D \nabla^2 C \quad r > R \quad (5.14)$$

5.3.1. Transformed and Non-dimensional Equations

For the numerical work, it is convenient to have a fixed rather than a moving boundary of the bubble. Therefore, the governing equations are transformed using a suitable variable (ζ) that “freezes” the moving boundary of the bubble. Also, in order to decrease the number of parameters and minimize computational errors, the governing

equations are non-dimensionalized. The transformed and non-dimensional forms of the mathematical model equations are:

$$\bar{\rho} = \frac{3Dt_0 C_0}{\rho_0 \bar{R}^2 R_0^2} \frac{\partial \bar{C}}{\partial \zeta} \Big|_{\zeta=1} - \frac{3\bar{R}\bar{\rho}}{\bar{R}} \quad (5.15)$$

$$(1 - 2\frac{\bar{R}}{\bar{C}_0})\bar{R} + \frac{3}{2}(1 - \frac{4}{3}\frac{\bar{R}}{\bar{C}_0})\frac{\bar{R}^2}{\bar{R}} = \frac{1}{M^2} \frac{\bar{P}_g - \bar{P}_\infty}{\bar{R}} - \frac{1}{We} \frac{1}{\bar{R}^2} - \frac{1}{Re} \frac{\bar{R}}{\bar{R}^2} + \frac{1}{M^2 \bar{C}_0} (\bar{\rho} \bar{T}_g + \bar{T}_g \bar{\rho}) + \frac{1}{We} \frac{\bar{R}}{\bar{C}_0 \bar{R}^2} - \frac{1}{Re} \frac{1}{\bar{C}_0} (\frac{\bar{R}\bar{R} - \bar{R}^2}{\bar{R}^2}) \quad (5.16)$$

$$\bar{P}_g = \bar{\rho} \bar{T}_g \quad (5.17)$$

$$\bar{T}_g = -\frac{3\bar{T}_g \bar{R}}{\bar{R}} - \frac{\bar{T}_g \bar{\rho}}{\bar{\rho}} - \frac{3\bar{R}\bar{T}_g \bar{\rho}}{M_w C_v \bar{R}} + \frac{6\sigma \bar{R}}{T_0 C_v \bar{\rho} \rho_0 \bar{R}^2 R_0} + \frac{12\mu R^2}{t_0 T_0 C_v \bar{\rho} \rho_0 \bar{R}^2} + \frac{3DC_p t_0 \bar{T}_1 C_0}{C_v \bar{\rho} \rho_0 \bar{R}^2 R_0^2} \frac{\partial \bar{C}}{\partial \zeta} \Big|_{\zeta=1} + \frac{3K_1 t_0}{C_v \bar{\rho} \rho_0 \bar{R}^2 R_0^2} \frac{\partial \bar{T}_1}{\partial \zeta} \Big|_{\zeta=1} \quad (5.18)$$

$$\bar{T}_1 = \frac{1}{\bar{R}^2} [\alpha^* \frac{\partial^2 \bar{T}_1}{\partial \zeta^2} + (-\frac{\bar{R}\bar{R}}{\zeta^2} + \frac{\bar{R}\bar{R}\zeta}{\zeta} + \frac{2\alpha^*}{\zeta}) \frac{\partial \bar{T}_1}{\partial \zeta} + 12\mu^* \frac{\bar{R}^2}{\zeta^6}] \quad (5.19)$$

$$\bar{C} = \frac{1}{\bar{R}^2} [D^* \frac{\partial^2 \bar{C}}{\partial \zeta^2} + (-\frac{\bar{R}\bar{R}}{\zeta^2} + \frac{\bar{R}\bar{R}\zeta}{\zeta} + \frac{2D^*}{\zeta}) \frac{\partial \bar{C}}{\partial \zeta}] \quad (5.20)$$

where:

$$\frac{1}{Re} = \frac{4\mu t_0}{\rho_1 R_0^2} \quad \frac{1}{We} = \frac{2\sigma t_0^2}{\rho_1 R_0^3} \quad \frac{1}{M^2} = \frac{t_0^2 p_0}{\rho_0 R_0^2} \quad (5.21)$$

$$\mu^* = \frac{\mu}{\rho_1 C_p T_0 t_0} \quad D^* = \frac{Dt_0}{r_0^2} \quad \alpha^* = \frac{\alpha t_0}{r_0^2} \quad \zeta = \frac{r}{R(t)}$$

$$\bar{R} = \frac{R}{R_0}, \quad \bar{R} = \frac{\dot{R} t_0}{R_0}, \quad \bar{T}_g = \frac{T_g}{T_0}, \quad \bar{T}_1 = \frac{T_1}{T_0}, \quad \bar{P} = \frac{P}{P_0}, \quad \bar{\rho} = \frac{\rho}{\rho_0}, \quad \bar{t} = \frac{t}{t_0}$$

5.3.2. Initial Conditions

Initially the bubble is at rest and is in equilibrium with the surrounding liquid. The following equations are used for the equilibrium condition.

$$\begin{aligned} \text{at } t=0 \quad P_0 = P_b + \frac{2\sigma}{R_0} \quad T_0 = 293 \text{ K} \quad \rho_0 = \frac{P_0 M_w}{\mathfrak{R} T_0} \\ \bar{\rho} = 1, \quad \bar{R} = 1, \quad \bar{\dot{R}} = 0, \quad (\bar{T}_1)_j = 1, \quad j = 1 \text{ to } 20 \\ (\bar{C})_j = 1, \quad j = 1 \text{ to } 20 \end{aligned} \quad (5.22)$$

$$\text{The characteristic time is:} \quad t_0 = \frac{2\pi}{\omega} = \frac{1}{f} \quad (5.23)$$

where, f is the frequency of the ultrasound.

Table 5.1 lists the various physical properties of water and Al-3.4 pct Cu alloy melt.

5.3.3 Boundary Conditions

The interface temperature (T_{int}) is obtained from the interfacial boundary condition, which states that at each instant of time the rate of energy transfer from the gas side of the gas-liquid interface is equal to the rate of energy transfer from the liquid side of the interface.

$$[\dot{m}h + \dot{q}]_g|_{r=R} = [\dot{m}h + \dot{q}]_l|_{r=R} \quad (5.24)$$

More details about the temperature profile at the phase boundary are available in the paper published by Naji Meidani and Hasan (1997).

Putting the relevant expressions in equation (5.24), one can easily show:

$$T_{int} \approx \frac{T_0(\sqrt{(K\rho C_p)_l} - \sqrt{t_0} C_p D \frac{\partial C}{\partial r} \Big|_{r=R}) + T_g(\sqrt{(K\rho C_p)_g} + \sqrt{t_0} C_p D \frac{\partial C}{\partial r} \Big|_{r=R})}{\sqrt{(K\rho C_p)_g} + \sqrt{(K\rho C_p)_l}} \quad (5.25)$$

The liquid temperature far from the bubble is assumed to remain unchanged:

$$T_1(\infty, t) = T_0 \quad (5.26)$$

In the water modelling, the boundary condition for concentration of dissolved gas in the liquid at the bubble interface is obtained from Henry's law:

$$C_{int} = K^{-1} P_g = \frac{C_{sat} P_g}{P_b} \quad (5.27)$$

Here, K is the constant of Henry's law.

In the case of liquid metals, the interfacial concentration of dissolved gas in the liquid metal has been obtained from Seivert's law:

$$C_{int} = q \sqrt{P_g} \quad (5.28)$$

where q is Seivert's constant and P_g is the gas pressure in the bubble (atm). In the following, the relevant expressions used in this work to obtain Seivert's constant q is discussed.

The nondimensional mass diffusion layer in the liquid is proportional to the following expression which satisfies the shell effect:

$$\bar{\delta}_m \approx \frac{\sqrt{\frac{D}{\omega}}}{R(t)} = \frac{\sqrt{\frac{D}{2\pi f}}}{R(t)} \quad (5.29)$$

The concentration of dissolved gas in the liquid far from the bubble is assumed to remain unchanged:

$$C(\infty, t) = C_i \quad (5.30)$$

For the calculation of temperature and dissolved gas concentration gradients in the liquid at the bubble interface, which appear in the continuity and energy equations of the gas, a second-order forward difference discretization method was applied. In this study, in addition to the rectified diffusion of dissolved air in water, the rectified diffusion of dissolved hydrogen in Al-3.4 pct Cu alloy melt has been theoretically studied.

Table 5.1. Input Parameters for Computations

Parameter [unit]	Water	Al-3.4 Pct Cu
α [m^2/sec]	1.44×10^{-7}	3.78×10^{-5}
σ [N/m]	0.0729	0.89
ρ_i [kg/m^3]	998.0	2300.0
μ [$(\text{N}\cdot\text{s})/\text{m}^2$]	1.053×10^{-3}	1.4×10^{-3}
C_{p_i} [$\text{J}/(\text{kg}\cdot\text{k})$]	4186.0	1265.0
K_i [$\text{W}/(\text{m}\cdot\text{k})$]	0.602	110.0
D [m^2/sec]	2.0×10^{-9}	0.5×10^{-6}
C_0 [m/s]	1480.0	4650.0
T_0 [K]	293.0	973.0
P_b [KP_a]	101.0	105.6, 110.2, 114.8

The solubility of hydrogen in Al-3.4 pct Cu liquid alloys is determined by the following relations presented by Poirier (1987):

$$\text{Log}_{10} S = -A / T + B \quad (5.31)$$

where S is the solubility in cm^3 of $\text{H}_2(\text{g})$ at standard pressure and temperature per 100 g of alloy, A and B are parameters that depend only on the concentration of copper in the Al-Cu alloys, and T is temperature in K. Using a regression analysis, the values of A and B obtained by Opie and Grant (1950) are:

$$A = 2550 + 358.9C_{\text{cu}}^{1/2} - 54.48C_{\text{cu}} + 0.6241C_{\text{cu}}^{3/2} \quad (5.32)$$

and

$$B = 2.620 + 0.3043C_{\text{cu}}^{1/2} - 0.08072C_{\text{cu}} + 0.004484C_{\text{cu}}^{3/2} \quad (5.33)$$

with C_{cu} as the wt pct of copper in the liquid.

From Equations (5.31), (5.32) and (5.33), the solubility of hydrogen in Al-3.4 pct Cu alloy at 973 K is calculated as:

$$S = 0.661 \text{ cm}^3/100\text{g} \quad (5.34)$$

The amount of hydrogen in liquid aluminium alloys is usually measured in cubic centimeters at standard conditions of pressure and temperature per 100 g of metal. Using the gas law, the following equivalence is found:

$$\frac{1 \text{ cc}_{\text{STD}} \text{ H}_2}{100 \text{ g}} = \frac{10^{-3} \times 2 \text{ g}}{22.4} = 8.9 \times 10^{-5} \text{ wt pct} \quad (5.35)$$

Using Eq. (5.35), Seivert's constant q in Eq. (5.28) can be determined as:

$$q = 8.9 \times 10^{-5} \text{ S} \quad (5.36)$$

5.4 Numerical Solution Methods

The mathematical model forms a set of coupled, highly nonlinear and stiff differential equations. In order to convert the PDEs into a system of stiff ODEs, the partial differential equations were discretized only in space direction using the second order central difference scheme. Due to having significantly different time and length scales in the mathematical model, the problem is stiff. Therefore, the modified Gear

method, which is good for solving a set of nonlinear stiff ordinary differential equations, was applied. The code, as explained earlier in section 3.4, is based on a variable-step, variable-order backward differentiation formula (BDF) method of order 1 to 5. It started the integration with a first order method and as the integration proceeded, the program automatically adjusted to a higher order method (and the step size) for optimal efficiency while satisfying prescribed accuracy requirements. The integration method was a step-by-step method and started with the known initial conditions. At each time-step the method employed a predictor-corrector scheme, wherein an initial guess for the solution was first obtained and then the initial guess was progressively improved upon by iteration until the solution converged, that is, further iteration produced little or no change in the solution.

5.5 Results and Discussion

During the ultrasonic degassing of a gassy liquid, the pressure experienced by the gas bubble is $P_{ap} = P_b - P_m \sin(2\pi f t)$, where P_b is the pressure of undisturbed liquid and P_m and f are the ultrasonic pressure field's amplitude and frequency, respectively. In order to ascertain the most effective parameters that govern the process of rectified diffusion, we need to know how the results are affected by the key variables such as, R_0 , C_i , P_m , f , and P_b . Therefore, in the mathematical model, the initial bubble radius, the initial concentration of the dissolved gas in the liquid, the ultrasonic pressure amplitude and frequency and the pressure of undisturbed liquid are parametrically varied. It is to be noted that the instantaneous bubble radius and the mass of gas contained in the bubble are averaged over the time intervals equal to the period of the ultrasound. Because of this averaging process, the curves in all the figures discussed below are rather jagged. Also, in the figures, the time variable is non-dimensionalized by the period of the ultrasound.

5.5.1 Results and Discussion for Water Modelling

In Figure 5.3, the calculated temporal variations of the average mass contained in an air bubble and the average bubble radius are shown. The left axis represents the average mass in the bubble and the right axis represents the average bubble radius. The ultrasonic frequency and the ultrasonic pressure amplitude are 35 kHz and 0.2 bar, respectively. As shown, the air bubble with the initial radius of 0.07 mm does not grow in an air-saturated water because the ultrasonic pressure is lower than the threshold pressure. The average size of the bubble and the average mass of gas within the bubble are decreased and the bubble becomes smaller than its initial size. In Figure 5.4 the temporal variations of the average bubble radius for two different ultrasonic pressure amplitudes are shown. The initial radius of the bubble and the ultrasonic frequency are 0.07 mm and 35 kHz, respectively. For the ultrasonic pressure amplitude of 0.3 bar, the bubble starts to grow in an air-saturated water. As shown in the figure, with increasing the ultrasonic pressure amplitude to 0.5 bar, the air bubble grows more than the previous case and the bubble volume reaches about five times of its initial value. It is to be noted that the nondimensional bubble volume is proportional to the cubic power of the nondimensional bubble radius. The corresponding time-averaged mass of gas contained in the bubble for two different ultrasonic pressure amplitudes is shown in Figure 5.5. This figure shows that the increase of the ultrasonic pressure amplitude promotes the process of rectified diffusion. Since the intensity of the ultrasonic pressure wave is proportional to the square of the ultrasonic pressure amplitude, therefore an increased ultrasonic pressure amplitude means an increased intensity of the ultrasonic wave which in turn increases the rate of bubble growth.

In Figure 5.6 the effects of the initial concentration of dissolved air in water on the time-averaged mass of air contained in the bubble are shown. The initial radius of the bubble is 0.1 mm and the ultrasonic pressure amplitude and frequency are 0.6 bar and 25 kHz, respectively. The results show that with increasing the initial concentration of dissolved air in water the average mass of gas contained in the bubble increases. In fact,

the rate of mass transfer into the bubble in a liquid with a large initial concentration of dissolved gas is greater compared to that of in a liquid with a small initial concentration.

Figures 5.7 and 5.8 are plotted to portray the effects of the ultrasonic frequency on rectified diffusion. Figure 5.7 demonstrates the time-averaged mass of gas contained in the bubble for three different ultrasonic frequencies, namely 35, 25 and 20 kHz. The initial radius of the bubble and the ultrasonic pressure amplitude are taken to be 0.07 mm and 0.3 bar, respectively. The figure shows that when the ultrasonic frequency is decreased from 35 kHz to 20 kHz, the average amount of gas contained in the bubble increases significantly. For an ultrasonic frequency of 20 kHz, the air bubble grows rapidly in an air-saturated water and the average mass of gas contained in the bubble reaches more than seventeen times of its initial value. The reason for this increase is that the subharmonic resonance frequency causes the bubble's pulsation amplitude to increase, which in turn results in the more rectified mass transfer per ultrasound cycle. In Fig. 5.8, the results are depicted for the ultrasonic pressure amplitude when it is increased to 0.5 bar. Similar to the previous figure, the initial radius of the bubble and the initial concentration of dissolved air in water are 0.07 mm and 100% of saturation value, respectively. This figure shows that with increasing the ultrasonic frequency from 25 kHz to 45 kHz, the average amount of gas contained in the bubble decreases from 12 to 2.3 times of its initial value.

In Fig. 5.9, the initial bubble radius and the ultrasonic pressure amplitude are considered to be 0.1 mm and 0.5 bar, respectively. The ultrasonic frequency is 25 kHz. The air bubble grows in an air-saturated water and the average mass of gas contained in the bubble reaches more than four times of its initial value. The bubble expands rapidly and the average bubble volume reaches about 4.5 times of its initial value.

Figure 5.10 demonstrates the history of average mass of gas contained in the bubble for different initial bubble radii. The initial concentration of dissolved air in water is considered to be 100% of the saturation value. The ultrasonic pressure amplitude and frequency are 0.5 bar and 25 kHz, respectively. The results show that for decreasing the initial bubble radius from 50 μm to 30 μm the average mass of gas contained in the bubble increases from about 30 to 140 times of its initial value. It is noted that the

average mass of gas contained in the bubble is nondimensionalized by the initial mass of gas within the bubble. It is to be recognized that, for a small bubble the initial mass of gas inside the bubble is smaller than that of for a big bubble.

5.5.2 Results and Discussion for Liquid Metal

Figure 5.11 shows the results of rectified diffusion of dissolved hydrogen in a molten Al-3.4 pct Cu alloy. The pressure of the undisturbed melt and the ultrasonic pressure amplitude are considered to be 1.056 and 1.3 bars, respectively. The ultrasonic frequency is 25 kHz and the initial concentration of dissolved hydrogen in molten aluminium is 100% of its saturation value. A hydrogen bubble, with the initial radius of 15 μm , grows and the average mass of gas contained in the bubble reaches about 400 times of its initial value. The average bubble radius increases rapidly to more than 9 times of its initial value. In Fig. 5.12 the initial bubble radius is increased to 20 μm . In this case, due to rectified diffusion, the average bubble radius increases to around 7 times of its initial value. The average mass of gas contained in the bubble reaches about 200 times of its initial value.

Figures 5.13-5.17 are plotted to demonstrate the effects of the variables R_0 , f , C_0 , P_m , and P_b on rectified diffusion of dissolved hydrogen in the Al-3.4 pct Cu alloy melt. In Figure 5.13, the history of the average mass of hydrogen gas contained in the bubble for different initial bubble radii are shown. The pressure of the undisturbed melt and the ultrasonic pressure amplitude are 1.056 and 1.3 bars, respectively. The ultrasonic frequency is considered to be 25 kHz. The initial concentration of dissolved hydrogen in molten aluminium is 100% of its saturation value. The results show that with decreasing the initial bubble radius from 25 μm to 15 μm , the average mass of hydrogen gas within the bubble increases (by rectified diffusion) from 115 to 400 times of its initial value.

Figure 5.14 shows the history of average mass of hydrogen gas contained in the bubble for different ultrasonic frequencies. The other conditions are the same as the previous figure. The results show that with decreasing the ultrasonic frequency from 35

kHz to 25 kHz, the average mass of hydrogen gas within the bubble increases from 65 to 195 times of its initial value.

In figure 5.15 the time variations of the average mass of hydrogen gas contained in the bubble for different ultrasonic pressure amplitudes are shown. The other conditions are the same as the previous case. As seen in the figure, with increasing the ultrasonic pressure amplitude from 1.2 bar to 1.5 bar the average mass of hydrogen gas within the bubble increases from around 120 to more than 150 times of its initial value. Also, the results show that the same bubble under the ultrasonic pressure amplitude of 1.1 bar does not grow.

The threshold pressures (minimum ultrasonic pressure amplitude required to start the bubble growth) for bubbles with initial radius of 15 μm , 20 μm and 25 μm were found to be 1.18, 0.9 and 0.87 bars, respectively. These results were obtained for the bubbles in the aluminium 3.4 pct cu alloy melt with the initial hydrogen concentration of 100% saturation. The ultrasonic frequency was taken to be 35 kHz. The reduction of the initial concentration to 50% of saturation value causes the threshold pressures to increase to 1.26, 1.15 and 1.08 bars, respectively, with all other conditions remaining the same as the previous case.

The history of average mass of hydrogen gas contained in the bubble for different initial concentrations of dissolved hydrogen is shown in Figure 5.16. The other conditions are the same as the previous figure (Fig. 5.15). The results show that, increasing the initial concentration from 30% to 100% of saturation, the average mass of hydrogen gas contained in the bubble increases from 80 to near 200 times of its initial value. Figure 5.17 represents the history of average mass of hydrogen gas contained in the bubble for different hydrostatic pressures at the bubble position. The initial bubble radius is considered to be 15 μm . The ultrasonic pressure amplitude and frequency were kept at 1.3 bar and 25 kHz, respectively. The initial concentration of dissolved hydrogen in the molten aluminium is 100% of its saturation value. The figure shows that a change of the hydrostatic pressure from 1.056 bar (20 cm below the liquid metal surface) to 1.148 bar (60 cm below the liquid metal surface) does not have any significant effect on rectified diffusion of dissolved hydrogen. In other words, the rectified diffusion effect is found to

be almost independent of the hydrostatic pressure of the melt for this range of variations in hydrostatic pressure.

5.6. Concluding Remarks

In this study, a general mathematical model has been developed to simulate the ultrasonic degassing of a gassy liquid. The radial motion of the bubble was considered to be governed by the compressible form of the Rayleigh-Plesset bubble dynamics equation. The analysis considered isolated micron size gas bubbles inside the liquid which initially contains some dissolved gas. The overall energy balance for the gas bubble is governed by the first law of thermodynamics. The gas pressure within the bubble was calculated by using ideal gas equation of state. The mass and the thermal energy exchange between the bubble and the surrounding liquid were taken into account by solving the relevant differential equations. For the air-water system, the boundary condition for concentration of dissolved gas in the liquid at the bubble interface was obtained from Henry's law while for the hydrogen-aluminium alloy system it was obtained from Sievert's law.

The model equations were suitably transformed to immobilize the moving boundary of the bubble. The transformed and non-dimensionalized form of the set of coupled, highly nonlinear and stiff ODE's was solved by the modified Gear scheme. It was found that the bubble growth rate depends on the initial bubble size, the initial concentration of dissolved gas in liquid and the ultrasonic specifications. A parametric study for the bubble growth by rectified diffusion was carried out for both water and liquid Al-3.4 pct Cu alloy. For some defined conditions, the time variations of the average bubble radius and the average mass contained in the air bubble were computed. The mathematical model results showed that for decreasing ultrasonic frequency, the time-averaged bubble radius and the average mass of gas contained in the bubble increases. Also, with decreasing of the initial bubble radius, the bubble growth rate increases. The theoretical results showed that, with the decrease of the initial concentration of dissolved gas in the liquid, the threshold pressure for bubble growth increases, while the amount of

bubble growth decreases. The modelling results for both air-water system and hydrogen-aluminium alloy system were qualitatively similar.

Nomenclature

C	concentration of dissolved gas in liquid	kg/m^3
C_i	initial concentration of dissolved gas in liquid	kg/m^3
C_v, C_p	specific heat at constant volume and constant pressure	$\text{J}/(\text{kg-K})$
C_o	speed of sound in liquid	m/s
D	mass diffusivity	m^2/s
E	internal energy of gas mixture	J
f	frequency of the ultrasound	Hz
K	thermal conductivity of liquid	$\text{W}/(\text{m-K})$
M_w	molecular weight of gas	g/mole
P	pressure	Pa
P_0	initial pressure	Pa
P_{ap}	applied pressure in liquid	Pa
P_b	pressure of undisturbed liquid	Pa
\dot{Q}_l	heat loss rates	W
R, R_0	bubble radius at any time and initial bubble radius	m
\dot{R}, \ddot{R}	bubble wall velocity and bubble wall acceleration	$\text{m/s}, \text{m/s}^2$
r	distance from bubble center	m
T	temperature	K
T_0	initial temperature	K
t	time	s
\dot{W}	work rate	W
ρ_l	density of liquid	kg/m^3
ρ_0	initial density of gas	kg/m^3
\bar{R}	universal gas constant	$\text{J}/(\text{kg-mole-K})$
α	thermal diffusivity	m^2/s
σ, μ	surface tension and dynamic viscosity of liquid	$\text{N/m}, (\text{N-s})/\text{m}^2$

δ_m mass diffusion layer thickness m

Superscripts

– variable non-dimensionalized by reference parameter

Subscripts

g gas

sat saturation

int interface

0 initial-state

l liquid

References

- Blake, F. G., The Onset of Cavitation in Liquids, *Acoustics Res. Lab., Harvard Univ., Tech. Memo.*, No. 12, 1949.
- Crum, L. A., Rectified Diffusion, *Ultrasonics*, Vol. 22, pp. 215-223, 1984.
- Crum, L. A., Measurements of the Growth of Air Bubbles by Rectified Diffusion *J. Acoust. Soc. Am.*, Vol. 68, pp. 203-211, 1980.
- Crum, L. A. and Prosperetti, A., Nonlinear Oscillation of Gas Bubbles in Liquids, an Interpretation of Some Experimental Results, *J. Acoust. Soc. Am.*, Vol. 73, pp. 121-127, 1983.
- Eller, A. and Flynn, H. G., Rectified Diffusion During Nonlinear Pulsation of Cavitation Bubbles, *J. Acoust. Soc. Am.*, Vol. 37, pp. 493-503, 1965.
- Eller, A., Bubble Growth by Diffusion in an 11-kHz Sound Field, *J. Acoust. Soc. Am.*, Vol. 52, pp. 1447-1449, 1972.
- Eskin, G., I., Cavitation Mechanism of Ultrasonic Melt Degassing, *J. of Ultrasonics Sonochemistry*, Vol. 2, No. 2, pp. 137-141, 1995.
- Fyillas. M. M. and Szeri, A. J., Dissolution or Growth of Soluble Spherical Oscillating Bubbles, *J. Fluid Mech*, Vol. 277, pp. 381-407, 1994.
- Hiedeman, E. A., Metallurgical effects of ultrasonic waves, *Journal of the Acoustical Society of America*, Vol. 26, No. 6, pp. 831-842, 1954.
- Hsieh, L. A. and Plesset, M., Theory of Rectified Diffusion of Mass into Gas Bubbles, *J. Acoust. Soc. Am.*, Vol. 33, pp. 206-215, 1961.
- Naji Meidani, A. R. and Hasan, M., A Numerical Study of the Complex Dynamics Behavior of a Reactive Gas Bubble in Water, *J. of Applied Mathematical Modelling*, Vol. 21, pp. 127-138., 1997.
- Opie, W. R. and Grant, N. J., *Trans. AIME, J. Metals*, Vol. 188, pp. 1237-1241, 1950.
- Poirier, D. R., Yeum, K. and Maples, A. L., A Thermodynamic Prediction for Microporosity Formation in Aluminum-Rich Al-Cu alloys, *J. Metallurgical Transactions A*, Vol. 18A, pp. 1979-1987, 1987.

Robert, P. H. and Wu, C., C., On Rectified Diffusion and Sonoluminescence, *J. Theore. Comput. Fluid Dynamics*, Vol. 10, pp. 357-372, 1998.

Trilling, L. The Collapse and Rebound of a Gas Bubble. *J. Appl. Phys.*, Vol. 23, pp. 14-17, 1952.

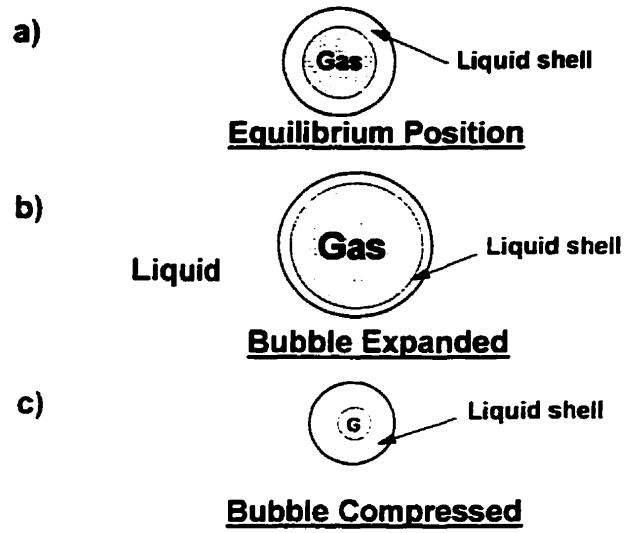


Fig. 5.1. Rectified diffusion

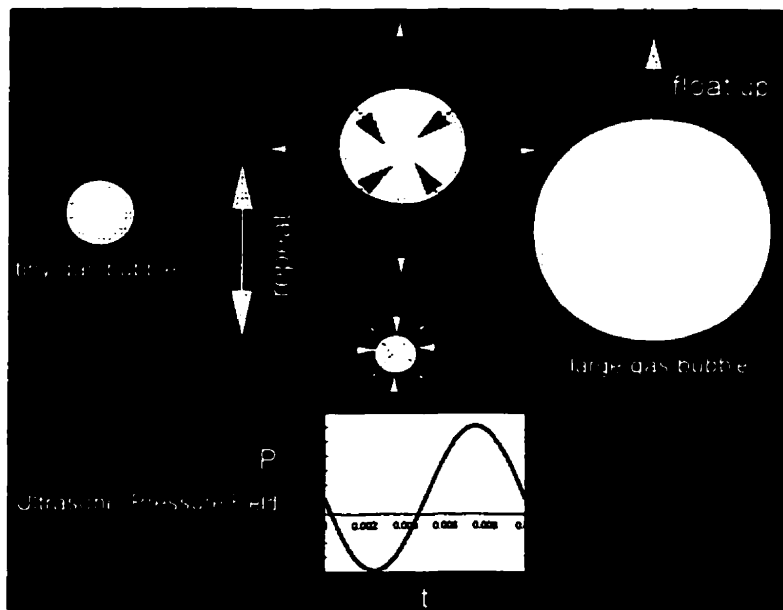


Fig. 5.2. Formation of a large gas bubble from a tiny gas bubble by the process of rectified diffusion.

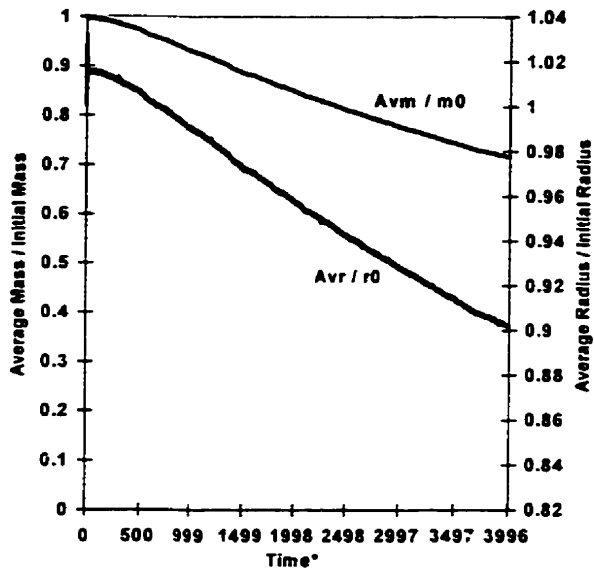


Fig. 5.3. Time variations of average bubble radius and average mass contained in the bubble under an ultrasonic pressure field of $P_{ap} = 1.01 - 0.2 \sin(2\pi f t)$, $f = 35$ kHz, $C_0 = 100\%$ Saturation, $R_0 = 0.07$ mm.

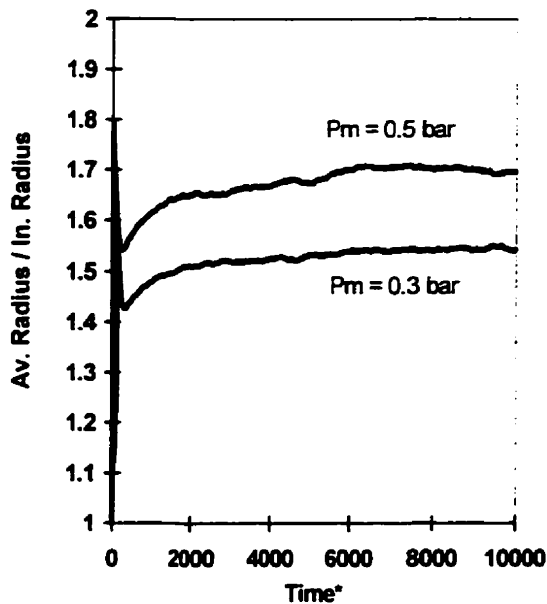


Fig. 5.4. Time variations of average bubble radius for different ultrasonic pressure amplitudes of $P_{ap} = 1.01 - P_m \sin(2\pi f t)$, $f = 35$ kHz, $C_0 = 100\%$ Saturation, $R_0 = 0.07$ mm.

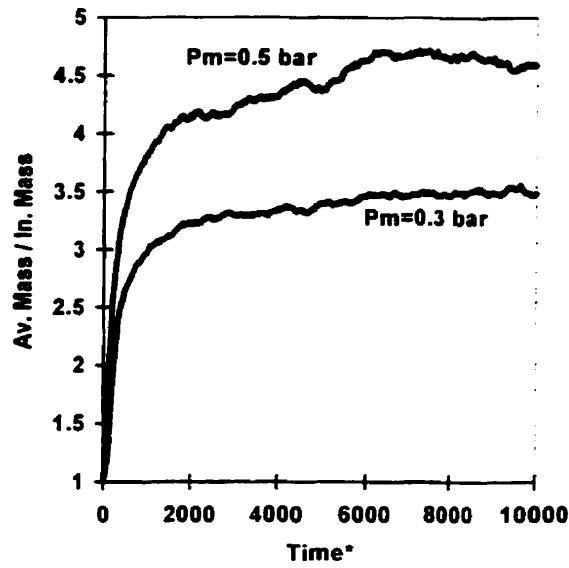


Fig. 5.5. Time variations of average mass contained in the bubble for different ultrasonic pressure amplitudes, $P_{ap} = 1.01 - P_m \sin(2\pi f t)$, $f = 35$ kHz, $R_0 = 0.07$ mm, $C_0 = 100\%$ Saturation.

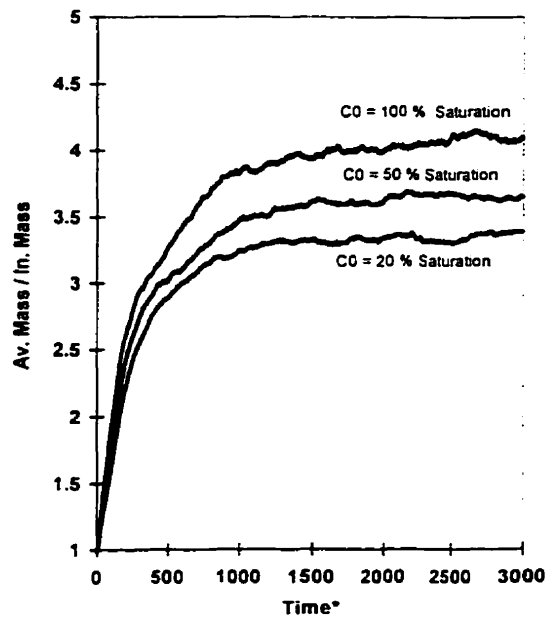


Fig. 5.6. Time variations of average mass contained in the bubble for different liquid concentrations under an ultrasonic pressure field of $P_{ap} = 1.01 - 0.6 \sin(2\pi f t)$, $f = 25$ kHz, $R_0 = 0.10$ mm.

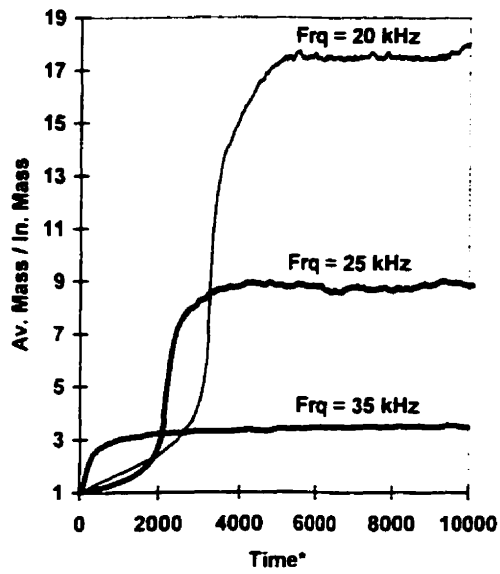


Fig. 5.7. Time variations of average mass of gas contained in the bubble for different ultrasonic frequencies under an ultrasonic pressure field of $P_{ap} = 1.01 - 0.3 \sin(2\pi f t)$, $R_0 = 0.07$ mm, $C_0 = 100$ % Saturation.

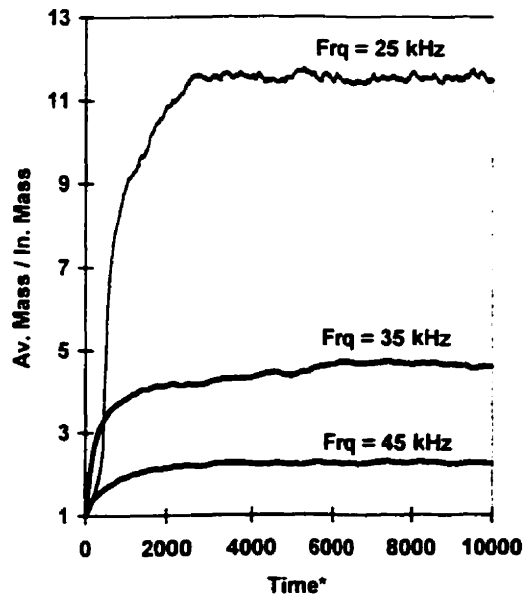


Fig. 5.8. Time variations of average mass of gas contained in the bubble for different ultrasonic frequencies under an ultrasonic pressure field of $P_{ap} = 1.01 - 0.5 \sin(2\pi f t)$, $R_0 = 0.07$ mm, $C_0 = 100$ % Saturation.

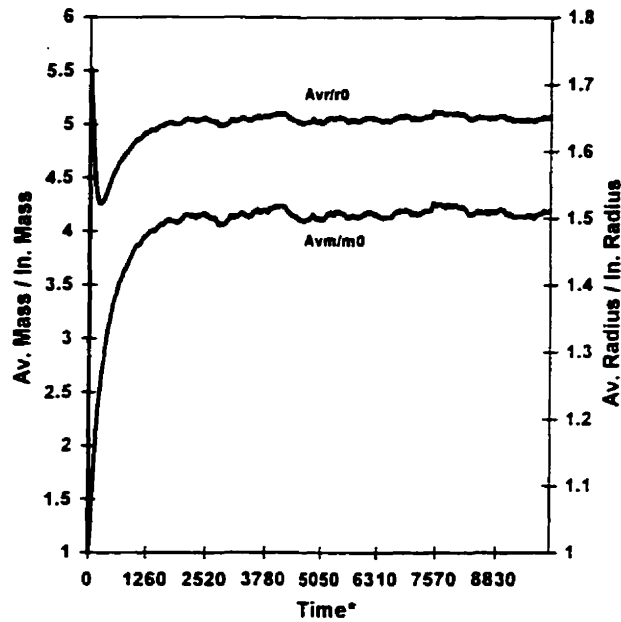


Fig. 5.9. Time variations of average bubble radius and average mass of gas contained in the bubble under an ultrasonic pressure field of $P_{ap} = 1.01 - 0.5 \sin(2\pi f t)$, $f = 25$ kHz, $C_0 = 100\%$ Saturation, $R_0 = 0.10$ mm.

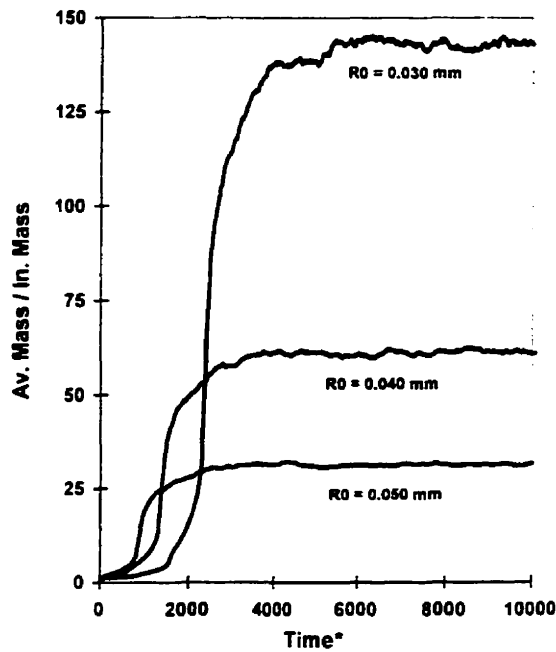


Fig. 5.10. History of average mass of gas contained in the bubble for different bubble initial radii under an ultrasonic pressure field of $P_{ap} = 1.01 - 0.5 \sin(2\pi f t)$, $f = 25$ kHz, $C_0 = 100\%$ Saturation.

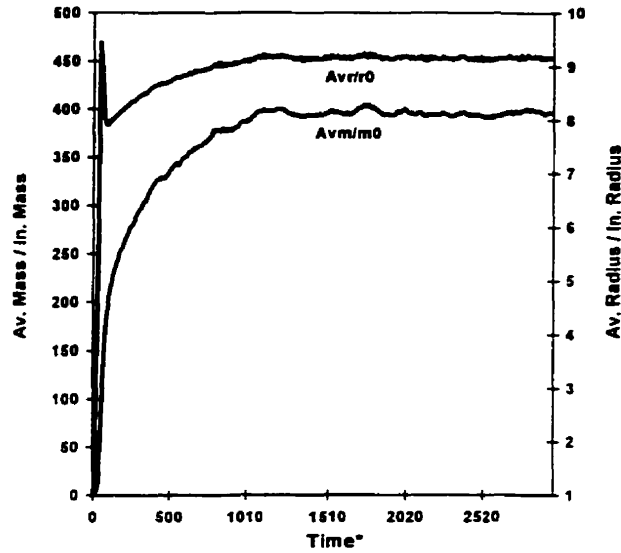


Fig. 5.11. Time variations of average bubble radius and average mass of hydrogen gas contained in the bubble under an ultrasonic pressure field of $P_{ap}=1.056-1.3 \sin(2\pi f t)$, $f = 25$ kHz, $R_0 = 0.015$ mm and $C_0 = 100\%$ Saturation.

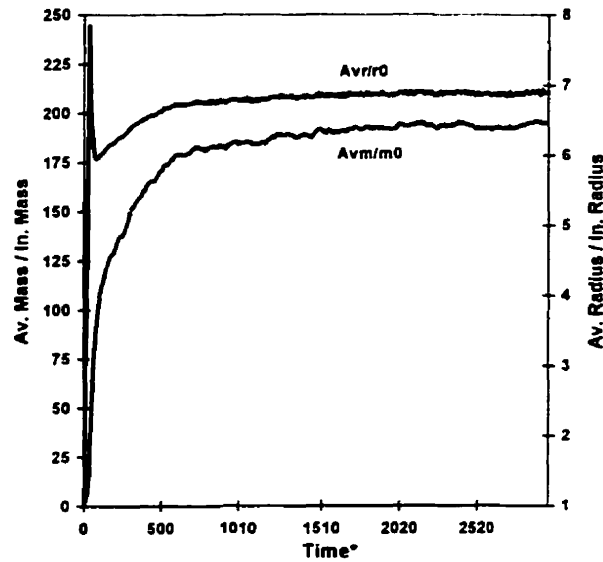


Fig. 5.12. Time variations of average bubble radius and average mass of hydrogen gas contained in the bubble under an ultrasonic pressure field of $P_{ap}=1.056-1.3 \sin(2\pi f t)$, $f = 25$ kHz, $R_0 = 0.020$ mm and $C_0 = 100\%$ Saturation.

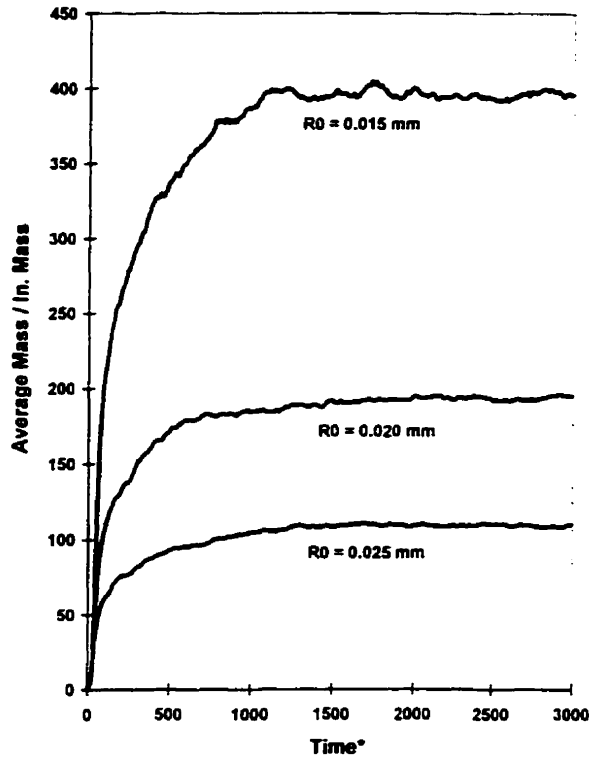


Fig. 5.13. History of average mass of hydrogen gas contained in the bubble for different bubble initial radii under an ultrasonic pressure field of $P_{ap}=1.056-1.3 \sin(2\pi f t)$, $C_0 = 100\%$ Saturation $f = 25$ kHz.

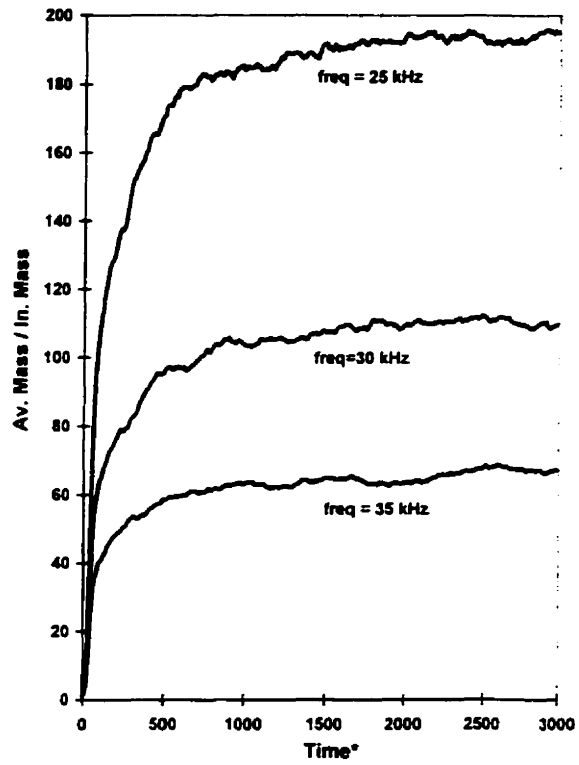


Fig. 5.14. History of average mass of hydrogen gas contained in the bubble for different ultrasonic frequencies, $P_{ap}=1.056-1.3 \sin(2\pi f t)$, $C_0 = 100\%$ Saturation and $R_0 = 0.020$ mm.

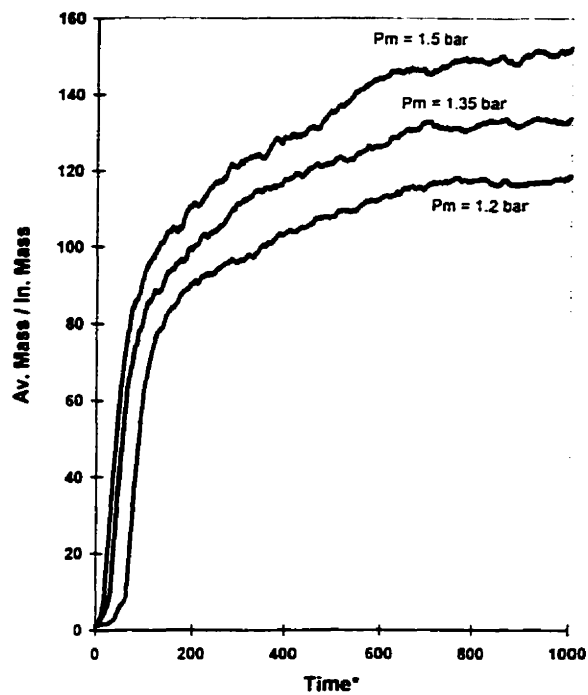


Fig. 5.15. History of average mass of hydrogen gas contained in the bubble for different ultrasonic pressure amplitudes, $P_{ap}=1.056-P_m \sin(2\pi f t)$, $C_0 = 100\% \text{ Sat.}$, $f = 35 \text{ kHz}$ and $R_0 = 0.015 \text{ mm}$.

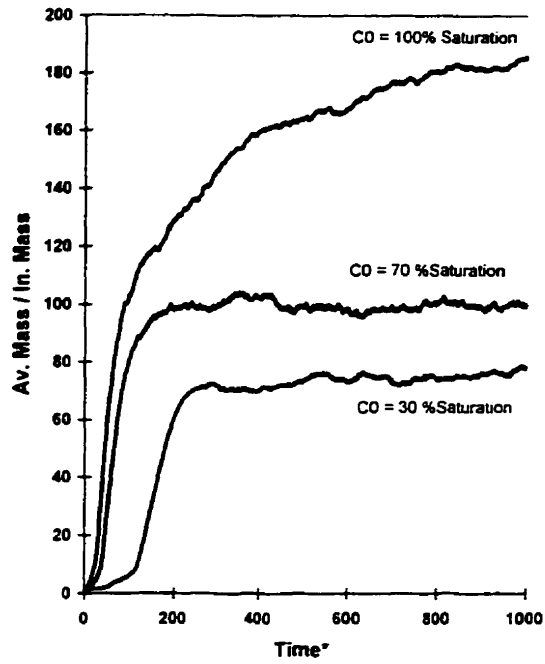


Fig. 5.16. History of average mass of hydrogen gas contained in the bubble for different initial concentrations of dissolved hydrogen, $P_{ap}=1.056-1.3 \sin(2\pi f t)$, $f = 25$ kHz and $R_0 = 0.020$ mm.

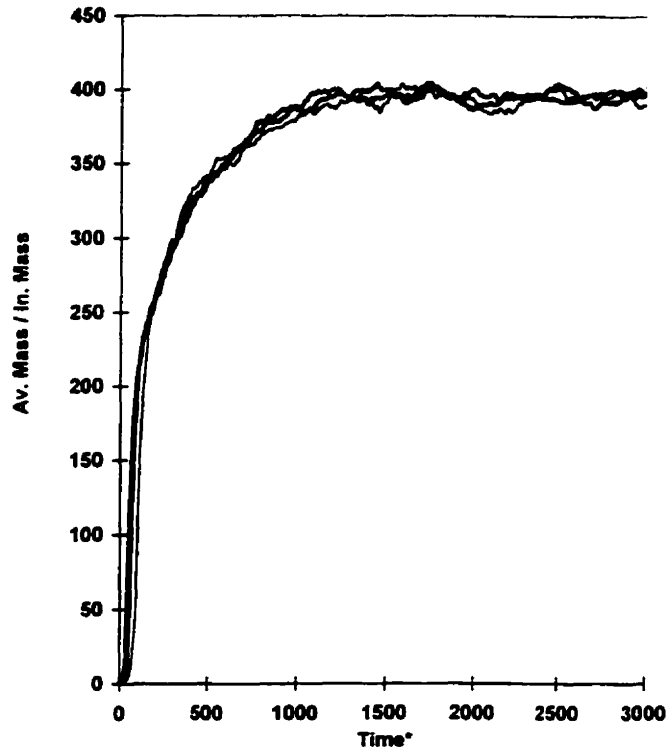


Fig. 5.17. History of average mass of hydrogen gas contained in the bubble for different hydrostatic pressures, $P_{ap}=P_b-1.3 \sin(2\pi f t)$, $P_b = 1.056 \text{ bar}, 1.102 \text{ bar}, 1.148 \text{ bar}$
 $R_0 = 0.015 \text{ mm}, C_0 = 100 \% \text{ Saturation}$ and $f = 25 \text{ kHz}$.

AN AQUEOUS EXPERIMENTAL INVESTIGATION OF BUBBLE GROWTH BY RECTIFIED DIFFUSION UNDER AN ULTRASONIC PRESSURE FIELD

6.1 Basic Theory of Ultrasound

6.1.1 Historical Prospective

The history of the generation of ultrasound dates back 100 years to the work of F. Galton who was interested in establishing the threshold levels of hearing both in animals and in humans. He produced a whistle which generated sound of known frequencies and was able to determine that the normal limit of human hearing is around 16000 to 18000 cycles s^{-1} (16-18 kHz). The whistle is an example of an ultrasonic transducer, a device that converts one form of energy (in this case gas motion) into another (ultrasound).

The first commercial exploitation of ultrasound came after the Titanic disaster of 1912 when a competition, organized to find methods of avoiding icebergs, received a suggestion from L. F. Davidson that the distance of an iceberg from a ship could be estimated from the time lapse between emitting a sound from a ship and receiving an echo from it. From this the pulse/echo ranging technique developed to produce the depth gauge and, during the First World War, ASDIC (Allied Submarine Detection Investigation Committee) for the location of submarines. Between 1920-1960 there were improvements in pulse/echo techniques, which led to SONAR (SOUND Navigation And Ranging) and flaw detection in metals and other materials. More recent progress in electric detection measurement techniques has given us the ability to use ultrasound in

diagnostic medicine for foetal imaging. Also diagnostic ultrasound can be used for chemical analysis particularly for remote sensing in flow systems. Concurrently, the potentialities of high-intensity ultrasound, including cleaning, emulsification, drilling and the various methods of processing materials, were realized.

Power ultrasound has been used successfully in metallurgy. Ultrasonic treatment of a melt and a solidifying melt results in two beneficial effects: degassing and a reduction in grain size. The smaller grain size results from the ultrasonic fragmentation of developing dendrites of the crystallizing metal.

To date a number of researchers have carried out investigations into the effect of power ultrasound on the solidification of non-ferrous and ferrous metals and alloys. For the latter, the investigations appear largely to have been almost exclusively located in the newly formed countries from the former Soviet Union. The reason for this is almost certainly the fact that the high power necessary to treat ferrous melts, typically 2.5 to 3.5 kW per kg of material, could only be achieved (until recently) by ultrasonic technology employing magnetostrictive transducers. In the West such technology has been phased out and replaced by the more electrically efficient piezoelectric systems especially for commercial applications such as ultrasonic cleaning and plastic welding. In the countries of the former Soviet Union the older methods are still in operation and have proved particularly useful in high temperature applications. With the new freedom of information which now exists there is a marrying of the two technologies so that what might have been regarded as "dated" equipment can now be rejuvenated and made more efficient with western know-how.

6.1.2 Ultrasonic Waves

Ultrasonic waves are stress waves, and for this reason they can exist only within mass media. They are transmitted from one mass to another by direct and intimate contact between the masses. In this respect, they differ from light and other forms of electromagnetic radiation which travel freely through vacuum. In other respects, these two forms of energy obey similar laws of propagation.

Ultrasonic waves also are termed elastic waves since it is the elastic property of the medium which is responsible for the sustained vibration required for ultrasonic wave propagation. Ultrasonic waves, which have been discussed in the present study, are longitudinal waves where vibrations of the particles in the material take place in the direction of motion of the sound. The imaginary layers in the materials of propagation are subjected to alternate compressional and tensile (rarefactional) stresses by the waves (see Figure 6.1).

The broad classification of ultrasound between 18 kHz and 100 MHz has been divided into two distinct regions; power between 20 and 100 kHz and diagnostic between 1 and 10 MHz. Essentially this division arises because of the fact that a much greater sound energy can be transmitted into a system at the lower frequencies.

In acoustic cavitation, to create and grow a bubble in a non-homogeneous liquid requires a finite time and it may be that the time required is less than that available during the rarefaction cycle. For example at 20 kHz, one cycle occurs every 20000th of a second, i.e. 50 μ sec. For 20 MHz, the rarefaction period lasts only 25 nsec (1 nsec = 10^{-9} second), which may be insufficient for bubble growth. Thus as frequency increases the production of cavitation becomes less likely. This difficulty, however, can be partially compensated by applying higher intensity sound waves.

6.1.2.1 Specific Acoustic Impedance

There is similarity between the variations of ultrasonic wave characteristics and those of certain quantities used in electrical A.C. theory. Thus acoustic pressure may be regarded as being analogous to electrical voltage, particle velocity to electrical current, and particle displacement to electrical charge. Using the acoustic equivalent of Ohm's law, a quantity known as the specific acoustic impedance Z_a , equivalent to electrical impedance, may be defined as:

$$\frac{p}{u} = Z_a \quad (6.1)$$

where u and p are the particle velocity and the acoustic pressure, respectively. Like electrical impedance, Z_a is, in general, a complex quantity but, for plane progressive waves, the imaginary component disappears leaving a real quantity. This real quantity can be shown to be equal to the product of the density ρ and the velocity c of the sound for the material and is called the characteristic impedance:

$$R = \rho c \quad (6.2)$$

The value of the characteristic impedance for a given material can be seen to depend only on its physical properties and thus it is independent of the wave characteristics and the frequency. Values of characteristic impedances for a number of familiar materials are given in Table 6.1.

6.1.2.2 Acoustic Intensity

The power at any point in an acoustic field may be conveniently expressed in terms of the intensity, defined as the rate of flow of acoustical energy through unit area of an imaginary plane surface drawn about the point in question and orientated at right angles to the direction of wave-motion. The intensity "I" may be expressed in watts per square meter (W m^{-2}), and its relationships with other acoustical quantities are as follows:

$$I = \frac{p_a u_a}{2} = \frac{u_a^2 \rho c}{2} = \frac{p_a^2}{2 \rho c} \quad (6.3)$$

where u_a and p_a are the particle velocity amplitude and the acoustic pressure amplitude, respectively. The intensity should remain constant at all points within unattenuated plane progressive waves.

Table 6.1 Acoustic velocities and characteristic impedances
for some commonly used materials at room temperature

Material	Longitudinal Wave velocity (m s^{-1})	Density (kg m^{-3})	Characteristic impedance ($\text{kg m}^{-2} \text{s}^{-1}$)
Aluminium	6400	2700	1.7×10^7
Brass	3500	8600	3.0×10^7
Copper	4700	8900	4.2×10^7
Gold	3700	10500	3.9×10^7
Iron	5900	7900	4.7×10^7
Lead	1200	11300	1.4×10^7
Nickel	5600	8900	5.0×10^7
Platinum	3900	21450	8.4×10^7
Silver	3200	19300	6.2×10^7
Steel	6000	7800	4.7×10^7
Barium titanate	5000	5400	2.7×10^7
Quartz	5700	2600	1.5×10^7
Acrylic	2670	1180	3.2×10^6
Nylon	2700	1140	3.0×10^6
Perspex (Lucite)	2700	1200	3.2×10^6
Glycerol	1900	1260	2.4×10^6
Lubricating oil	1400	800	1.1×10^6
Olive oil	1400	900	1.3×10^6
Water	1500	1000	1.5×10^6
Air	330	1.3	430
Hydrogen	1300	0.90	110
Oxygen	320	1.4	450

6.1.2.3 Wave Reflection and Transmission

When plane waves strike a plane boundary separating two materials, some of the sound energy is transmitted forward and the remainder reflected backward (see Figure 6.2). The relative amounts of reflected and transmitted intensities are expressed by the reflection and transmission coefficients. It can be shown that:

$$\text{Reflection Coefficient} = \frac{(R_1 - R_2)^2}{(R_1 + R_2)^2} \quad (6.4)$$

$$\text{Transmission Coefficient} = \frac{4 R_1 R_2}{(R_1 + R_2)^2} \quad (6.5)$$

where R_1 and R_2 are the characteristic impedances for the two materials. Using the values of the characteristic impedances given in Table 6.1, reflection and transmission coefficients can be calculated for pairs of different materials. The equations show that the transmission coefficient approaches unity and the reflection coefficients to zero when R_1 and R_2 have approximately similar values. The materials are then said to be well matched or coupled. On the other hand, when the two materials have substantially dissimilar characteristic impedance, e.g. for a solid or liquid in contact with a gas, the transmission and reflection coefficients tend to zero and 100 percent, respectively. The materials are then said to be mismatched or poorly coupled.

6.1.2.4 Attenuation of Plane Waves

Ideally, the intensity of the progressive plane waves should remain constant at all distances from the source. In practice this is not so because of the attenuation of ultrasound as it progresses through the medium. Several factors contribute to attenuation. Diffraction, scattering and absorption are three major causes of attenuation. The extent of

attenuation is inversely related to the frequency. This can be shown by using the example of sound attenuation through pure water. Sound at 118 kHz is reduced to half of its intensity after passing through 1 km of water. The distance required to achieve the same reduction of intensity for 20 kHz sound is much greater, at 30 km (this explains why submarine communications are carried out at very low frequencies).

6.1.3 Standing Acoustic Waves

When sound waves are reflected, the incident and reflected waves interfere with one another and a standing wave pattern is formed. If, after a single reflection, the acoustic pressure or particle velocity amplitudes A at various distances from the reflecting surface are measured, the amplitude variation is obtained (see Figure 6.3). It is seen that the neighbouring maxima (antinode) and minima (partial nodes), respectively, are one half-wavelength apart and that the distance between a maximum and its neighbouring minimum is a quarter-wavelength. The ratio of the amplitude at the maximum to that at the minimum is called the standing wave ratio, a quantity dependent on the reflection coefficient at the boundary and the attenuation coefficient for the material. For high standing wave ratios, the amplitudes at the minima tend to zero. When this phenomenon is observed, it is said that the material is in a state of resonance (see Figure 6.4).

6.1.4 Bubble Entrapped in Standing Waves

It has long been realized that bubbles can be trapped in a liquid by a standing acoustic field. Experiments for rectified diffusion of an individual gas bubble have been carried out by acoustically levitating an air bubble in a standing wave formed in a water column. When a longitudinal wave encounters the interface of water and air (free-surface), it is reflected. Wave reflection takes place whenever waves in one medium try to enter another medium where acoustic impedances are not identical. The greater the difference between the acoustic impedances, the higher the reflectivity. It is to be noted that, the characteristic impedance of air is 430 kg/m^2 while the characteristic impedance

of water is $1.5 \times 10^6 \text{ kg/m}^2$ at room temperature (see Table 6.1). Using the equations (6.4) and (6.5), the reflection and transmission coefficients for the interface of water and air can be calculated which are 0.999 and 0.001, respectively. These coefficients show that almost all ultrasonic waves are reflected from the interface of water and air. Incident and reflected waves form a standing wave which does not propagate. In fact, a standing wave is formed when two sinusoidal waves of the same frequency (and thus the same wavelength) propagating in opposite directions are superposed. It is essentially an oscillator with a spatial spread. The stationary points are called nodes (in the resonance case), and the points of maximum amplitude are called antinodes. Therefore, the interface of water-air in the water column is a pressure node.

If a bubble is small compared to the wavelength of sound, then at any instant the translational force exerted on the bubble by the sound field (Bjerknes force) is equal to the bubble volume times the negative gradient of the acoustic pressure (see Sec. 2.8). The average acoustic force on a bubble located at a distance 'z' is then given by:

$$\langle F_A(z, t) \rangle = -\langle V(t) \nabla P(z, t) \rangle \quad (6.6)$$

where $V(t)$ is bubble volume and $P(z, t)$ is time and space varying pressure field which can be closely approximated along the axis of the column by:

$$P(z, t) = P_b - P_A(z) \cos(2\pi f t) \quad (6.7)$$

Here, P_b , $P_A(z)$ are pressure of undisturbed liquid and space-dependent amplitude of the stationary wave, respectively. The coordinate z is measured vertically along the axis of the column. For a spherical bubble of equilibrium radius R_0 and instantaneous radius $R(t)$, the magnitude of the average acoustic force, obtained by inserting Eq. (6.7) into Eq. (6.6):

$$F_A = 4 / 3 \pi R_0^3 |\nabla P_A| \langle [R(t) / R_0]^3 \cos(2\pi f t) \rangle \quad (6.8)$$

When the bubble maintains a fixed position in the column, this force is balanced by the magnitude of the average buoyancy force:

$$F_B = 4/3\pi R_0^3 \rho_l g \langle [R(t)/R_0]^3 \rangle \quad (6.9)$$

where ρ_l is the liquid density and g is the acceleration of the gravity. Upon equating these two forces one gets:

$$\frac{\langle (R/R_0)^3 \cos(2\pi f t) \rangle}{\langle (R/R_0)^3 \rangle} = \frac{\rho_l g}{|\nabla P_A|} \quad (6.10)$$

where $|\nabla P_A|$ is evaluated at the position of the bubble. The ratio of ρg to $|\nabla P_A|$ is essentially the ratio of the hydrostatic pressure gradient to the acoustic pressure gradient.

The translational force exerted by a standing wave on a bubble smaller than the resonance size is directed from regions of low-pressure amplitude to regions of high-pressure amplitude. For a bubble bigger than the resonance size, this force is directed from the regions of high-pressure amplitude to the regions of low-pressure amplitude. Therefore, in a standing wave field, a bubble moves toward pressure maxima (antinode) or minima (partial nodes) if it is smaller or larger than the resonance size, respectively.

6.2 Ultrasonic Technology

6.2.1 Ultrasonic Transducers

An ultrasonic transducer is an instrument designed to generate the disturbance from which the ultrasonic energy emanates. Therefore, any device capable of generating ultrasound is an ultrasonic transducer. The device may be a whistle, a piezoelectric plate, a magnetostrictive stack driving a piston, a diaphragm driven electromagnetically, a siren, or any of the various types of mechanical devices such as rotating eccentric. All of these methods have been used to generate ultrasonic energy. The effect, in which a voltage

impressed across two surfaces of a piezoelectric crystal induces stresses in the material, is presently the most common method of generating ultrasonic energy in commercial systems.

The performance of a transducer depends on its acoustical matching to the medium under investigation. Matching the impedance of a transducer to both the electrical circuitry and the sample is important to the success of any experiment, because if this is not achieved, then power transfer from an energy source in an electrical form will not be transmitted into the sample. This is because an impedance mismatch causes reflection of the ultrasound wave.

6.2.1.1 Magnetostrictive Transducers

Magnetostriction refers to a change in the dimension of a suitable ferromagnetic material, e.g. nickel or nickel alloy, by the application of a magnetic field. Historically magnetostrictive transducers were the first to be used on an industrial scale to generate high power ultrasound. A magnetostrictive transducer is usually in the form of a rod (or bar) acting as the magnetic core within a solenoid. Applying a varying current to the coil produces a variation in the dimensions of the bar. In typical cleaning applications the nickel core is silver brazed to the stainless steel plate, which couples the ultrasonic vibrations to the liquid. The unit is thus very resistant to mechanical damage since there is no obvious mode of degradation. Such transducers offer a very high driving force, are very robust and can routinely stand temperatures of up to 180°C. The allowable frequency shift for a typical magnetostrictive transducer is much larger than it is for a power-type piezoelectric transducer. Traditionally they are still employed in situations where continuous high powers are required in rugged processing applications, e.g. in melt degassing and metal crystallization. They have the additional property of being water-cooled. In Figure 6.5 a typical magnetostrictive transducer used for degassing of aluminium melts is shown.

The major drawback to magnetostrictive transducers is that they are not particularly efficient in terms of electrical power consumption. However, the advent of

non-metallic, ceramic-based, ferrite materials (MFe_2O_4 , M = divalent metal, e.g. Ni, Zn, or Pb) has led to an increased electrical efficiency. However, a general disadvantage of all such transducers is that their useful frequency ranges do not exceed 100 kHz.

6.2.1.2 Piezoelectric Transducers

The most common types of transducers used for both the generation and the detection of ultrasound employ piezoelectric materials. Such materials have the following two complementary properties:

(a) The direct effect - when pressure is applied across the large surfaces of the section a charge is generated on each face equal in size but opposite in sign. This polarity is reversed if tension is applied across the surfaces.

(b) The inverse effect- if a charge is applied to one face of the section and an equal but opposite charge is applied to the other face, then the whole section of crystal will either expand or contract depending on the polarity of the applied charges.

Thus on applying rapidly reversing charges to a piezoelectric material, fluctuations in dimensions will be produced. This effect can be harnessed to transmit ultrasonic vibrations from the crystal section through whatever medium it is in contact with.

Early piezoelectric devices were based on quartz transducers, but quartz is not a particularly good material for this purpose because of its mechanical properties: it is a somewhat fragile material and is difficult to machine. Three substitutes are commonly used: barium titanate ($BaTiO_3$), lead metaniobate ($PbNb_2O_6$) and the mixed crystal lead zirconate titanate. These materials cannot be obtained as large single crystals and so, instead, they are ground with binders and sintered under pressure at above $1000^\circ C$ to form a ceramic. The crystallites of the ceramic are then aligned by cooling from above the ferroelectric transition temperature in a magnetic field.

It is not possible to drive a given piece of piezoelectric material efficiently at every frequency. Optimum performance will only be obtained at the natural resonance frequency of the particular sample, and this depends upon its dimensions. To reinforce the rather fragile ceramic transducers it is normal practice to clamp piezoelectric elements

between metal blocks, which serve both to protect the delicate crystalline material and to prevent it from overheating by acting as a heat sink. Usually, two elements are combined so that their overall mechanical motion is additive. The block modifies, by sheer size, the nature of the ultrasonic vibrations generated. In this way, a rugged reliable transducer is obtained. In Figure 6.6 the construction of such a piezoelectric sandwich transducer is shown. It is generally one half-wavelength long (although multiples of this can be used). The peak to peak amplitudes generated by such systems are normally of the order of 10-20 μm and they are electrically efficient. Generally, piezoelectric devices are not suitable for continuous usage at high temperatures. This is because the ceramic material will degrade under these conditions. For continuous use under high temperature conditions a magnetostrictive device may prove to be more reliable.

6.2.2 Piezoelectric Probe Receivers (Hydrophones)

The piezoelectric probes receivers are used principally for measuring ultrasonic pressure amplitude and frequency in different parts of acoustic fields in fluids, or for determining the intensity distributions in front of transmitting transducers. The requirements of their design are that the dimensions of the sensitive element should be small compared with the wavelength (typically less than one-tenth), that the frequency response be constant over the whole of the required range, and that the sensitivity of the piezoelectric element be constant for all directions.

Ideally, for an omnidirectional response, the receiver should be spherical in shape. Cylindrical transducers, in the forms of tubes, are more easily constructed and are quite suitable if one is concerned only with measurements in a single plane. They are capable of vibrating in a number of different modes, i.e. radial, length, and wall-thickness, and there is usually enough overlap between these modes to give rise to a fairly flat response over a wide band of frequencies. Ceramic tubes of outside diameter 1.5 mm, length 1.5 mm, and wall thickness 0.3 mm are easily obtained commercially and can be used to measure intensities at frequencies of up to 100 kHz in liquids and 25 kHz in gases,

without disturbing the acoustic fields. In Figure 6.7 the schematic construction of a hydrophone with piezoelectric hollow cylinder transducer is shown.

Another type of transducer is formed out of a disc of piezoelectric ceramic that its construction is shown schematically in Figure 6.8. The disc used is 0.48 mm in diameter and 0.1 mm in thickness. The hydrophone converts acoustic power incident on its face into an electrical signal. The sensor element is polarized in the thickness direction. The undesired radial modes of vibration of the disc have effectively been eliminated using an absorbing backing material consisting of a composite of epoxy and tungsten attached to the back electrode. This type of hydrophone is suitable for the measurement of plane sine waves.

6.2.3 Types of Sonicator System

There are various types of sonicator system, which may be used for applying the ultrasonic energy to a system. Two of them, which have been used extensively, are the probe and the cleaning bath systems. It is clear that, in their construction, both types of piezoelectric or magnetostrictive transducers can be used.

6.2.3.1 Ultrasonic Probe

In order to increase the amount of ultrasonic power available, it is desirable to introduce the energy directly into the system rather than rely on its transfer through the water of a tank and then the container wall. The simplest method of achieving this would be to have the face of an ultrasonically vibrating transducer immersed in the liquid system. It is possible to amplify this vibrational amplitude by attaching a specially designed length of metal rod to the end of the transducer. This rod extension is more correctly termed a sonic horn or velocity transformer, and it not only magnifies the acoustic energy available but also allows the transducer to be kept clear since only the tip of the rod needs to be immersed in the liquid. It is the complete assembly of transducer plus horn which is referred to as an ultrasonic probe system.

6.2.3.2 Ultrasonic Cleaning Bath

The construction of an ultrasonic cleaning bath is simple. A laboratory model generally consists of a stainless steel tank of rectangular cross-section with transducers firmly attached underneath the flat base (piezoelectric transducers are normally bonded with epoxy). Some tanks also have some form of thermostatted heater. A few modern laboratory-scale models have adjustable power but these are in a minority. The frequency and power of an ultrasonic bath depends upon the type and number of transducers used in its construction. Generally, the ultrasonic power available in a bath using modern piezoelectric transducers is of quite low intensity (of the order of $1-5 \text{ W cm}^{-2}$), with an operating frequency of approximately 40 kHz. In the experimental set up (see section 6.3.1) this type of the ultrasonic bath with one operating transducer was used. It was originally provided with two transducers in which the second one was kept inactive by disconnecting its electrical power.

6.3 Experimental Investigation

In order to lend credibility to the mathematical model developed in Chapter 5, an aqueous physical model was developed. The experimental work was conducted to simulate the single bubble growth by the process of rectified diffusion. It consisted of a small water column which was placed in an ultrasonic bath. A small air bubble was injected into the water column and it was levitated by the generated standing waves. When the ultrasonic pressure amplitude was higher than the threshold pressure, the air bubble was seen to grow. The bubble-growth predictions from the mathematical model are compared with the experimental measurements.

6.3.1 Experimental Apparatus and Procedure

The schematic diagram of the experimental set up is illustrated in Figure 6.9. A transparent acrylic square column (6 cm × 6 cm × 30 cm) with wall thickness of about 3 mm was used. A square cross-section was chosen to avoid optical distortion. The column containing distilled water with a depth of around 23 cm was positioned in a stainless steel tank. The steel tank was filled with distilled water up to about 7 cm and the water acted as a coupling fluid. The coupling fluid was used to avoid the formation of an air gap. The latter would have caused a very high attenuation of the imposed ultrasound waves. It was also used to provide the possibility of varying the intensity of the transmitted sound waves into the column. The highest intensities are obtained when the column bottom is located in the coupling fluid at vertical intervals of one half-wavelength above the tank.

A standing acoustic longitudinal wave was excited in the column by a single piezoelectric transducer attached to the bottom of the tank. The piezoelectric transducer was connected to a function generator with adjustable power levels. The maximum power of the transducer was 35 W with the emitting face of about 10 cm². The intensity of the ultrasonic waves generated by the transducer was changeable from a maximum value of 3.5 W cm⁻² to ten different lower levels.

Using the value of the characteristic impedances of water and acrylic given in Table (6.1), the reflection and transmission coefficients for the interface of water and acrylic were calculated and found to be 0.131 and 0.869, respectively. It showed that most ultrasonic plane waves (87%) were transmitted into the water column through the bottom of the acrylic column.

A small air bubble was injected by a syringe connected to a modified thin needle from the top of the column. To prevent floatation of the bubble before the implementation of the acoustic waves, the bubble was held on a thin 0.2 mm diameter wire which was coated with a thin film of paraffin wax (see Figure 6.10). The initial diameter of the small bubble was measured by a scaled microscope.

The generated sine wave in water had the frequency of 38.5 kHz and had a series of minima (partial nodes) and maxima (antinodes) along the axial direction of the column. During the irradiation of the ultrasound, the air bubble was levitated at a position about 1.9 cm below the free surface of the liquid. It was observed that the distance between the two neighbouring bubbles levitated at the axial direction was around 2 cm (about one half-wavelength). The generated bubble had a radius of 0.3 mm which was larger than the resonance size. The calculated resonance bubble radius for the ultrasonic frequency of 38.5 kHz is around 0.085 mm. It was verified that the bubble was levitated near the pressure minima. The ratio of the hydrostatic pressure gradient to the acoustic pressure gradient (see Eq. 6.10) at the bubble position was computed which was about 0.002.

At first ($t = 0$), the ultrasound was turned on and simultaneously the stop watch was started. The gas bubble grew by the process of rectified diffusion of dissolved air in water since the ultrasound pressure amplitude was beyond the threshold value. During the irradiation of ultrasound, the wire was far from the air bubble. After irradiation of the ultrasound waves for a certain period of time and in order to measure the diameter of the bubble by the microscope, the wire was used again to hold the bubble. During the measurement of the bubble diameter, the ultrasound and stop watch were turned off. The sound field was then turned back on and the process was continued. In Figure 6.11, the photograph of the experimental set up is shown.

6.3.1.1 Preparation of Water (in the column)

The high concentration of dissolved air in water was maintained by bubbling air through distilled water according to the following method. The distilled water was first cooled and then put in a 2 L insulated jug. A compressed air line from the main air line in the laboratory was used through a partially opened needle valve. The air tube was connected to an air diffuser (used in a fish tank) and was placed in the distilled water inside the jug. The air was then bubbled through the liquid for a few hours.

6.3.2 Measuring System

The measuring system included systems to measure the bubble diameter, the ultrasonic pressure amplitude and frequency and the dissolved oxygen in water. A detailed description for each of the measurement systems is given in the following sections.

6.3.2.1 Bubble Diameter Measurement

In order to measure the bubble diameter, a built-in scale microscope with working distance of 79 mm (Specwell, M830-S) was used. Adjustable focus provided clear viewing of the bubble. In Figure 6.11, the microscope employed in the experimental set up is shown.

6.3.2.2 Ultrasonic Pressure Amplitude and Frequency Measurement

In order to measure the applied acoustic pressure amplitude and frequency in water, a ceramic hydrophone (Model SPRH-S-1000) was used. The hydrophone was of the needle type with a flat tip made of a ceramic disk which worked as an active element. A needle type ceramic hydrophone is suitable for monitoring negative and positive pressures and because of the small size, its effect on the acoustic field is small. Figure 6.12 shows the hydrophone employed in the present experiment. In order to compare its small size a pencil is also shown in the figure. During the measurement, the calibrated hydrophone was connected to a pre-amplifier and a digital oscilloscope (Tektronix, TDS210). By using an extension module (interface), the oscilloscope screen display was printed. In Figure 6.13 a typical print out of the oscilloscope screen is shown.

6.3.2.3 Measurement of Dissolved Oxygen in Water

The initial concentration of dissolved oxygen in water was measured using a dissolved oxygen meter (ORION-Model 810). The oxygen probe consists of an anode/cathode electrode system and a KCL based electrolyte separated from the environment by an oxygen-permeable membrane. When a polarizing voltage is imposed across the electrode it reduces dissolved oxygen at the cathode, causing a measurable current to flow. The higher the oxygen content of the sample, the more current flows. A thermistor is built into the probe measurement system and compensates for the membrane temperature. The Orion meter uses this data to calculate the dissolved oxygen content of the sample in either parts per million (ppm) or percent saturation (% Sat) whichever mode display is required and selected. The meter simultaneously displays water temperature along with the measurement results.

To measure directly the dissolved oxygen in water, the probe was dipped in the water column. During the measurement the sample was stirred with moving the probe back and forth. Another way of the measurement was using a standard 300 ml B.O.D. bottle, a funnel with a built-in magnetic stir bar and a magnetic stirrer. The BOD bottle was first filled with the water sample and then the funnel was put in the bottle. The probe was inserted into the funnel and they were all together placed on the magnetic stirrer. In Figure 6.11 the photographs of the dissolved oxygen meter and the magnetic stirrer are shown.

6.3.3 Experimental Results and Comparison with Mathematical

Model predictions

In the experiment, the initial bubble radius was 0.3 ± 0.02 mm which was measured using the microscope. By means of a needle type hydrophone connected to a pre-amplifier and a digital oscilloscope, the ultrasonic pressure amplitude and frequency were measured which were 0.9 ± 0.03 bar and 38.5 ± 0.5 kHz, respectively. The initial

concentration of dissolved air in water was measured, as mentioned earlier, which was $95\% \pm 1\%$ of the saturation value at the experimental conditions. The temperature of water inside the column was $20^{\circ}\text{C} \pm 1\%$. In Figure 6.14, the bubble growth predictions are compared with the experimental results. The time-averaged bubble radius versus time for both cases are shown. The average bubble radius and time are non-dimensionalized using the initial bubble radius and the period of the ultrasonic wave, respectively. After 5×10^6 oscillations of the transducer (after more than 2 minutes) the average bubble radius reached around 1.7 times of its initial value. The figure shows a quite reasonable overall agreement between the theoretical predictions and the experimental results. The experimental results approach the mathematical model predictions although the computed bubble growth rate was a little bit more than the experimental measurements especially at the early stage of the experiment. The difference may be justified from the analysis of the errors which is discussed in the next section.

6.3.4 Experimental Error Analysis

Errors always creep into all physical experiments, regardless of the care exerted. It is better to speak of uncertainty instead of experimental errors because the magnitude of an error is always uncertain. But the term error rather than uncertainty is used extensively. In this section we have mostly used the former definition whenever we have talked about uncertainty.

One of the types of errors comes from the apparatus or instrument construction which affects the results. Another type of errors arise due to the observer for not being consistent when estimating reading such as the amplitude or frequency on analog meters. The third type of errors result if the process involved includes certain uncontrolled or poorly controlled variables that results in changing conditions.

Most of the foregoing errors have occurred in the present experimental investigation. One of the errors was due to the bubble size measurement by the microscope during the bubble growth. Also, the bubble held on the thin wire was not of a perfect spherical shape. In the literature, bubble sizing was obtained by allowing the

bubble to rise through a known distance. Actually, for obtaining the bubble radius, measuring the time required to transverse this distance and using an approximate drag law imply many errors.

Another source of error might be due to the air absorption from the top surface in the water column. Since the bubble was far enough from the top surface of the water and the initial concentration of dissolved air in water was near saturation condition, this effect can be ignored. In general, argon gas can be blown from the upper part of the column to prevent the possible dissolution of air from the top. Although this was not done in the present experiments.

Ideally, the liquid should be clean and liquid surrounding the bubble should have the same initial concentration of dissolved gas as the bulk liquid. In practice this is not so because of the non-uniformity of the concentration of the liquid and the small size of the bubble compared to the size of the bulk liquid. In other words, the initial concentration of dissolved gas in the liquid surrounding the bubble might have differed from the initial concentration of the bulk liquid which was measured by the dissolved oxygen meter. Calibration of the hydrophone and the measurements of the ultrasonic pressure amplitude and frequency usually have some errors.

6.3.4.1 General Uncertainty in the Experimental Results

The measurements of the variables (bubble radius, concentration of dissolved gas in liquid, ultrasonic pressure amplitude and frequency, etc.) have uncertainties associated with them. The values of the material properties that were obtained from reference sources also have uncertainties. The uncertainties in the individual variables propagate into the results through a data reduction equation. Equation (6.11) is such an equation that relates the desired experimental result R (bubble radius growth) to measured variables and to quantities that were obtained from reference sources. Although some of the quantities like the gas constant for air is known with a great degree of certainty.

$$R = \frac{DC_0 \mathfrak{R} T_0}{R_0 P_0} \left[\frac{2 \left(1 - \frac{\pi^2 f^2 \rho_l R_0^2}{6\gamma P_0} \right)}{3\gamma \left(1 - \frac{4\pi^2 f^2 \rho_l R_0^2}{3\gamma P_0} \right)} \left(\frac{P_A}{P_0} \right)^2 - \frac{2\sigma}{R_0 P_0} \right] t + R_0 \quad (6.11)$$

Equation (6.11) is the mathematical expression for the rate of change of equilibrium bubble radius obtained by Eller (1972) through a perturbation solution.

In this analysis only the influence of uncertainties of the measured parameters to the experimental results are studied:

$$R = R(X_i) = R(C_0, T_0, f, P_A, R_0, t) \quad (6.12)$$

where R, C_0, T_0, f, P_A, R_0 and t are the bubble radius, initial concentration of dissolved gas in liquid, liquid temperature, ultrasonic pressure frequency and amplitude, initial bubble radius and time, respectively.

The nondimensionalized form of the uncertainty in the results is given by:

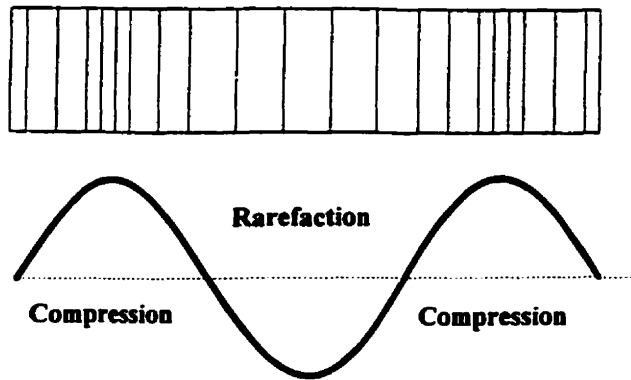
$$\begin{aligned} \frac{U_R^2}{R^2} = & \left(\frac{C_0}{R} \frac{\partial R}{\partial C_0} \right)^2 \left(\frac{U_{C_0}}{C_0} \right)^2 + \left(\frac{T_0}{R} \frac{\partial R}{\partial T_0} \right)^2 \left(\frac{U_{T_0}}{T_0} \right)^2 + \left(\frac{f}{R} \frac{\partial R}{\partial f} \right)^2 \left(\frac{U_f}{f} \right)^2 + \\ & \left(\frac{P_A}{R} \frac{\partial R}{\partial P_A} \right)^2 \left(\frac{U_{P_A}}{P_A} \right)^2 + \left(\frac{R_0}{R} \frac{\partial R}{\partial R_0} \right)^2 \left(\frac{U_{R_0}}{R_0} \right)^2 + \left(\frac{t}{R} \frac{\partial R}{\partial t} \right)^2 \left(\frac{U_t}{t} \right)^2 \end{aligned} \quad (6.13)$$

where U_R / R is the relative uncertainty of the experimental results. The factors U_{X_i} / X_i are the relative uncertainties for each variable.

Figure 6.15 shows the relative uncertainty of the experimental results obtained from using Equation (6.13) and the relative uncertainties of each variable, which were already introduced in section 6.3.3. It is noted that, for the calculation of derivatives in equation (6.13), the data reduction equation (Eq. 6.11) was used.

References

- Blitz, J., *Ultrasonics: Methods and Applications*, Butterworths & Co., 1971.
- Coleman, H. W. and Sreele, W. G, *Experimentation and Uncertainty Analysis for Engineers*, Second Edition, John Willy & Sons, Inc., 1999.
- Crum, L. A., Measurements of the Growth of Air Bubbles by Rectified Diffusion *J. Acoust. Soc. Am.*, Vol. 68, pp. 203-211, 1980.
- Ensminger, D., *Ultrasonics: Fundamentals, Technology, Applications*, Marcel Dekker, Inc., 1988.
- Gooberman, G. L., *Ultrasonics, Theory and Application*, The English Universities Press LTD, 1968.
- Holman, I. P., *Experimental Methods for Engineers*, 6th Edition, McGraw-Hill, Inc., 1994.
- Kenneth, S. S., *Ultrasound, Its Chemical, Physical and Biological Effects*, VCH Publisher, Inc., 1988.
- Kobayashi, M., Kamata, C. and Ito, K., Cold Model Experiments of Gas Removal from Molten Metal by an Irradiation of Ultrasonic Waves, *ISIJ International*, Vol. 37, pp. 9-15, 1997.
- Leighton, T., G., Lingard, R., J., Walton, A., J. and Field, J., E., Acoustic Bubble Sizing by Combination of Subharmonic Emissions with Imaging Frequency, *Ultrasonics*, Vol. 29, pp. 319-321, 1991.
- Lewin, P. A. and Chivers, R. C., Two Miniature Ceramic Ultrasonic Probes, *J. Phys., E: Sci. Instrum.*, Vol. 14, pp. 1420-1424, 1981.
- Mason, T. J., *Sonochemistry: the Use of Ultrasound in Chemistry*, The Royal Society of Chemistry Co., 1990.
- Mason, T. J., *Practical Sonochemistry*, Ellis Horwood Company, 1991.
- Mason, T. J., Power Ultrasound and Energy Efficiency in the Steel Industry, *Foundry Trade Journal*, 452p., 1994.
- Rozenberg, L. D., *High-Intensity Ultrasonic Fields*, Plenum Press, New York, 1971.



Transducer controls: Frequency

**The medium controls: Wavelength
Velocity
Attenuation**

Fig. 6.1. Sound motion in a liquid medium.

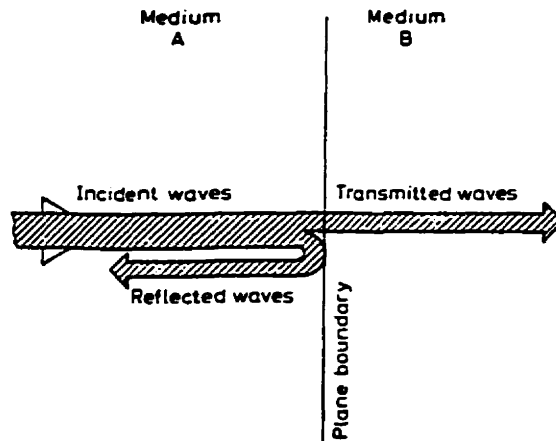


Fig. 6.2. Reflection and transmission for normal incidence at a plane boundary.

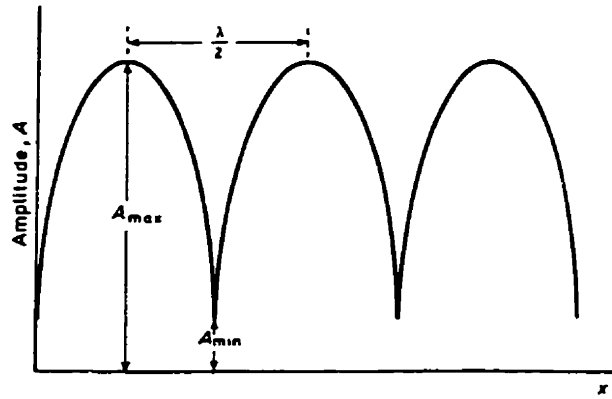


Fig. 6.3. Variation of amplitude A with distance x from the source of a stationary wave system.

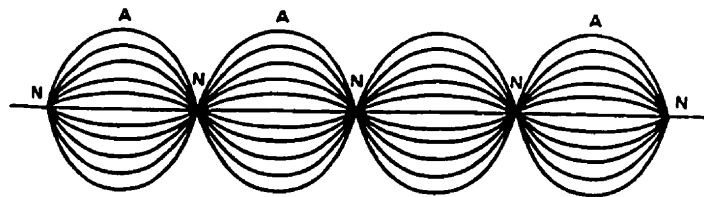


Fig. 6.4. Envelope of stationary wave pattern showing nodes N and antinodes A

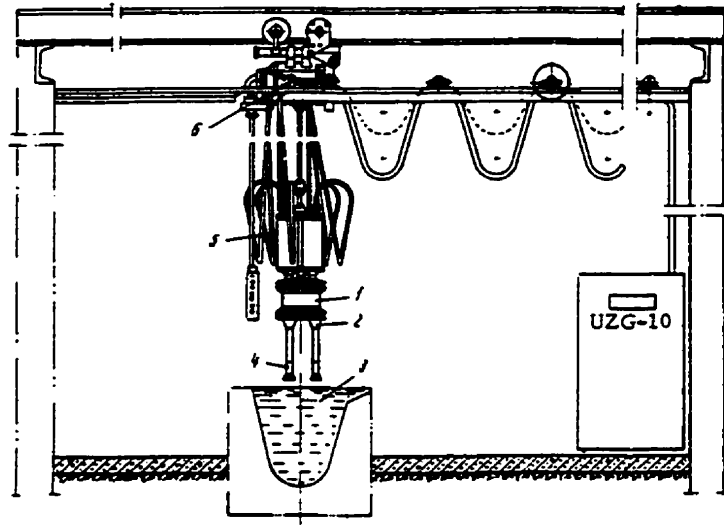


Fig. 6.5. Magnetostrictive transducer used in an ultrasonic degasifier, 1) water-cooled cell; 2) magnetostrictive transducer; 3) aluminum-melt; 4) titanate bit; 5) degassing automation block; 6) telpher.

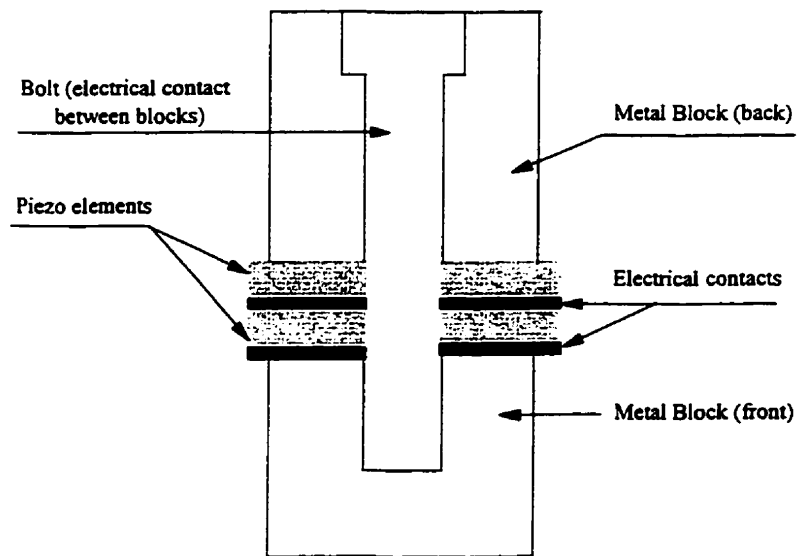


Fig. 6.6 Sandwich transducer with ceramic piezoelectric elements.

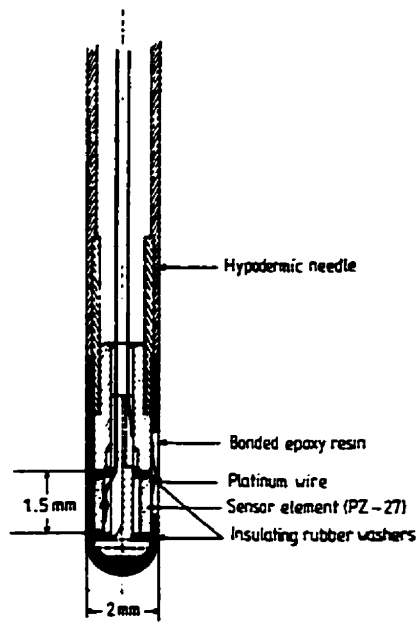


Fig. 6.7. Schematic construction of a hydrophone with a hollow piezoelectric cylinder transducer.

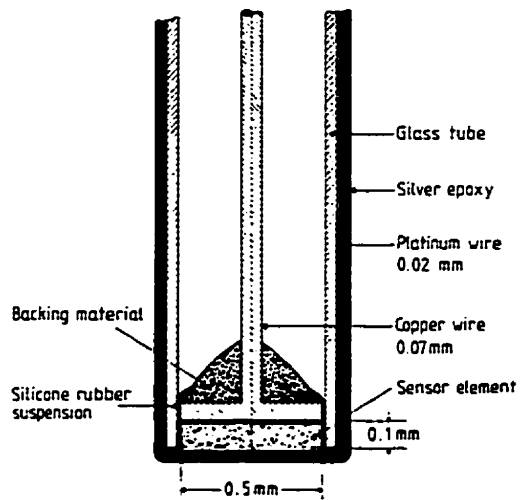


Fig. 6.8. Schematic construction of a hydrophone with a piezoelectric disc transducer.

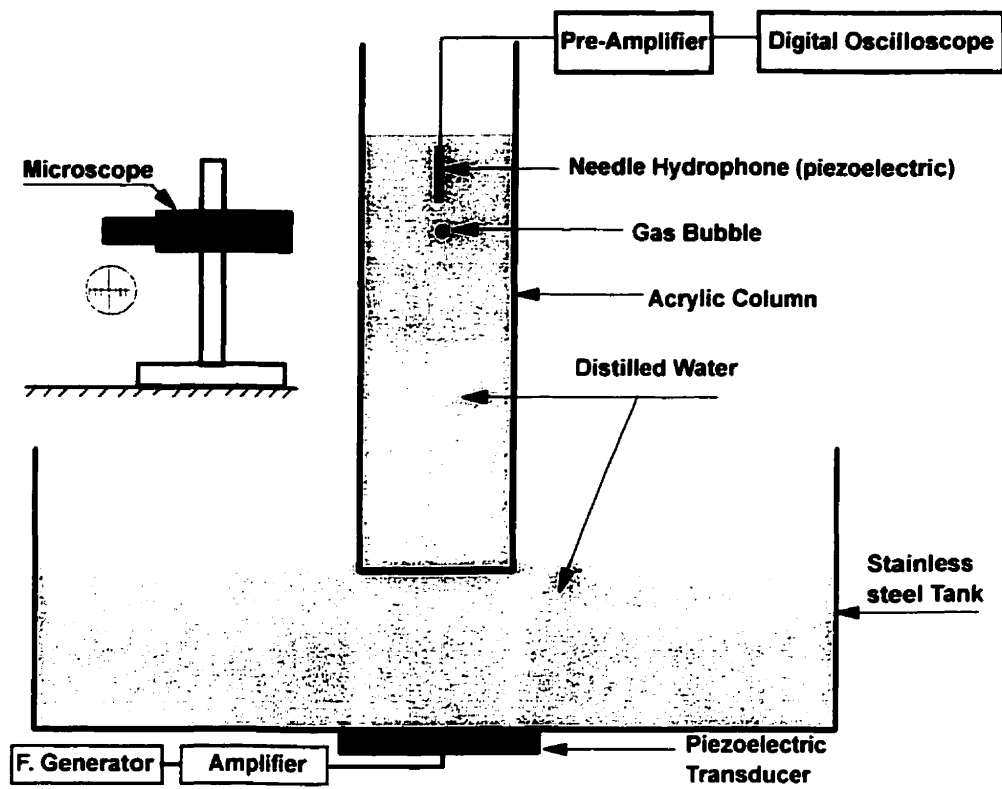


Fig. 6.9. Schematic diagram of the experimental set up

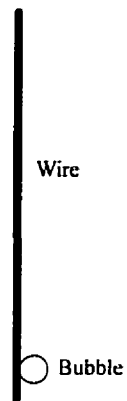


Fig. 6.10. Bubble attached to the wire coated with paraffin wax

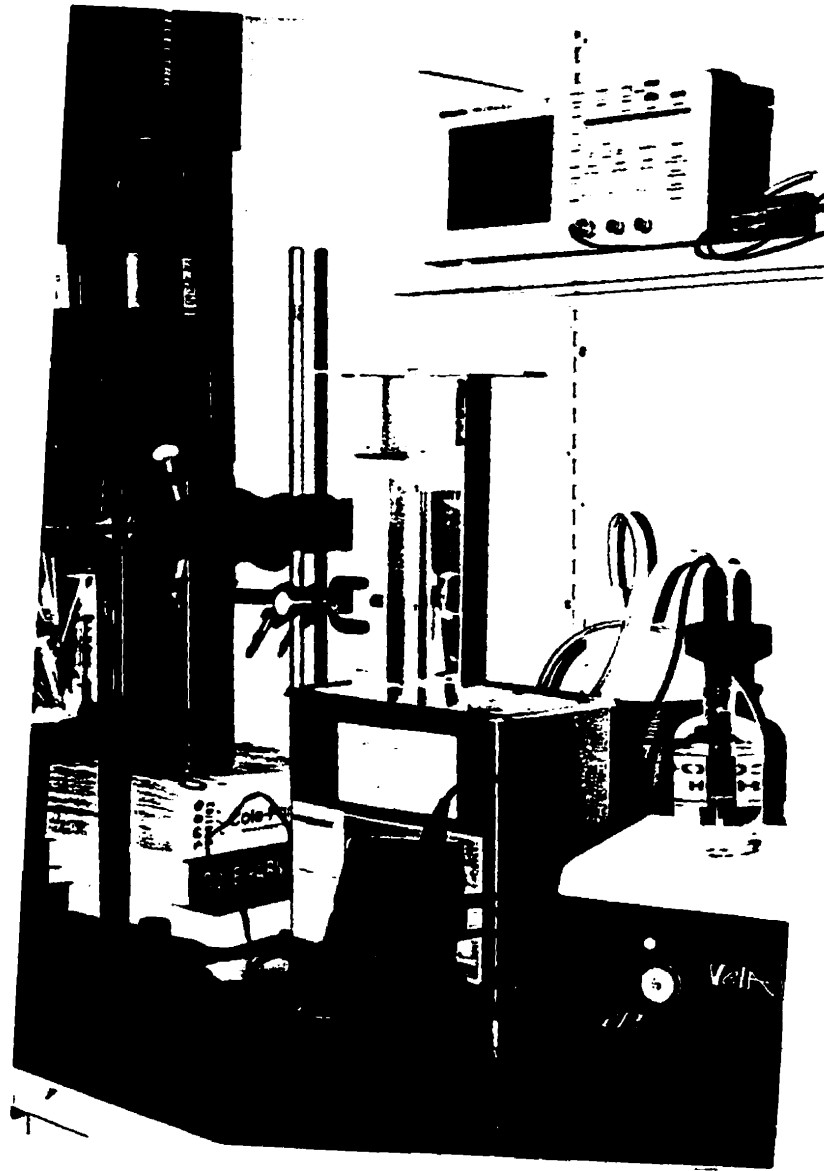


Fig. 6.11. Photograph of the experimental set up.

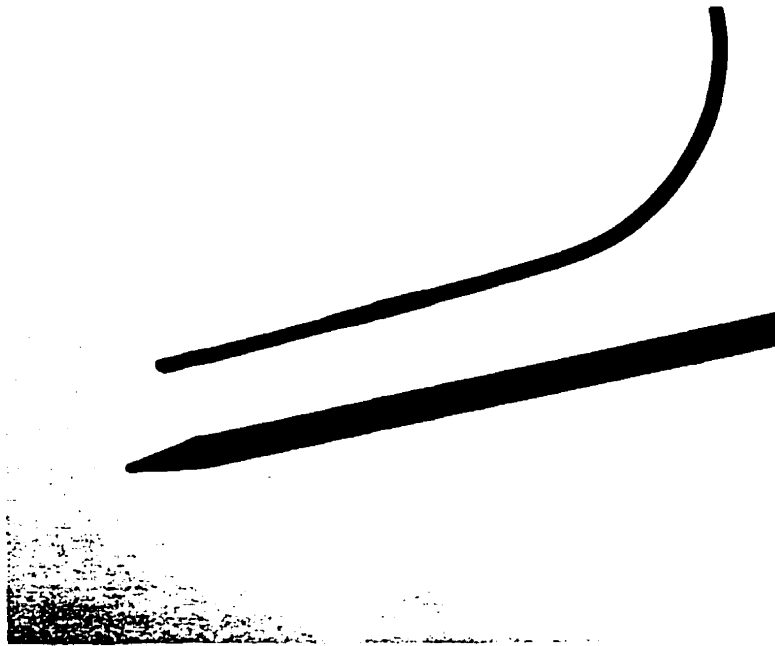


Fig. 6.12. Photograph of the needle type hydrophon.

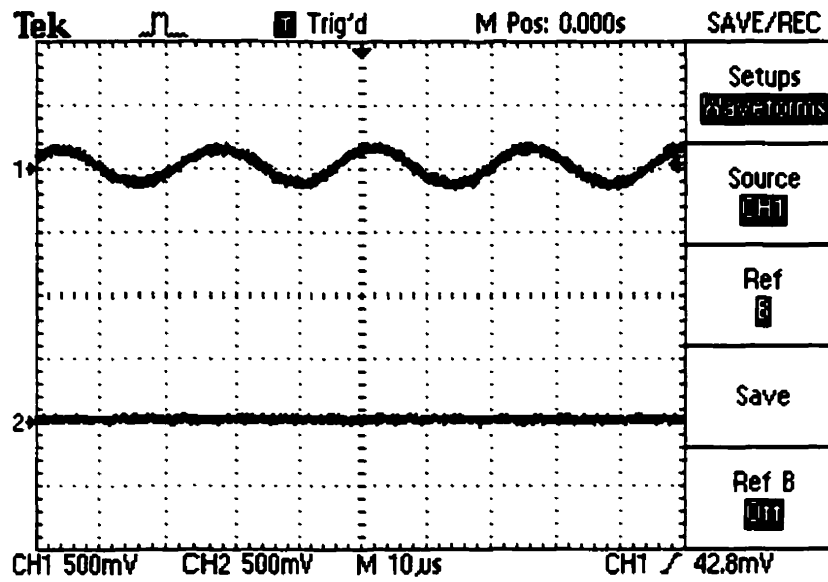


Fig. 6.13. Typical print out of the oscilloscope screen.

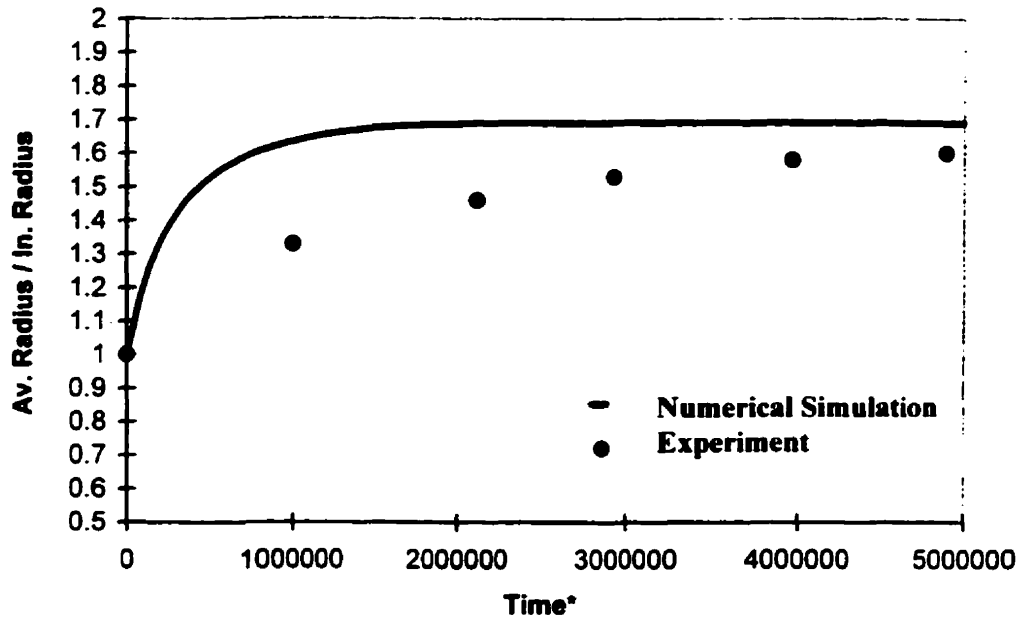


Fig. 6.14. Comparison of the mathematical model's calculations with the experimental results for the bubble growth, $P_{ap}=1.01-0.9 \sin(2\pi f t)$, $f = 38.5 \text{ kHz}$, $R_0 = 0.3 \text{ mm}$ and $C_0 = 95\% \text{ Saturation}$.

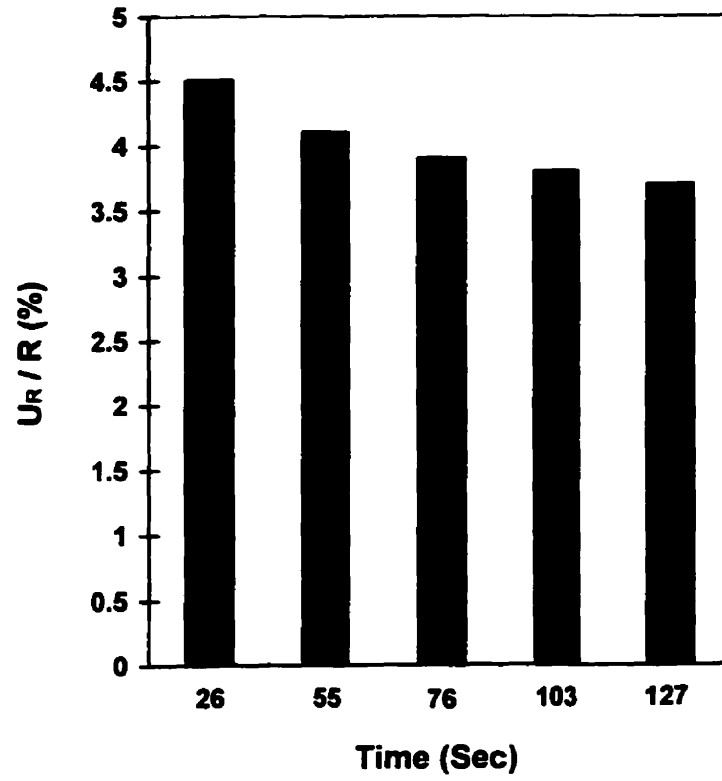


Fig. 6.15. Uncertainty in the experimental results

A NUMERICAL STUDY OF THE COMPLEX DYNAMIC BEHAVIOR OF A REACTIVE GAS BUBBLE IN A NON-REACTIVE LIQUID

7.1. Introduction

It is well known that a bubble containing a chemically reactive gas, when subjected to an impulse pressure of sufficient strength, will undergo compression and can eventually explode. In a bubbly liquid the properties of the individual phases are combined in such a way that, essentially, the liquid contains the kinetic energy and the gas contains the potential energy. If the bubble gas is a reactive mixture, heat generation by chemical reactions is superimposed on the basic bubble's dynamic behavior and unexpected hazards may occur, mostly because of the action of the accumulated high kinetic energy of the liquid. In the present work, a strong motivation for studying the reactive bubble phenomenon is that in a nuclear power plant, oxygen-hydrogen bubbles may develop in abnormally high-temperature water and can constitute an explosion hazard.

7.2. Literature Review

The first analysis of bubble dynamics of a non-reactive gas-filled cavity, under the assumption that the gas undergoes isothermal compression, was made by Rayleigh

(1917). The mechanism of the explosion of a single reactive gas bubble in a liquid was first studied by Soloukhin (1961). An experimental and theoretical investigation on a linear array of reactive bubbles was made by Hasegawa and Fujiwara (1982), who observed that the explosion of one bubble caused the next to explode, and, consequently, a sequential explosion of bubbles was produced. They studied the behavior of a single exploding gas bubble in glycerin, which was photographed by a high-speed camera and compared with theoretical calculations. Kedrinskii and Mader (1987) studied numerically a reactive bubbly liquid. They performed a numerical simulation of an equi-molar acetylene-oxygen gas bubble immersed in water. They found that the pressure threshold decreases with the increase of the initial bubble radius, while the induction period increases.

Gülhan and Beylich (1989) also performed both experimental and numerical studies of the effect of impulse pressure on a single reactive gas bubble and a nonreactive argon bubble. They found that the light emission during the explosion inside the reactive gas bubble is much more intensive than that of a collapsed nonreactive argon bubble. They showed that the temporal behavior for reactive and nonreactive gas bubbles is different. They pointed out that, for a fixed set of parameters, there is a lower limit of impulse pressure beyond which no explosion of the bubble occurs.

Prosperetti (1991) studied numerically the thermal behavior of oscillating inert gas bubbles. In his theoretical model he assumed a uniform gas pressure inside the bubble but allowed for the variations of temperature and density of the gas mixture. The uniform gas pressure assumption is valid when the magnitude of the radial velocity of a bubble interface is much less than the velocity of sound in the gas. His study showed that under a low liquid impulse pressure, the effect of conductive heat transfer inside the bubble is considerable.

Kang and Butler (1993) theoretically studied the collapse and ignition of reactive gas-filled bubbles. Their study showed that the effect of heat transfer at the gas/liquid interface can play an important role on bubble behavior especially in the later stages of bubble collapse. To account for this effect an approximate solution for the interface

temperature was developed using an assumed temperature profile for the integral form of the liquid energy balance equation.

In this chapter, a mathematical model is developed to simulate the nonlinear volume and thermal oscillation characteristics of a single reactive gas bubble in water and in glycerin. The dynamics of reactive gas bubbles with different exothermicities are studied theoretically by solving the coupled momentum and energy equations for the liquid surrounding the bubble. The effects of the exothermicity of the gas inside the bubble, the initial bubble diameter, and the liquid impulse pressure on the bubble dynamics and explosion limits are specifically investigated. It is noted that the exothermicity of the bubble gas is varied by changing the mole fraction of the mixture of stoichiometric oxygen-hydrogen with the inert gas, argon, as a diluent.

7.3. Mathematical Modelling

In order to mathematically tackle the effect of impulse pressure on a gas bubble, a number of reasonable assumptions about the physical characteristics of the phenomenon are made:

- i) The bubble remains spherical and the bubble center is motionless. Physical experiments show that the former assumption is valid for bubbles under 4 mm in diameter. The radial velocity of the bubble surface under an imposed liquid pressure field is generally high, usually of the order of 50 m/s, which is about three orders of magnitude larger than the translational velocity of the bubble in the liquid. Therefore, the bubble inside the liquid can be assumed stationary.
- ii) The gas in the bubble is thermodynamically uniform except in a thin layer near the interface.
- iii) The bubble gas is thermally perfect but calorically imperfect.
- iv) Mass transfer at the interface (condensation, evaporation, and dissolution) is neglected.

The mathematical model is based on the differential form of the following conservation equations:

1- Mass conservation equation

2- Conservation of momentum for the liquid surrounding the gas bubble

3- Conservation of energy for the gas mixture and the liquid

The above conservation equations, along with the equation of state for the gas mixture and the reaction rates for the reactants mixture, form the closed set of modeled equations. The differential form of the above equations can be written as follows:

Mass conservation equation for the gas mixture:

$$\frac{d}{dt}(\rho \frac{4}{3} \pi R^3) = 0 \quad (7.1)$$

The equation for bubble radius is based on the Trilling equation:

$$(1 - 2 \frac{\dot{R}}{C_0}) R \ddot{R} + \frac{3}{2} (1 - \frac{4}{3} \frac{\dot{R}}{C_0}) \dot{R}^2 = \frac{1}{\rho_\infty} \left[P_B(t) - P_\infty + \frac{R}{C_0} \frac{dP_B(t)}{dt} \right] \quad (7.2)$$

where P_B is the pressure exerted by liquid on the wet side of the bubble surface.

$$P_B(t) = P_s - \frac{2\sigma}{R} - \frac{4\mu\dot{R}}{R} \quad (7.3)$$

In order to obtain Eq. (7.2), Trilling (1952) assumed that the liquid surrounding the bubble is slightly compressible with constant sound speed. The derivatives of the density have been replaced by corresponding derivatives of the pressure with the help of the sound speed relation ($C_0^2 = dP / d\rho$).

The energy equation for the liquid is of the form:

$$\frac{\partial T_l}{\partial t} + \frac{R^2 \dot{R}}{r^2} \frac{\partial T_l}{\partial r} = \alpha \left(\frac{\partial^2 T_l}{\partial r^2} + \frac{2}{r} \frac{\partial T_l}{\partial r} \right) + \frac{\mu}{\rho C_p} \phi_r, \quad r \geq R \quad (7.4)$$

where the viscous dissipation function is:

$$\phi_r = 12 \frac{V_r^2}{r^2} \quad (7.5)$$

The velocity of liquid V_r can be found from the continuity equation in spherical coordinates and is:

$$V_r = \frac{R^2}{r^2} \dot{R} \quad (7.6)$$

The ideal gas equation of state is:

$$P_g = \frac{\rho \overline{\mathcal{R} T_g}}{M_w} \quad (7.7)$$

For the modeling of the chemical reaction of the gas mixture, a two-step reaction model based on the Korobeinkov induction-exothermic model (1972) is used. Therefore, the reaction rate $\dot{\omega}$ is split into two stages:

i) Nonexothermic induction reaction; the rate of reaction is given by:

$$\dot{\omega}_1 = \frac{d\eta}{dt} = -\frac{1}{\tau_{ind}} = -a_1 \rho \exp\left(-\frac{e_1}{\mathcal{R} T_g}\right) \quad (7.8a)$$

ii) Exothermic reaction; the rate of reaction is given by:

$$\dot{\omega}_2 = \frac{d\beta}{dt} = \begin{cases} 0 & \text{for } \eta > 0 \\ -a_2 P_g^2 \left[\beta^2 \exp\left(-\frac{e_2}{\mathcal{R} T_g}\right) - (1-\beta)^2 \exp\left(-\frac{e_2 + q}{\mathcal{R} T_g}\right) \right] & \text{for } \eta \leq 0 \end{cases} \quad (7.8b)$$

The overall energy balance for the bubble gas is given by:

$$\frac{dE}{dt} = \dot{Q}_p - \dot{Q}_1 - \dot{W} \quad (7.9)$$

where

$$E = \rho \nabla C_v T_g \quad (7.10)$$

$$\dot{W} = P_B \frac{dV}{dt} \quad (7.11)$$

$$\dot{Q}_1 = -4\pi R^2 K_1 \left. \frac{\partial T_1}{\partial r} \right|_{r=R} \quad (7.12)$$

$$\dot{Q}_p = \nabla \rho q \dot{\omega}_2 \quad (7.13)$$

Here, \dot{W} is the rate of work done on the gas bubble during the collapse of the bubble or is the rate of work done against the pressure in the liquid during the bubble growth. Also, in the above equation, P_b is the liquid pressure at the bubble boundary, \dot{Q}_l is the rate of heat loss between the gas bubble and the surrounding liquid, and \dot{Q}_p is heat production rate, respectively.

7.3.1. Transformed and Non-dimensional Equations

For the numerical work, it is convenient to have a fixed rather than a moving boundary of the bubble. Therefore, the governing equations are transformed using a suitable variable (ζ) that “freezes” the moving boundary of the bubble. Also, in order to decrease the number of parameters and minimize computational errors, the governing equations are non-dimensionalized. The transformed and non-dimensional forms of the mathematical model equations are:

$$\bar{\rho} = -3 \frac{\bar{R}}{\bar{R}} \quad (7.14)$$

$$\begin{aligned} \left(1 - 2 \frac{\bar{R}}{\bar{C}_0}\right) \bar{R} + \frac{3}{2} \left(1 - \frac{4}{3} \frac{\bar{R}}{\bar{C}_0}\right) \frac{\bar{R}^2}{\bar{R}} = \frac{1}{M^2} \frac{\bar{P}_b - \bar{P}_\infty}{\bar{R}} - \frac{1}{We} \frac{1}{\bar{R}^2} - \frac{1}{Re} \frac{\bar{R}}{\bar{R}^2} + \frac{1}{M^2 \bar{C}_0} (\bar{\rho} \bar{T}_g + \bar{T}_g \bar{\rho}) \\ + \frac{1}{We} \frac{\bar{R}}{\bar{C}_0 \bar{R}^2} - \frac{1}{Re} \frac{1}{\bar{C}_0} \left(\frac{\bar{R} \bar{R} - \bar{R}^2}{\bar{R}^2} \right) \end{aligned} \quad (7.15)$$

$$\bar{R}^2 \frac{\partial^2 \bar{T}_l}{\partial \bar{t}^2} = \alpha \cdot \frac{\partial^2 \bar{T}_l}{\partial \zeta^2} + \left(-\frac{\bar{R} \bar{R}}{\zeta^2} + \bar{R} \bar{R} \zeta + \frac{2\alpha}{\zeta} \right) \frac{\partial \bar{T}_l}{\partial \zeta} + 12\beta \cdot \frac{\bar{R}^2}{\zeta^6} \quad (7.16)$$

$$\bar{T}_s = -\frac{t_0 q \dot{\omega}_2}{C_v T_0} - \frac{3 \bar{R} \bar{T}_g \bar{R}}{C_v M_w \bar{R}} + \frac{6 \sigma}{T_0 \rho_0 R_0 C_v} \frac{\bar{R}}{\bar{R}^2 \bar{\rho}} + \frac{12 \mu}{\rho_0 t_0 T_0 C_v} \frac{\bar{R}^2}{\bar{R}^2 \bar{\rho}} + \frac{3 K_1 t_0}{C_v \rho_0 R_0 \bar{\rho} \bar{R}} \frac{\partial \bar{T}_l}{\partial \zeta} \Big|_{\zeta=1} \quad (7.17)$$

$$\bar{P}_g = \bar{\rho} \bar{T}_g \quad (7.18)$$

where $\frac{1}{Re} = \frac{4\mu t_0}{\rho_1 R_0^2}$, $\frac{1}{We} = \frac{2\sigma t_0^2}{\rho_1 R_0^3}$, $\frac{1}{M^2} = \frac{t_0^2 P_0}{\rho_0 R_0^2}$

$$\zeta = \frac{r}{R(t)}, \quad \alpha^* = \frac{\alpha t_0}{R_0^2}, \quad \beta^* = \frac{\mu}{\rho_1 C_p T_0 t_0} \quad (7.19)$$

$$\bar{t} = \frac{t}{t_0}, \quad \bar{R} = \frac{R}{R_0}, \quad \bar{\dot{R}} = \frac{\dot{R} t_0}{R_0}, \quad \bar{T}_g = \frac{T_g}{T_0}, \quad \bar{T}_1 = \frac{T_1}{T_0}$$

$$\bar{P} = \frac{P_g}{P_0}, \quad \bar{\rho} = \frac{\rho}{\rho_0}, \quad \bar{C} = \frac{C_0 t_0}{R_0}$$

The initial conditions for the set of equations are:

$$\bar{t} = 0$$

$$\bar{R} = 1, \quad \bar{\dot{R}} = 0, \quad \bar{\rho} = 1, \quad \bar{P} = 1, \quad \eta = 1, \quad \beta = 1, \quad \bar{T}_g = 1, \quad \bar{T}_1 = 1 \quad (7.20)$$

The non-dimensional thermal boundary layer thickness in the liquid is of the order:

$$\frac{\delta_t}{R_0} \approx \frac{1}{\sqrt{Pe}} \quad (7.21)$$

where Pe is the pecelet number

$$Pe = \frac{\dot{R} R_0}{\alpha_1} \quad (7.22)$$

Taking into account the order of magnitude of the variables in Eq. (7.22), $\dot{R} \approx 50$ m/s, $R_0 \approx 2.0 \times 10^{-3}$ m and $\alpha_1 \approx 1.0 \times 10^{-7}$ m²/s, and putting their values in Eq. (7.21) one can show that:

$$\frac{\delta_t}{R_0} \approx 10^{-3} \quad (7.23)$$

From the above estimation the number of grid points in the surrounding liquid was taken to be 10 equidistant grid points with a non-dimensional inter-grid distance of 10^{-4} . To ensure that the results were not sensitive to the number and distribution of grid points, numerical tests were performed with various numbers of equidistant grid points above 10

and the results were found to be insensitive (varied less than 0.1 %) to the inter-grid distance below 10^{-4} .

7.3.2. Initial Conditions

Initially, the bubble is at rest and is in equilibrium with the surrounding liquid. In this study, the following equations are used for the equilibrium condition:

$$P_0 = 0.1 \text{ MPa}, \quad T_0 = 298 \text{ K}$$

$$\rho_0 = \frac{P_0 M_w}{\mathfrak{R} T_0}, \quad t_0 = \pi R_0 \sqrt{\frac{\rho_l}{3\gamma P_0}} \quad (7.24)$$

For the calculation of the characteristic bubble collapse time t_0 the half period of linearized oscillation due to a small perturbation around $P_0 = 0.1 \text{ MPa}$ is used, where

$$\gamma = C_p / C_v \quad (7.25)$$

7.3.3. Boundary Conditions

The boundary conditions for equation (7.16) are:

$$1 \leq \zeta \leq 1.0011$$

$$\bar{T}_l = \bar{T}_{int} \quad \text{for } \zeta = 1 \quad (7.26)$$

$$\bar{T}_l = 1 \quad \text{for } \zeta \geq 1.0011$$

Note that for the calculation of the heat flux at the interface the energy equation for liquid (Eq. 7.16) is solved numerically using the coordinate ζ that “freezes” the moving boundary of the bubble.

The interface temperature (T_{int}) is obtained approximately from the interfacial boundary condition, which states that the rate of heat conducted from the gas side into the

gas-liquid interface is equal to the rate of heat conducted out at the liquid side of the interface. Figure 7.1 shows schematically how the interface temperature T_{int} is obtained. More details about the temperature profile at the phase boundary are available in the paper published by Naji Meidani and Hasan (1997).

$$K_g \left(\frac{T_g - T_{int}}{\delta_g} \right) \approx K_l \left(\frac{T_{int} - T_0}{\delta_l} \right) \quad (7.27)$$

$$\delta_i \approx \sqrt{\alpha_i \Delta t} \quad , \quad i = g \text{ or } l$$

where δ is the thermal boundary layer thickness, α is thermal diffusivity ($K / \rho C_p$) and Δt is a characteristic time (e.g., t_0) common to the gas and the liquid.

Putting the δ_g and δ_l in Eq. (7.27), one can easily show:

$$T_{int} \approx \frac{T_g + T_0 \sqrt{\frac{(K\rho C_p)_l}{(K\rho C_p)_g}}}{1 + \sqrt{\frac{(K\rho C_p)_l}{(K\rho C_p)_g}}} \quad (7.28)$$

For the calculation of the temperature gradient at the interface, which appears in the energy balance equation, a second-order forward difference discretization method is applied using three equispaced points, namely T_{int} , T_1 , and T_2 . Therefore, the gradient of temperature at the bubble interface can be written in a discretized form as:

$$\left. \frac{\partial \bar{T}_1}{\partial \zeta} \right|_{\zeta=1} = \frac{1}{\Delta \zeta} \left(-\frac{1}{2} \bar{T}_2 + 2\bar{T}_1 - \frac{3}{2} \bar{T}_{int} \right) \quad (7.29)$$

The relationship between the liquid pressure at transducer location (in a shock tube) and P_∞ which appears in Equation (7.15) is:

$$P_{tdc} = P(t)|_{\text{transducer}} = P_{\infty} + \frac{P_1}{r_m} \left(2R\dot{R}^2 + R^2\ddot{R} - \frac{R^4\dot{R}^2}{2r_m^3} - \frac{2R^3\dot{R}^3 + R^4\dot{R}\ddot{R}}{C_0 r_m^2} \right) \quad (7.30)$$

It is noted that R must be evaluated at $t - r_m / C_0$ where r_m is the distance between the transducer location and the bubble position in the shock tube.

7.4. Numerical Solution Method

The mathematical model forms a set of coupled, highly nonlinear differential equations (Eqs. 7.14-7.18). Due to significantly different time scales in the mathematical model the problem is stiff. Therefore the modified Gear method, which is good for solving a set of nonlinear, stiff, ordinary differential equations, is applied. The code is based on a variable-step, variable-order backward differentiation formula (BDF) method of order 1 to 5. It starts the integration with a first order method and as the integration proceeds, automatically adjusts the method order (and the step size) for optimal efficiency while satisfying prescribed accuracy requirements. The integration method is a step-by-step method and starts with the known initial conditions. At each step, the method employs a predictor-corrector scheme, wherein an initial guess for the solution is first obtained and then the guess is progressively improved upon by iteration until the iteration converges, that is, further iteration produces little or no change in the solution.

Note that Eqs. 7.14, 7.15 and 7.17 are ordinary differential equations, while Equation (7.16) is a partial differential equation. In order to solve Eq. (7.16) by the modified Gear method, it was discretized explicitly using the central difference scheme. The discretized form of Eq. (7.16) was written for ten equidistant grid points having a non-dimensional inter-grid distance of 10^{-4} . Thus, at each time step, Eqs. 7.14, 7.15 and 7.17, along with the 10 discretized equations, representing temperatures at 10 grid points from the boundary of the bubble to a non-dimensional distance of 10^{-3} into the liquid were simultaneously solved using the Gear scheme. For the set of stiff ordinary

differential equations the independent variable is time and the dependent variables (unknowns) are:

$$R, \dot{R}, \rho, \eta, \beta, T_g, P, (T_l)_j \quad j = 1 \text{ to } n$$

where “n” is the number of grid points employed in the radial direction. Initial conditions for the gas bubble were introduced in Eq. (7.20). Initial and boundary conditions for the liquid energy balance equation are:

$$\text{I. C. } \{\bar{T}_j(j = 1, n) = 1 \quad \text{at } \bar{t} = 0 \quad (7.31)$$

$$\text{B. Cs. } \begin{cases} \bar{T}_{(\zeta=1, i)} = \bar{T}_i \\ \bar{T}_{n+1} = 1 \end{cases} \quad \text{at } \bar{t} \neq 0$$

7.5. Results and Discussion

The ignition of chemically reactive gases in a bubble can occur upon bubble compression if the liquid impulse pressure is of sufficient strength. This is due to the fact that a rapid pressure pulse causes the bubble to undergo essentially adiabatic compression, resulting in a temperature rise up to the ignition point of the gas mixture. The goal of the present study is to clarify the effects of the exothermicity of the gas mixture, the initial bubble diameter and the liquid impulse pressure on bubble behavior inside water and glycerin. The chemical composition of a gas mixture is a useful parameter for classifying the explosion hazards of non-reactive liquids containing reactive gas bubbles of a specific size that are subjected to impulse pressure loadings. In order to investigate this issue properly, stoichiometric oxygen-hydrogen gas mixtures are considered with different ratios of argon as a diluent. In Table 7.1, input parameters used in computations are shown. For determining the chemical thermodynamics of different reactive gas mixtures the STANJAN (Stanford university V3.93) package was used. The rate constants for a diluted stoichiometric oxyhydrogen mixture were selected from the

work of Taki et al. (1978). For the temperature dependence of gas properties in polynomial form the reader is referred to Andrews et al. (1981).

Table 7.1. Input parameters for computations

Parameter [unit]	Glycerin	Water
α [m^2/s]	0.95×10^{-7}	1.47×10^{-7}
C_p [$\text{J}/(\text{kg}\cdot\text{K})$]	2427.0	4179.0
ρ_l [kg/m^3]	1260.0	997.0
μ [$(\text{N}\cdot\text{s})/\text{m}^2$]	1.49	1.002×10^{-3}
σ [N/m]	0.063	0.0715
C_0 [m/s]	1986.0	1500.0
K [$\text{W}/(\text{m}\cdot\text{K})$]	0.286	0.613
T_0 [K]	298.0	298.0
P_0 [MPa]	0.1	0.1
$\bar{\mathcal{R}}$ [$\text{J}/(\text{kg}\cdot\text{mole}\cdot\text{K})$]	8314.5	8314.5
a_1 [$\text{m}^3/(\text{kg}\cdot\text{s})$]	3.0×10^8	3.0×10^8
a_2 [$\text{m}^4/(\text{N}^2\cdot\text{s})$]	1.5×10^{-5}	1.5×10^{-5}
$e_1/\bar{\mathcal{R}}$ [k]	9800.0	9800.0
$e_2/\bar{\mathcal{R}}$ [k]	2000.0	2000.0

Figures 7.2-7.29 are plotted to portray the effects of exothermicity of the gas mixture, the initial bubble diameter, the liquid impulse pressure profile and viscosity of the liquid on ignition threshold and bubble dynamics. In the combustion model [Equation (7.8a,b)] the value of $\eta = 0$ marks the ignition point, which is the end of the induction period and the start of the exothermic reaction. If a bubble undergoes an ignition, there will be a sharp increase and subsequent rapid fall of temperature of the gas in the bubble. In order to have a better understanding of the exothermicity effects, the strength of the external liquid impulse pressure is also varied. The liquid impulse pressure may have different shapes. It can be assumed in the form of an instantaneous jump of the liquid pressure (at $t = 0$) to a specified level that is sustained for the duration of the event. In other words, the impulse pressure can be modeled as a step function when its duration is much longer than the period of the radius oscillation cycle of the bubble. Also, the liquid impulse pressure may have a gaussian profile. One should note that in a shock tube

experiment, the liquid impulse pressure is measured by a pressure transducer located at the shock tube wall.

7.5.1 Sustained Liquid Impulse Pressure

In all figures reported in this section, the bubble radius has been non-dimensionalized with the initial radius. In the figures, where the temporal variations of bubble radius and the temperature of the bubble are provided, one notes that the thermal oscillation cycle is opposite to the radius oscillation cycle of the bubble. This is to be expected theoretically. Under an imposed impulse pressure, with the compression of the bubble, the temperature within the bubble must rise due to compression work on the bubble.

In Figures 7.2-7.7 the bubble is assumed to have an initial diameter of 5 mm. In Figure 7.2 the history of the gas temperature within the bubble under 0.8 MPa sustained liquid pressure profile is shown. The gas mixture is a stoichiometric oxygen-hydrogen with the remaining 90% by volume of argon as a diluent. In order to get a clear view of the temperature history along with the bubble size the temporal bubble radius profile is also superimposed. The figure shows that liquid pressure surrounding the reactive bubble is high enough to compress the bubble to the ignition point. It is noted that the ignition of the reactive gas mixture occurs after the first compression cycle. The gas temperature inside the bubble sharply increases up to about 2420 K in a few microseconds. The bubble expands to about 1.2 times its initial radius in order to release the thermal energy, which is generated due to the reaction and compression work, in the form of expansion work. As the bubble starts to expand the gas temperature and the gas pressure decrease rapidly due to the increase in gas volume. For the case shown in Figure 7.2, the period of pulsation is around 220 μsec .

Figure 7.3 shows the history of bubble radius and gas temperature under 0.4 MPa sustained pressure. The ignition of the gas mixture occurs near the end of the second bubble compression cycle. Note that in the first compression cycle the bubble reaches about 900°K, which is lower than the ignition temperature. The maximum bubble radius

after explosion for this condition is larger than in the previous case due to the lower sustained imposed liquid pressure. It is to be recognized that the sustained liquid pressure acts as a retarding force during the bubble's expansion cycle. In Figure 7.4 the liquid pressure is considered to be 0.2 MPa. The gas inside the bubble attains a maximum temperature of 510°K, which is far lower than the ignition temperature. It is to be noted that in the present analysis the bubble was assumed to attain a uniform temperature instantaneously during its oscillation. In other words it was assumed that no temperature gradient develops within the bubble except at the thin thermal boundary layer near the interface.

In Figures 7.5-7.7 the history of gas temperature within the bubble, along with the bubble size for a gas mixture with more exothermicity, 70% Ar + 30% (2H₂+O₂), are shown. In Figure 7.5 the bubble is compressed to about 42 % of its original size under 0.8 MPa imposed liquid pressure. The gas temperature within the bubble reaches the ignition point near the end of the first compression cycle. After explosion the bubble expands to about 1.4 times the initial radius. The gas temperature within the bubble rapidly increases to around 3310°K, and the period of radial oscillation reaches around 260 μsec. Figure 7.6 shows the history of gas temperature and bubble radius for a 0.4 MPa sustained liquid pressure. The ignition of the gas mixture occurs near the end of the third bubble compression cycle. Note that in the first and second compression cycles the gas temperature within the bubble reaches about 840°K, which is lower than the ignition temperature. The maximum bubble radius after explosion for this condition is larger than in the previous case due to less strength of the imposed liquid pressure. In Figure 7.7 the bubble behavior under 0.2 MPa liquid pressure is shown. Due to the insufficient strength of the sustained liquid pressure the gas mixture attains a maximum temperature of only 495°K, which is well below the ignition temperature. Therefore, the bubble radius never exceeds its initial value.

Another case of interest is the reactive gas bubble with an initial diameter of 2.5 mm. The gas mixture is a stoichiometric oxygen-hydrogen with 70% argon as a diluent. Figures 7.8-7.10 are plotted to show the behavior of a gas bubble with smaller (half) diameter compared to the previous cases, and under different liquid impulse pressures. In

Figure 7.8 the liquid pressure is 0.8 MPa, which is sufficient to compress the bubble to the ignition point. After explosion the bubble gas temperature sharply increases to around 3305°K and the bubble rapidly expands to about 2.7 times of its initial volume. It is noted that the nondimensional bubble volume is equal to the cubic of the nondimensional bubble radius.

Figure 7.9 shows the history of gas temperature and bubble radius under a 0.4 MPa sustained liquid pressure profile. It is interesting to note that the ignition of the gas bubble occurs not at the first cycle but near the end of seventh compression cycle. The comparison of Figures 7.6 and 7.9 indicates that with the decrease in the initial bubble diameter, the liquid threshold pressure for bubble explosion increases. In Figure 7.10 the history of gas temperature along with bubble radius under 0.2 MPa liquid pressure are shown. The gas mixture within the bubble attains a maximum temperature around 490°K, which is well below the ignition temperature.

A comparison of Figures 7.4 and 7.7 shows that the gas temperatures are well below the ignition point. In these figures the liquid impulse pressure is the same but the exothermicity is different. They show that the maximum value of the gas temperature decreases with increasing exothermicity of the gas mixture. It is to be noted that a higher exothermicity means a low argon / oxygen-hydrogen ratio. Therefore, due to the relatively low heat capacity of argon compared to that of oxygen and hydrogen, increasing the exothermicity (decreasing the argon ratio) results in a decrease in the maximum gas temperature.

Figures 7.2-7.7 indicate that, with increasing exothermicity, the threshold pressure increases because of the relatively low heat capacity of argon. Figures 7.2 and 7.5 demonstrate that with increasing exothermicity the maximum bubble radius increases and the period of oscillation becomes longer. This is due to the release of a relatively greater amount of thermal energy upon the reaction of gases within the bubble. As time progresses the bubble continues to oscillate with a small damping effect due to the relatively low viscosity of water.

Figures 7.5 and 7.8 show that with a decrease in the initial bubble diameter, the period of bubble oscillation decreases. The period of bubble radius oscillation in Figure

7.5 is 260 μsec , while the period of pulsation in Figure 7.8 is 125 μsec . It can be seen also from these figures that for the smaller bubble, the bubble pulsations are more damped. The damping effect is due more to using the compressible (acoustic) bubble dynamics equation, which is more effective for the smaller bubble with the higher frequency of oscillations.

Figures 7.11-7.13 are plotted to demonstrate the effects of viscosity of liquid on bubble dynamics and bubble explosion limit. In this regard, the liquid is changed from water to glycerin because of the high viscosity of glycerin (1500 times as large as that of water). In Figure 7.11 the history of bubble radius and gas temperature under a sustained liquid pressure of 0.2 MPa are shown. The initial bubble radius is 2.5 mm and the gas mixture is a stoichiometric oxygen-hydrogen with 70% argon as a diluent. As one can see, the liquid impulse pressure is below the threshold pressure to initiate the reaction. Comparison of Figure 7.11 with Figure 7.10 clearly shows the effect of viscous damping on the bubble radius oscillations. In the case of using glycerin, the amplitude of the radius oscillation cycle decreases with a high rate of decay.

The history of bubble radius under different sustained liquid pressures of 0.8 MPa (case A), 0.4 MPa (case B), and 0.2 MPa (case C) are shown in Figure 7.12. The initial bubble diameter is 5 mm and the gas is a stoichiometric mixture of oxygen-hydrogen (10%) with 90% argon as a diluent. For the case of A = 0.8 MPa, the calculated bubble radius shows that the ignition occurs at near the end of the first collapse cycle. Then the bubble rapidly expands to about 1.7 times of its initial volume. For the case B (0.4 MPa), as shown in the figure, the explosion is not initiated at the first cycle but it occurs at the second cycle. Then the bubble expands to about 2.2 times of its initial volume, which is more than the previous case A. This is due to the fact that higher sustained liquid pressure suppresses the bubble expansion more. Figure 7.12 also shows that under the sustained liquid pressure of 0.2 MPa (case C), no explosion occurs and the bubble behaves like a nonreactive gas bubble. For the same bubble size and exothermicity as Figure 7.12, the calculated threshold pressure for explosion (explosion limit) was found to be 0.37 MPa and occurred at the second and third compression cycles while the liquid was water and glycerin, respectively. Comparison of Figure 7.12 with Figures 7.2-7.4 shows that the

viscous damping affects the bubble radius history and the bubble explosion limit. Decrease of the amplitude of bubble radius oscillations and time-lag of the explosion are the results of the viscous damping effects.

The history of bubble radius for a bubble with the initial diameter of 2.5 mm is shown in Figure 7.13. The other conditions correspond to Figure 7.12. It shows that the bubble explosion is only initiated for the bubble under the sustained liquid pressure of 0.8 MPa. The threshold pressure to initiate the reaction for this size of bubble (2.5 mm diameter) was 0.41 MPa. Also, the calculated threshold pressure for the bubble with the initial diameter of 2 mm was 0.43 MPa. It is seen that as the initial bubble diameter decreases, the threshold pressure for explosion (explosion limit) increases.

7.5.2 Gaussian Liquid Impulse Pressure

In general, the dynamic response of a reactive gas bubble is dependent on the liquid pressure history, bubble size, properties of the fluid medium, and initial conditions. In Figures 7.14-7.27 the applied liquid pressure has gaussian profiles with peak values of 1.0 and 0.5 MPa and rise times of 0.2 and 0.1 msec. The rise time is the time lapse that the liquid pressure takes to reach from the base pressure (atmospheric pressure) to the peak pressure. The reactive gas mixtures within the bubble are 90% Ar +10% (2H₂+O₂) and 70% Ar +30% (2H₂+O₂). The initial bubble diameters are considered to be 2.5 and 5 mm. The history of bubble radius and gas temperature for each different bubble size and exothermicity of the gas mixture under different applied liquid pressure profiles are shown in these figures. It is noted that water and glycerin are modeled as the liquid surrounding the bubble.

Figure 7.14 shows the history of bubble radius and gas temperature for a 5 mm bubble in glycerin. The gas within the bubble is a mixture of 90% Ar +10% (2H₂+O₂). The applied liquid pressure has a gaussian profile with a rise time of 0.1 msec and a peak value of 0.5 MPa as shown in the figure. The calculated results show that the minimum bubble radius coincides with the maximum gas temperature. The gas temperature within the bubble increases at the end of the first collapse phase and reaches around 680°K,

which is below the ignition point. After the compression, the bubble expands and its volume increases to more than 2.7 times of its initial volume due to the characteristics of the gaussian liquid pressure profile. Effect of the liquid pressure on the bubble is similar to the action of a weight on a spring. When the weight is eliminated, the compressed spring rapidly expands. Figure 7.15 shows the history of bubble radius and gas temperature for the same conditions as Figure 7.14 but the rise time of the liquid pressure profile is changed to 0.2 msec. In this case, the pulse width, which is twice of the rise time (0.4 msec), is near the half period of the bubble resonance frequency (0.38 msec). Therefore, the bubble is compressed more than the previous case and the gas temperature reaches the ignition point of the gas mixture. After the explosion the bubble expands to more than 10 times of its initial volume during 1 msec to release its internal energy generated due to the reaction and compression work. As the bubble starts to expand, the gas temperature within the bubble rapidly decreases from 1900°K and reaches 300°K within about 1 msec.

Figure 7.16 shows the history of bubble radius and gas temperature for the same conditions as Figure 7.15 but the peak value of applied liquid pressure profile is changed to 1 MPa. After explosion the bubble expands and its volume increases to more than 4 times of its initial value and gas temperature decreases from 2430°K to 440°K in about 0.7 msec. In Figure 7.17, P_B , the pressure exerted by the liquid (glycerin) on the wet side of the bubble surface is shown. In order to get a clear view of the history of this pressure and the corresponding instantaneous bubble size, the temporal bubble radius is also superimposed in the figure. The parametric conditions for this figure correspond to Figure 7.16. As shown, P_B has a peak value of 7.2 MPa at the end of bubble collapse. It rapidly decreases to near zero and then increases to around 0.3 MPa. This figure shows that the variations of P_B are consistent with the bubble radius history.

In Figures 7.18 and 7.19 the peak value of the applied liquid pressure is 0.5 MPa and the initial bubble diameter is 2.5 mm. The gas mixture is the same as the previous figures (90% Ar + 10%(2H₂+O₂)). In Figure 7.18 the history of bubble radius and gas temperature are shown. It is noted that water is considered as the liquid surrounding the bubble. The gas temperature within the bubble increases at the end of the first collapse

phase and reaches a maximum value of around 730°K, which is below the ignition point. After one oscillation cycle, the bubble expands more than its initial size due to the characteristics of the gaussian liquid pressure profile. The temperature of the bubble oscillates between 210°K and 480 °K in subsequent cycles. Figure 7.19 shows the history of bubble radius and gas temperature. The conditions are the same as in Figure 7.18 but glycerin is considered as the fluid surrounding the bubble. The ignition of the gas mixture does not occur because the gas temperature reaches around 770°K which is below the ignition point. The expansion of the bubble to more than its initial size is due to the characteristics of the imposed gaussian liquid pressure profile. A comparison of Figures 7.18 and 7.19 shows that, when the bubble is in glycerin, the amplitude of bubble radius oscillations is progressively damped due to the higher viscosity of glycerin compared to water.

Figures 7.20 and 7.21 show the history of bubble radius and the pressure exerted by the liquid on the bubble surface (P_B). The parametric conditions for these figures correspond to Figures 7.18 and 7.19. In Figures 7.20 and 7.21 the liquids are considered to be water and glycerin, respectively. In Figure 7.20, after the first bubble collapse, P_B rapidly decreases from the peak value of 1.05 MPa to about 0.23 MPa and then it oscillates between 0.32 and 0.04 MPa. In Figure 7.21, P_B rapidly decreases from the peak value of 1.0 MPa to 0.2 MPa and then it oscillates around 0.1 MPa. Both figures show that with the increase of P_B , the amplitude of the radius oscillation cycle of the bubble decreases and vice versa. Also, as indicated in Equation (7.3), with the increase of the liquid viscosity, P_B decreases.

In Figures 7.22-7.23, the reactive gas mixture within the bubble is changed from 90%Ar + 10%(2H₂+O₂) to 70%Ar+30% (2H₂+O₂). As shown in these figures, the applied liquid pressure has a gaussian profile with a peak value of 1.0 MPa and rise time of 0.2 msec. The initial bubble diameter is assumed to be 5 mm and the liquids are considered to be water and glycerin, respectively. A comparison of these two figures with Figures 7.16 and 7.17 shows that, after explosion, the gas temperatures increase more than the previous cases due to using a gas mixture with more exothermicity. Also, the

release of a relatively greater amount of thermal energy upon explosion, causes the bubble to expand more.

In Figures 7.24 and 7.25 the peak value of the applied liquid pressure is changed from 1.0 to 0.5 MPa. The initial bubble diameter is 2.5 mm and the gas mixture is 70%Ar+30% (2H₂+O₂). In Figures 7.24 and 7.25 water and glycerin are modeled as the liquid surrounding the bubble, respectively. In both cases, due to insufficient strength of the liquid impulse pressures, the gas mixtures attain maximum temperatures of only 690°K (water) and 720°K (glycerin), which are well below the ignition temperature. The bubble radii are seen to exceed their initial values because of the characteristics of the gaussian liquid pressure profile. In Figure 7.25, the attenuation of bubble radius oscillation cycle indicates the high damping effect of glycerin. Also, comparison of Figures 7.24 and 7.25 with Figures 7.18 and 7.19 show that the maximum value of the gas temperature decreases with increasing exothermicity of the gas mixture. A higher exothermicity means a low argon / oxygen-hydrogen ratio. Therefore, due to the relatively low heat capacity of argon compared to that of oxygen and hydrogen, increasing the exothermicity results in a decrease in the maximum gas temperature. It is noted that this is true for a nonignited gas mixture.

7.5.3 History of Gas Pressure

Figures 7.26-7.29 are plotted to demonstrate the history of gas pressure within the bubble for different liquid impulse pressure profiles. In order to get a clear view of the gas pressure history along with the instantaneous bubble size, the temporal bubble radius is also superimposed. In all these figures, the initial diameter of the bubble is taken to be 2.5 mm and the liquid surrounding the bubble is considered to be glycerin. The gas mixture is a stoichiometric oxygen-hydrogen with 70% argon as a diluent. Figure 7.26 shows the history of bubble radius and gas pressure. The liquid pressure has a gaussian profile with a peak value of 1.0 MPa as shown in the figure. It is interesting to note that the gas pressure curve has two peak values of 2.0 and 5.5 MPa. The first one is due to the compression work on the bubble but the second one is due to the compression work plus

the explosion of gas mixture. In Figure 7.27, the liquid pressure has a gaussian profile with the peak value of 0.5 MPa, which is below the threshold pressure (see Figure 7.25). The other conditions are identical to Figure 7.26. As shown in the figure, the gas pressure has only one peak value of 1.05 MPa and this is mainly due to the compression work on the bubble.

In Figure 7.28, the bubble is under a sustained liquid pressure of 0.8 MPa which is above the threshold pressure for the explosion of the gas mixture. As one can see, the gas bubble explodes at the ignition point and the bubble expands to near 2.7 times of its initial volume. Because of the explosion, the gas pressure within the bubble reaches 10.0 MPa rapidly. In Figure 7.29, the bubble is under a sustained liquid pressure of 0.4 MPa which is below the threshold pressure. It is noted that the gas pressure cycle is opposite to the radius oscillation cycle of the bubble. This is to be expected theoretically. During collapse of the bubble, the gas pressure within the bubble must rise due to the compression work on the bubble. As shown in the figure, the peak of gas pressure within the bubble reaches near 1.4 MPa which is far less than the gas pressure in Figure 7.28.

7.6. Comparison with Experiments

Hasegawa and Fujiwara (1982) carried out bubble explosion experiments using an argon-diluted stoichiometric oxygen-hydrogen gas bubble inside liquid glycerin. Using a high-speed photographic technique they demonstrated the events of explosion and subsequent bubble dynamics. In their experiments the bubble was 10 mm in diameter and the pressure pulse profile in glycerin at the transducer location was triangular in shape. The mathematical model discussed earlier in this chapter was used to simulate the results of the Hasegawa and Fujiwara's experiments. The temporal behavior of the bubble radius obtained in their experiments and that predicted by the present model are compared in Figure 7.30. The theoretical model used as input the same experimental conditions reported by the authors. The figure shows a good agreement between the mathematical model and the experiment. Although the theoretically predicted bubble dynamics period quite clearly matches the experiment a small difference in amplitude is evident. This

difference can be justified by the fact that in Hasegawa and Fujiwara's experiments, the pressure profile recorded at the transducer location is not an exact triangular shape due to the interaction among adjacent bubbles and tube wall, especially after ignition. Also, for a bubble with a 5 mm initial radius, which is a relatively large bubble, the deviation of the bubble from a spherical shape was quite considerable in the experiment.

7.7. Concluding Remarks

In this study, a mathematical model is developed to simulate the nonlinear volume and thermal oscillation characteristics of a single reactive gas bubble in water and glycerin. The radial motion of the bubble is considered to be governed by the compressible form of the Rayleigh-Plesset bubble dynamics equation. The bubble is assumed to be spherical and contains a stoichiometric mixture of oxygen and hydrogen gas with the inert argon gas as a diluent. The thermo-fluid mechanics interaction of the gas inside the bubble is considered by assuming a thin thermal boundary layer inside the bubble near the bubble interface. The thermal energy exchange between the bubble and the surrounding liquid is taken into account by solving a differential energy balance equation for the liquid surrounding the bubble. The chemical reaction of the oxygen-hydrogen gas mixture is modeled by using a two-step Arrhenius-type reaction scheme suggested by Korobeinkov. The model equations are suitably non-dimensionalized, and the resulting coupled stiff set of highly nonlinear ODE's is solved by the modified Gear scheme. A parametric study on the present model has been specifically carried out to ascertain the effects of exothermicity of the reactive gas mixture and the initial bubble diameter on bubble dynamics under various liquid pressure profiles. The results from the model show that the incident liquid pressure on the bubble wall must be of sufficient strength to compress the bubble and ignite its reactive gas content. If ignition does not occur, the bubble is seen to oscillate below its initial equilibrium radius. For a nonignited bubble, due to the low heat capacity of the argon gas compared to the oxygen-hydrogen mixture, the maximum gas temperature increases with the decrease of the initial oxygen-hydrogen content. When the liquid pressure is of sufficient strength the bubble ignites and

the maximum temperature that the bubble attains during its thermal oscillation depends upon its equilibrium mole fraction of the stoichiometric oxygen-hydrogen mixture. For an ignited bubble, with the increase of exothermicity, the maximum radius that the bubble attains during its radial oscillation increases. With the decrease of the initial bubble diameter the liquid threshold pressure for bubble explosion increases. The results also show that when the imposed liquid pressure profile is gaussian the radius of a nonreactive bubble may exceed its initial value. This is due to the characteristics of the gaussian liquid pressure profile. For a bubble in a liquid with high viscosity (like glycerin), the amplitude of the bubble radius oscillations decreases due to the high level of viscous damping effect. The mathematical model's results for the history of bubble radius were compared with the experimental data, which show a good agreement between the mathematical model and the experiment.

7.8. Nomenclature

a_1	induction reaction rate constant	$\text{m}^3/(\text{Kg}\cdot\text{s})$
a_2	exothermic reaction rate constant	$\text{m}^4/(\text{N}^2\cdot\text{s})$
C_v, C_p	specific heat at constant volume and constant pressure	$\text{J}/(\text{kg}\cdot\text{K})$
C_0	sound speed of liquid	m/s
E	internal energy of gas mixture	J
e_1, e_2	activation energies per mass of gas mixture	J/kg
K	thermal conductivity	$\text{W}/(\text{m}\cdot\text{K})$
M_w	molecular weight of gas mixture	g/mole
P	pressure	Pa
P_0	initial pressure	Pa
P_∞	far field pressure in liquid	Pa
P_{tdc}	liquid pressure at transducer location	Pa
\dot{Q}_p, \dot{Q}_l	heat production and heat loss rates	W
q	heat of reaction of gas mixture	J/kg
R, R_0	bubble radius and initial bubble radius	m
\dot{R}, \ddot{R}	bubble wall velocity and bubble wall acceleration	$\text{m}/\text{s}, \text{m}/\text{s}^2$
r	distance from bubble center	m
T	temperature	K
T_0	initial temperature	K
t	time	s
t_0	characteristic time for bubble collapse	s
\dot{W}	work rate	W
∇	volume of bubble	m^3
ρ	density of gas mixture	kg/m^3
ρ_0	initial density of gas mixture	kg/m^3
ρ_l	density of liquid	kg/m^3

α	thermal diffusivity	m^2/s
σ, μ	surface tension and dynamic viscosity of liquid	$\text{N}/\text{m}, (\text{N}\cdot\text{s})/\text{m}^2$
η, β	reaction progress variables	
$\dot{\omega}$	reaction rate	$1/\text{s}$
\mathfrak{R}	gas constant	$\text{J}/(\text{kg}\cdot\text{K})$
$\overline{\mathfrak{R}}$	universal gas constant	$\text{J}/(\text{kg}\cdot\text{mole}\cdot\text{K})$
δ	thermal layer thickness	m

Superscripts

– variable non-dimensionalized by reference parameter

Subscripts

g	gas mixture
i	interface
l	liquid
0	initial state

References

- Andrew, J. R. and Biblarz O., Temperature Dependent of Gas Properties in Polynomial Form, *Naval Postgraduate School Report*, Monterey, CA, 1981.
- Gülhan, A. and Beylich A. E., Detonation Wave Phenomena in Bubbled Liquid, *Proc. 17th Int. SWSTS*, Bethlehem, USA, pp. 825-830, 1989.
- Hasegawa, T. and Fujiwara, T., Detonation in Oxyhydrogen Bubbled Liquids, *Proc. 19th Int. Symp. on Combustion*, Pittsburgh, USA, pp. 675-683, 1982.
- Kang, J. and Butler, P. B., Shock Initiation of Hydrogen/Oxygen/Argon Bubbles in a Non-reactive Liquid, *Combust. Sci. and Tech.*, Vol. 90, pp. 173-192, 1993.
- Kedrinskii, V. K. and Mader, C. L., Accidental Detonation in Bubble Liquids, *Proc. 16th Int. SWSTS*, Aachen, FRG, pp. 371-374, 1987.
- Korobeinikov, V. A. Propagation of Blast Waves in a Combustible Gas *Astronautica Acta*, Vol. 17, pp. 529-537, 1972.
- Naji Meidani, A. R. and M. Hasan, A Numerical Study of the Complex Dynamics Behavior of a Reactive Gas Bubble in Water, *J. of Applied Mathematical Modelling*, Vol. 21, pp. 127-138, 1997.
- Prosperetti, A., The Thermal Behavior of Oscillating Gas Bubbles, *J. Fluid Mech.*, Vol. 222, pp. 587-616, 1991.
- Rayleigh, L., On the Pressure Developed in a Liquid During the Collapse of a Spherical Cavity, *Phil. Mag.*, Vol. 34, pp. 94-98, 1917.
- Solouhkin, R. I., Bubble Mechanism of Shock Ignition in a Liquid. *Dokl. Akad. Nauk. SSSR*, Vol. 136, No.2, pp. 311-312, 1961.
- Taki, S. and Fujiwara T., Numerical Analysis of Two-dimensional Unsteady Detonations *AIAA journal*, Vol. 16, No. 1, pp. 73-77, 1978.
- Trilling, L. The Collapse and Rebound of a Gas Bubble. *J. Appl. Phys.*, Vol. 23, pp. 14-17, 1952.

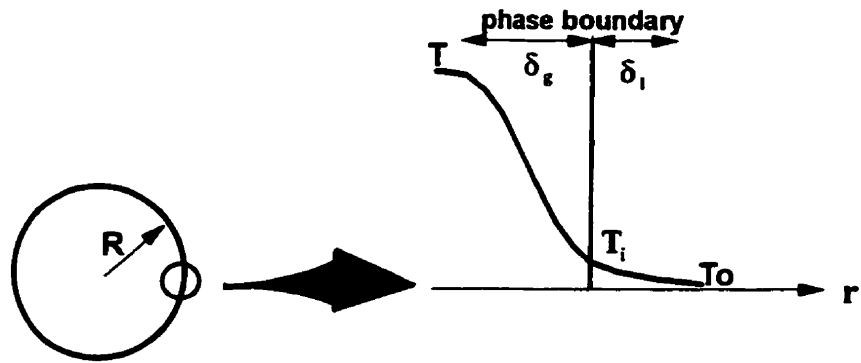


Fig. 7.1. Schematic of temperature profile at the phase boundary.

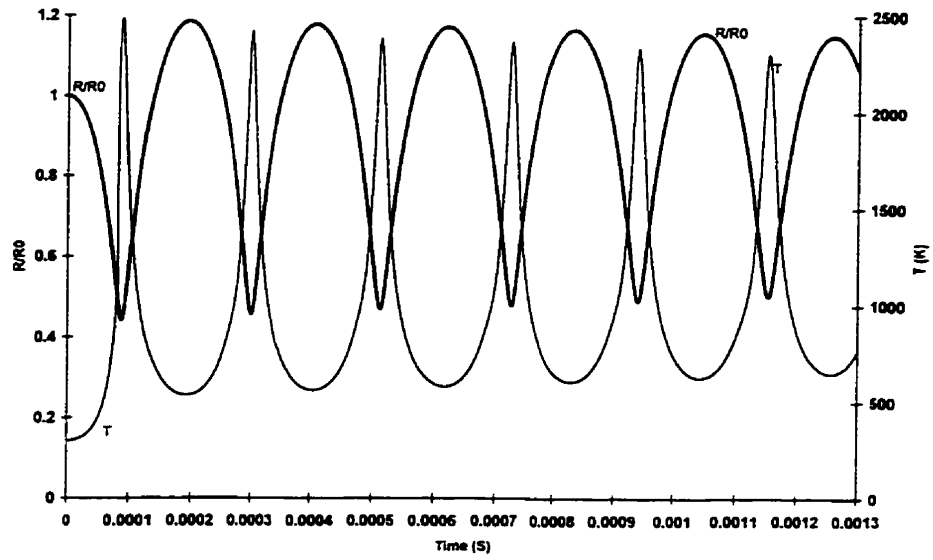


Fig. 7.2. History of bubble radius and gas temperature in water for a mixture of 90% Ar + 10% ($2\text{H}_2 + \text{O}_2$) under a sustained liquid pressure of 8 bars ($d_0 = 5\text{mm}$).

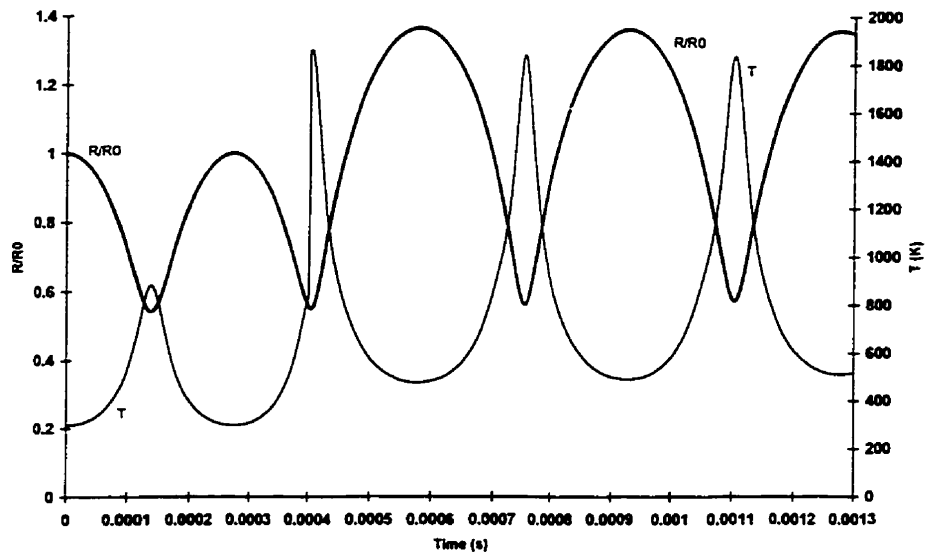


Fig. 7.3. History of bubble radius and gas temperature in water for a mixture of 90% Ar + 10% ($2\text{H}_2 + \text{O}_2$) under a sustained liquid pressure of 4 bars ($d_0 = 5\text{mm}$).

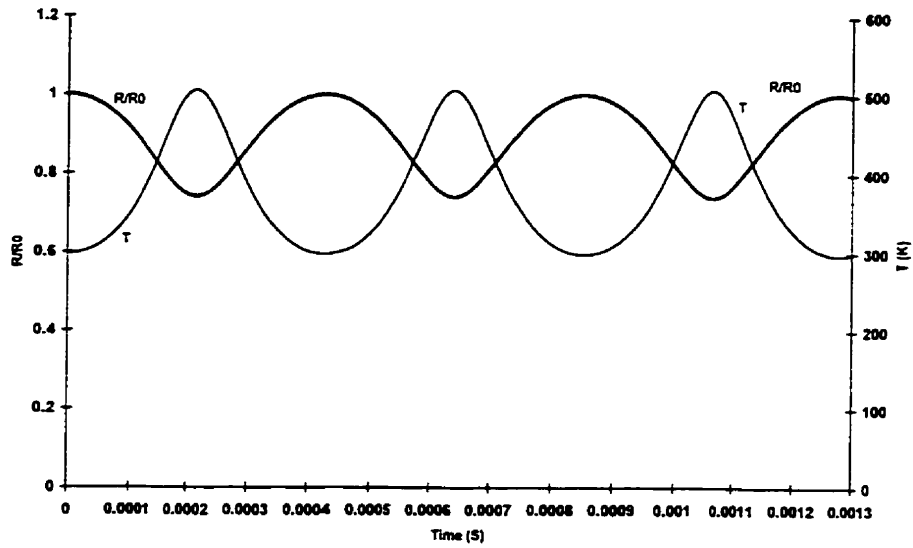


Fig. 7.4. History of bubble radius and gas temperature in water for a mixture of 90% Ar + 10% (2H₂ + O₂) under a sustained liquid pressure of 2 bars ($d_0 = 5$ mm).

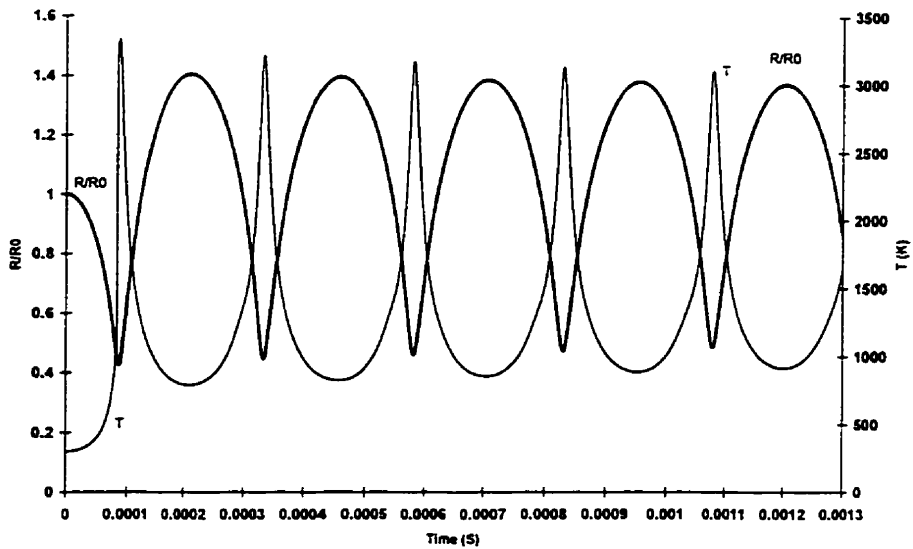


Fig. 7.5. History of bubble radius and gas temperature in water for a mixture of 70% Ar + 30% (2H₂ + O₂) under a sustained liquid pressure of 8 bars ($d_0 = 5$ mm).

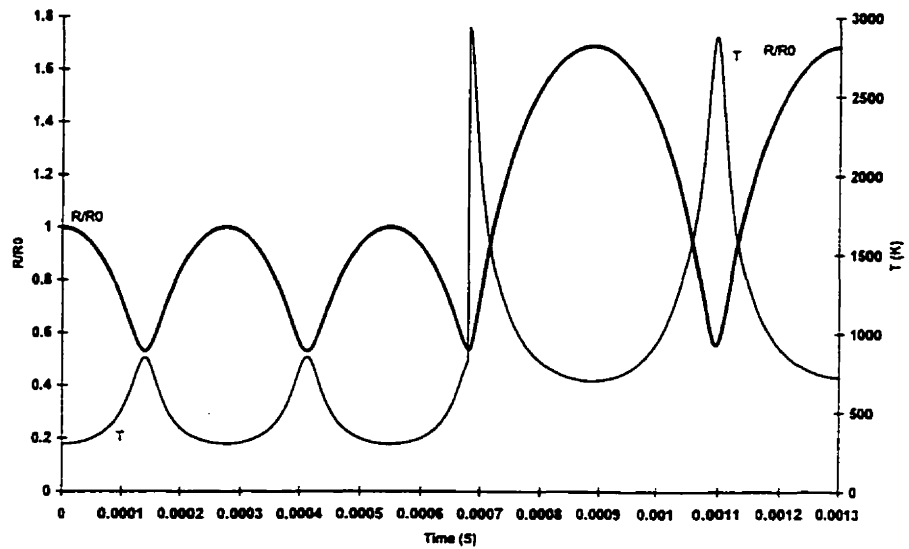


Fig. 7.6. History of bubble radius and gas temperature in water for a mixture of 70% Ar + 30% ($2\text{H}_2 + \text{O}_2$) under a sustained liquid pressure of 4 bars ($d_0 = 5$ mm).

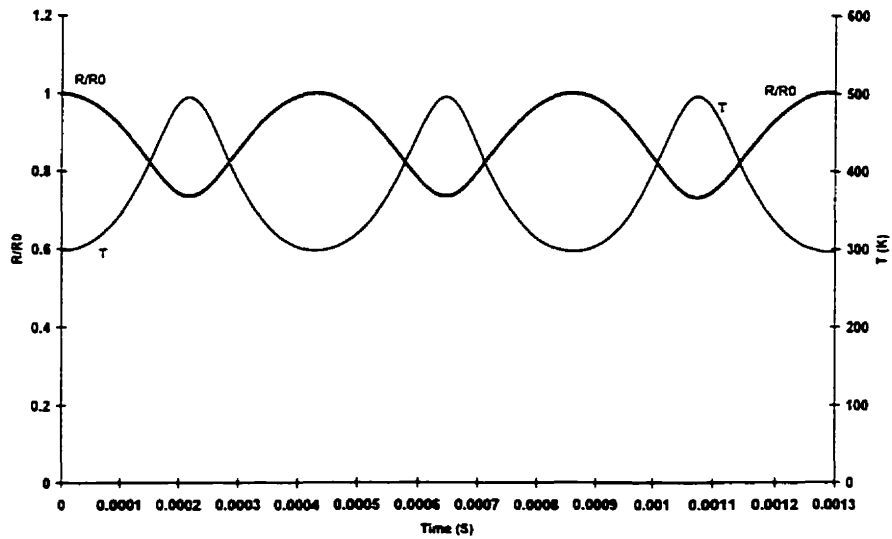


Fig. 7.7. History of bubble radius and gas temperature in water for a mixture of 70% Ar + 30% ($2\text{H}_2 + \text{O}_2$) under a sustained liquid pressure of 2 bars ($d_0 = 5$ mm).

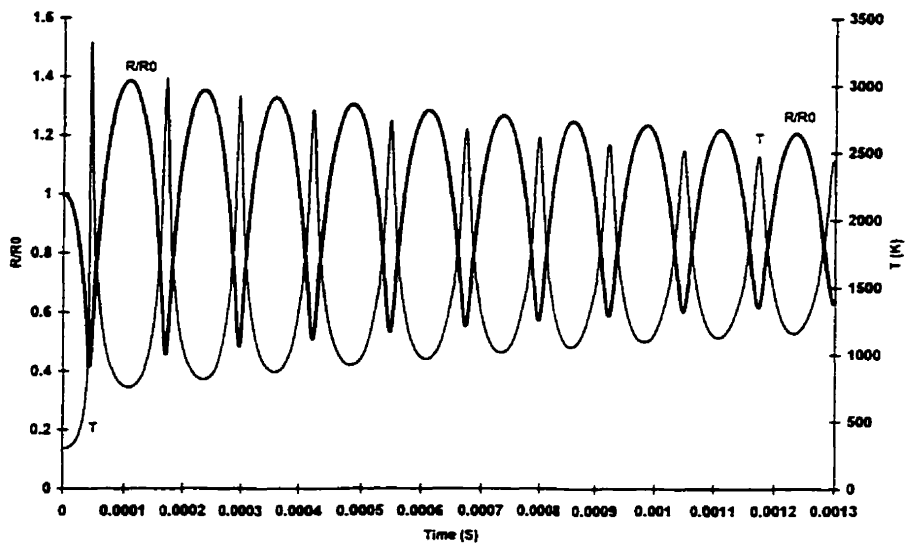


Fig. 7.8. Temporal behavior of bubble radius and gas temperature in water for a mixture of 70% Ar + 30% ($2\text{H}_2 + \text{O}_2$) under a sustained liquid pressure of 8 bars ($d_0 = 2.5$ mm).

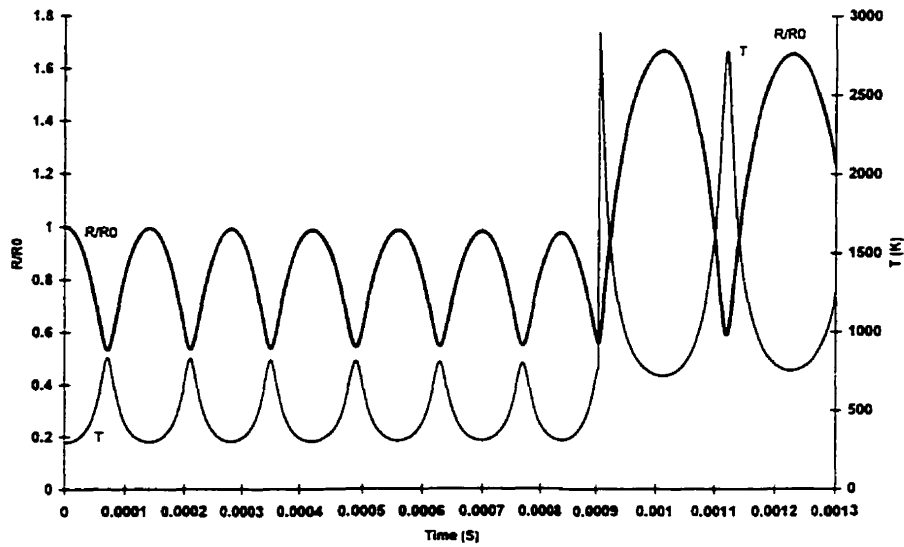


Fig. 7.9. Temporal behavior of bubble radius and gas temperature in water for a mixture of 70% Ar + 30% ($2\text{H}_2 + \text{O}_2$) under a sustained liquid pressure of 4 bars ($d_0 = 2.5$ mm).

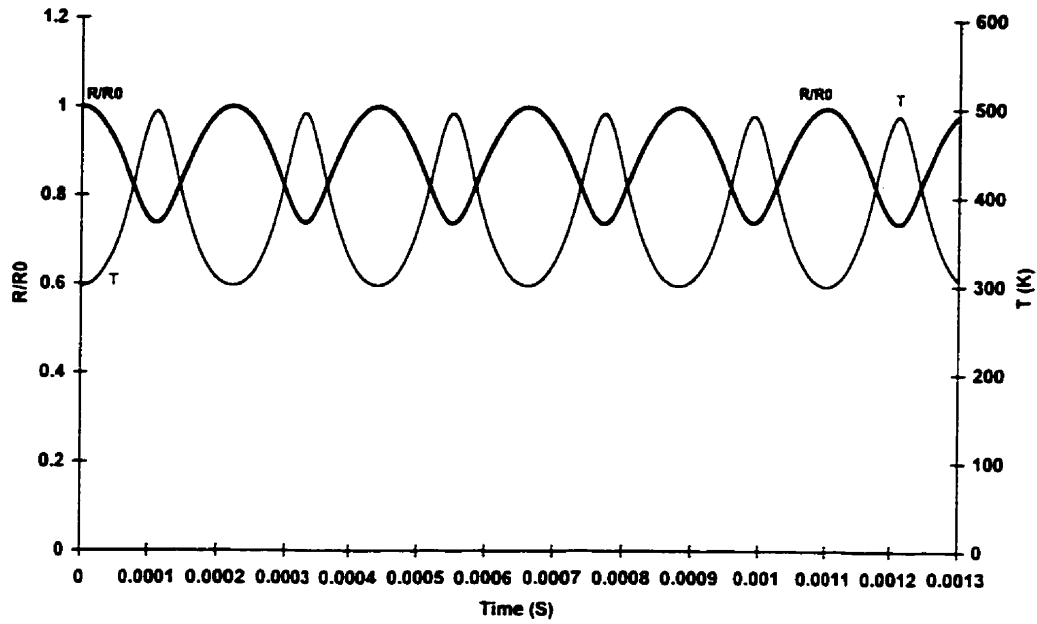


Fig. 7.10. Temporal behavior of bubble radius and gas temperature for a mixture of 70% Ar + 30% ($2\text{H}_2 + \text{O}_2$) under a sustained liquid pressure of 2 bars in water ($d_0 = 2.5$ mm).

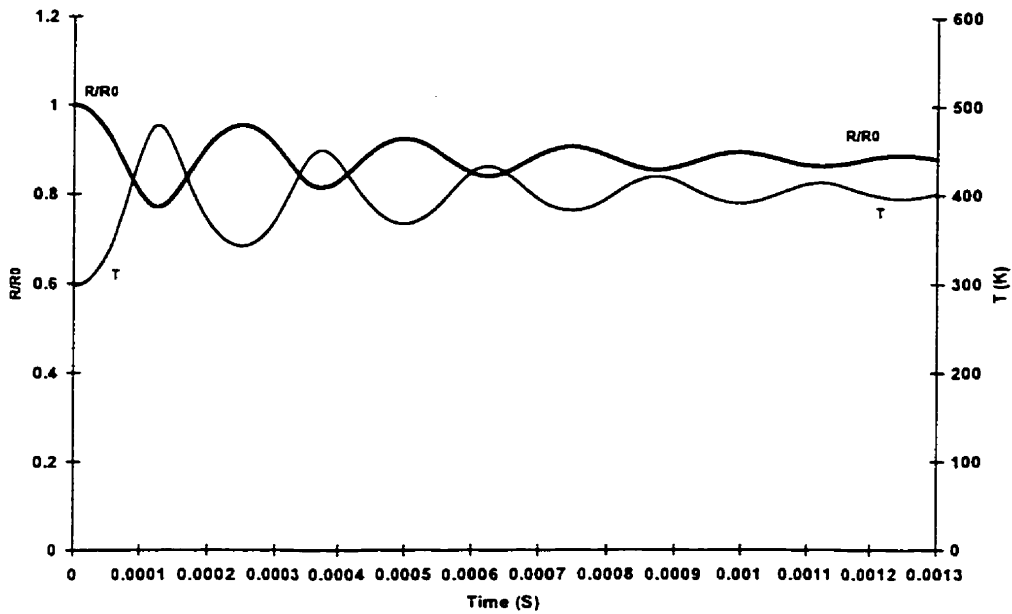


Fig. 7.11. Temporal behavior of bubble radius and gas temperature for a mixture of 70% Ar + 30% ($2\text{H}_2 + \text{O}_2$) under a sustained liquid pressure of 2 bars in glycerin ($d_0 = 2.5$ mm).

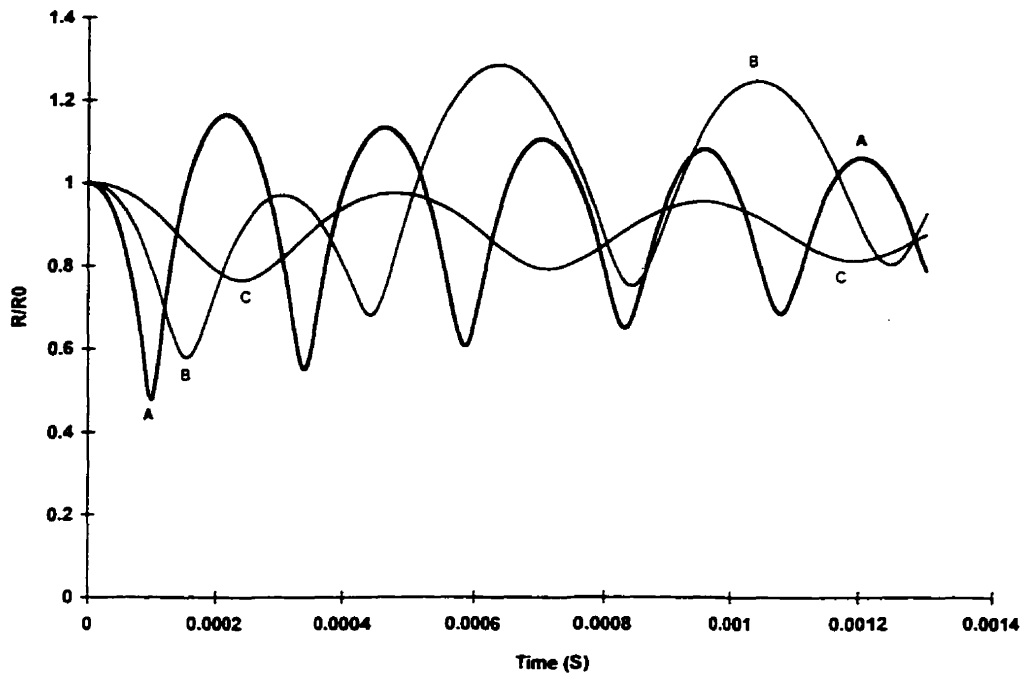


Fig. 7.12. History of bubble radius in glycerin under different sustained liquid pressures of A = 8 bar, B = 4 bar and C = 2 bar for a mixture of 90% Ar+10% (2H₂ + O₂), d₀ = 5 mm.

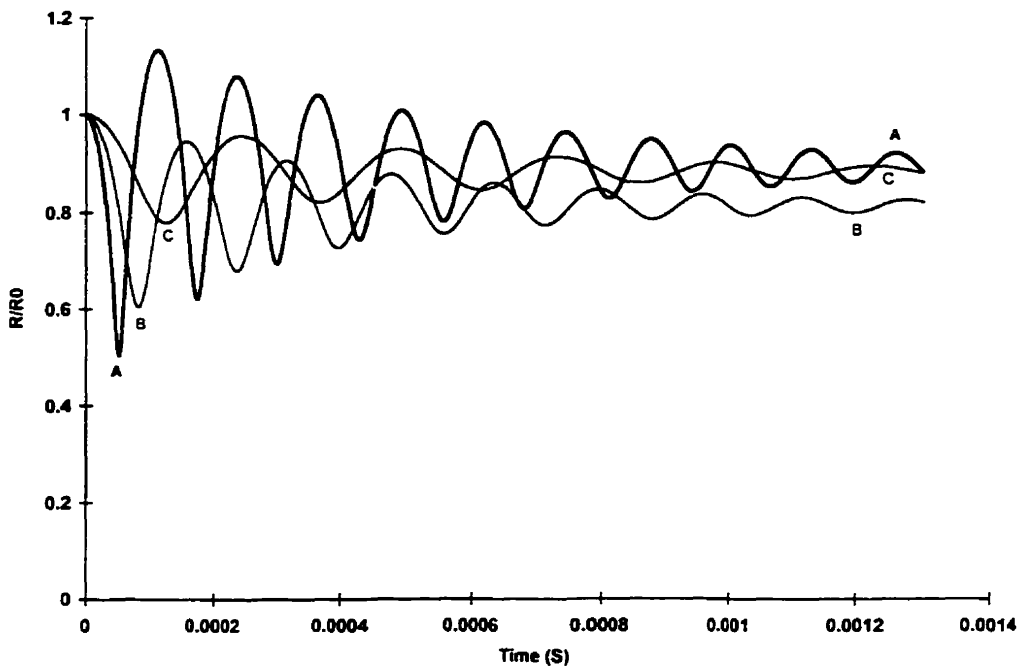


Fig. 7.13. History of bubble radius in glycerin under different sustained liquid pressures of A = 8 bar, B = 4 bar and C = 2 bar for a mixture of 90% Ar+10% (2H₂ + O₂), d₀ = 2.5 mm.

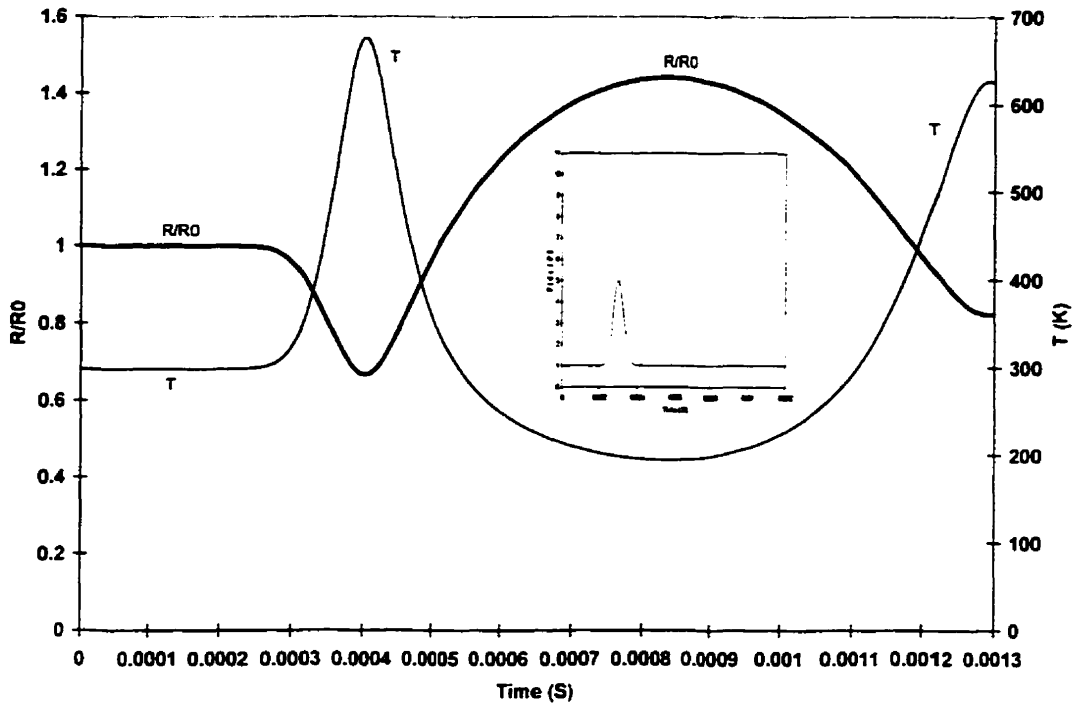


Fig. 7.14. History of bubble radius and gas temperature for a mixture of 90% Ar + 10% (2H₂ + O₂) under a gaussian liquid pressure profile in glycerin, P_{max} = 5 bar, RT = 0.1 msec (d₀ = 5 mm).

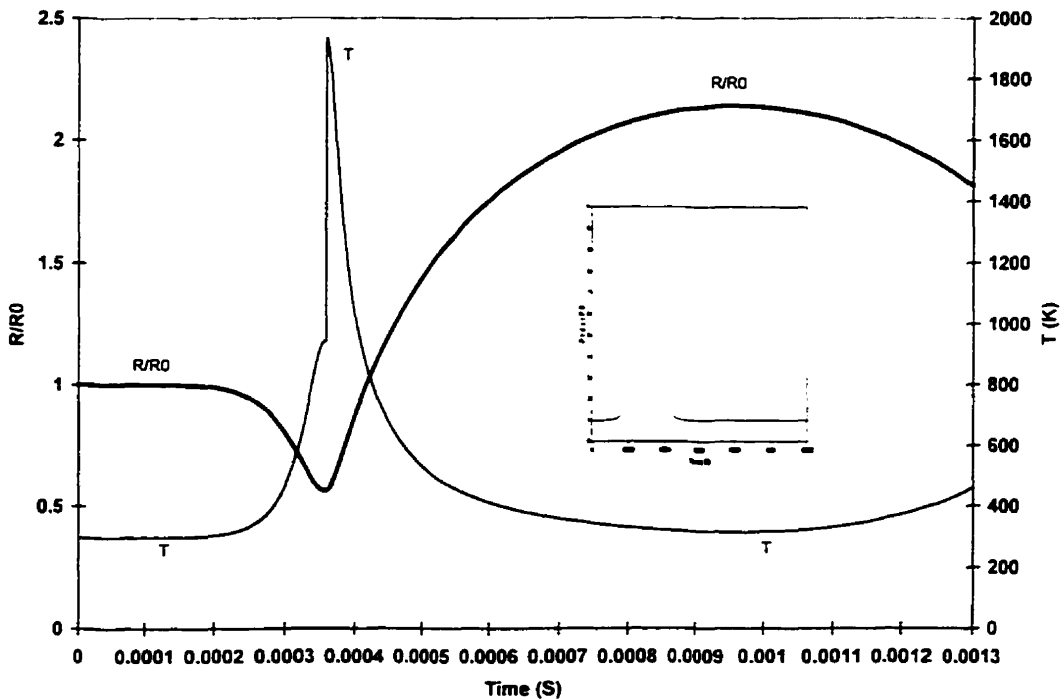


Fig. 7.15. History of bubble radius and gas temperature for a mixture of 90% Ar + 10% (2H₂ + O₂) under a gaussian liquid pressure profile in glycerin, P_{max} = 5 bar, RT = 0.2 msec (d₀ = 5 mm).

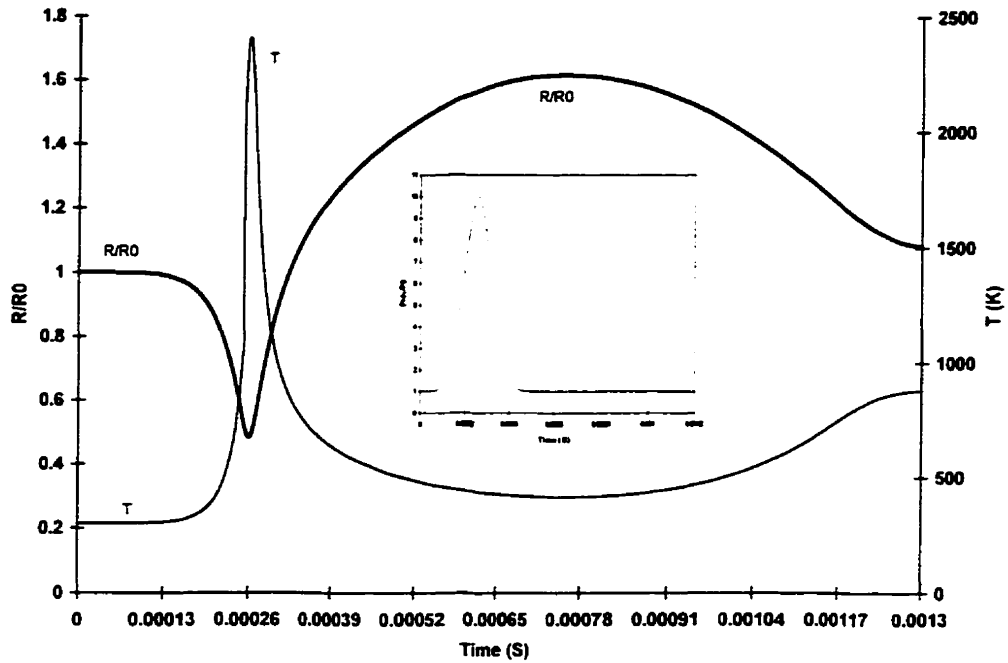


Fig. 7.16. History of bubble radius and liquid pressure at the bubble surface for a mixture of 90% Ar + 10% (2H₂ + O₂) under a gaussian liquid pressure profile in glycerin, P_{max} = 10 bar (d₀ = 5 mm).

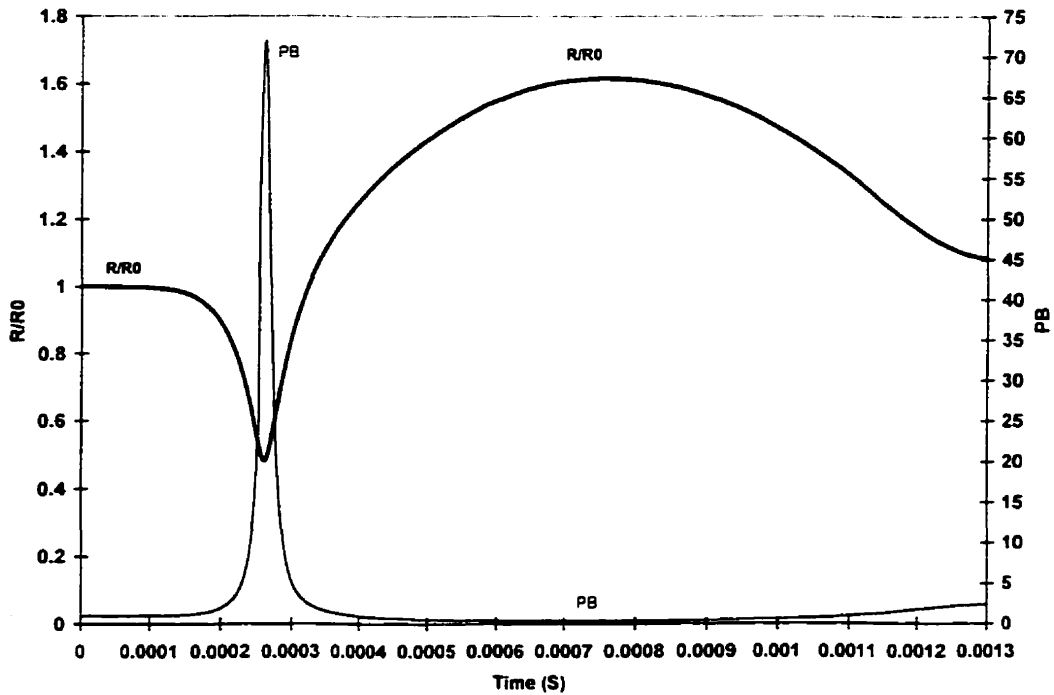


Fig. 7.17. History of bubble radius and liquid pressure at the bubble surface (bar) for a mixture of 90% Ar + 10% (2H₂ + O₂) under a gaussian liquid pressure profile in glycerin, P_{max} = 10 bar (d₀ = 5 mm).

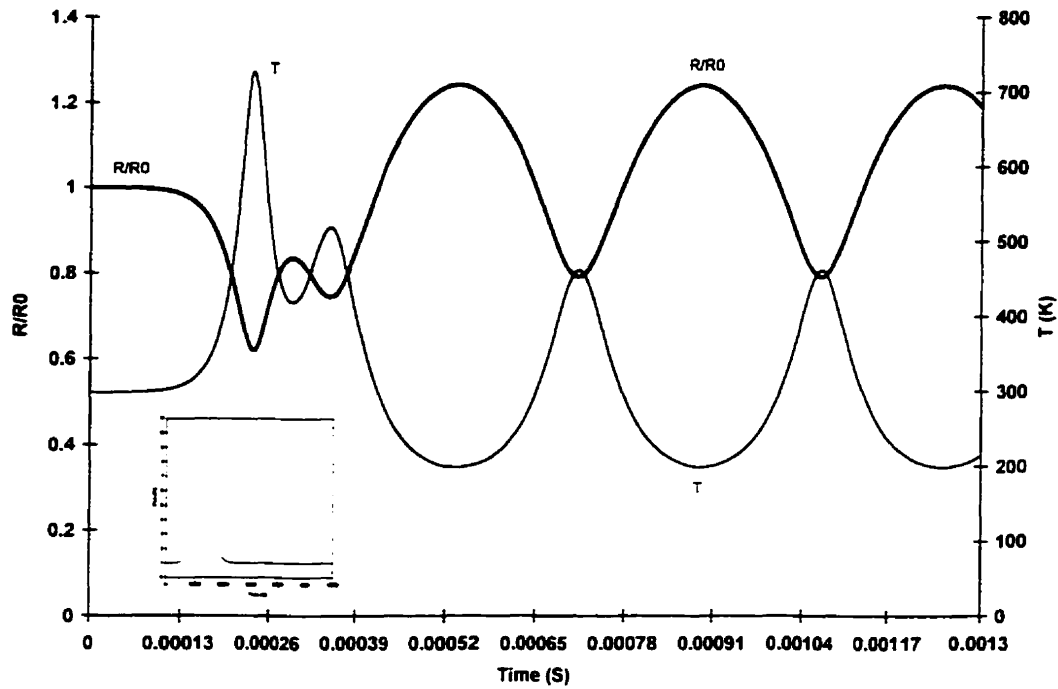


Fig. 7.18. History of bubble radius and gas temperature for a mixture of 90% Ar +10% (2H₂ + O₂) under a gaussian liquid pressure profile in water, P_{max} = 5 bar (d₀ = 2.5 mm).

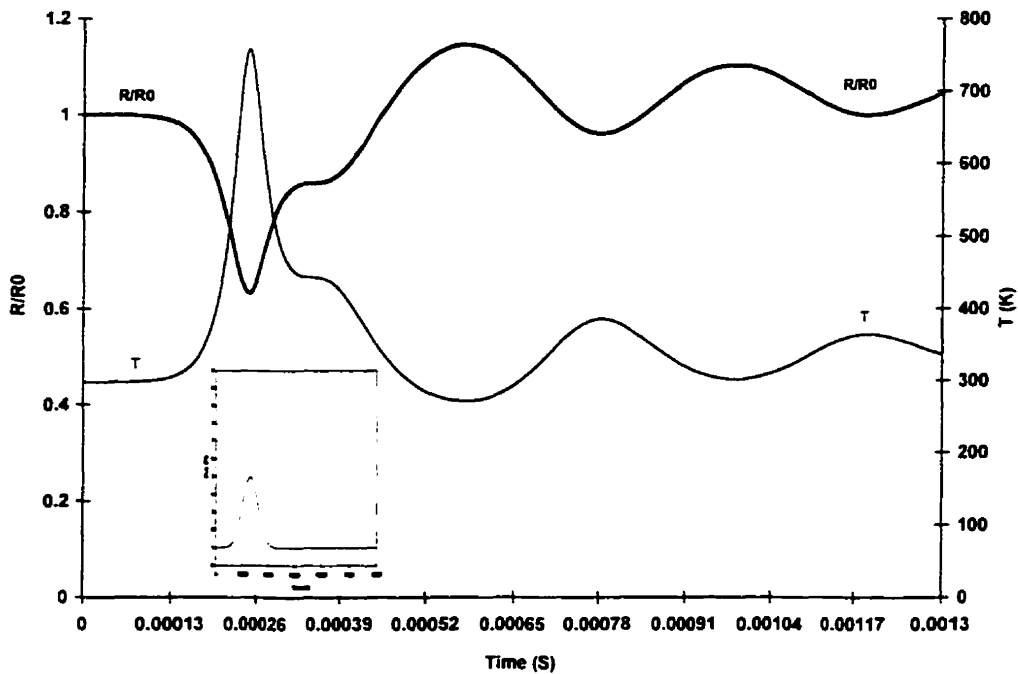


Fig. 7.19. History of bubble radius and gas temperature for a mixture of 90% Ar +10% (2H₂ + O₂) under a gaussian liquid pressure profile in glycerin, P_{max} = 5 bar (d₀ = 2.5 mm).

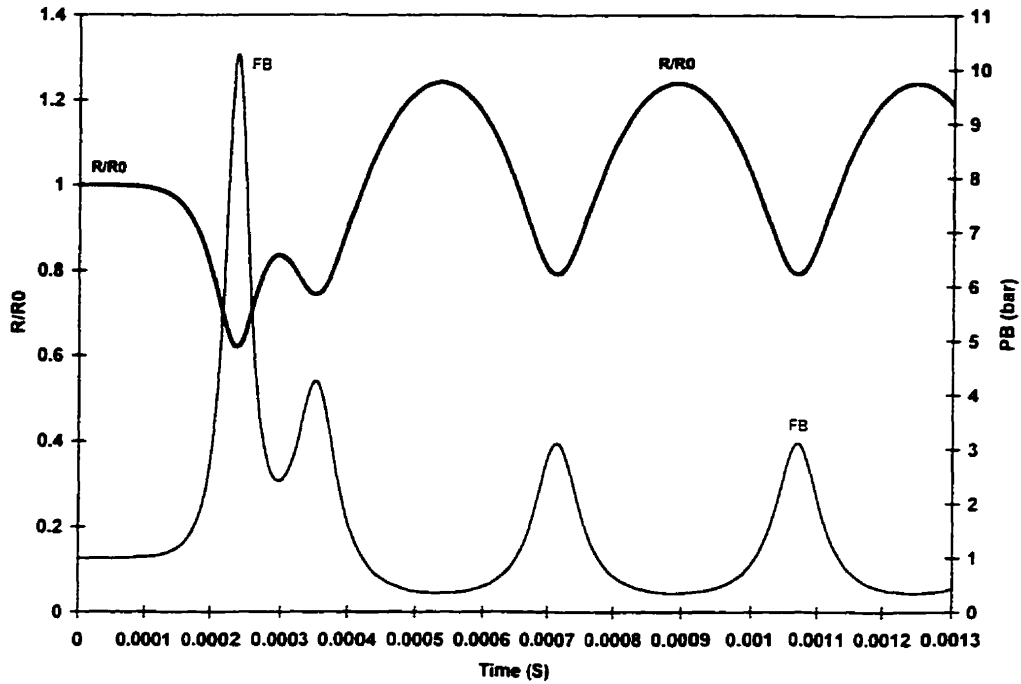


Fig. 7.20. History of bubble radius and liquid pressure at the bubble surface for a mixture of 90% Ar + 10% (2H₂ + O₂) under a gaussian liquid pressure profile in water, P_{max} = 5 bar (d₀ = 2.5 mm).

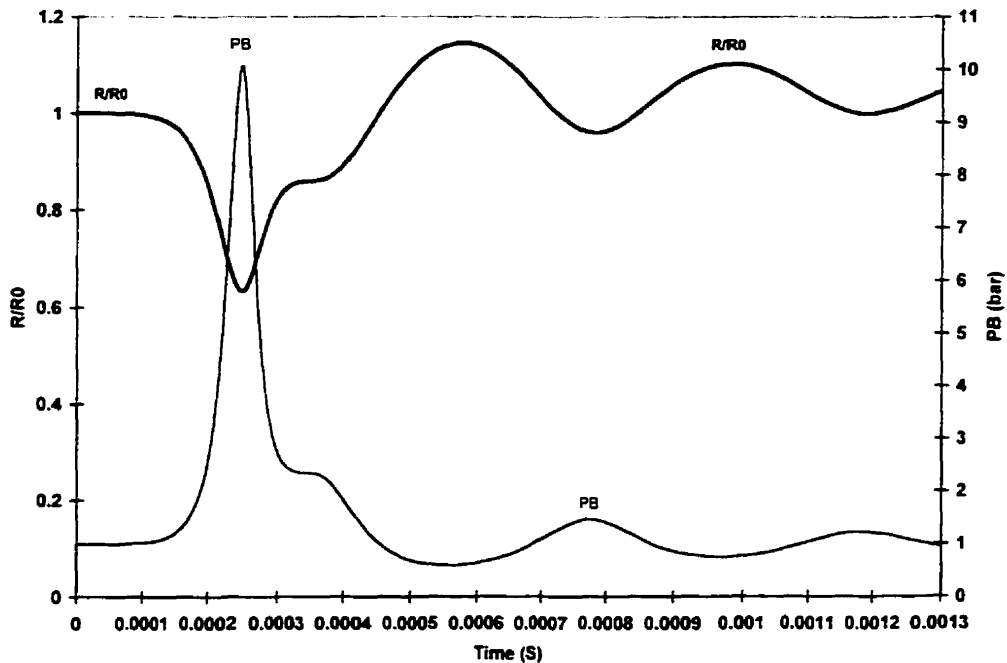


Fig. 7.21. History of bubble radius and liquid pressure at the bubble surface for a mixture of 90% Ar + 10% (2H₂ + O₂) under a gaussian liquid pressure profile in glycerin, P_{max} = 5 bar (d₀ = 2.5 mm).

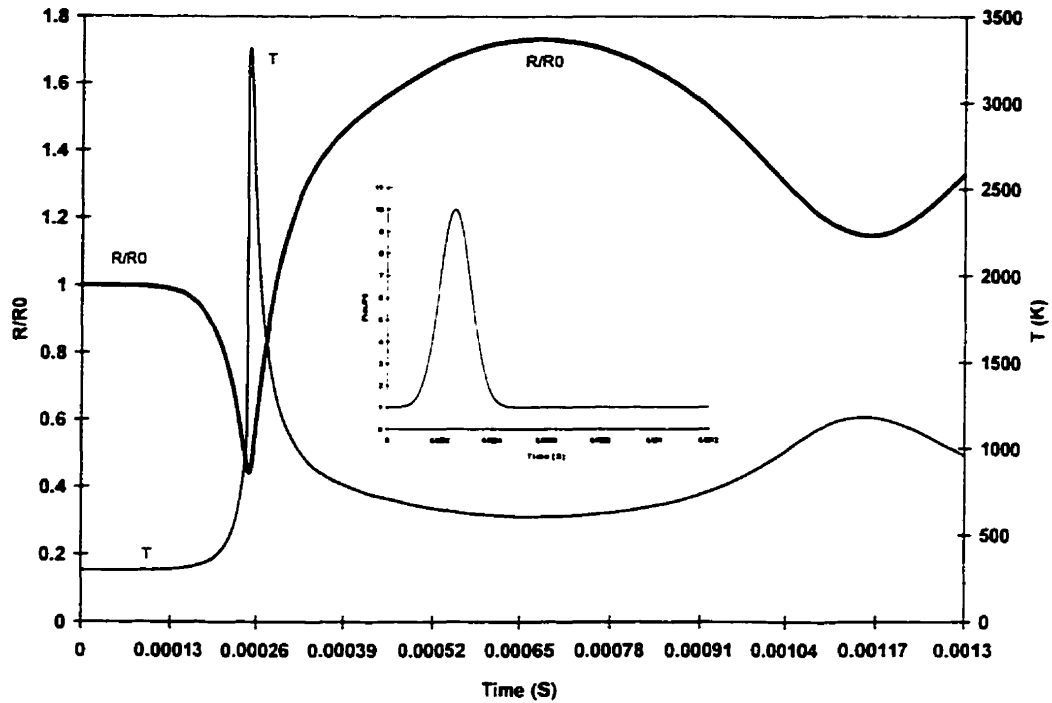


Fig. 7.22. History of bubble radius and gas temperature in water for a mixture of 70% Ar + 30% (2H₂ + O₂) under a gaussian liquid pressure profile, P_{max} = 10 bar (d₀ = 5 mm).

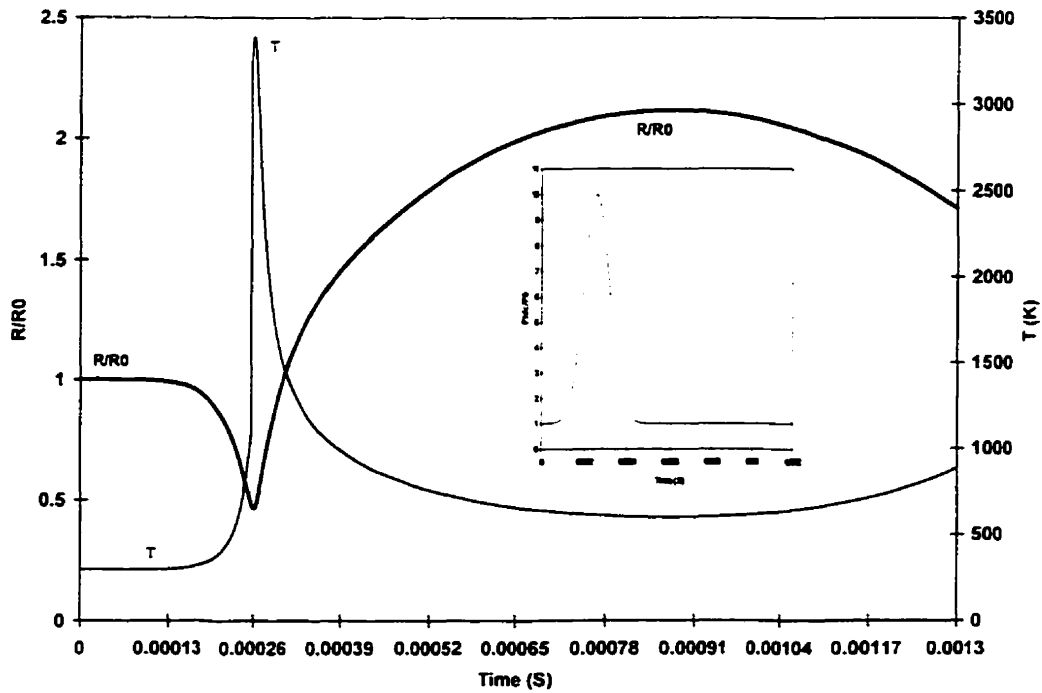


Fig. 7.23. History of bubble radius and gas temperature in glycerin for a mixture of 70% Ar + 30% (2H₂ + O₂) under a gaussian liquid pressure profile, P_{max}=10 bar (d₀ = 5 mm).

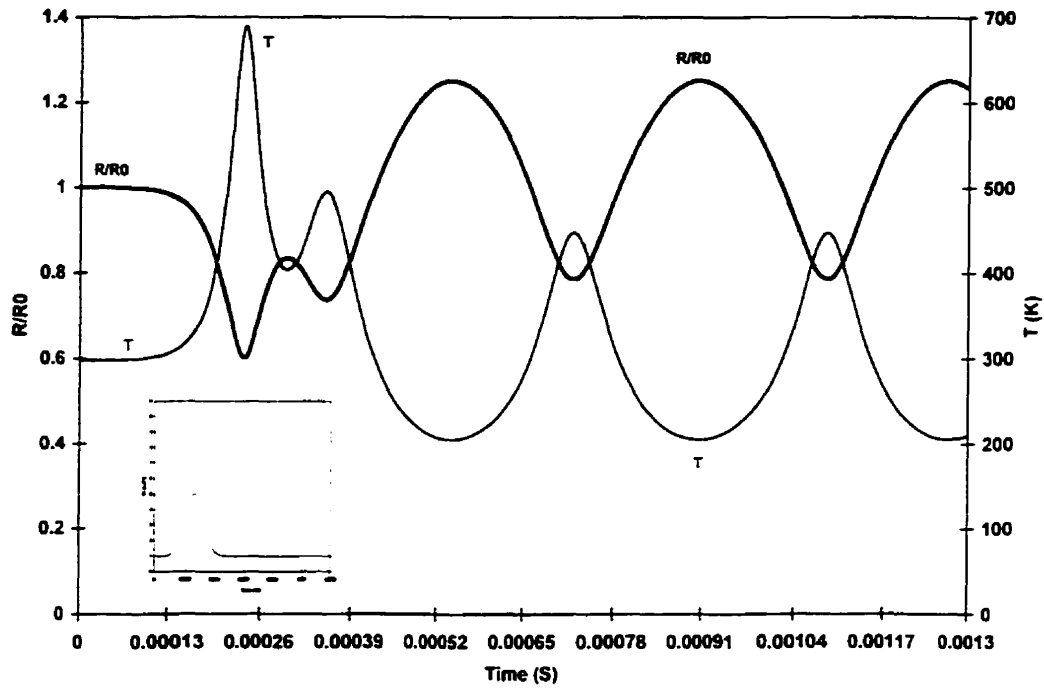


Fig. 7.24. History of bubble radius and gas temperature in water for a mixture of 70% Ar + 30% (2H₂ + O₂) under a gaussian liquid pressure profile, P_{max} = 5 bar (d₀ = 2.5 mm).

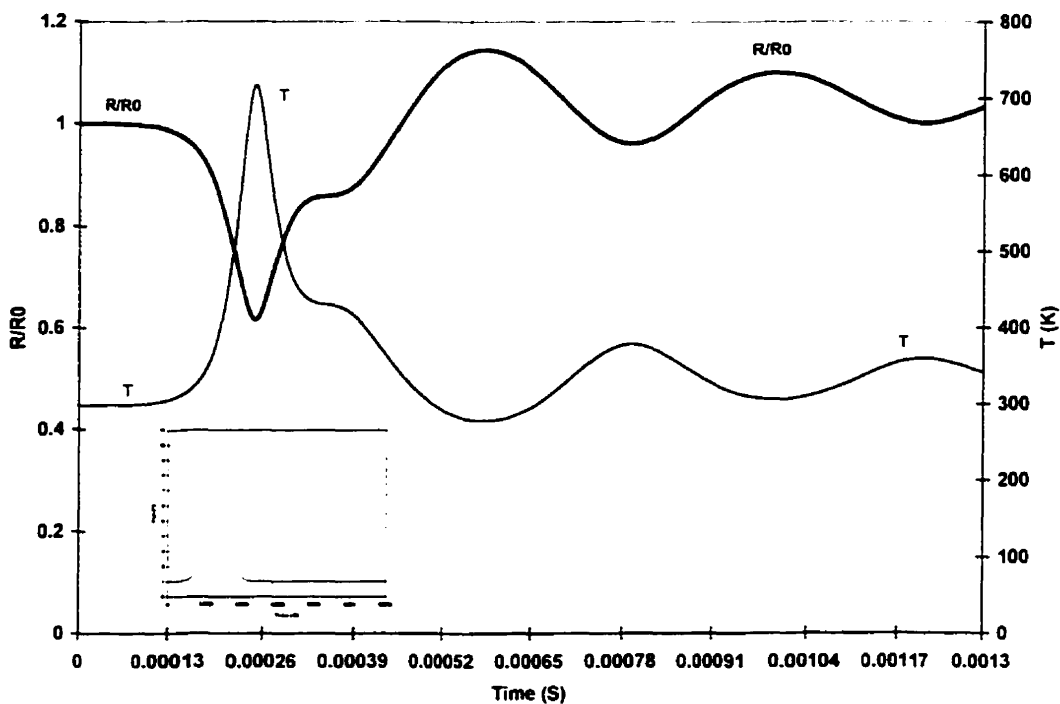


Fig. 7.25. History of bubble radius and gas temperature in glycerin for a mixture of 70% Ar + 30% (2H₂ + O₂) under a gaussian liquid pressure profile, P_{max} = 5 bar (d₀ = 2.5 mm).

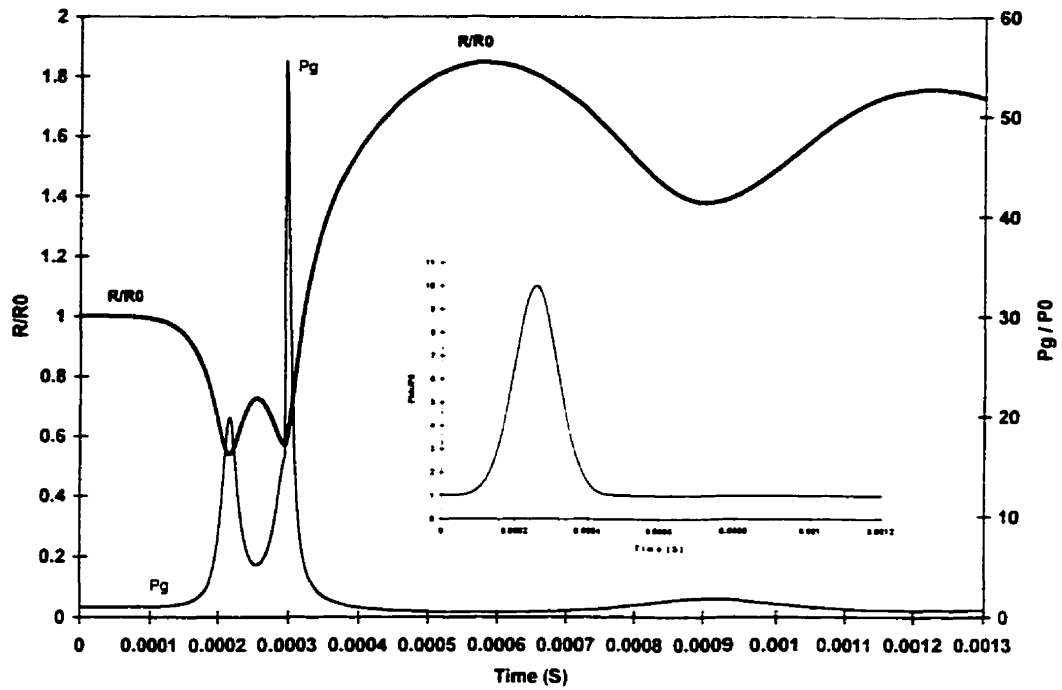


Fig. 7.26. History of bubble radius and gas pressure in glycerin for a mixture of 70% Ar + 30% ($2H_2 + O_2$) under a gaussian liquid pressure profile, $P_{max} = 10$ bar ($d_0 = 2.5$ mm).

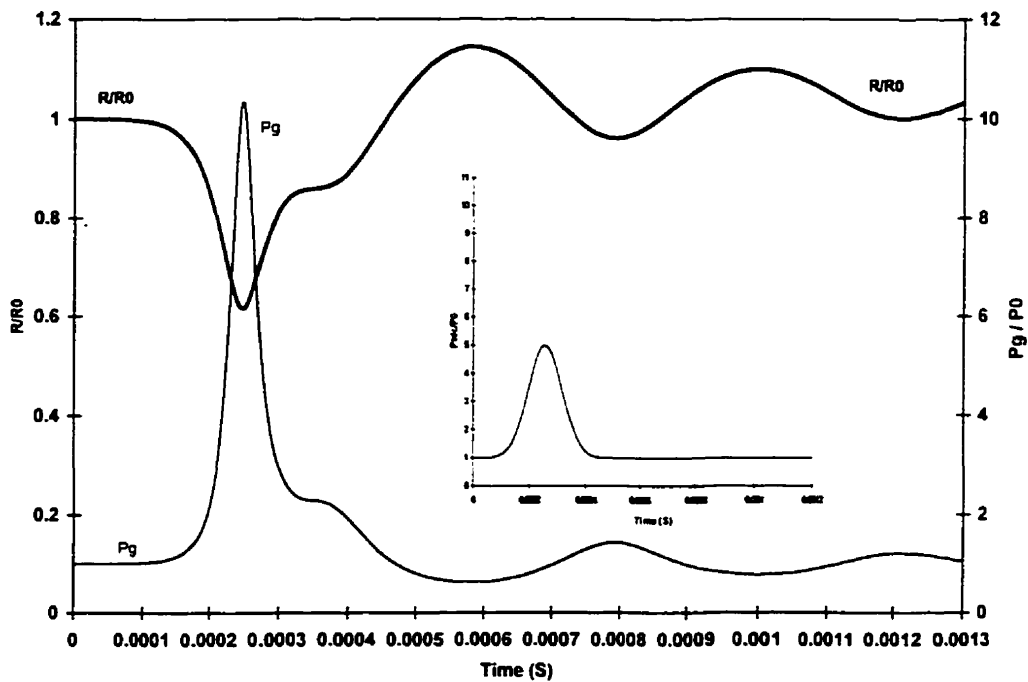


Fig. 7.27. History of bubble radius and gas pressure in glycerin for a mixture of 70% Ar + 30% ($2H_2 + O_2$) under a gaussian liquid pressure profile, $P_{max} = 5$ bar ($d_0 = 2.5$ mm).

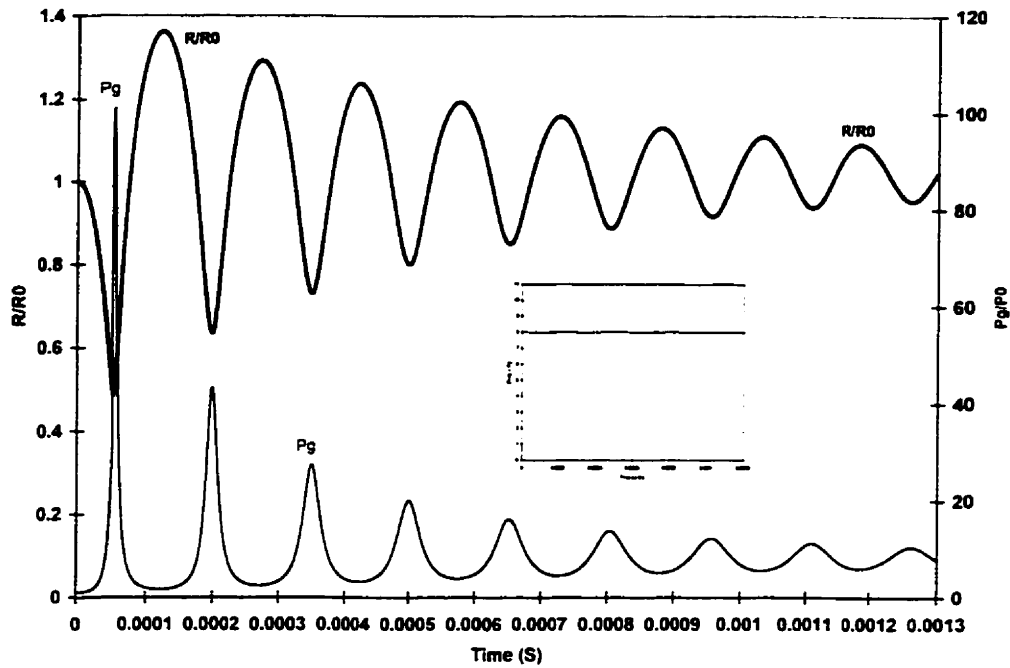


Fig. 7.28. History of bubble radius and gas pressure in glycerin for a mixture of 70% Ar + 30% ($2H_2 + O_2$) under a sustained liquid pressure profile of 8 bars ($d_0 = 2.5$ mm).

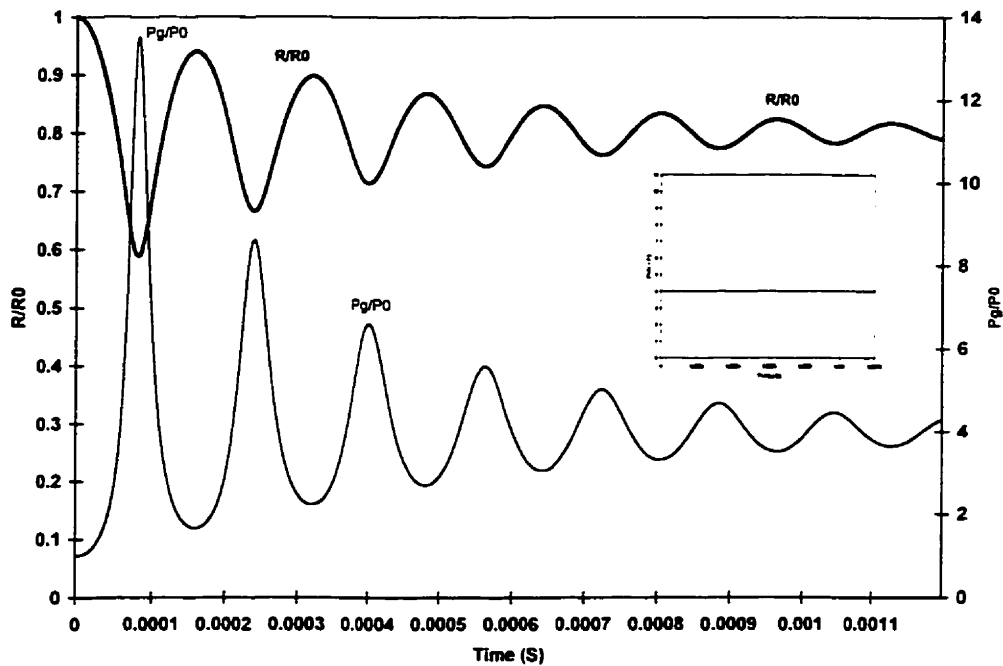


Fig. 7.29. History of bubble radius and gas pressure in glycerin for a mixture of 70% Ar + 30% ($2H_2 + O_2$) under a sustained liquid pressure profile of 4 bars ($d_0 = 2.5$ mm).

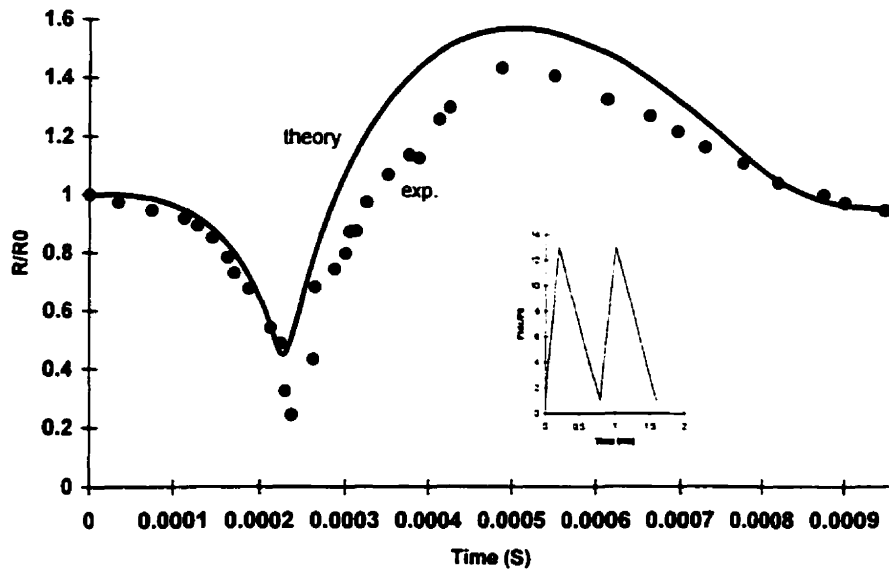


Fig. 7.30. Comparison of the model's calculation with the Hasegawa and Fujiwara experiment for a mixture of 70% Ar + 30% ($2H_2 + O_2$) and $d_0 = 10$ mm.

SUMMARY AND CONCLUDING REMARKS

8.1 Overall Conclusions

The research carried out in the present work is concerned primarily with the mathematical modelling of the complex phenomenon of bubble dynamics. Specifically, two applications of bubble dynamics in metals processing operations have been studied which clarify the mechanisms of ultrasonic grain refinement and ultrasonic melt degassing. The modelling studies accomplished and the new results obtained during the course of this research comprise four parts, which are summarized below along with some general conclusions:

1. The first part of this study is concerned with the transient dynamic behavior of a hydrogen gas bubble in a solidifying aluminium-3.4 wt pct copper alloy melt under various ultrasonic pressure fields. A theoretical study was carried out to demonstrate the possibility of the dynamic grain refinement of aluminium alloys by utilizing externally applied high-powered ultrasonic waves and the hydrogen bubble present in the melt. The results showed that, during the process of bubble collapse, the melt pressure surrounding the bubble increases very rapidly. If the pressure in the vicinity of the dendrites exceeds a threshold value, dendrite fracturing takes place. The peak pressure generated in the melt is in the order of several hundreds to thousands atmospheres depending on the initial bubble size, the pressure of the undisturbed melt and the ultrasonic's specifications. Moreover, the results, which were obtained for pre-resonant, resonant and post-resonant

frequencies, showed that the ultrasonic frequencies, beyond the resonance frequency of the bubble, do not have any useful effect on the melt. The computed dynamic pressure field in the melt surrounding the hydrogen bubble demonstrated that, even far from the bubble's surface, the melt pressure is sufficiently high to fracture the dendrite arms and produce nuclei for equiaxed crystal growth.

2. The second part of this study models the dynamics of a stable bubble in a gassy liquid (melt) under various ultrasonic pressure fields. A comprehensive mathematical model has been developed to simulate the bubble growth by rectified diffusion. The model was used to determine the threshold pressure and the effects of ultrasonic specifications on rectified diffusion of the dissolved air in water. The results show that an air bubble grows in water when the ultrasonic pressure amplitude is more than the threshold pressure. In this case, the bubble volume rapidly reaches several times its initial volume and the gas bubble can achieve sufficient potential to float to the surface under the action of the hydrodynamic buoyancy force. The mathematical model with some modifications was also used to simulate a hydrogen bubble growth in an aluminium 3.4% copper alloy melt. A parametric study was carried out to demonstrate the effects of initial bubble size, the initial concentration of dissolved hydrogen gas in the molten aluminium alloy and the ultrasonic's specifications on the process of rectified diffusion. The obtained results for the hydrogen-aluminium alloy system are qualitatively similar to that of the air-water system.

3. An aqueous physical modelling was carried out to investigate the bubble growth by the process of rectified diffusion. The experimental set up and the measurement system were developed and the experimental procedure was described. The results of aqueous physical modelling for a single air bubble growth were compared to the results of the mathematical model. The comparison showed an overall reasonable agreement between the experiments and the predictions.

4. A mathematical model was developed to simulate the nonlinear volume and thermal oscillation characteristics of a reactive gas bubble in water and in glycerin. The results showed that the applied liquid pressure must be of sufficient strength to compress the bubble and ignite its reactive gas content. Under a sustained liquid pressure, if ignition does not occur, the bubble is seen to oscillate below its initial equilibrium radius. When the imposed liquid pressure is of sufficient strength, the bubble ignites and, for a fixed sustained liquid pressure, the maximum temperature that the bubble attains during its thermal oscillation depends upon its equilibrium mole fraction of the stoichiometric oxygen-hydrogen mixture. For an ignited bubble, with the increase of exothermicity, the maximum radius that the bubble attains during its radial oscillation increases and the period of radial oscillation also increases. With the decrease of the initial bubble diameter, the liquid threshold pressure for bubble explosion increases, while the period of bubble oscillation decreases. The results also showed that, under a gaussian liquid pressure profile, the bubble radius exceeds its initial value for a non-reactive mixture because of the characteristics of the gaussian liquid pressure profile. Moreover, in a liquid with high viscosity (like glycerin), the amplitude of the bubble radius oscillations clearly decreases due to the high level of viscous damping effect.

The mathematical models, developed from first principles in the present research, form a set of coupled, highly nonlinear and stiff differential equations. The task of solving the comprehensive mathematical models concerning bubble dynamics is very complex. The equation for bubble dynamics is an ordinary differential equation while the other equations are partial differential equations. In order to convert the PDEs into a system of stiff ODEs, the partial differential equations were discretized only in space direction using a *semi-discrete* method. For the numerical work, the model equations were transformed to freeze the fast moving boundary of the bubble. The transformed and non-dimensional forms of the mathematical model equations have been solved numerically by the modified Gear method.

8.2 Contributions to Knowledge

The major and novel contributions of the present work are summarized by the following statements:

1. A comprehensive mathematical model for the transient dynamic behavior of a hydrogen gas bubble in a solidifying aluminium alloy melt under an ultrasonic pressure field has been presented. The effects of bubble size and ultrasonic frequency on bubble dynamics and the pressure field generated in the melt surrounding the bubble have been numerically studied.

2. Numerical simulations for the growth of an air bubble in water as well as the hydrogen bubble growth in a molten aluminium alloy have been carried out. The effects of the characteristics of ultrasonic pressure field, initial bubble size and initial concentration of dissolved gas on the evolution of bubble have been studied.

3. A physical study of an air bubble growth inside water due to rectified diffusion of dissolved air was carried out.

4. A mathematical model for the reactive bubble in an inert liquid has been developed. The effects of exothermicity of gas mixture, initial bubble size, liquid viscosity and liquid impulse pressure profile on bubble dynamics and temperature-pressure fields within the bubble have been investigated. The results of the mathematical model were compared with the available experimental data.

5. The mathematical models and the experimental set up presented in this study are novel. All the results generated using the present models are new. Also, all the models and associated computational codes developed in this work are generic in nature and can be easily implemented for other gases and liquids not considered in the present study.

8.3 Recommendations for Future Work

1. A laboratory scale experimental work is suggested to study the ultrasonic grain refinement of a solidifying light alloy melt.

2. For the water modelling experiments, the following refinements are suggested:

i) Some modifications of the experimental set up are necessary to study the rectified diffusion for micron size bubbles. For example, a bubble generator that can produce reproducible micron size bubbles is necessary and a powerful microscope is also required. The theoretical results presented in Chapter 5 showed that under the same ultrasonic specifications, with decreasing of the initial bubble radius the bubble growth rate increases. Also, in the experiment, the bubbles of subresonant size move to the maximum point of the standing pressure waves. Therefore, the rate of bubble growth for micron size bubbles is large. All the above statements could be verified by the suggested experimental set up.

ii) In order to study the bubble growth continuously a high speed digital camera with a very fast framing speed and equipped with a powerful lens is required to take clear and precise pictures of the bubble at various instants of time.

3. It is recommended to investigate the effect of a surfactant to the rate of bubble growth during the process of rectified diffusion.

4. The present study for the bubble growth under an ultrasonic pressure field can be used as a basis for the development of a model representing multi-bubbles and their interactions. This model can be used to predict ultrasonic degassing of a gassy liquid. A laboratory scale experimental work can be carried out to study the ultrasonic degassing of a light alloy melt.

5. Modelling of the dynamics of a reactive gas bubble can be used to develop a theoretical investigation of wave propagation in reactive bubbly liquids. A

numerical simulation of shock propagation in a chemically reactive two-phase liquid containing explosive gas bubbles would be a challenging undertaking.

Table A.1. The effect of ultrasound on mechanical properties of steels (Abramov, 1987).

Steel	Metal state	Crystallization condition	Test temperature (°C)	Yield stress, σ_s (MPa)	Tensile strength, σ_b (MPa)	Relative elongation, δ (%)	Relative contraction, ψ (%)	Impact strength (MJ m ⁻²)
50 (0.5%C)	Cast	C	20		490	10	15	0.15
		US	20		630	18	28	0.28
U10 (1.0%C)	Cast	C	20	400	489	2	5	
		US	20	410	850	3	9	
40KhN (0.4%C, 1%Cr, 0.5%Ni)	Cast	C	20	560	880	9	14	
		US	20	570	900	12	25	
40KhN5S (C:4%Cr, 1%Cr, 5%Ni)	Deformed and heat treated	C	20	2300	2380	4	40	0.38
		US	20	2430	2530	4	50	0.57
Kh20N20M3 (20%Cr, 20%Ni, 3%Mo)	Cast	C	20		490	42	40	
		US	20		550	54	68	
		C	900		140	22	18	1.1
		US	900		170	28	26	1.7
Kh18N15R3 (18%Cr, 15%Ni, 3%B)	Cast	C	900		180	3	0	
		US	900		240	11	14	
		C	900		180	7	25	
		US	900		220	11	40	

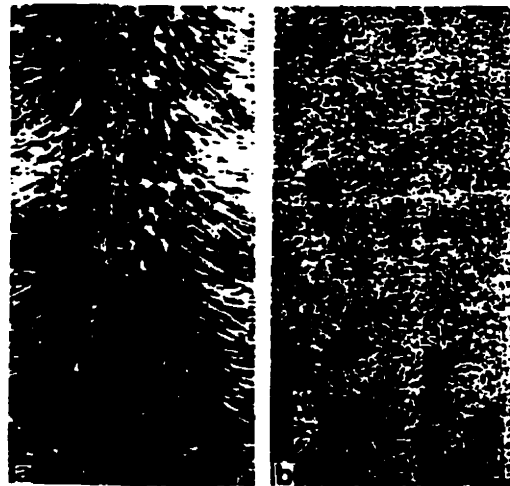


Fig. A.1. Elimination of columnar structure and formation of fine equiaxed grains in ultrasonically treated of a steel (H25T) (Abramov, 1987).

PUBLICATIONS

The following papers have been published or submitted from the present research work:

1. Naji Meidani, A. R. and M. Hasan, A Numerical Study of the Complex Dynamics Behavior of a Reactive Gas Bubble in Water, *Applied Mathematical Modelling*, Vol. 21, pp. 127-138, 1997.
2. Naji Meidani, A. R. and Hasan M, Effect of a Hydrogen Bubble in a Solidifying Al-Cu Alloy Melt Under Various Ultrasonic Pressure Fields, *Computer Applications in Metallurgy and Materials Processing, the Proceedings of the 37th Annual Conference of Metallurgists of CIM*, Calgary, pp. 94-113, 1998.
3. Naji Meidani, A. R. and Hasan M, An Aqueous Physical and Mathematical Modelling of Ultrasonic Degassing of Molten Metals, *Control and Optimization in Minerals, Metals and Materials Processing, the Proceedings of the 38th Annual Conference of Metallurgists of CIM*, Quebec, pp. 201-219, 1999.
4. Naji Meidani, A. R. and Hasan M, Dynamic Behavior of a Hydrogen Gas Bubble during Ultrasonic Treatment of Molten and Solidifying Al-Cu Alloys, *Computer Applications in Metals Processing, the Proceedings of the 40th Annual Conference of Metallurgists of CIM*, Toronto, 2001.
5. Naji Meidani, A. R. and M. Hasan, Mathematical and Physical Modelling of Bubble Growth Due to Ultrasound, Submitted to *Applied Mathematical Modelling*, MS # AMM 3106 (36 pages), May, 2001.
6. Naji Meidani, A. R. and M. Hasan, Effect of Ultrasound on a Small Hydrogen Bubble in a Solidifying Al-Cu Alloy Melt, Submitted to *Metallurgical and Materials Transactions B*, MS # 01-286-B (43 pages), June, 2001.
7. Naji Meidani, A. R. and M. Hasan, A Study of a Reactive Bubble Under Applied Pressure Pulses, Submitted to the *Canadian Journal of Chemical Engineering*, MS # 8450 (49 pages), June, 2001.